The Search for Higgs Boson Production in Association with a Top-Quark Pair in pp Collisions at $\sqrt{s} = 8$ TeV in the Lepton Plus Jets Final State

John Garland Wood

Charlottesville, VA

B.S., The University of California, Berkeley, 2008

A Dissertation presented to the Graduate Faculty

of the Unversity of Virginia in Candidacy for the Degree of

Doctor of Philosophy

Department of Physics

University of Virginia

May, 2015

Abstract

The most important goal of the Large Hadron Collider (LHC) is to elucidate the mechanism of electroweak symmetry breaking. The Higgs mechanism is thought to be a prime candidate for this, which consequently predicts the existence of an additional particle, the Standard Model (SM) Higgs boson. The newly discovered boson announced on July 4th, 2012, with a mass of $\sim$125 GeV/c^2, has so far been shown to be consistent with a SM Higgs boson. However, the final confirmation of this new particle as the SM Higgs depends on subsequent measurements of all of its properties. The observation of this new particle in association with top-quark pairs would allow the couplings of this particle to top and bottom quarks to be directly measured. $t\bar{t}H$ with Higgs decaying to $b\bar{b}$ is an excellent channel to explore due to the dominant branching ratio of Higgs to $b\bar{b}$ and the kinematic handle the $t\bar{t}$ system offers on the event. However, it presents a plethora of difficult challenges due to a low signal to background ratio and uncertainties on kinematically similar SM backgrounds. This work discusses the search for Higgs boson production in association with a top-quark pair in pp collisions at $\sqrt{s} = 8$ TeV, collected by the Compact Muon Solenoid (CMS) experiment at the LHC. The search has been performed and published in two stages. The first analysis used the first 5.1 fb^{-1}, and was followed up by the second analysis with the full 2012 dataset, using a total integrated luminosity of 19.5 fb^{-1}.

We approve the dissertation of John Garland Wood.

Date of Signature

Supervisor: Prof. Christopher Neu

Committee Member: Prof. Hank Thacker

Committee Member: Prof. Edward Murphy

PhD Committee Chair: Prof. Craig Group

Contents

Contents iv

List of Figures viii

List of Tables xx

Acknowledgements xxiii

1 Introduction 1

2 Theoretical Background 4

2.1 An Overview of Quantum Field Theory 4

2.2 Abelian Gauge Theories of Particle Interactions 7

2.3 Non-Abelian Gauge Theories of Particle Interactions 9

2.4 The Higgs Mechanism in an Abelian Theory 12

2.5 The Higgs Mechanism in a non-Abelian Theory 14

2.6 Glashow Weinberg Salam Theory 16

2.7 The Standard Model of Particle Physics 22

2.8 Higgs Production in pp Collisions at the LHC 25

2.9 $t\bar{t}H$ Production in pp Collisions at the LHC 27

2.10 Background Processes to $t\bar{t}H$ 28

2.11 Potential BSM Effects on $t\bar{t}H$ production 31

3 The Large Hadron Collider 33

3.1 The LHC Accelerator Complex 35

3.2 LHC Magnets 43

3.3 LHC RF Technology 49

3.4 The LHC Cryogen System 52

3.5 The LHC Vacuum System 53

4 The Compact Muon Solenoid 55

4.1 The Tracker 57

4.1.1 The Silicon Pixel Detector 59

4.1.2 The Silicon Strip Detector 61

4.2 The Electromagnetic Calorimeter 64

4.2.1 Vacuum Photo-Triodes 68

4.2.2 Test Rig at UVa 69

4.2.3 Results of UVa Tests 70

4.3 The Hadronic Calorimeter 73

4.4 Muon Chambers 78

4.5 Data Collection Overview 82

5 Particle Reconstruction at CMS 86

5.1 Iterative Tracking 86

5.2 Calorimeter Clustering 87

5.3 Calorimeter Energy Calibration 88

5.4 Linking 90

5.5 Physics Object Reconstruction 91

5.5.1 Muon Reconstruction 91

5.5.2 Electron Reconstruction 92

5.5.3 Charged Hadron Reconstruction 93

5.5.4 Photon and Neutral Hadron Reconstruction 93

5.5.5 Jet Reconstruction 94

5.5.6 Missing Transverse Energy Reconstruction 96

6 Analysis I: The first 5.08 fb^{-1} of 8 TeV data 98

6.1 Data and Simulated Samples 100

6.1.1 Data Samples 101

6.1.2 Signal Samples 102

6.1.3 Background Samples 102

6.1.4 MC pileup reweighting 103

6.1.5 Additional Pileup Corrections 104

6.2 Event Selection 106

6.2.1 Event cleaning 106

6.2.2 Trigger 107

6.2.3 Muon Selection 107

6.2.4 Electron Selection 108
6.2.5 Lepton selection and trigger efficiencies 109
6.2.6 Jet selection 110
6.2.7 b-tagging selection 111
6.2.8 Lepton + Jets Selection 114
6.3 Multivariate Analysis 117
6.3.1 Artificial Neural Network Overview 118
6.3.2 MVA Input Variables, Data to Monte Carlo Comparisons 122
6.3.3 MVA Output, Data to Monte Carlo Comparisons 140
6.4 Systematic Uncertainties 142
6.5 Statistical Methods 148
6.6 Results and Conclusions 151

7 Analysis II: The Complete 19.5 fb^{-1} of 8 TeV data 153
7.1 Data and Simulated Samples 153
7.1.1 Data Samples 154
7.1.2 Signal Samples 154
7.1.3 Background Samples 154
7.1.4 MC pileup reweighting 155
7.1.5 Top p_{T} Reweighting 156
7.2 Event Selection 157
7.2.1 b-tag discriminant reweighting 158
7.2.2 Lepton + Jets Selection 159
7.3 Multivariate Analysis 160
7.3.1 Boosted Decision Tree Overview 160
7.3.2 MVA Input Variables, Data to Monte Carlo Comparisons 162
7.3.3 MVA Output, Data to Monte Carlo Comparisons 177
7.4 Systematic Uncertainties 177
7.5 Statistical Methods 185
7.6 Results and Conclusions 187

8 Analysis Improvements 189
8.1 aMC@NLO, MadSpin, and Pythia8 Monte Carlo 189
8.2 Analysis Techniques Under Development 191

9 Conclusions and Summary 195

Bibliography **198**

List of Acronyms **212**

List of Figures

1.1 The CMS experiment has observed a new boson at m$\sim$125 GeV/c^2 2

1.2 A Feynman diagram of the $t\bar{t}H$ process, with Higgs$\rightarrow b\bar{b}$, and the $t\bar{t}$-system decaying semi-leptonically 3

2.1 Leading and Next to Leading Order Feynman diagrams for the coulomb scattering process 6

2.2 The global average of α_s, the QCD coupling constant [1]. 7

2.3 A visual representation of the Higgs potential [2] 12

2.4 Experimental milestones of the Standard Model 24

2.5 Higgs production cross-sections at the LHC, for 7-14 TeV pp collisions 25

2.6 Feynman diagrams for the three largest Higgs production modes at the LHC . . 26

2.7 Feynman diagram for $t\bar{t}H$ production 27

2.8 Feynman diagrams for the semileptonic $t\bar{t}H$ process and its irreducible background, $t\bar{t} + b\bar{b}$ 28

2.9 Feynman diagrams for the $t\bar{t}W$ and $t\bar{t}Z$ background processes 29

2.10 Feynman diagrams for the single t s,t, and tW background processes 29

2.11 Feynman diagrams for the W, Z plus jets, and diBoson (WW, WZ, ZZ) production. 30

2.12 Measurements of $t\bar{t}H$ backgrounds at CMS [3] 30

2.13 The cancellation of the divergent Higgs mass from a loop of top-quarks is cancelled by a loop of supersymmetric top-quarks, stop-quarks [4], ... 32

3.1 Aerial view of the LHC complex, spanning the French-Swiss border [5] 33

3.2 Integrated Luminosity delivered to the CMS experiment from 2010-12 [6] 35

3.3 The LHC accelerator complex, taking protons from a bottle of Hydrogen at the Linac2, all the way to the LHC ring [7] 36

3.4 Features of the Linac2, the first stage of acceleration in the LHC injection chain 37

3.5 Features of the PS booster, the second stage of the LHC injection chain 38

3.6 Features of the PS, the third stage of the LHC injection chain 41

3.7 Features of the SPS, the fourth and final stage of the LHC injection chain 42
3.8 The LHC ring is divided into eight octants [8] 44
3.9 The single turn injection scheme. A septum magnet makes the initial alignment. The kicker magnet times the injection and makes the final alignment. Bumper magnets align the LHC beam with the injected beam [9] 45
3.10 Layout of Interaction Region 8, where one proton beam is injected into the LHC ring. A transfer line from the SPS bring a proton in from the right. In green, a septum magnet aligns the beam horizontally with the LHC. In blue, a kicker magnet makes the final vertical alignment into the LHC, and is timed to fill one of the 400 MHz buckets of the RF capture system [8] 45
3.11 The initial filling of 6 batches of protons from the PSB to the PS, leaves 12 empty buckets in the PS bunch structure. The rise time of the SPS magnet creates an additional gap in the SPS bunch structure. Additional gaps emerge due to the rise time of the LHC injection and dumping kicker magnets [8] 46
3.12 Features of the dipole magnets used in the LHC 47
3.13 Features of the dipole magnets used in the LHC 48
3.14 Features of the 400 MHz superconducting RF system used in the LHC 49
3.15 A klystron uses a weak RF signal coupled to a resonance cavity to bunch an electron beam, which in turn creates an amplified RF signal as it passes through a second resonance cavity tuned to the same frequency [10]. 50
3.16 One of sixteen 300 kW, 400 MHz klystrons that power the superconducting RF cavities that accelerate the proton beam [11]. 51
3.17 Layout of the five cryogenic islands, which are home to the eight facilities that provide liquid helium to the LHC [12] 52
3.18 Features of the 4.5 K refrigeration system [13] 52
3.19 Cross section schematic of the cryogenic distribution system in the LHC tunnel [8] 53
3.20 Beam screen for the LHC, with slits to allow for easy pumping of residual gas molecules in the beam-pipe [14]. 54

4.1 A cutaway diagram of the CMS detector. Two humans are present at the bottom of the image to provide scale [15]. 55
4.2 A slice of the CMS detector showing how various particles interact and deposit energy. The trajectory of charged particles is measured in the tracker; electrons and photons deposit most of their energy in the ECAL; charged and neutral hadrons deposit most of their energy in the HCAL; the muon chambers measures the trajectory of muons or long-lived charged particles [16]. 56

4.3 A side view of the tracker. The pixel detector is the innermost sub-system, with three concentric rings of detectors in the barrel, and two in the endcap. The tracker inner barrel (TIB) is a silicon strip detector, with four concentric rings. The tracker inner disks (TID) are three layers deep. The tracker outer barrel (TOB) is six concentric rings and the tracker end caps (TEC) are nine layers deep [15]. 58

4.4 A head-on view of the beam-line and barrel components of the tracker [17]. . . . 58

4.5 The three barrel and two disk layers of the silicon pixel tracker provide coverage of $|\eta| < 2.5$ [15]. 59

4.6 The readout electronics chain for the pixel detector [15]. 60

4.7 In 2012 pp collisions at $\sqrt{s} = 8$ TeV, the pixel detector performed with a resolution of 11.8 μm. The above is a plot of the residual difference between a pixel and the results of a fit to a particle track [18]. 61

4.8 A silicon strip module, with two 500 μm thick sensors [15]. 62

4.9 Schematic of the readout sequence of the silicon strip detector [15]. 63

4.10 Measurements of the performance of the silicon strip track using pp collisions from 2011 at $\sqrt{s} = 7$ TeV 63

4.11 Layout of the ECAL sub-detector [15] 64

4.12 Typical Lead Tungstate crystal, with APD attached to the rear face in the left frame, and a VPT attached in the right frame [15]. 64

4.13 A simulation of the evolution of a electromagnetic shower being initiated by an electron entering the center of the front face [19]. 65

4.14 A module of 500 crystals (25 crystals wide by 20 crystal tall) [15]. 66

4.15 Schematic of the On-Detector Readout for the ECAL [15]. 67

4.16 A section of the ECAL end-cap, a Dee. Two Dees form a disk with an inner bore for the beam-line to pass through. 5x5 modules, or supercrystals, are mounted in preparation for installation at CMS [15]. 68

4.17 Vacuum Photo-Triode devices used in the ECAL end-caps (EE) 68

4.18 Features of the UVa VPT test stand 71

4.19 3 runs of 5 VPTs, exposed to blue LED light, and fit to a sum of two exponentials. 72

4.20 3 runs of 5 VPTs, exposed to orange LED light, and fit to a sum of two exponentials. 73

4.21 Longitudinal cross-section of the HCAL with the four sub-systems labeled [15]. . 74

4.22 Closeup of the HCAL barrel section. The center section of each of the 18 wedges are labeled, optical cables lay across the joint of the center and staggered edge sections of each wedge. The blue lines show the approximate azimuthal division of the wedge [15]. 75

4.23 Over 1 million Russian shells of military artillery were re-processed in the construction of the HCAL [20] 76

4.24 Optical readout chain of the HCAL scintillator tiles [15]. 76

4.25 HCAL endcap, 18 azimuthal divisions of alternating layers of brass and plastic scintillator [15]. 77

4.26 Longitudinal cross-section of the HCAL forward calorimetry, the HF [15]. 77

4.27 Longitudinal cross-section of one of the 5 wheels of the muon system. Drift tubes are placed in 4 concentric layers, with 2 being placed inside the return yoke of the magnet, and 12 azimuthal divisions [15]. 79

4.28 A cross-section view of a drift cell. The anode wire is held at 3600 V, creating a potential difference with the walls. Electric field lines are shown in blue [15]. . . 80

4.29 RPC layout for the barrel and endcaps 80

4.30 Exploded diagram of an RPC [21] 81

4.31 Cross-section of one quarter of the muon endcap system, with the 4 disks of CSC systems shown in red [15]. 81

4.32 A CSC station with 7 layers, making 6 gas chambers. Cathode strips are shown in yellow, perpendicular to the vertical anode wires in orange [15]. 82

4.33 A block diagram of the L1 trigger [15] 83

4.34 A schematic of the e/γ trigger algorithm [15]. 83

4.35 Layout of the CMS DAQ [15] 84

5.1 Results of the uncertainty on the ECAL intercalibration coefficients for the barrel (left) and endcaps (right) [22]. 89

5.2 Instantaneous luminosity response to the crystals as measured by the laser and LED system. Additional crystal calibration constants are derived to normalize the crystal response over the range of collected data [23] 90

5.3 Results of using a χ^2 minimization procedure to estimate the neutral hadron energy contribution in the HCAL using simulated events[24] 91

5.4 Muon validation plots for the particle-flow reconstruction 92

5.5 Electron validation plots for the particle-flow reconstruction 93

5.6 The anti-kt jet clustering algorithm with distance parameter R=1.0 [25] 94

5.7 Commissioning of the particle-flow algorithm on jets, involved comparing the energy measured from charged hadron tracks, to energy measured in calorimeter clusters linked to the tracks [26]. 95

5.8 A b-meson will travel a distance L_{xy} before decaying and creating a secondary vertex. The impact parameter, d_0 measures the longitudinal displacement of the two vertices [27]. 96

6.1 This figure shows the breakdown of jet-to-parton assignments for the two jets with the minimum ΔR separation in the event for events with greater or equal 4 b-tagged jets. 99

6.2 Comparison of number of reconstructed vertices for data (black) and the $t\bar{t}$ MC sample before (blue) and after (red) pileup reweighting. After pileup reweighting, the MC matches the data well. 104

6.3 H_T distribution for 8 TeV lepton plus jet events with ≥ 4 jets and ≥ 2 tags shown for different amounts of pileup. The left-hand plot shows low pileup, the middle plot shows medium pileup, and the right-hand plot shows high pileup. 105

6.4 H_T distribution for 8 TeV lepton plus jet events with ≥ 4 jets and ≥ 2 tags. The left-hand plot shows the distribution before correction. The right-hand plot shows the distribution after correction. Note that the ratio in the right-hand plot is flatter than the left-hand plot. 106

6.5 Muon and electron ID, isolation selection and trigger efficiency scale factors in bins of p_T and η. 110

6.6 Number of jets (left) and number of b-tagged jets (right) in data and simulation for events with $\geq$4 jets + $\geq$2 b-tags in the lepton+jets channel at 8 TeV. The background is normalized to the SM expectation; the uncertainty band (shown as a hatched band in the stack plot and a green band in the ratio plot) includes statistical and systematic uncertainties that affect both the rate and shape of the background distributions. The $t\bar{t}H$ signal ($m_H = 125\,\mathrm{GeV}/c^2$) is normalized to 30 $\times$ SM expectation. 117

6.7 A simple example of a MLP type ANN, with one layer of input neurons that make connections to a hidden layer, which is connected to the output layer [28] 118

6.8 The CFMlpANN architecture used in this analysis features two hidden layers, and 10 input variables for each jet/tag category (11 variables for the $\geq$6jets, $\geq$4b-tags category) 119

6.9 Comparisons of the testing and training samples used to optimize the CFMlpANN weights for each jet/tag category 121

6.10 Lepton + jets data/MC comparison for the ≥6 jets + 2 tag category. The uncertainty band includes statistical and systematic uncertainties that affect both the rate and shape of the background distributions. 127

6.11 Lepton + jets data/MC comparison for the ≥ 6 jets + 2 tag category. The uncertainty band includes statistical and systematic uncertainties that affect both the rate and shape of the background distributions. 128

6.12 Lepton + jets data/MC comparison for the 4 jets + 3 tag category. The uncertainty band includes statistical and systematic uncertainties that affect both the rate and shape of the background distributions. 129

6.13 Lepton + jets data/MC comparison for the 4 jets + 3 tag category. The uncertainty band includes statistical and systematic uncertainties that affect both the rate and shape of the background distributions. 130

6.14 Distributions of the five ANN input variables with rankings 1 through 5, in terms of separation, for the 5 jets + 3 b-tags category of the lepton+jets channel at 8 TeV. Definitions of the variables are given in the text. The background is normalized to the SM expectation; the uncertainty band (shown as a hatched band in the stack plot and a green band in the ratio plot) includes statistical and systematic uncertainties that affect both the rate and shape of the background distributions. The $t\bar{t}H$ signal ($m_H = 125\,\mathrm{GeV}/c^2$) is normalized to the total background yield, for easier comparison of the shapes. 131

6.15 Distributions of the five ANN input variables with rankings 6 through 10, in terms of separation, for the 5 jets + 3 b-tags category of the lepton+jets channel at 8 TeV. Definitions of the variables are given in the text. The background is normalized to the SM expectation; the uncertainty band (shown as a hatched band in the stack plot and a green band in the ratio plot) includes statistical and systematic uncertainties that affect both the rate and shape of the background distributions. The $t\bar{t}H$ signal ($m_H = 125\,\mathrm{GeV}/c^2$) is normalized to the total background yield, for easier comparison of the shapes. 132

6.16 Lepton + jets data/MC comparison for the ≥6 jets + 3 tag category. The uncertainty band includes statistical and systematic uncertainties that affect both the rate and shape of the background distributions. 133

6.17 Lepton + jets data/MC comparison for the ≥6 jets + 3 tag category. The uncertainty band includes statistical and systematic uncertainties that affect both the rate and shape of the background distributions. 134

6.18 Lepton + jets data/MC comparison for the 4 jets + 4 tag category. The uncertainty band includes statistical and systematic uncertainties that affect both the rate and shape of the background distributions. 135

6.19 Lepton + jets data/MC comparison for the 4 jets + 4 tag category. The uncertainty band includes statistical and systematic uncertainties that affect both the rate and shape of the background distributions. 136

6.20 Lepton + jets data/MC comparison for the 5 jets + 4 tag category. The uncertainty band includes statistical and systematic uncertainties that affect both the rate and shape of the background distributions. 137

6.21 Lepton + jets data/MC comparison for the 5 jets + 4 tag category. The uncertainty band includes statistical and systematic uncertainties that affect both the rate and shape of the background distributions. 138

6.22 Lepton + jets data/MC comparison for the $\geq$ 6 jets + 4 tag category. The uncertainty band includes statistical and systematic uncertainties that affect both the rate and shape of the background distributions. 139

6.23 Lepton + jets data/MC comparison for the $\geq$ 6 jets + 4 tag category. The uncertainty band includes statistical and systematic uncertainties that affect both the rate and shape of the background distributions. 140

6.24 The distributions of the CFMlpANN output for lepton+jets events at 8 TeV in the various analysis categories. Background-like events have a low CFMlpANN output value. Signal-like events have a high CFMlpANN output value. The background is normalized to the SM expectation; the uncertainty (shown as a hatched band in the stack plot and a green band in the ratio plot) includes statistical and systematic uncertainties that affect both the rate and shape of the background distributions. The $t\bar{t}H$ signal ($m_H = 125\,\mathrm{GeV}/c^2$) is normalized to 30 $\times$ SM expectation. 141

6.25 Comparison of the MVA discriminator for JES shift upwards (red) and downwards (blue) relative to the nominal (black) shape for the $t\bar{t}H(120)$ signal (left) and the main background sample $t\bar{t}+$ light flavor (right). The plots shown are from the $\geq$6 jet $\geq$4 tag category in the lepton+jets channel. All plots are normalized to unit area. 143

6.26 Comparison of the MVA discriminator for b-tag scale factor shift upwards (red) and downwards (blue) relative to the nominal (black) shape for the $t\bar{t}H(120)$ signal (left) and the main background sample $t\bar{t}$ + light flavor (right). The plots are from the ≥6 jets + ≥4 tags category in the lepton+jets channel. All plots are normalized to unit area. 144

6.27 Comparison of the MVA discriminator for additional PU correction systematic upwards (red) and downwards (blue) relative to the nominal (black) shape for the $t\bar{t}H(120)$ signal (left) and the main background sample $t\bar{t}$ + light flavor (right). The plots are from the ≥6 jets + ≥4 tags category in the lepton+jets channel. All plots are normalized to unit area. 145

6.28 The rate and shape variations for selected categories due to the Q^2 uncertainty. . 147

6.29 A dedicated CFMlpANN trained to isolate $t\bar{t} + b\bar{b}$ from $t\bar{t} + jets$. The left plot shows is for the case of nominal $t\bar{t}+b\bar{b}$ cross-section, the right plot shows the case for x2 $t\bar{t}+b\bar{b}$ cross-section. The left-most region of both plots is the most sensitive to the $t\bar{t}+b\bar{b}$ normalization, and shows no significant improvement in data to MC agreement, justifying the reasoning that an uncertainty larger than 50% is needed. 148

6.30 The expected and observed 95% CL upper limits on the signal strength parameter $\mu = \sigma/\sigma_{SM}$ for the lepton+jets channel using the 2012 dataset. These limits were extracted using the asymptotic method. 152

7.1 Comparison of number of reconstructed vertices for data (black) and the sum of all background MC samples before (red) and after (blue) pileup reweighting. After pileup reweighting, the MC matches the data well. 156

7.2 The scale factors from top differential crosse section group, the fitting as well as the $\pm 1\sigma$ variations. 157

7.3 Leading jet p_{T} distribution for 8 TeV lepton plus jet events with ≥4 jets and ≥2 tags. The left-hand plot shows the distribution before top p_{T} reweighting. The right-hand plot shows the distribution after top p_{T} reweighting. Note that the ratio in the right-hand plot is flatter than the left-hand plot. 157

7.4 Comparison of yields for the different categories (top), number of jets (bottom left), and number of tagged jets (bottom right) in data and Monte Carlo for events with one lepton μ or e, ≥ 4 jets and ≥ 2 tags. 160

7.5 Example of a decision tree, which chooses a set of variables to cut on, in order to produce a region of events with high signal purity 161

7.6 Comparisons of the testing and training samples used to optimize the BDT weights for each jet/tag category 163

7.7 Data/MC comparisons for events with one lepton and ≥6 jets + 2b- tags. The uncertainty band includes statistical and systematic uncertainties that affect both the rate and shape of the background distributions. 167

7.8 Data/MC comparisons for events with one lepton and 4 jets + 3 b-tags. The uncertainty band includes statistical and systematic uncertainties that affect both the rate and shape of the background distributions. 168

7.9 Data/MC comparisons for events with one lepton and 5 jets + 3 b-tags. The uncertainty band includes statistical and systematic uncertainties that affect both the rate and shape of the background distributions. 169

7.10 Data/MC comparisons for events with one lepton and ≥6 jets + 3 b-tags. The uncertainty band includes statistical and systematic uncertainties that affect both the rate and shape of the background distributions. 170

7.11 Data/MC comparisons for events with one lepton and ≥6 jets + 3 b-tags. The uncertainty band includes statistical and systematic uncertainties that affect both the rate and shape of the background distributions. 171

7.12 Data/MC comparisons for events with one lepton and 4 jets + 4 b-tags. The uncertainty band includes statistical and systematic uncertainties that affect both the rate and shape of the background distributions. 172

7.13 Data/MC comparisons for events with one lepton and 5 jets +≥4 b-tags. The uncertainty band includes statistical and systematic uncertainties that affect both the rate and shape of the background distributions. 173

7.14 Data/MC comparisons for events with one lepton and 5 jets +≥4 b-tags. The uncertainty band includes statistical and systematic uncertainties that affect both the rate and shape of the background distributions. 174

7.15 Data/MC comparisons for events with one lepton and ≥6 jets + ≥4 b-tags. The uncertainty band includes statistical and systematic uncertainties that affect both the rate and shape of the background distributions. 175

7.16 Data/MC comparisons for events with one lepton and ≥6 jets + ≥4 b-tags. The uncertainty band includes statistical and systematic uncertainties that affect both the rate and shape of the background distributions. 176

7.17 Final BDT output for lepton + jet events. Background-like events have a low BDT output value. Signal-like events have a high BDT output value. The uncertainty band includes statistical and systematic uncertainties that affect both the rate and shape of the background distributions. The top, middle and, bottom rows are events with 4, 5, and ≥6 jets, respectively, while the left, middle, and right-hand columns are events with 2, 3, and ≥4 b-tags, respectively. The $t\bar{t}H$ signal ($m_H = 125\,\mathrm{GeV}$) is normalized to 30 × SM expectation. 178

7.18 Comparison of the MVA discriminator for JES shift upwards (red) and downwards (blue) relative to the nominal (black) shape for the $t\bar{t}H(125)$ signal (left) and the main background sample $t\bar{t}\ + b\bar{b}$ (right). The plots are from the ≥ 6 jet ≥ 4 tag category in the lepton+jets channel. All plots are normalized to unit area. 179

7.19 Comparison of the MVA discriminator when shifting the light flavor contamination in the heavy flavor scale factor determination shift upwards (red) and downwards (blue) relative to the nominal (black) shape for the $t\bar{t}H(125)$ signal (top row) and $t\bar{t}\ +b\bar{b}$ and $t\bar{t}$ +LF background samples (middle row and bottom row respectively). The plots are from the LJ ≥ 6 jet ≥ 4 category. All plots are normalized to unit area. 180

7.20 Comparison of the MVA discriminator when shifting the heavy flavor contamination in the light flavor scale factor determination shift upwards (red) and downwards (blue) relative to the nominal (black) shape for the $t\bar{t}H(125)$ signal (top row) and $t\bar{t}\ + b\bar{b}$ and $t\bar{t}$ +LF background samples (middle row and bottom row respectively). The plots are from the LJ ≥ 6 jet ≥ 4 category. All plots are normalized to unit area. 180

7.21 Comparison of the MVA discriminator when shifting to account for the statistical uncertainty on the heavy flavor scale factor extraction. Two classes of distortion in the scale factor are considered: linear distortions (labeled "Stat. Error 1") and nonlinear distortions (labeled "Stat. Error 2"). Both shift upwards (red) and downwards (blue) relative to the nominal (black) shape for the $t\bar{t}H(125)$ signal (top row) and $t\bar{t}\ + b\bar{b}$ and $t\bar{t}$ +LF background samples (middle row and bottom row respectively) are shown. The plots are from the ≥ 6 jet ≥ 4 category. All plots are normalized to unit area. 181

7.22 Comparison of the MVA discriminator when shifting to account for the statistical uncertainty on the light flavor scale factor extraction. Two classes of distortion in the scale factor are considered: linear distortions (labeled "Stat. Error 1") and nonlinear distortions (labeled "Stat. Error 2"). Both shift upwards (red) and downwards (blue) relative to the nominal (black) shape for the $t\bar{t}H(125)$ signal (top row) and $t\bar{t}$ $+b\bar{b}$ and $t\bar{t}$ +LF background samples (middle row and bottom row respectively) are shown. The plots are from the ≥ 6 jet ≥ 4 category. All plots are normalized to unit area. 181

7.23 Comparison of the MVA discriminator when shifting to account for the uncertainty on the charm jets scale factor extraction. Two classes of distortion in the scale factor are considered: linear distortions (labeled "Error 1") and nonlinear distortions (labeled "Error 2"). Both shift upwards (red) and downwards (blue) relative to the nominal (black) shape for the $t\bar{t}H(125)$ signal (top row) and $t\bar{t}+c\bar{c}$ and $t\bar{t}$ +LF background samples (middle row and bottom row respectively) are shown. The plots are from the ≥ 6 jet ≥ 4 category. All plots are normalized to unit area. 182

7.24 Comparison of the MVA discriminator for shifts in top quark p_{T} reweighting upwards (red) and downwards (blue) relative to the nominal (black) shape for the $t\bar{t}$ +LF background (left) and the $t\bar{t}$ $+b\bar{b}$ (right). The plots are from the ≥ 6 jets + ≥ 4 tags category in the lepton+jets channel. All plots are normalized to unit area. 183

7.25 Comparison of the MVA discriminator when shifting the Q^2 scale up and down by its uncertainties. Shown are the shift upwards (red) and downwards (blue) relative to the nominal (black) shape for the $t\bar{t}$ $+b\bar{b}$ (top row) $t\bar{t}$ $+b$ (middle row) and $t\bar{t}$ +LF (bottom) background samples. The plots are from the LJ ≥ 6 jet ≥ 4 category. All plots are normalized to unit area. 184

7.26 The expected and observed 95% CL upper limits on the signal strength parameter $\mu = \sigma/\sigma_{SM}$ for the lepton+jets channel using the 2012 dataset. These limits were extracted using the asymptotic method. 187

8.1 The number of reconstructed jets passing selection (left) and that have additionally been b-tagged (right) for $t\bar{t}H$, $t\bar{t}+jets$, and $t\bar{t}+b\bar{b}$ samples generated with the aMC@NLO and Pythia 8 framework 191

8.2 The invariant mass of the W boson in the $t\bar{t}$ decay for the case of the MC truth (red), correctly associated reconstructed jets (blue), and incorrectly associated reconstructed jets (green) 192

8.3 The cosine of the angle between the momentum three-vectors for the b-quarks from the top decays (left), the lepton and the up-type W boson daughter (center), and the lepton and the down-type W boson daughter (right) 192
8.4 The difference in the ϕ coordinate between the momentum three-vectors for the b-quarks from the top decays (left), the lepton and the up-type W boson daughter (center), and the lepton and the down-type W boson daughter (right) 193
8.5 Jet times lepton charge, for the b-jet associated with the same top as the lepton. Green shows incorrectly associated reconstructed jets, blue shows correctly associated jets, and red is the MC truth 194

List of Tables

2.1 The quantum numbers Isospin and Hypercharge are assigned for each of the $SU(2)$ and $U(1)$ symmetries respectively 20

4.1 Fit Results for VPT Conditioning Studies at U.Va. and Brunel, Blue Reference LED 72

4.2 Fit Results for VPT Conditioning Studies at U.Va., Orange LED 73

6.1 The datasets analyzed for this analysis. 102

6.2 List of signal MC datasets and cross sections used to determine the SM expectation. 102

6.3 List of background MC datasets and cross sections used for normalization. 103

6.4 List of lepton+jets triggers 107

6.5 Tight and loose muon definition 108

6.6 Tight and loose muon definition 109

6.7 Jet definition 111

6.8 Jet Energy Resolution (JER) scale factors 111

6.9 Expected event yields in 5 fb^{-1} for signal and backgrounds in the μ+jets channel. 115

6.10 Expected event yields in 5 fb^{-1} for signal and backgrounds in the e+jets channel. 115

6.11 Expected event yields in 5 fb^{-1} for signal and backgrounds in the μ+jets channel. 116

6.12 The ANN inputs for the nine jet-tag categories in the 8 TeV $t\bar{t}H$ analysis in the lepton+jets and dilepton channels. The choice of inputs is optimized for each category. Definitions of the variables are given in the text. The best input variable for each jet-tag category is denoted by ★. 123

6.13 Summary of the systematic uncertainties considered on the inputs to the limit calculation. Except where noted, each row in this table will be treated as a single, independent nuisance parameter. 142

6.14 Relative yield change due to JES shift up/down for the ≥ 6 jets + ≥ 4 tags category in the lepton+jets channel. 143

6.15 Relative yield change due to b-tag scale factor shift up/down for the ≥6 jets + ≥4 tags category in the lepton+jets channel. 144

6.16 Cross section uncertainties used for the limit settings. Each column in the table is an independent source of uncertainty, except for the last column which represents uncertainties uncorrelated with any others. Uncertainties in the same column for two different processes (different rows) are completely correlated. 146

6.17 Expected and observed upper limits for SM Higgs for lepton + jets channel using the first 5.1 fb^{-1} of the 2012 dataset. These limits were extracted using the asymptotic method. 151

7.1 The datasets analyzed for this analysis. 154

7.2 List of signal MC datasets and cross sections used to determine the SM expectation. 154

7.3 List of background MC datasets and cross sections used for normalization. 155

7.4 Observed data event yields, expected event yields in 19.5 fb^{-1} for signal and backgrounds in the lepton+jets channel. 160

7.5 Event variables used in dilepton and lepton+jets BDT training and their descriptions. 164

7.6 BDT input variable assignments for the lepton+jets categories. 165

7.7 List of variables used as inputs in each of the ttbb/ttH BDTs. See table 7.5 for definitions. 165

7.8 Relative yield change due to JES shift up/down for the ≥3 tag category in the dilepton channel and the ≥ 6 jets + ≥ 4 tags category in the lepton+jets channel. 177

7.9 This table summarizes the rate effect of the six independent nuisance parameters that characterize the b-tag uncertainties. (Note: The b-tag rate uncertainties associated with JES variations are already included with the JES rate uncertainties in Table 6.14. The impact of statistical uncertainties is in the heavy-flavor and light-flavor scale factor extraction is incorporated using two separate nuisance parameters, as described above. The uncertainty labeled “Stat. Err. 1” represents statistical uncertainties resulting a linear distortion of the CSV scale factor, while the one labeled “Stat. Err. 2” corresponds to nonlinear distortions. 182

7.10 Relative yield change due to varying the top quark p_{T} reweighting. The “up” variation corresponds to apply twice as much correction to the top quark p_{T} distribution as the nominal, while the “down” correction corresponds to applying no correction to the default MC top quark p_{T} distribution. 183

7.11 Cross section uncertainties used for the limit settings. Each column in the table is an independent source of uncertainty, except for the last column which represents uncertainties uncorrelated with any others. Uncertainties in the same column for two different processes (different rows) are completely correlated. 184

7.12 This table summarizes the rate effect of shifting Q^2 scale uncertainty for Madgraph. Note that the shifts are made independently for the following topologies: $t\bar{t}\ +0p$, $t\bar{t}\ +1p$, $t\bar{t}\ +2p$, $t\bar{t}+c\bar{c}$, $t\bar{t}\ +b$, and $t\bar{t}\ +b\bar{b}$ 184

7.13 Summary for the of the systematic uncertainties considered on the inputs to the limit calculation. Except where noted, each row in this table will be treated as a single, independent nuisance parameter. 185

7.14 Specific effect of systematics on predicted background yields for events with ≥ 6 jets and ≥ 4 b-tags. Here we only consider the sum of the largest backgrounds, $t\bar{t}$ +lf, $t\bar{t}\ +b$, $t\bar{t}\ +b\bar{b}$, and $t\bar{t}+c\bar{c}$. These three backgrounds account for 94% of all background events. The signal is 3.5% of the yield of the three main backgrounds. The signal fraction is directly comparable to the variations of the background in the table. The table shows that the signal is much smaller than many of the background variations. 186

7.15 Expected and observed upper limits for SM Higgs for lepton + jets channel using the 2012 dataset. These limits were extracted using the asymptotic method. . . . 187

Acknowledgements

First and foremost, the analysis described in this dissertation would be impossible without the thousands of individuals that have contributed to the design, construction, and commissioning of the Large Hadron Collider (LHC) and Compact Muon Solenoid (CMS) experiment. The countless years of passion and dedication that have been poured into these machines have resulted in the most sophisticated tools ever available to mankind to explore the frontiers of high energy physics. I am extremely grateful for the opportunity to participate in this collaboration and to contribute to the understanding of physics at the TeV energy scale.

I would like to thank Mike Arenton, Dave Cockerill and Alexander Ledovskoy for their tutelage and mentorship in regards to my studies with the UVa Vacuum Photo-Triode (VPT) rig. This project has been a critical to improving my understanding of electronics, firmware, and signal analysis, and has been both a challenging and exciting experience. I would also like to thank Thomas Anderson, Brian Franchise, Joseph Goodell, Al Tobias, and Evan Wolfe for all of their help in maintaining the 4 T magnet and ensuring the VPT rig has survived long enough to collect and analyze the data on these devices. I woud also like to thank Professors Brad Cox and Bob Hirosky of the CMS research group here at UVa for always challenging me to improve the VPT rig and analysis, while still providing me with all of the tools and input I needed to succeed.

The $t\bar{t}H$ analysis group at CMS has been provided an incredibly supportive environment to learn about particle physics and data analysis. I would like to thank Professor Kevin Lannon of the University of Notre Dame (ND) and Professors Richard Hughes and Brian Winer of the Ohio State University (OSU) for pushing the group as hard as possible while still maintaining a high level of quality for the work and studies presented each week. Additional thanks go out to the post-doctoral and graduate students at these Universities: Darren Puigh and Geoff Smith of ND and Jason Slaunwhite, Andrew Brinkerhoff, Wuming Luo, and Anna Woodard of OSU, without whom, this analysis would not have been published twice, nor would I be reflecting so fondly on a period of times that involved an intense set of deadlines and a lot of late nights.

To my fellow graduate students and good friends here at UVa: Thomas Anderson, Tanwa

Apornthip, Alexandr Arakelyan, Sana Deshmukh, Ryan Duve, Adam Fallon, Brian Francis, Joe Johnson, Manolis Kargiantoulakis, Micah Shiable, Julie Spencer, Niranjan Sridhar, Evan Wolfe, and too many more to list, you know who you are, thank you for so many wonderfully hazy nights that have helped me from going insane in graduate school. To my friends abroad: Supaksh Gupta, Kat Hunter, Ryan Karlsgodt, Kevin Karlsgodt, Ginny Morris, Mark Nicholson, Matt Pierce, Mikey Sheffield, Tyler Vickers, and the many others who also know who you are, thank you for continuing to be amazing friends throughout all these years apart.

I would like to give special thanks to Dr. Sarah Boutle, who has been an amazing mentor and friend. I owe so much of my understanding of particle physics, the LHC, and CMS to the countless conversations and coffee breaks we shared. I have been incredibly lucky to also have a role model of someone who has balanced a successful career as a scientist and still manages to maintain a caring, well-grounded personality with a great sense of humor, even during the most daunting and stressful of situations.

These acknowledgements would be incomplete without mention of Professor Chris Neu, who hooked me on studying particle physics at CMS during our first conversation together. Since then, I have had the privilege of being his student for the past six years. It has been an incredibly rewarding experience. Under his guidance, I have travelled around the world, analyzed and unblinded a historically significant dataset in the field of particle physics, and participated in one of the largest scientific collaborations in the history of mankind. I cannot thank him enough for everything I have learned, and for all of the amazing scientific opportunities he has provided.

I would like to acknowledge all of the love and support given to me by my family. Aunt Carolyn and cousin Gaylon, thank you for all of the Thanksgiving feasts, and for making me feel at home on the East Coast. Little sister, Carrie, thank you for always reminding me to keep an open heart and mind in all matters in life. Mom and Dad, thank for you encouraging me to follow my dreams and giving me every opportunity to do the things I love.

To the love of my life, Whitney Wegman, you have been the most incredible source of inspiration and happiness for me throughout the three and a half years we have been together at this point. I cannot have done this without all of your love and support.

Chapter 1

Introduction

On July 4th, 2012, the Compact Muon Solenoid (CMS) and A Toroidal LHC Apparatus (ATLAS) experiments announced the discovery of a new boson of mass $\sim 125\,\text{GeV}$ [31][32]. The particle has been shown to be increasingly consistent with the description of the boson predicted by the Higgs mechanism of the SM, as measurements on its mass, width, and quantum numbers are completed. Figure 1.1 shows a consistent mass peak between the $H \to ZZ$ and $H \to \gamma\gamma$ channels at the CMS experiment. However, there are several properties of this new boson, which remain to be tested.

The Yukawaka-coupling of the Higgs boson to the top quark in the SM is the largest coupling among the fundamental particles and is well predicted - thus offering an excellent test of the nature of the coupling of the Higgs to fermions, as well as a potential probe into physics Beyond the Standard Model (BSM) that would alter this value from the SM prediction. The production of the Higgs boson in association with top-quark pairs is the best production mode at the LHC that offers direct access to the top-Higgs coupling. The dominant production mode of Higgs at the LHC, gluon-gluon fusion, involves a triangle loop of strongly-coupled fermions, which includes all of the other quarks, as well as the potential for BSM particles, and thus does involve a pure top-Higgs coupling.

$t\bar{t}H$ production also has the ability to constrain some extensions of the SM that would not modify the Higgs branching fractions enough to be seen within current experimental precision. Such models include Little Higgs models, models with extra dimensions, top-color models, and composite Higgs models that introduce a vector-like top partner, a t', that can decay to tH, bW, or tZ states. Both $t't'$ and $t't$ production would produce a $t\bar{t}H$ final state, or one that is indistinguishable from it ($tHbW$). Upper limits on $t\bar{t}H$ production would also provide limits on the previously described models, which would be complementary to existing direct searches for t' particles, which attempt to reconstruct the t' resonance.

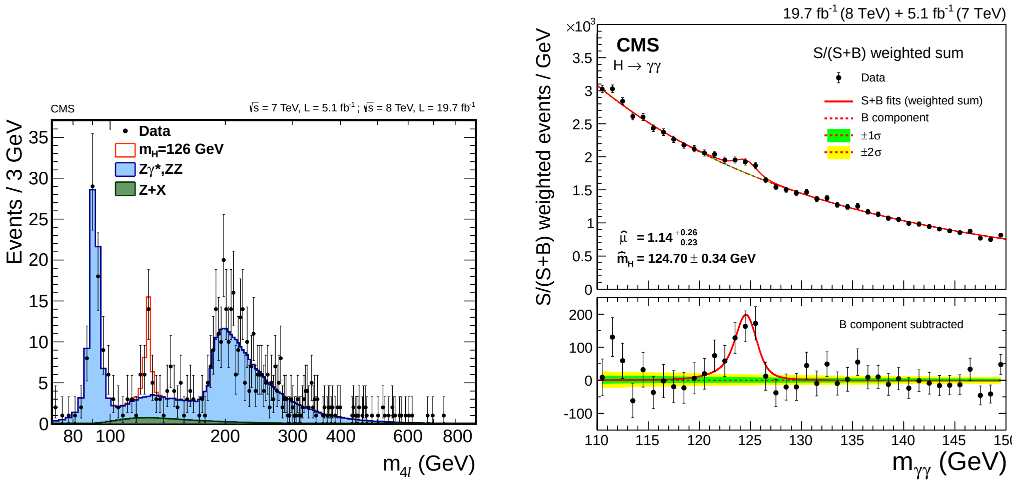

(a) $H \rightarrow\ ZZ$ channel [29] (b) $H \rightarrow \gamma\gamma$ channel [30]

Figure 1.1: The CMS experiment has observed a new boson at m$\sim$125 GeV/c^2

The $t\bar{t}H$ channel has a rich set of possible final states. Each top quark will decay to a b quark and a W boson. The W boson will subsequently decay to two quarks, or a lepton and a neutrino. These decays are classified as either hadronic, semi-leptonic, or di-leptonic for zero, one, or both top quarks decaying leptonically respectively. The Higgs may to decay to b quark, W, Z, τ, or γ pairs. In fact, this is one of the only production modes at the LHC which has access to every Higgs decay mode, as other production mechanisms are swamped by large backgrounds preventing measurements of all Higgs decay types.

The search is performed with the CMS experiment, a modern, general purpose particle detector capable of reconstructing and identifying hadronic jets, photons, electrons, muons, and tau leptons. The hermetic design, and its high precision and efficiency in reconstructing and tracking every particle in a pp collision, also makes it suitable for reconstructing missing transverse energy from the calculated momentum imbalance of all of the measured particles in the event. This missing transverse energy is often the signature of a neutrino, which is the only SM particle capable of escaping detection. The detector uses a 3.8 T axial magnetic field, produced by the solenoid it is named after, to bend charged particles as they travel through the detector. The measured curvature of their tracks allows the momentum of the particles to be calculated to a high precision. Tracks are formed and particles are reconstructed by a combination of sub-detector systems which work together to form the final final reconstructed image of each particle in the collision.

This thesis will focus on a semi-leptonic decay of the top quarks, with the Higgs decaying to a b-quark pair. Figure 1.2 is a Feynman diagram of the $t\bar{t}H$ process. The largest background to this process is top-quark pair production with extra jets originating from Initial State Radiation (ISR) or Final State Radiation (FSR) radiation, $t\bar{t}+jets$. The irreducible background is formed

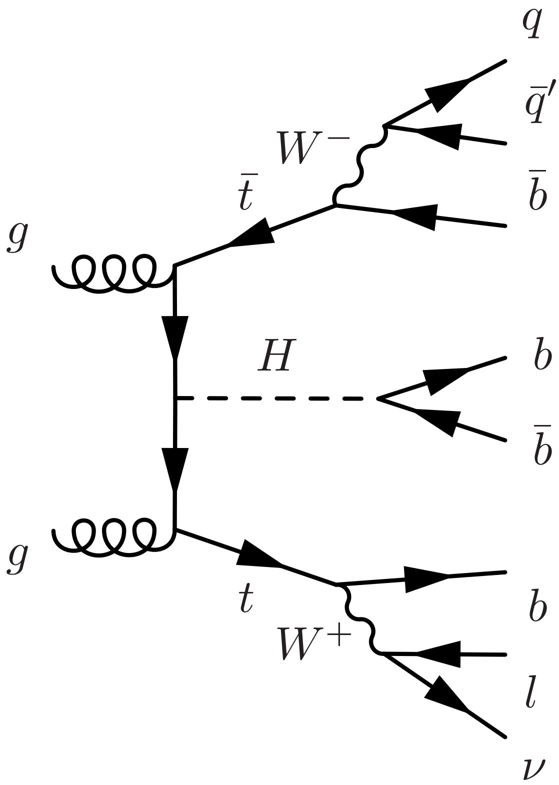

Figure 1.2: A Feynman diagram of the $t\bar{t}H$ process, with Higgs$\rightarrow b\bar{b}$, and the $t\bar{t}$-system decaying semi-leptonically

by top-quark pairs, where a gluon is radiated and decays to a b-quark pair, $t\bar{t}+b\bar{b}$. In addition to the large backgrounds, the high jet multiplicity in the $t\bar{t}H$ final state gives rise to a combinatorics problem in associating each jet with its role in the $t\bar{t}H$ system. This inevitably leads to misidentifying which jets are the decay product of the Higgs, and thus additionally smears out the resolution on the mass of the Higgs. Due to the similarity of the $t\bar{t}+b\bar{b}$ background and the combinatorics issue, no single variable is suitable for signal extraction. A Multi-Variate Analysis (MVA) technique is used in an attempt to isolate the $t\bar{t}H$ signal from the $t\bar{t}+jets$ background. The MVA provides a one-dimensional discriminant based on several input variables related to the kinematics of the event. This discrimant is then used to perform signal extraction and set upper-limits on $t\bar{t}H$ production. The results of two searches will be presented. The first result used the first 5.1 fb^{-1} of the 2012 dataset, with center of mass energy of 8 TeV, and was published in the Journal of High Energy Physics (JHEP), May 2013. The second result was update with the full 19.4 fb^{-1} 8 TeV dataset, and was published in JHEP, Spetember 2014.

Chapter 2

Theoretical Background

The Standard Model (SM) of particle physics represents the sum of knowledge about the fundamental particles and their interactions with each other. It is a Quantum Field Theory (QFT) that represents the interactions of each of the fundamental forces through the symmetry of a mathematical object known as a Lie group. It is the theory that dictates the rate that the $t\bar{t}H$ process is produced, as well as the kinematics of every particle involved. As such, its predictions are critical for modeling the characteristic signature of the $t\bar{t}H$ signal in the CMS detector, as well as the background processes, like $t\bar{t}+b\bar{b}$ which leave a kinematically similar final-state signature.

2.1 An Overview of Quantum Field Theory

Quantum Field Theory (QFT) was developed out of the need for a relativistic description of quantum mechanics. Since the Einstein relation $E = mc^2$ allows for the creation of particle-antiparticle pairs, the single-particle description used in non-relativistic quantum mechanics, fails to describe this phenomenon [33]. The single-particle description additionally fails when considering that Heisenberg's uncertainty relation, $\Delta\ E \cdot \Delta\ t = \hbar$, allows for an arbitrary number of intermediate, virtual particles to be created. By quantizing a field representing a certain type of particle, multi-particle states are naturally described as discreet excitations of that field.

Lorentz invariance, and the need to preserve causality, also define a fundamental relationship between matter and antimatter. The propagation of a particle across a space-like interval is treated equivalently to an anti-particle propagating in the opposite direction [33]. This is done so that the net probability amplitude for the particles to have an effect on a measurement occurring across a space-like interval cancel each other, thus preserving causality. This cancellation requirement additionally implies that the particle and anti-particle have the same mass, with opposite quantum numbers such as spin or electric charge.

The Lorentz transformations for a scalar field are different than for a field with internal degrees of freedom, such as spin. A rotation on a vector field, will affect both its location, as well as its orientation [33]. This means the Lorentz invariant equation of motion describing a scalar field will have a different form than equations of motion for a field with non-zero spin. The most relevant equations describe the particles of SM, which contain spins of 0, 1/2, and 1. They are described by the Klein-Gordon, Dirac, and Proca equations respectively.

Klein-Gordon equation, for scalar (spin 0) fields

$$(\partial^2 + m^2)\phi = 0 \tag{2.1}$$

Dirac equation, for spinor (spin 1/2) fields

$$(i\gamma^\mu \partial_\mu - m)\psi = 0 \tag{2.2}$$

Proca equation, for vector (spin 1) fields

$$\partial_\mu(\partial^\mu A^\nu - \partial^\nu A^\mu) + m^2 A^\nu = 0 \tag{2.3}$$

With these equations, one can build a theory of free particles. The Lagrangian formulation is the most appropriate since all expressions are explicitly Lorentz invariant [33]. The Lagrangians for the Klein-Gordon, Dirac, and Proca equations are given as:

Klein-Gordon Lagrangian, for real and complex scalar fields

$$\begin{aligned} \mathcal{L} &= \partial_\mu \partial^\mu \phi^2 - \frac{1}{2} m^2 \phi^2 \\ \mathcal{L} &= (\partial_\mu \phi)^* (\partial^\mu \phi) - m^2 (\phi)^* (\phi) \end{aligned} \tag{2.4}$$

Dirac Lagrangian, for spinor fields

$$\mathcal{L} = i\bar{\psi}\gamma^\mu \partial_\mu \psi - m\bar{\psi}\psi \tag{2.5}$$

Proca Lagrangian, for vector fields

$$\mathcal{L} = -\frac{1}{4} F_{\mu\nu} F^{\mu\nu} + m^2 A^\nu A_\mu \tag{2.6}$$

where $F_{\mu\nu}$, is the field strength tensor, defined as $F_{\mu\nu} = \partial_\mu A_\nu - \partial_\nu A_\mu$

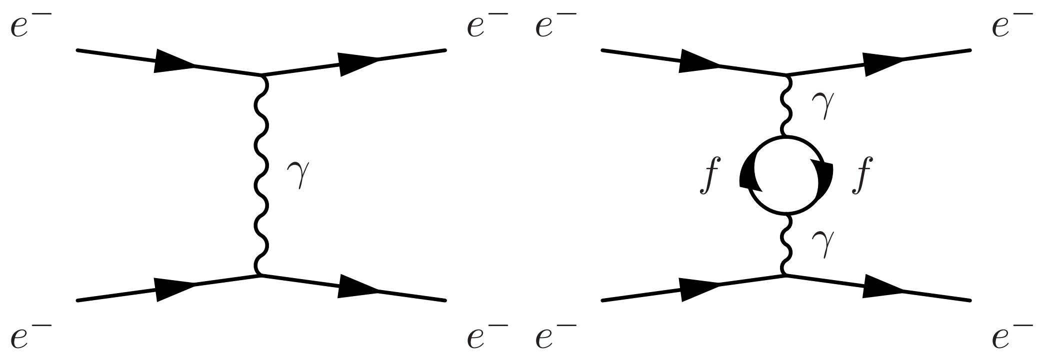

(a) A LO Feynman diagram (b) A NLO Feynman diagram

Figure 2.1: Leading and Next to Leading Order Feynman diagrams for the coulomb scattering process

Interactions are generated by coupling multiple fields together in a single term, such as $ieA_\mu\bar{\psi}\psi$ and treating it as a perturbation to the free-field theory. This implies every interaction between particles is carried out by a virtual mediating particle. When two electrons scatter off one another, they are really exchanging a virtual photon, the mediator of the electromagnetic force. The $W^\pm$ and Z bosons mediate the weak force, while the gluons mediate the strong force.

$$\mathcal{L} = \mathcal{L}_{Free} + \mathcal{L}_{Interacting} \tag{2.7}$$

In order to calculate the probability and dynamics of two particles interacting with one another, an integral, constrained by energy and momentum conservation, over the phase space of outgoing particles and the scattering amplitude, $\mathcal{M}$, is evaluated. The scattering amplitude is calculated by using the propagator (Green's function of the free-particle theory) for the incoming, mediating, and outgoing particles, with an appropriate weighting function, or vertex factor, for each point the particles interact in the scattering process, and then integrating over the momentum of the mediating particle. Richard Feynman developed a set of rules for the writing down the propagators and vertex factors directly from the Lagrangian, and easily computing the scattering amplitude. He also introduced an elegant pictographic notation useful for visualizing particle interactions, known as Feynman diagrams.

With these tools, one can calculate the probability amplitudes of a given process occurring to Leading Order (LO) without any difficulties. However, when calculations in Next to Leading Order (NLO) are performed, and loop diagrams of virtual particles are considered, the probability amplitudes associated with a given process diverge to infinity. This occurs when one integrates over all of the possible momentum allowed by intermediate, loops of virtual particles, which due to Heisenberg's uncertainty principle, are allowed to take on any value of momentum. Figure 2.1 shows an example of a LO and NLO process.

The systematic removal of divergences from a theory is called renormalization. The di-

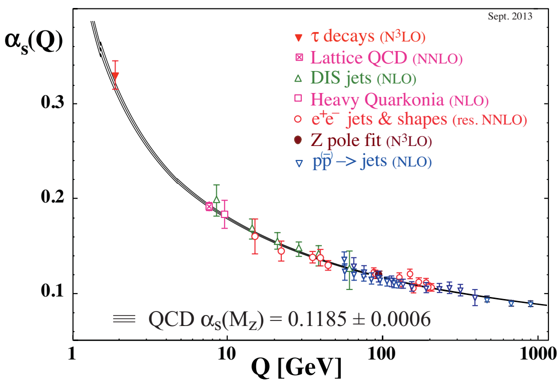

Figure 2.2: The global average of α_s, the QCD coupling constant [1].

vergences are absorbed into the definitions of the free parameters of the theory, making the parameters a function of the energy scale the process occurs at, instead of a constant. This allows for the calculations of fundamental processes to be completed, as long as the energy scale of the interaction is known. A modern interpretation of renormalization was provided by Kenneth Wilson [34] [35]. Instead of seeing the effects of high-momentum calculations after moving to NLO in perturbation theory, one uses an effective Lagrangian, computed by integrating out shells of momentum beginning at the energy cutoff of the theory, where the NLO effects begin to dominate. The dimensions of integration are then rescaled and the result of evaluating the integral over the momentum shell is absorbed into the definition of free parameters. The processes is iterated until the energy scale of the interaction is reached. The functional dependence of the parameters is then directly present in the resulting effective Lagrangian, instead of appearing suddenly when accounting for the one-loop contributions at NLO. Regardless of how strange this procedure may seem, the running of the coupling constant as a function of interaction energy has been validated experimentally time and time again, as shown in Figure 2.2 [1].

2.2 Abelian Gauge Theories of Particle Interactions

In 1930, Herman Weyl introduced the idea that the interactions between fields can be generated by requiring them to be invariant under gauge transformations of a local symmetry [36]. For electromagnetism, the local symmetry is that of the Lie group, $U(1)$. It is an abelian group, which has the property that the generators of the group symmetry commute with themselves. The $U(1)$ symmetry is invariant under phase rotations. By requiring local gauge invariance, the Lagrangian must be unchanged under the transformation:

$$\psi(x) \to e^{i\alpha(x)}\psi(x). \tag{2.8}$$

Consider the Lagrangian for a free spin 1/2 particle:

$$\mathcal{L} = \bar{\psi}(i\gamma^\mu \partial_\mu - m)\psi \tag{2.9}$$

The first term in the Lagrangian, involving the derivative, acts on $\psi(x)$, creating a new term in the Lagrangian, breaking its invariance under the local phase transformation.

$$\mathcal{L} \rightarrow \mathcal{L} - (\partial_\mu \alpha)\bar{\psi}\gamma^\mu \psi \tag{2.10}$$

Thus, a new term must be added to the original Lagrangian to cancel out the term arising from the local phase transformation. This is achieved by defining the covariant derivative:

$$D_\mu = \partial_\mu + ieA_\mu \tag{2.11}$$

where A_μ is a new vector field that transforms as follows:

$$A_\mu(x) \rightarrow A_\mu(x) - \frac{1}{e}\partial_\mu \alpha(x) \tag{2.12}$$

The covariant derivative thus transforms like

$$\begin{aligned} D_\mu \psi(x) &\rightarrow [\partial_\mu + ie(A_\mu - \frac{1}{e}\partial_\mu \alpha)]e^{i\alpha(x)} D_\mu \psi(x) \\ &= e^{i\alpha(x)}[\partial_\mu + ie(A_\mu - \frac{1}{e}\partial_\mu \alpha + \frac{1}{e}\partial_\mu \alpha)] D_\mu \psi(x) \\ &= e^{i\alpha(x)}(\partial_\mu + ieA_\mu)\psi(x) \\ &= e^{i\alpha(x)} D_\mu \psi(x) \end{aligned} \tag{2.13}$$

This covariant derivative transforms in the same way that $\psi(x)$ does, and the new locally gauge invariant Lagrangian becomes

$$\begin{aligned} \mathcal{L} &= \bar{\psi}(i\gamma^\mu D_\mu - m)\psi - \frac{1}{4}F^{\mu\nu}F_{\mu\nu} \\ &= i\bar{\psi}\gamma\partial_\mu \psi - \bar{\psi}\gamma^\mu \psi \ A_{mu} - m\bar{\psi}\psi - \frac{1}{4}F^{\mu\nu}F_{\mu\nu} \end{aligned} \tag{2.14}$$

where

$$F^{\mu\nu} = (\partial^\mu A^\nu - \partial^\nu A^\mu) \tag{2.15}$$

and $\frac{1}{4}F^{\mu\nu}F_{\mu\nu}$ is the kinetic energy term of the Proca equation for the new vector field.

This new Lagrangian is identical to the QED Lagrangian, except it was derived beginning with a free Dirac theory and requiring the field to be locally gauge invariant under $U(1)$ transformations. This necessitated the introduction of a new vector field, A_μ, as well as an interaction term for it. This implies that the electromagnetic force can be represented by the requirement of local $U(1)$ symmetry on a free Dirac particle.

It should be noted, that if the photon had mass, an additional term from the Proca equation would have to be added to the Lagrangian, $m^2 A_\mu A^\mu$. This term complicates the picture since it is not invariant under local phase transformations, and cannot be compensated for through a different choice of A_μ. This implies that the bosons of a gauge theory must be massless in order to preserve local gauge invariance.

2.3 Non-Abelian Gauge Theories of Particle Interactions

In 1954, Yang and Mills worked to extend this idea to symmetries of different gauge groups [37]. Their most important accomplishment was developing this procedure for non-abelian groups. These are groups where the transformation does not involve a simple variable $\alpha(x)$, but rather an entire matrix of dimension n>2. These matrices do not commute with each other, and their work developed the procedure for applying local gauge invariance described above to the more complex, higher dimensional symmetries, such as $SU(2)$ and $SU(3)$. Consider the case of $SU(2)$ symmetry. The theory is appropriate for describing the dynamics of two fermion fields, represented as a doublet:

$$\psi = \begin{pmatrix} \psi_1(x) \\ \psi_2(x) \end{pmatrix} \tag{2.16}$$

This will transform under the $SU(2)$ transformation as a two-component spinor:

$$\psi \rightarrow \exp\langle\, i\alpha^i \frac{\sigma_i}{2} \rangle \psi \tag{2.17}$$

where σ^i are the Pauli matrices:

$$\sigma^1 = \begin{pmatrix} 0 & 1 \\ 1 & 0 \end{pmatrix} ,\ \sigma^2 = \begin{pmatrix} 0 & -i \\ i & 0 \end{pmatrix} ,\ \sigma^3 = \begin{pmatrix} 1 & 0 \\ 0 & -1 \end{pmatrix} \tag{2.18}$$

and have the commutation relation defined by:

$$\left[\frac{\sigma^i}{2}, \frac{\sigma^j}{2} \right] = i\epsilon^{ijk} \frac{\sigma^k}{2} \tag{2.19}$$

Similar to the case of the $U(1)$ Abelian symmetry, in order to form a Lagrangian that is locally gauge invariant, three vector fields, A^i_μ, $i = 1, 2, 3$, are introduced, and coupled to ψ through the covariant derivative:

$$D_\mu = (\partial_\mu - igA^i_\mu \frac{\sigma^i}{2}) \tag{2.20}$$

to ensure that the derivative covaries with the transformation, the fields, A^i_μ will transform like:

$$A^i_\mu \frac{\sigma^i}{2} \to A^i_\mu \frac{\sigma^i}{2} + \frac{1}{g}(\partial_\mu \alpha^i)\frac{\sigma^i}{2} + i\left[\frac{\alpha^i \sigma i}{2},\, A^i_\mu \frac{\sigma^i}{2}\right] \tag{2.21}$$

The third term, which was absent from the abelian form of the transformation, is necessary to account for the non-commutation of the Pauli matrices. This non-commutation also changes the form of the field-strength tensor, $F^i_{\mu\nu}$:

$$F^i_{\mu\nu} = \partial_\mu A^i_\nu - \partial_\nu A^i_\mu + g\epsilon^{ijk} A^j_\mu A^k_\nu \tag{2.22}$$

The entire $SU(2)$ invariant Lagrangian can then be written as:

$$\begin{aligned} \mathcal{L}_{Yang-Mills} &= -\frac{1}{4} F^i_{\mu\nu} F^{i\mu\nu} + \bar{\psi}(i\gamma^\mu D_\mu)\psi \\ &= -\frac{1}{4} F^i_{\mu\nu} F^{i\mu\nu} + \bar{\psi}(i\gamma^\mu \partial_\mu - igA^i_\mu \frac{\sigma^i}{2})\psi \end{aligned} \tag{2.23}$$

This procedure generalizes to any continuous group of symmetries. The basic steps involve identifying the generators of the transformation:

$$\psi(x) \to e^{i\alpha^a t^a} \psi \tag{2.24}$$

where t^a are a set of matrices with the commutation relationship:

$$[t^a,\, t^b] = if^{abc} t^c \tag{2.25}$$

where f^{abc} is the structure constant for the group. The covariant derivative is then defined as:

$$D_\mu = \partial_\mu - igA^a_\mu t^a \tag{2.26}$$

where the fields, A^a_μ, transform like:

$$A^a_\mu \to A^a_\mu + \frac{1}{g}\partial_\mu \alpha^a + f^{abc} A^b_\mu \alpha^c \tag{2.27}$$

the field strength tensor is then formed as:

$$F^a_{\mu\nu} = \partial_\mu A^a_\nu - \partial_\nu A^a_\mu + f^{abc} A^b_\mu A^c_\nu \tag{2.28}$$

and finally, the locally, gauge invariant Lagrangian will have the form:

$$\begin{aligned} \mathcal{L}_{\text{General, non-Abelian}} &= -\frac{1}{4}F^a_{\mu\nu}F^{a\mu\nu} + \bar{\psi}(i\gamma^\mu D_\mu)\psi \\ &= -\frac{1}{4}F^a_{\mu\nu}F^{a\mu\nu} + \bar{\psi}(i\gamma^\mu \partial_\mu - igA^a_\mu t^a)\psi \end{aligned} \tag{2.29}$$

In 1964, Murray Gell-Mann and George Zweig independently developed a model of hadron interactions that describe the spectrum of baryons and mesons in terms of combinations of fundamental particles, which Gell-Mann named quarks [38] [39] [40]. In their model, three quarks: u, d, s formed an $SU(3)$ flavor symmetry. However, this did not explain the appearance of only two and three-quark combinations, the mesons and baryons. It also could not explain the spin statistics of the baryons. The Δ^{++}, Δ^{-}, and Ω^{-}, particles all have uuu, ddd, sss quark combinations, respectively, with their spins aligned. That is to say, these baryons seem to violate the Pauli-exclusion principle since all three quarks seem to occupy the same quantum state simultaneously.

In 1964, O.W. Greenberg solved this problem by proposing that quarks also have an additional quantum number, color, that come in three types: red, green, blue [41]. The requirement that all stable hadrons be color neutral: either possessing equal amounts of all three colors in qqq combinations, or a $q\bar{q}$ pair sharing the same color, also explained the observation of only 2 and 3 quark combinations in experiments. These three colors form an $SU(3)$ symmetry, and is the gauge symmetry describing the interactions of quarks and leptons. This theory is known as Quantum Chromodynamics (QCD). Its derivation follows from the procedure outlined above. This group has eight generators, known as the Gell-Mann matrices, and are defined as:

$$\begin{aligned} &t^1 = \frac{1}{2}\begin{pmatrix} 0 & 1 & 0 \\ 1 & 0 & 0 \\ 0 & 0 & 0 \end{pmatrix}, \; t^2 = \frac{1}{2}\begin{pmatrix} 0 & -i & 0 \\ i & 0 & 0 \\ 0 & 0 & 0 \end{pmatrix}, \; t^3 = \frac{1}{2}\begin{pmatrix} 1 & 0 & 0 \\ 0 & -1 & 0 \\ 0 & 0 & 0 \end{pmatrix} \\ &t^4 = \frac{1}{2}\begin{pmatrix} 0 & 0 & 1 \\ 0 & 0 & 0 \\ 1 & 0 & 0 \end{pmatrix}, \; t^5 = \frac{1}{2}\begin{pmatrix} 0 & 0 & -i \\ 0 & 0 & 0 \\ i & 0 & 0 \end{pmatrix} \\ &, \; t^6 = \frac{1}{2}\begin{pmatrix} 0 & 0 & 0 \\ 0 & 0 & 1 \\ 0 & 1 & 0 \end{pmatrix}, \; t^7 = \frac{1}{2}\begin{pmatrix} 0 & 0 & 0 \\ 0 & 0 & -i \\ 0 & -i & 0 \end{pmatrix}, \; t^8 = \frac{1}{2\sqrt{3}}\begin{pmatrix} 1 & 0 & 0 \\ 0 & 1 & 0 \\ 0 & 0 & -2 \end{pmatrix} \end{aligned} \tag{2.30}$$

and a Lagrangian defined as:

$$\begin{aligned} \mathcal{L}_{QCD} &= -\frac{1}{4}G^a_{\mu\nu}G^{a\mu\nu} + \bar{\psi}(i\gamma^\mu D_\mu) \\ &= -\frac{1}{4}G^a_{\mu\nu}G^{a\mu\nu} + \bar{\psi}(i\gamma^\mu \partial_\mu - igA^a_\mu t^a) \end{aligned} \tag{2.31}$$

where t^a are the Gell-Mann matrices defined in equation 2.30 and the fields A^a_μ are the eight mediators of the QCD force, the *gluons*.

Like all non-abelian gauge theories, it is asymptotically free, meaning that the strength of the coupling constant, α_s, decreases as the momentum-transfer, Q in interaction increases. This allows the use of perturbation theory for high-momentum calculations, therefore allowing calculations of hadronic-processes for experimental evaluation.

The idea of local gauge invariance was successful in describing the dynamics of QED and QCD, which only contain massless gauge bosons. Theorists had long postulated that the weak force was so weak because it was being facilitated by massive bosons, but adding a mass term for a boson breaks the local gauge invariance. So, a tool was needed to reconcile the concept of local gauge invariance, which works so well for the other forces, with the prospect of the weak force being facilitated by massive gauge bosons.

2.4 The Higgs Mechanism in an Abelian Theory

In 1964 Peter Higgs introduced the idea that the gauge bosons can acquire their mass through the breaking of an underlying symmetry [42]. In other words, the natural symmetry of the Lagrangian describing a particular interaction could be different than the symmetry we observe in nature. Consider an abelian example of complex scalar field theory, coupled to itself and to an electromagnetic field [33].

$$\mathcal{L} = -\frac{1}{4}(F_{\mu\nu})^2 + |D_\mu \phi|^2 - V(\phi) \tag{2.32}$$

where $D_\mu = \partial_\mu + ieA_\mu$, is the familiar covariant derivative, and the Lagrangian is invariant under the $U(1)$ transformation as described earlier. The potential term, $V(\phi)$ has the form

$$V(\phi) = -\mu^2 \phi^* \phi + \frac{\lambda}{2}(\phi^* \phi)^2 \tag{2.33}$$

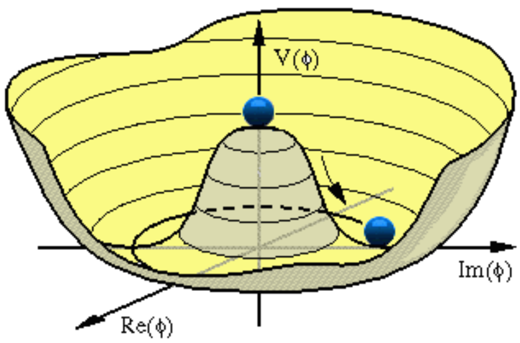

Figure 2.3: A visual representation of the Higgs potential [2]

if $\mu^2 > 0$ the shape of the potential no longer has a minimum at $\langle \phi \rangle = 0$. Figure 2.3 shows a plot of the potential energy of ϕ in terms of each of its components. The new minimum potential energy occurs at:

$$\langle\phi\rangle = \phi_0 = \left(\frac{\mu^2}{\lambda}\right)^{1/2} \tag{2.34}$$

and while the field has a ground state at the zero-potential point it is in an unstable equilibrium. Any quantum fluctuation about this point will take the field into the lower-energy configuration with a ground state about the new minimum. When the Lagrangian is expanded about equation 2.34, the field, ϕ is rewritten as:

$$\phi(x) = \phi_0 + \frac{1}{\sqrt{2}}(\phi_1(x) + i\phi_2(x)) \tag{2.35}$$

the potential term, $V(x)$, then becomes:

$$V(x) = -\frac{1}{2\lambda}\mu^4 + \frac{1}{2}\cdot 2\mu^2\phi_1^2 + \mathcal{O}(\phi_i^3) \tag{2.36}$$

where we can notice that ϕ_1 has acquired a mass term with, $m^2 = 2\mu^2$, while the scalar field ϕ_2 remains massless, and is known as the Goldstone boson. The covariant derivative is also transformed as:

$$|D_\mu\phi|^2 = \frac{1}{2}(\partial_\mu\phi_1)^2 + \frac{1}{2}(\partial_\mu\phi_2)^2 + \sqrt{2}e\phi_0\cdot\ A_\mu\partial^\mu\phi_2 + e^2\phi_0^2A_\mu A^\mu + ... \tag{2.37}$$

where cubic and quartic terms of A_μ, ϕ_1, and ϕ_2 have been dropped. The important term is the last one, which can be interpreted as a mass term of the vector field, A_μ

$$\Delta\mathcal{L}_M = \frac{1}{2}m_A A_\mu A^\mu = e^2\phi_0^2 A_\mu A^\mu \tag{2.38}$$

where $m_A = 2e^2\phi_0^2$, has arisen from consequences of a non-zero vacuum expectation value of the ϕ field. The remaining, massless Goldstone boson, ϕ_2 is not a physical particle, but rather a consequence of the choice of gauge. This is illustrated when we can use the $U(1)$ gauge symmetry to rotate the field $\phi(x)$ such that the field disappears.

$$\begin{aligned}\phi \to \phi' &= e^{i\alpha}(\phi_1 + \phi_2)\\ &= (\cos\alpha + i\sin\alpha)(\phi_1 + \phi_2)\\ &= (\phi_1\cos\alpha - \phi_2\sin\alpha) + i(\phi_1\sin\alpha + \phi_2\cos\alpha)\\ &= (\phi_1 - \phi_2\tan\alpha) + i(\phi_1\tan\alpha + \phi_2)\end{aligned} \tag{2.39}$$

Choosing $\alpha = -\tan\phi_2/\phi_1$ will make ϕ' a real quantity and eliminate its imaginary component, ϕ_2'. The Lagrangian can then be rewritten in terms of the rotated field ϕ' and see that the massless boson is indeed removed from the theory.

$$\begin{aligned}\mathcal{L} = &\frac{1}{2}(\partial_\mu \phi_1')(\partial^\mu \phi_1') - \frac{1}{2} \cdot\ 2\mu^2 \phi_1' \phi_1' \\ &- \frac{1}{4}(F^{\mu\nu} F_{\mu\nu}) + \frac{1}{2} \cdot\ e^2 \phi_0^2 A_\mu A^\nu \\ &+ \phi_0 e^2 \phi_1' A_\mu A^\mu + \frac{1}{2} e^2 \phi_1'^2 A_\mu A^\mu + \mathcal{O}(\phi'^3)...\end{aligned} \tag{2.40}$$

The degree of freedom that ϕ_2 represents, is absorbed as a longitudinal polarization of the A_{mu} field, mathematically forbidden for massless gauge bosons, but necessary for massive bosons.

For this case of an abelian symmetry $U(1)$, it was shown that if a complex scalar field, which interacts with itself and another vector field, can gain a non-zero vacuum expectation value. The Lagrangian can be expanded about this new minimum, generating a mass term for the vector field. One of the degrees of freedom of the original complex scalar field is then absorbed as a longitudinal polarization state of the massive vector field.

2.5 The Higgs Mechanism in a non-Abelian Theory

Before describing the electroweak gauge theory of $SU(2) \otimes\ U(1)$, it will be helpful to see the effects of the Higgs mechanism for the non-Abelian group, $SU(2)$ by itself. Consider an example of an $SU(2)$ gauge field coupled to a scalar field that transforms like a real-valued vector under $SU(2)$ transformations [33]. The field ϕ will have the form:

$$\phi = \begin{pmatrix} \phi_1 \\ \phi_2 \\ \phi_3 \end{pmatrix} \tag{2.41}$$

where the components, ϕ_i are real-valued fields. The $SU(2)$ transformation for this scalar field will also look like:

$$\phi \to e^{i\alpha^i T^i} \phi \tag{2.42}$$

where the matrices, T^i are defined as:

$$iT^1 = \begin{pmatrix} 0 & 0 & 0 \\ 0 & 0 & 1 \\ 0 & -1 & 0 \end{pmatrix},\ T^2 = \begin{pmatrix} 0 & 0 & -1 \\ 0 & 0 & 0 \\ 1 & 0 & 0 \end{pmatrix},\ T^3 = \begin{pmatrix} 0 & 1 & 0 \\ -1 & 0 & 0 \\ 0 & 0 & 0 \end{pmatrix} \tag{2.43}$$

The Lagrangian for this field will feature a Higgs potential term along with the previously mentioned $SU(2)$ gauge fields, A_μ^a coupled to the scalar field, ϕ, and is given by:

$$\mathcal{L} = -\frac{1}{4} F_{\mu\nu}^a F^{a\mu\nu} + |D_\mu \phi|^2 + \mu^2 \phi^* \phi - \frac{\lambda}{4}(\phi^* \phi)^2 \tag{2.44}$$

where $F_{\mu\nu}^a$, the field strength tensor is defined as:

$$F^a_{\mu\nu} = (\partial_\mu A^a_\nu - \partial_\nu A^a_\mu) + g\epsilon^{abc} A^b_\mu A^c_\nu \tag{2.45}$$

and the covariant derivative is defined as:

$$D_\mu = (\partial_\mu + igA^a_\mu T^a)\phi \tag{2.46}$$

Similarly to the Abelian case, the Higgs potential will induce a spontaneous symmetry breaking, and one of the components of the field ϕ will gain a vacuum expectation value. After this breaking and expanding around the ground state potential, the field ϕ will have the form:

$$\phi = \frac{1}{\sqrt{2}} \begin{pmatrix} 0 \\ 0 \\ v+h \end{pmatrix} \tag{2.47}$$

There has been no loss in generality in assuming this form since, similarly to the abelian case, we can use the gauge symmetry of $SU(2)$ to rotate the field into this configuration. Goldstone's theorem tells us that we should expect two massive gauge bosons corresponding to the T^1, and T^2 generators, while the T^3 generator will correspond to a massless gauge boson, since ϕ is still invariant under T^3 transformations.

As in the Abelian case, the mass terms for the gauge bosons are generated from the covariant derivative term, $|D_\mu \phi|^2$

$$\begin{aligned} D_\mu\phi &= \frac{1}{\sqrt{2}} \left(\partial_\mu + gA^1_\mu \begin{pmatrix} 0 & 0 & 0 \\ 0 & 0 & 1 \\ 0 & -1 & 0 \end{pmatrix} + gA^2_\mu \begin{pmatrix} 0 & 0 & -1 \\ 0 & 0 & 0 \\ 1 & 0 & 0 \end{pmatrix} + gA^3_\mu \begin{pmatrix} 0 & 1 & 0 \\ -1 & 0 & 0 \\ 0 & 0 & 0 \end{pmatrix} \right) \begin{pmatrix} 0 \\ 0 \\ v+h \end{pmatrix} \\ &= \frac{1}{\sqrt{2}} \begin{pmatrix} 0 \\ 0 \\ \partial_\mu \end{pmatrix} + \frac{gA^1_\mu}{\sqrt{2}} \begin{pmatrix} 0 \\ v+h \\ 0 \end{pmatrix} - \frac{gA^2_\mu}{\sqrt{2}} \begin{pmatrix} v+h \\ 0 \\ 0 \end{pmatrix} \\ &= \frac{1}{\sqrt{2}} \begin{pmatrix} g(v+h)A^1_\mu \\ g(v+h)A^2_\mu \\ \partial_\mu h \end{pmatrix} \end{aligned} \tag{2.48}$$

Therefore

$$|D_\mu\phi|^2 = \frac{1}{2}\partial_\mu h \partial^\mu h + \frac{g^2 v^2}{2}\left((A^1_\mu)^2 + (A^2_\mu)^2\right) + \frac{g^2}{2}(h^2 + 2hv)\left((A^1_\mu)^2 + (A^2_\mu)^2\right) \tag{2.49}$$

This theory produces two massive bosons, A^1_μ and A^2_μ, both with mass, $m_A = gv$. These fields have h, and h^2 couplings to the Higgs boson. The third gauge field, A^3_μ, remains massless and is not coupled to the Higgs field. This model is beginning to resemble a description of electroweak physics; however, a third massive boson is necessary, as is a new gauge symmetry in order to generate it. That is the subject of the next section.

2.6 Glashow Weinberg Salam Theory

Glashow, Weinberg, and Salam published their theory unifying electromagnetic and weak forces in the 1960s [43] [44] [45]. It begins with the requirement of a $SU(2)_L \otimes\ U(1)$ symmetry and incorporates the Higgs mechanism to give mass to the gauge bosons of the weak force. As described earlier, the $U(1)$ symmetry requires introducing a vector field, which will be labeled B_μ, and an interaction term, which is absorbed into the covariant derivative, D_μ. The transformation will also be parameterized with a quantum number, Y, known as hypercharge. The $SU(2)$ symmetry requires the introduction of three new vector fields, which will be labeled $W^i_\mu, i = 1, 2, 3$. The quantum number associated with this gauge group is isospin, and is determined by the T^3 operator, acting on an $SU(2)$ doublet on the third generator of the group. The $SU(2) \otimes\ U(1)$ transformation, $U(x)$, will then be given by:

$$U(x) = e^{i\alpha^a(x)\tau^a} e^{iY\alpha(x)} \tag{2.50}$$

where $\tau^a = \sigma^a/2$, the Pauli matrices, 2.18. These gauge fields will be coupled, via the covariant derivative, to a doublet of complex scalar fields ϕ, with hypercharge $Y = +1/2$. A Higgs potential will be added to generate the spontaneous symmetry breaking that will give mass to three of the gauge fields, and leave one massless. In order to preserve the $SU(2)_L \otimes\ U(1)$ symmetry, the new covariant derivative will take the form:

$$D_\mu = (\partial_\mu - igW^a_\mu \tau^a - \frac{i}{2}g' B_\mu) \tag{2.51}$$

The subscript L on $SU(2)_L$ refers to experimental observations of the weak force violating parity maximally, by only interacting with the left-handed chiral component of a field. Right versus left chirality is determined by whether the spin of a particle is aligned or anti-aligned with its direction of motion, and in general a particle is represented by a linear combination of its right and left-handed components. This idea was first proposed by Chen Ning Yang and Tsung-Dao Lee, in the 1950s. Their ideas were validated by the experimental discovery of parity violation in 1957, through the beta decays of Cobalt 60 atoms by C.S Wu. That same year, Yang and Lee were awarded the Nobel Prize for their insight [46]. In this model, then, the left-handed components of the particles participate in the weak interaction and are formed into doublets, while the right handed components are singlets, and will only interact with the electromagnetic field, B_μ. The quantum numbers will be given by $+1/2$ for the upper component of the $SU(2)$ doublet, and -1/2 for the lower component. The fermion content of this theory is then given by:

$$\begin{gathered} \begin{pmatrix} \nu_L \\ e_L \end{pmatrix}, e_R \\ \begin{pmatrix} u_L \\ d_L \end{pmatrix}, u_R, d_R \end{gathered} \tag{2.52}$$

where the right-handed neutrino, ν_R, has been omitted since it has zero charge, and isospin, and therefore does not participate in any of the interactions of this theory. The complete Lagrangian is given by a sum of free-particle terms for massless bosons, fermions, and Higgs scalar fields; the Higgs potential; and a Yukawa coupling term between the fermions and the Higgs, which generates their masses.

$$\mathcal{L}_{GWS} = \mathcal{L}_{BosonKE} + \mathcal{L}_{Higgs} + \mathcal{L}_{FermionKE} + \mathcal{L}_{Yukawa} \tag{2.53}$$

The Higgs potential will have the form:

$$\mathcal{L}_{Higgs} = (D_\mu\phi)^\dagger(D^\mu\phi) + \mu^2\phi^\dagger\phi - \lambda(\phi^\dagger\phi)^2 \tag{2.54}$$

The Higgs potential will break the symmetry of the Lagrangian when one of the four degrees of freedom in the complex scalar doublet, ϕ, spontaneously acquires a vacuum expectation value. In this case, it will generate three massive gauge bosons, one massless gauge boson, and a massive scalar field. After gaining a vacuum expectation value, and expanding about this value, the scalar fields will have the form:

$$\langle\phi\rangle = \frac{1}{\sqrt{2}}\begin{pmatrix} 0 \\ v+h \end{pmatrix} \tag{2.55}$$

where no loss of generality has occurred since we are always able to rotate into this form through the appropriate gauge transformations, similar to what was described in the Abelian case. It should also be noted that this form is not invariant to any of the individual generators t^a, however ϕ will be invariant to a combination of $T^3 + Y$ generators. Per Goldstone's theorem, we should expect this linear combination of fields to be the massless vector boson after symmetry breaking.

The massless eigenstate will be the electromagnetic field, $A_\mu \sim A^3_\mu + B_\mu$. The electric charge quantum number, Q, is then defined as

$$Q = T^3 + Y \tag{2.56}$$

As before, the generation of the masses for the gauge bosons are generated by the interaction of their fields with the Higgs field via the covariant derivative.

$$D_\mu\phi = \frac{1}{\sqrt{2}}\left(\partial_\mu - \frac{ig}{2}A^1_\mu\begin{pmatrix}0 & 1\\ 1 & 0\end{pmatrix} - \frac{ig}{2}A^2_\mu\begin{pmatrix}0 & -i\\ i & 0\end{pmatrix} - \frac{ig}{2}A^3_\mu\begin{pmatrix}1 & 0\\ 0 & -1\end{pmatrix}\right)\begin{pmatrix}0\\ v+h\end{pmatrix} \tag{2.57}$$

$$= \frac{1}{\sqrt{2}}\begin{pmatrix}(\frac{g}{2}(v+h)A^2_\mu) + i(\frac{g}{2}(v+h)A^1_\mu)\\ \partial_\mu + i(\frac{1}{2}(v+h)(gA^3_\mu - g'B_\mu))\end{pmatrix}$$

Taking the dot product of this with its hermitian conjugate gives the $|D_\mu\phi|^2$ term:

$$\begin{aligned}|D_\mu\phi|^2 =& \frac{1}{2}\partial_\mu h\partial^\mu h + \frac{1}{2}\frac{g^2v^2}{4}((A^1_\mu)^2 + (A^2_\mu)^2) + \frac{v^2}{4}(gA^3_\mu - g'B_\mu)^2\\ &+ \frac{1}{2}g^2 4(h^2+2vh)((A^1_\mu)^2 + (A^2_\mu)^2) + \frac{1}{2}\frac{1}{4}(h^2+2vh)(gA^3_\mu - g'B_\mu)\end{aligned} \tag{2.58}$$

From equation 2.58 we can identify three massive and one massless gauge bosons, corresponding the the charged and neutral weak currents, and the electromagnetic current.

$$\begin{aligned}W^\pm_\mu &= \frac{1}{\sqrt{2}}(A^1_\mu \mp iA^2_\mu) &&\text{with mass } m_W = g\frac{v}{2};\\ Z^0_\mu &= \frac{1}{\sqrt{g^2+g'^2}}(gW^3_\mu - g'B_\mu) &&\text{with mass } m_Z = \frac{v}{2}\sqrt{g^2+g'^2};\\ A_\mu &= \frac{1}{\sqrt{g^2+g'^2}}(gW^3_\mu + g'B_\mu) &&\text{with mass } m_A = 0;\end{aligned} \tag{2.59}$$

where the last field, A_μ is absent from the covariant derivative term, but already identified as the massless gauge boson of the theory due to its gauge invariance under a $T^3 + Y$ rotation. Using these definitions the covariant derivative has the following form:

$$\begin{aligned}D_\mu =& \partial_\mu - \frac{ig}{\sqrt{2}}(W^+T^+ + W^-T^-)\\ &- \frac{i}{\sqrt{g^2+g'^2}}Z^0_\mu(gT^3 - g'Y) - \frac{gg'}{\sqrt{g^2+g'^2}}A_\mu(T^3+Y)\end{aligned} \tag{2.60}$$

where $T^\pm = \frac{1}{2}(\sigma^1 \pm \sigma^2)$. From this form, we can identify the fundamental electric charge, e, as

$$e = \frac{gg'}{\sqrt{g^2 + g'^2}} \tag{2.61}$$

The similarity in the forms between Z^0_μ and A_μ suggest that their relationship can be expressed in a simpler form, as the rotation of underlying gauge fields A^3_μ and B_μ through the weak mixing angle, θ_W

$$\begin{pmatrix} Z^0_\mu \\ A_\mu \end{pmatrix} = \begin{pmatrix} \cos\theta_W & -\sin\theta_W \\ \sin\theta_W & \cos\theta_W \end{pmatrix} \begin{pmatrix} A^3_\mu \\ B_\mu \end{pmatrix} \tag{2.62}$$

where $\tan\theta_W = \frac{g'}{g}$. Expanding 2.62, we have the definitions of the Z^0_μ and A_μ fields in terms of θ_W

$$\begin{aligned} Z^0_\mu &= A^3_\mu \cos\theta_W - B_\mu \sin\theta_W \\ A_\mu &= A^3_\mu \sin\theta_W + B_\mu \cos\theta_W \end{aligned} \tag{2.63}$$

The weak mixing angle, θ_W, also provides a simple relationship between the $W^\pm_\mu$ and Z^0_μ fields:

$$m_W = m_Z \cos\theta_W \tag{2.64}$$

The covariant derivative, D_μ is also rewritten in terms of the mass eigenstates of the gauge fields

$$D_\mu = (\partial_\mu - \frac{ig}{\sqrt{2}}(W^+_\mu + W^-_\mu T^-) - \frac{ig}{\cos\theta_W} Z^0_\mu (T_3 - sin^2\theta_W Q) - ieA_\mu Q) \tag{2.65}$$

where $g = e/\cos\theta_W$. The square of the covariant derivative is then written as

$$\begin{aligned} |D_\mu|^2 = &\frac{1}{2}\partial_\mu h \partial^\mu h + \frac{1}{2} m^2_W W^+_\mu W^{\mu+} + \frac{1}{2} m^2_W W^-_\mu W^{\mu-} + \frac{1}{2} m^2_Z Z^0_\mu Z^{\mu 0} \\ &+ (\frac{h^2}{v^2} + \frac{h}{v})[\frac{1}{2} m^2_W (W^+_\mu W^{\mu+} + W^-_\mu W^{\mu-}) + \frac{1}{2} m^2_Z Z^0_\mu Z^{\mu 0}] \end{aligned} \tag{2.66}$$

With the form of the covariant derivative in place, the fermionic kinematic term of the Lagrangian can be described. As mentioned earlier, the masses of the fermions in the model will be generated by the Yukawa interaction term with the Higgs, so this term only involves the covariant derivatives acting on the left-handed doublet and right-handed singlet states of this model. The quantum number assignments for the leptons, which are chosen in order to reproduce the known values of their electric charges, are shown in table 2.1. The values of these quantum numbers enter into the covariant derivative via the Z^0_μ term of equation 2.65. The fermionic kinetic energy term of the Lagrangian is given by:

	ν_L	e_L	e_R	u_L	d_L	u_R	d_R
Isospin	+1/2	-1/2	0	+1/2	-1/2	0	0
Hypercharge	-1/2	-1/2	-1	+1/6	1/3	2/3	-1/3
Electric Charge	0	-1	-1	2/3	-1/3	2/3	-1/3

Table 2.1: The quantum numbers Isospin and Hypercharge are assigned for each of the $SU(2)$ and $U(1)$ symmetries respectively

$$\begin{aligned}\mathcal{L}_{Fermion} = {} & \bar{E}_L(i\gamma^u D_\mu)E_L + \bar{e}_R(i\gamma^u D_\mu)e_R \\ & \bar{Q}_L(i\gamma^u D_\mu)Q_L + \bar{u}_R(i\gamma^u D_\mu)u_R + \bar{d}_R(i\gamma^u D_\mu)d_R\end{aligned} \tag{2.67}$$

Expanding the covariant term for the left-handed electron shows its explicit coupling to the gauge boson fields.

$$\begin{aligned}\mathcal{L}_{E_L} = {} & \begin{pmatrix}\bar{\nu_L} & \bar{e_L}\end{pmatrix} \left((i\gamma^\mu(\partial_\mu - \frac{ig}{\sqrt{2}}(W^+_\mu T^+ + W^-_\mu T^-) - \frac{ig}{\cos\theta_W} Z^0_\mu(T^3 - \sin^2\theta_W Q) - ieA_\mu Q)\ ) \right) \begin{pmatrix}\nu_L \\ e_L\end{pmatrix} \\ = {} & \bar{\nu_L} i\gamma^\mu\partial_\mu\nu_L + \bar{e_L} i\gamma^\mu\partial_\mu e_L + \frac{ig}{\sqrt{2}} W^+_\mu \bar{\nu_L}\gamma^\mu e + \frac{ig}{\sqrt{2}} W^-_\mu \bar{e_L}\gamma^\mu\nu_L \\ & + \frac{ig}{\cos\theta_W}\bar{\nu_L}(1/2)\gamma^\mu\nu_L + \frac{ig}{\cos\theta_W}\bar{e_L}\gamma^\mu(-1/2 + \sin^2\theta_W(+1))e_L + (ie)\bar{e_L}\gamma^\mu A_\mu(-1)\end{aligned} \tag{2.68}$$

All of the terms will be combined with the final, spontaneously-broken GWS Lagrangian at the end of this section.

The final term to discuss in the theory, before combining all of the results, is the Yukawa interaction term between the fermion fields and the Higgs. For the electron, this term takes the form:

$$\begin{aligned}\mathcal{L}_{Yukawa} = {} & -\lambda_e\bar{E_L}\cdot\phi\ e_R - \lambda_e E_L\cdot\phi\ \bar{e_R} \\ = {} & -\frac{\lambda_e}{\sqrt{2}}(v+h)(\bar{e_L}e_R + e_L\bar{e_R}) \\ = {} & - -\frac{\lambda_e v}{\sqrt{2}}(\bar{e_L}e_R + e_L\bar{e_R}) + -\frac{\lambda_e}{\sqrt{2}}(\bar{e_L}e_R + e_L\bar{e_R})h\end{aligned} \tag{2.69}$$

where the mass of the electron is identified as $m_e = \frac{\lambda_e v}{\sqrt{2}}$. In order to generate the masses of the particles, each fermion has its own unique λ value. So while the Higgs mechanism is able to generate the masses in a way that preserves the underlying $SU(2)\otimes\ U(1)$ symmetry, it does not explain the hierarchy of masses since each λ value is unique to each lepton. The second term in equation 2.69 is the coupling of the Higgs particle, h, to the fermions. The coupling is proportional to the mass of the particle. The largest of these is to the top quark, with $m_t = 173.21 \pm 0.51 \pm 0.71 GeV$.

The Yukawa coupling for the quarks is necessarily modified when additional quarks besides the u and d are added to the theory. This is because there can be additional coupling terms that mix generations. This occurs when the mass eigenstate of the quarks is not the same as the interaction eigenstate. The modification requires the expansion of the u_L and d_L components into a vector of left handed quarks. If we let

$$u^i_L = (u_L, c_L, t_L), \quad d^i_L = (d_L, s_L, b_L) \tag{2.70}$$

represent the up- and down-type quarks in the original weak interaction basis, then the vectors, u^i_L' and d^i_L', can be defined as the diagonalized basis for the Higgs coupling. They are related through a unitary transformation.

$$u^i_L = U^{ij}_u u^{j\prime}_L, \quad d^i_L = U^{ij}_d d^{j\prime}_L \tag{2.71}$$

The interaction terms with the charged gauge boson currents must then be rewritten as

$$J^{\mu+}_W = \frac{1}{\sqrt{2}} \bar{u^i_L} \gamma^\mu d^i_L = \frac{1}{\sqrt{2}} \bar{u^{i\prime}_L} \gamma^\mu (U^\dagger_u U_d) d^{j\prime}_L = \frac{1}{\sqrt{2}} \bar{u^{i\prime}_L} \gamma^\mu V_{ij} d^{j\prime}_L \tag{2.72}$$

where V_{ij} is the 3x3 Cabibbo-Kobayashi-Maskawa (CKM) matrix describing the mixing among six quarks [47] [48]. It is an extension of the Glashow-Iliopoulos-Maiaini mechanism, which was a 2x2 matrix that predicted the existence of a fourth quark, the charm quark [49]. The GIM mechanism was an attempt to suppress flavor-changing-neutral currents, which occur at LO in a three-quark model, but not in a four-quark model. The CKM matrix, however, was motivated by an attempt to explain CP violation in the weak interaction. At the time of its publication, the bottom and top quarks were not predicted. After these were discovered, they were awarded the nobel prize in physics in 2008.

At this point, all the of the pieces are ready to write down the GWS Lagrangian, after the Higgs mechanism has spontaneously broken the $SU(2) \otimes U(1)$ symmetry.

$$\begin{aligned}
\mathcal{L}_{Unbroken} = & -\frac{1}{4} A^a_{\mu\nu} A^{\mu\nu\ a} - \frac{1}{4} F_{\mu\nu} F^{\mu\nu} \\
& + |D_\mu \phi|^2 + \mu^2 (\phi^\dagger \phi) - \lambda (\phi^\dagger \phi)^2 \\
& + \bar{E_L} (i\gamma^\mu D_\mu) E_L + \text{ similar terms for } e_R, U_L, u_R, d_R \\
& - \lambda_e \bar{E_L} \cdot \phi \ e_R + h.c. + \text{ similar terms for } e_R, U_L, u_R, d_R
\end{aligned} \tag{2.73}$$

$$
\begin{aligned}
\mathcal{L}_{GWS} = & -\frac{1}{4}(Z^0_{\mu\nu})^2 - \frac{1}{2}(W^+_{\mu\nu}W^-_{\mu\nu}) - \frac{1}{4}(F_{\mu\nu})^2 \\
& + ig\cos\theta_W \left((W^-_\mu W^+_\nu - W^-_\nu W_\mu)\partial^\mu Z^{0\nu} + W^+_{\mu\nu}W^{-\mu}Z^{0\nu} + W^-_{\mu\nu}W^{+\mu}Z^{0\nu}\right) \\
& + ie\left((W^-_\mu W^+_\nu - W^-_\nu W^+_\mu)\partial^\mu A^\nu + W^+_{\mu\nu}W^{-\mu}A^\nu - W^-_{\mu\nu}W^{+\mu}A^\nu\right) \\
& + g^2\cos^2\theta_W \left(W^+_\mu W^-_\nu Z^{0\mu}Z^{0\nu} - W^+_\mu W^{-\mu}Z^0_\nu Z^{0\nu}\right) \\
& + g^2\left(W^+_\mu W^-_\mu A^\mu A^\nu - W^+_\mu W^{-\mu}A_\nu A^\nu\right) \\
& + ge\cos\theta_W \left(W^+_\mu W^-_\nu (Z^{0\mu}A_\nu + Z^{0\nu}A^\mu) - 2W^+_\mu W^{-\mu}A^\nu\right) \\
& + \frac{1}{2}g^2(W^+_\mu W^-_\nu)(W^{+\mu}W^{-\nu} - W^{+\nu}W^{-\mu}) \\
& + \frac{1}{2}\partial_\mu h\partial^\nu h - v^2\lambda h^2 + \frac{1}{2}m^2_W W^+_\mu W^{+\mu} + \frac{1}{2}m^2_W W^-_\mu W^{-\mu} + \frac{1}{2}m^2_Z Z^0_\mu Z^{0\mu} \\
& + (\frac{h^2}{v^2} + \frac{h}{v})\left(\frac{1}{2}m^2_W(W^+_\mu W^{+\mu} + W^-_\mu W^{-\mu}) + \frac{1}{2}m^2_Z Z^0_\mu Z^{0\mu}\right) - \lambda v h^3 - \frac{1}{4}\lambda h^4 \\
& + \bar{E}_L(i\gamma^\mu\partial_\mu)E_L + \bar{e}_R(i\gamma^\mu\partial_\mu)e_R + \bar{Q}_L(i\gamma^\mu\partial_\mu)Q_L + \bar{u}_R(i\gamma^\mu\partial_\mu)u_R + \bar{d}_R(i\gamma^\mu\partial_\mu)d_R \\
& + g(W^+_\mu J^{\mu+}_W + W^-_\mu J^{\mu-}_W + Z^0_\mu J^\mu_Z) + eA_\mu J^\mu_{EM} \\
& - \frac{\lambda_e v}{\sqrt{2}}(\bar{e}_L e_R + \bar{e}_R e_L) + -\frac{\lambda_e h}{\sqrt{2}}(\bar{e}_L e_R + \bar{e}_R e_L) \\
& - \frac{\lambda_u v}{\sqrt{2}}(\bar{u}_L u_R + \bar{u}_R u_L) + -\frac{\lambda_u h}{\sqrt{2}}(\bar{u}_L u_R + \bar{u}_R u_L) \\
& - \frac{\lambda_d v}{\sqrt{2}}(\bar{d}_L d_R + \bar{d}_R d_L) + -\frac{\lambda_d h}{\sqrt{2}}(\bar{d}_L d_R + \bar{d}_R d_L)
\end{aligned}
\tag{2.74}
$$

where the currents of the electroweak interaction, $J^{\mu+}_W$, $J^{\mu-}_W$, J^μ_Z, J^μ_A are defined as:

$$
\begin{aligned}
J^{\mu+}_W &= \frac{1}{\sqrt{2}}\left(\bar{\nu}_L\gamma^\mu e_L + \bar{u}^{i\prime}_L\gamma^\mu V_{ij}d^{j\prime}_L\right) \\
J^{\mu-}_W &= \frac{1}{\sqrt{2}}\left(\bar{e}_L\gamma^\mu \nu_L + \bar{d}^{i\prime}_L\gamma^\mu V_{ij}u^{j\prime}_L\right) \\
J^\mu_Z &= \frac{1}{\cos\theta_W}(\bar{\nu}_L\gamma^\mu(+1/2)\nu_L + \bar{e}_L\gamma^\mu(-1/2+\sin^2\theta_W)e_L + \bar{e}_R\gamma^\mu\sin^2\theta_W e_R \\
&\quad + \bar{u}_L\gamma^\mu(1/2 - 2/3sin^2\theta_W)u_L + \bar{u}_R\gamma^\mu(-2/3sin^2\theta_W)u_R \\
&\quad + \bar{d}_L\gamma^{mu}(-1/2 + 1/3sin^2\theta_W)d_L + \bar{d}_R\gamma^\mu(1/3sin^2\theta_W)d_R) \\
J^\mu_{EM} &= \bar{e}_{L,R}\gamma^\mu(-1)e_{L,R} + \bar{u}_{L,R}\gamma^\mu(2/3)u_{L,R} + \bar{d}_{L,R}\gamma^\mu(-2/3)d_{L,R}
\end{aligned}
\tag{2.75}
$$

382 2.7 The Standard Model of Particle Physics

The Standard Model of particle physics, extends the GWS model by incorporating the QCD interaction between the quarks and gluons. The symmetry of this theory is that of:

$$SU(3)_C \otimes\ SU(2)_L \otimes\ U(1)_\gamma \tag{2.76}$$

The Lagrangian of the model is given by

$$\mathcal{L}_{SM} = \mathcal{L}_{GWS} - \frac{1}{4} G^a_{\mu\nu} G^{a\mu\nu} + g_S C^a_\mu J^{a\mu}_{QCD} \tag{2.77}$$

where the current for the QCD interaction, $J^{a\mu}_{QCD}$ is defined as:

$$J^a_{QCD} = \bar{u^i}\gamma^\mu t^a u^i + \bar{d^i}\gamma^\mu t^a d^i \tag{2.78}$$

where t^a are the Gell-Mann matrices defined in equation 2.30. The field strength tensor for the eight gluon fields, $G^a_{\mu\nu}$, is defined as

$$G^a_{\mu\nu} = (\partial_\mu C^a_\nu - \partial_\nu C^a_\mu) - g_S f^{abc} C^b_\mu C^c_\mu \tag{2.79}$$

The experimental evidence in favor of the SM is compelling. It has not only been able to describe existing phenomena to great precision, but has also predicted the existence of new forms of matter and interactions among fundamental particles. The UA1 [50] [51] and UA2 [52] [53] experiments at CERN, under the leadership of Carlo Rubbia, discovered the W and Z bosons in 1983. The experiments observed a handful of events, in $p\bar{p}$ collisions, at $\sqrt{s} = 540\,\text{GeV}$, and were able to measure the masses to be $M_W \sim\ 80\,\text{GeV}$ and $M_Z \sim\ 95\,\text{GeV}$. This was the first direct observation of the massive weak bosons predicted by the Glashow-Weinberg-Salam theory of weak interactions.

In the following years, from 1989-2000, the Large electron-positron (LEP) collider at CERN conducted precision measurements of the SM [54] [55]. Along with high-precision measurements on on the W, Z masses:

$$\begin{aligned} m_Z &= 91.1875 \pm 0.0021\,\text{GeV} \\ m_W &= 80.376 \pm 0.0033\,\text{GeV} \end{aligned} \tag{2.80}$$

the experiment was also able to put stringent limits on the existence of more than three families of leptons and quarks by measuring the width of the Z boson. Figure 2.4(a) shows the comparison of two, three, and four family hypotheses to data.

Another milestone for the Standard Model occurred in 1995 when the CDF [60] and D0 experiments [61] at the Tevatron announced the observation of the top quark, with $m_t \sim\ 176$ GeV, in $p\bar{p}$ collisions at $\sqrt{s} = 1.8$ TeV. Figure 2.4(b) shows a plot from 2012, the latest top quark mass measurements from CDF, which reports a $m_t = 173.18 \pm 0.56 \pm 0.75$ GeV. It was the last quark predicted by the CKM matrix to be observed, and earned Makoto Kobayashi and Toshihide Maskawa the nobel prize in 2008 for their work extending the quark sector to three

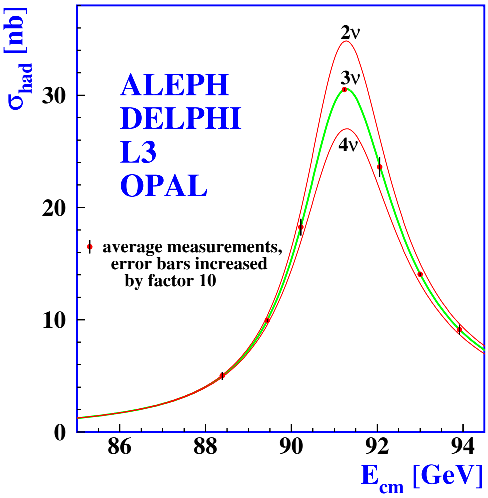

(a) Measurement of the width of Z boson from LEP, comparing the hypotheses of 2, 3, or 4 neutrino generations [56]

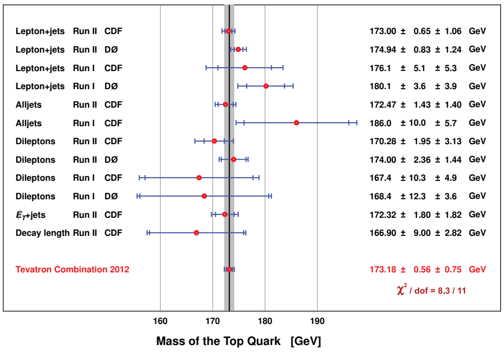

(b) Measurement of the top mass from the CDF detector at the Tevatron [57]

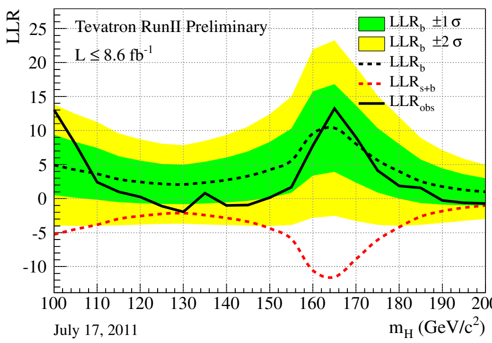

(c) Exclusions of Higgs mass values as of 2011, from the LEP and Tevatron experiments [58]

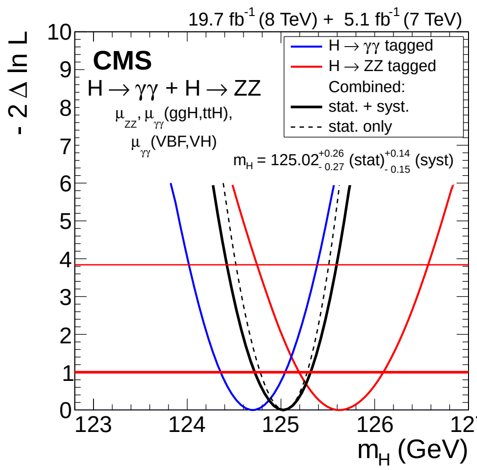

(d) Measurement of the Higgs mass from the CMS detector at the LHC [59]

Figure 2.4: Experimental milestones of the Standard Model

families and parameterizing their electroweak mixing.

After the discovery of the top-quark, the last remaining particle that was predicted by the Standard Model, and remained to be observed was the Higgs Boson. Although the LEP and Tevatron experiments were unable to observe the Higgs, they were able to exclude a large range of possible masses [58]. The combined results of both experiments, as of 2011, only allowed the possible masses of $115 < m_{Higgs} < 155$ GeV, and $m_{Higgs} > 176$ GeV, as shown in figure 2.4(c).

Yet another milestone was reached in 2012, when the CMS and ATLAS detectors at CERN announced the observation of a new boson, with characteristics strikingly similar to the elusive Higgs boson of the SM. Figure 2.4(d) shows the latest measurement results on the mass from the $H \to \gamma\gamma$ and $H \to ZZ$ channels, with a $m_H = 125.02 \pm 0.27 \pm 0.15$ GeV. One of the most important remaining goals is to measure the couplings of this new boson to all of the other particles in the Standard Model. Of particular interest is the coupling to the top-quark, since it offers the largest value of the Higgs Yukawa coupling to measure. This offers a test of the nature of the coupling, as well as a probe into deviations from its value.

2.8 Higgs Production in pp Collisions at the LHC

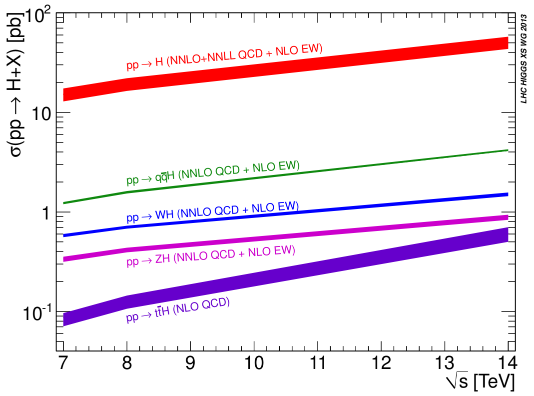

Figure 2.5: Higgs production cross-sections at the LHC, for 7-14 TeV pp collisions

The rest of the thesis will describe the search for Higgs-boson production in proton-proton collisions at the LHC, so it will be useful to understand the production mechanisms for the Higgs in this scenario. At the LHC collision energies $7 - 14$ TeV, there are four dominant production mechanisms that produce Higgs events: gluon-gluon fusion (ggf), vector-boson fusion (vbf), associated production with vector bosons (VH), and associated production with top-quark pairs (ttH). Figure 2.5 shows the relative cross sections for each of these mechanisms.

Gluon-gluon fusion, which proceeds via a heavy-quark loop [62], is the dominant production mechanism at the LHC. The QCD radiative corrections to the total cross section have been computed at the next-to-leading order (NLO) and at the next-to-next-to-leading order (NNLO

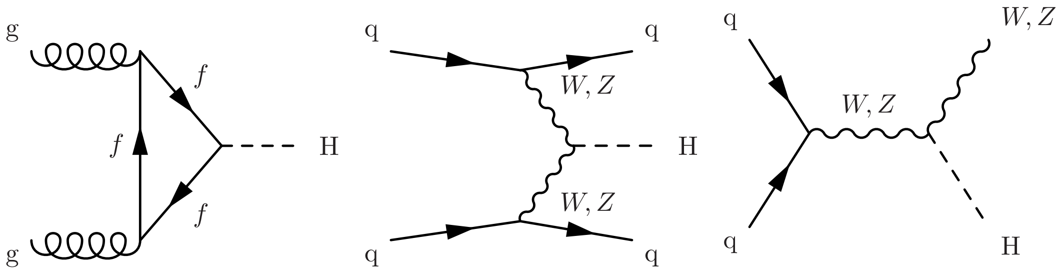

(a) Gluon-Gluon Fusion (b) Vector Boson Fusion (c) Associated Production with W, Z

Figure 2.6: Feynman diagrams for the three largest Higgs production modes at the LHC

accuracy). The cross section for Higgs production at $m_H = 125\,\text{GeV}$ and $\sqrt{s} = 8\,\text{TeV}$, the cross section is given as:

$$\sigma_{ggF} = 19.27 \quad \pm \quad \text{QCD Scale Unc.}^{+7.2\%}_{-7.8\%} \quad \pm \quad \text{PDF+}\alpha_S \text{ Unc.}^{+7.4\%}_{-6.9\%} \quad \text{pb}^{-1} \tag{2.81}$$

Figure 2.6(a) shows a Feynman diagram for this process. The triangle loop contains all strongly coupled fermions, which is dominated by the top-quark since its Yukawa coupling to the Higgs is the largest.

Vector-boson fusion proceeds through the fusion of W^+W^- or Z^0Z^0 gauge bosons [62]. The characteristic signature of the production mode is the associated production of two quarks, typically at a low angle relative to the proton beam. This process has been calculated to NNLO for QCD and NLO for electroweak (EW) corrections [62]. The cross section at $m_H = 125\,\text{GeV}$ and $\sqrt{s} = 8\,\text{TeV}$ is given as:

$$\sigma_{VBF} = 1.653 \quad \pm \quad \text{EW Unc.}^{+4.5\%}_{-4.5\%} \quad \pm \quad \text{QCD Scale Unc.}^{+0.2\%}_{-0.2\%} \quad \pm \quad \text{PDF+}\alpha_S \text{ Unc.}^{+2.6\%}_{-2.8\%} \quad \text{pb}^{-1} \tag{2.82}$$

Figure 2.6(b) shows a Feynman diagram for VBF production. The large coupling to the W, Z bosons helps to make this the sub-dominant production mechanism at the LHC. However, the gluon content of the proton at TeV energies is much larger than that of the valence quarks, thus the relative suppression.

The third largest production mechanism for Higgs bosons at the LHC is through associated production with a W or Z boson [62]. It has been calculated to NNLO for QCD and NLO for EW corrections. This process is also sometimes referred to as, "Higgstrahlung", since it resembles the bremsstrahlung process of an electron radiating a photon. The higher order electroweak corrections are similar to that of Drell-Yan, so much of the technology to compute the cross-section can be borrowed from existing EW calculations. The cross section for $m_H = 125\,\text{GeV}$ and $\sqrt{s} = 8\,\text{TeV}$ is:

$$
\begin{aligned}
\sigma_{WH} &= 0.7046 \quad \pm \quad \text{QCD Scale Unc.}^{+1.0\%}_{-1.0\%} \quad \pm \quad \text{PDF+}\alpha_S \text{ Unc.}^{+2.3\%}_{-2.3\%} \quad \text{pb}^{-1} \\
\sigma_{ZH} &= 0.4153 \quad \pm \quad \text{QCD Scale Unc.}^{+3.1\%}_{-3.1\%} \quad \pm \quad \text{PDF+}\alpha_S \text{ Unc.}^{+2.5\%}_{-2.5\%} \quad \text{pb}^{-1}
\end{aligned}
\tag{2.83}
$$

Figure 2.6(c) shows the Feynman diagram for VH production. This channel is most useful for identifying hadronic decays of the Higgs, since the associated gauge boson can decay to leptons, giving a strong kinematic handle over backgrounds that would normally overwhelm a similar search in the ggF channel.

2.9 $t\bar{t}H$ Production in pp Collisions at the LHC

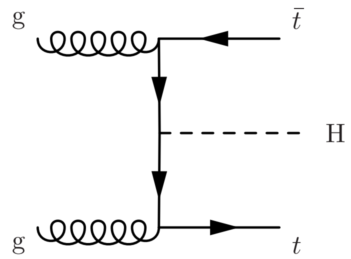

Figure 2.7: Feynman diagram for $t\bar{t}H$ production

The $t\bar{t}H$ production mode is the fourth-largest production mode at the LHC [62]. This production mode has been calculated to NLO in QCD [63] [64] and has been studied recently with the state of the art NLO tools using the aMC@NLO [65] and POWHEG (PYTHIA+HERWIG) [66] frameworks. Studies have also been performed interfacing NLO QCD studies [67] with the Sherpa parton shower framework [68]. Additional studies on the effects of spin correlations with the aMC@NLO and Madspin framework have also been performed [69].

It has been found that the additional of NLO effects increases the cross-section relative to LO by $\sim 20\%$. The largest theoretical uncertainty comes from the variation of the renormalization and factorization scale, the QCD coupling α_S, and the PDF uncertainty. The renormalization and factorization scales are set to $\mu_R = \mu_F = (1/2)(m_T + m_T + m_H)$ and are varied by a factor of 2 to determine the cross-section's dependence on these parameters. Three different PDF sets, MSTW2008, CTEQ6.6, and NNPDF2.0 were used with the appropriate corresponding values of α_S to determine the combined effect of varying PDF+α_S. The cross section for $m_H = 125\,\text{GeV}$ and $\sqrt{s} = 8\,\text{TeV}$ is given by:

$$
\sigma_{ttH} = 0.1293 \quad \pm \quad \text{QCD Scale Unc.}^{+3.8\%}_{-9.3\%} \quad \pm \quad \text{PDF+}\alpha_S \text{ Unc.}^{+8.1\%}_{-8.1\%} \quad \text{pb}^{-1} \tag{2.84}
$$

A search for the Higgs in this production mode is additionally challenging due to this large

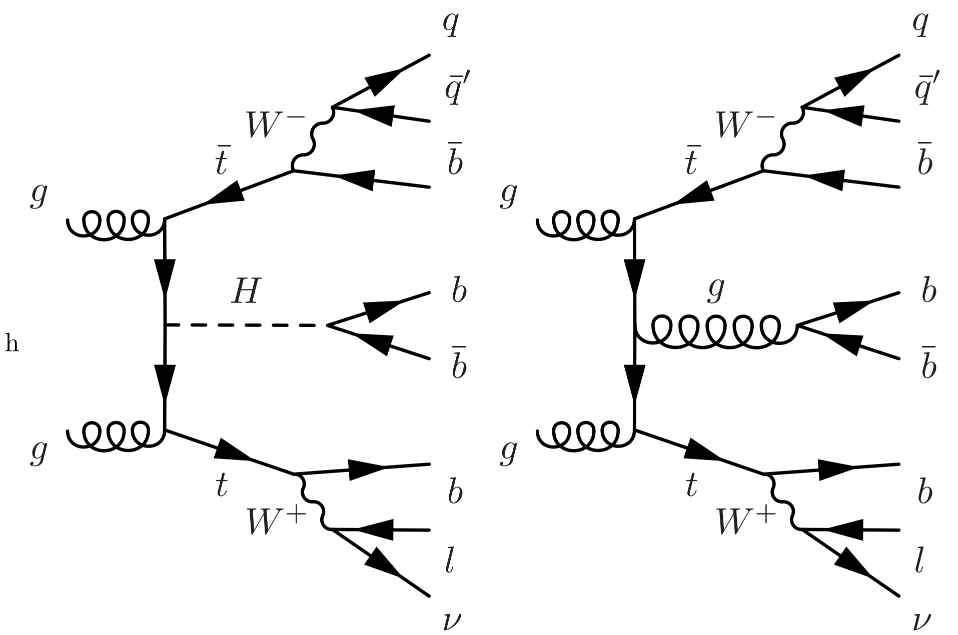

(a) Semileptonic $t\bar{t}H$, with $H \rightarrow\ b\bar{b}$ (b) Semileptonic $t\bar{t}+b\bar{b}$

Figure 2.8: Feynman diagrams for the semileptonic $t\bar{t}H$ process and its irreducible background, $t\bar{t}+b\bar{b}$

$\sim$ 10% error on the theoretical cross-section. Figure 2.7 shows a Feynman diagram for this process before the branching of the top-quarks or Higgs to final states.

When asking for the Higgs to decay to b-quark pairs, yet another complication arrises when trying to identify which b quarks came from a top decay or from a Higgs decay. For example, in the semileptonic decay of top quarks, there will be four b quarks, and two light-flavor quarks in the final state. This means there are 15 (six choose four) possibilities to associate quarks to the top system. Although this is potentially constrained by b-tagging (more on this later), and kinematic requirements (such as forming the top or W masses), the number of remaining possibilities smears out the resolution on peaking variables such as the invariant mass of b-quark pairs.

2.10 Background Processes to $t\bar{t}H$

The dominant background for $t\bar{t}H$ production of top-quark pairs with additional ISR/FSR jets, $t\bar{t}+jets$. The irreducible component of this background occurs when the extra radiation produces a final state with two additional b quarks, $t\bar{t}+b\bar{b}$. Figure 2.8 compares the Feynman diagrams for the semileptonic decays of $t\bar{t}H$ and $t\bar{t}+b\bar{b}$.

Additional difficulties come from the theoretical uncertainty on the $t\bar{t}+b\bar{b}$ background [62]. The process has been calculated to NLO QCD in Sherpa [68] and OpenLoops [70] [71] [72]. These studies have shown that, depending on the event selection, and use of NLO PDF inputs,

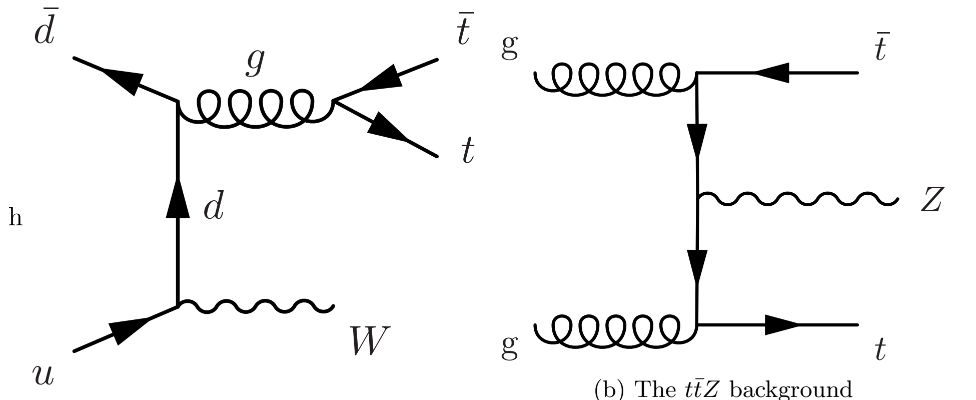

(a) The $t\bar{t}W$ background

(b) The $t\bar{t}Z$ background

Figure 2.9: Feynman diagrams for the $t\bar{t}W$ and $t\bar{t}Z$ background processes

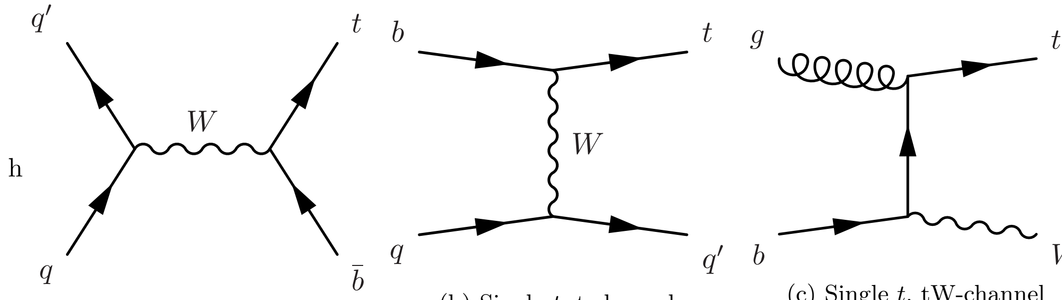

(a) Single t, s-channel

(b) Single t, t-channel

(c) Single t, tW-channel

Figure 2.10: Feynman diagrams for the single t s,t, and tW background processes

the difference between LO and NLO calculations on the cross section can be anywhere from 0.99% to 1.96%.

The light flavor component of the $t\bar{t} + jets$ background also enters in the selection when any of the jets from the $t\bar{t}$ system or extra radiation are misidentified as b jets. The cross-section for the $t\bar{t} + jets$ process is $\sim 245\,\mathrm{pb}^{-1}$. This is a factor of 1800 compared to $t\bar{t}H$, so even if a b-tagging algorithm performs with a 1% mis-identification rate of light-jets, there will still be a large contribution from this process that will leave a very similar signature in the detector as $t\bar{t}H$.

The next largest background is the production of vector bosons in association with top-quark pairs, $t\bar{t}W$ and $t\bar{t}Z$. Figure 2.9 shows Feynman diagrams from these two processes. They have cross-sections of $\sigma_{ttW} = 0.249\,\mathrm{pb}^{-1}$ and $\sigma_{ttZ} = 0.208\,\mathrm{pb}^{-1}$, which are only a factor of $\sim$2 greater than the $t\bar{t}H$ process. These processes can enter the semileptonic $t\bar{t}H$ selection by a semileptonic $t\bar{t}$ decay, while the vector bosons decay to quarks, or through a hadronic $t\bar{t}$ decay, while the vector bosons decay to quarks, and in the case of $t\bar{t}Z$, one of the leptons is not identified in the reconstruction.

Single-top production is also an important background to consider in a search for $t\bar{t}H$ production. Figure 2.10 shows Feynman diagrams for this process. It does not have as large of a

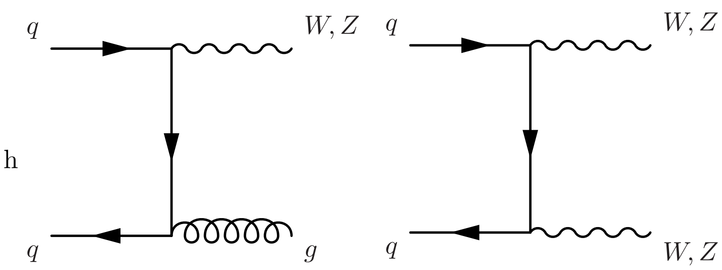

(a) W, Z plus jets (b) DiBoson Production

Figure 2.11: Feynman diagrams for the W, Z plus jets, and diBoson (WW, WZ, ZZ) production.

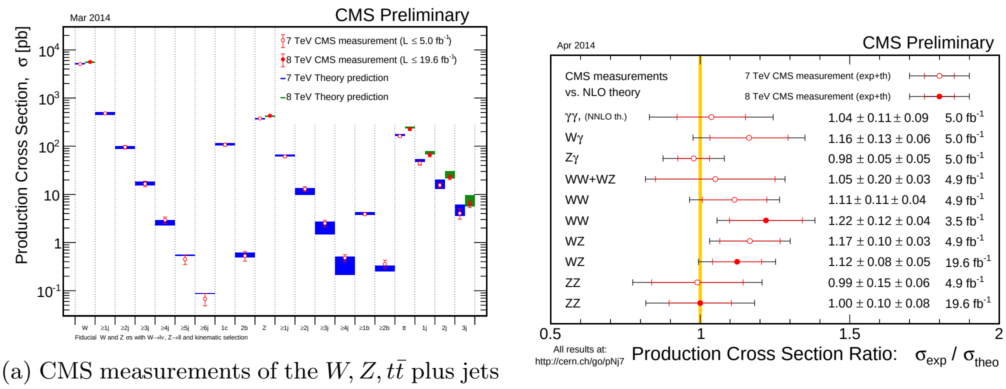

(a) CMS measurements of the $W, Z, t\bar{t}$ plus jets backgrounds

b

(b) CMS measurements of DiBoson Production

Figure 2.12: Measurements of $t\bar{t}H$ backgrounds at CMS [3]

contribution as the other backgrounds, since it requires additional radiation in order to have a similar final state jet multiplicity as $t\bar{t}H$. However, since a top-quark is still involved in the process, the final state kinematics of its decay products will be very similar. Single-t production has a cross section of $\sigma_t = 71.3\,\text{pb}^{-1}$, while single-$\bar{t}$ production has a cross section of $\sigma_{\bar{t}} = 43.6\,\text{pb}^{-1}$, due to charge asymmetry of the valence quarks of the proton

The last backgrounds to consider are the electroweak production of W and Z bosons in association with jets, as well as WW, WZ, and ZZ pairs in association with jets. Figure 2.11 shows the Feynman diagrams for these processes, where the V, stands in for either a W or Z boson. For a semileptonic selection of $t\bar{t}H$ events, Z plus jets events enter from a misidentification of one of the leptons from the Z boson decay. Extra FSR/ISR radiation is also to leave a similar signature in the signal region of a $t\bar{t}H$ search, so it mainly contributes to control regions of the data.

All of these backgrounds, except for $t\bar{t}+b\bar{b}$, have been measured at CMS. With the exception of a small degree of tension in the WW cross-section measurement, all backgrounds are in good agreement with SM predictions. Figure 2.12(a) shows the results of CMS measurements on V+jets and $t\bar{t} + jets$ backgrounds. Figure 2.12(b) shows the same, but for diboson production.

2.11 Potential BSM Effects on $t\bar{t}H$ production

The phenomenological motivation for the existence of physics beyond the Standard Model come from the observation of phenomenon or states of matter not described by the theory. Observations of the cosmic microwave background from the Plank telescope have estimated that only $\sim 5\%$ of the observable universe is composed of ordinary matter [73]. The remaining composition is divided between dark matter and dark energy ($\sim 27\%$, and $\sim 68\%$ respectively). Evidence for dark matter also comes from discrepancies between the observed rotational velocities of galaxies, and the observed mass distributions, suggesting the presence of an additional form of matter which does not interact electromagnetically [74].

Additionally, in 1998, the Super-Kamiokande experiment proved that neutrinos oscillated between flavors, implying indirectly that they also have mass [75]. This is something not described in the SM. Due to their neutral charge, these particles are extremely difficult to detect, so experiments have only been able to measure differences in the mass squared between the three mass eigenstates. In 2005, the KamLAND experiment reported $|\Delta m_{12}^2 = 0.000079eV^2|$ [76]. In 2006, the MINOS experiment reported $|\Delta m_{23} = 0.0027eV^2|$ [77].

One of the largest theoretical problems with the SM comes from the mechanism which made it all possible, the Higgs. In equation 2.73 there are terms that couple the Higgs boson to itself, $-\lambda v h^3$, and $-\frac{1}{4}\lambda h^4$. When computing NLO effects, these terms lead to a divergence in the Higgs mass, when considering the effect of a loop of fermions on the Higgs propagator. The corrections are of the form $\Delta m_H = -\frac{\lambda_f^2}{8\pi^2}\Lambda_{UV}$, and are very large compared to the LO calculation. Where Λ_{UV} is the high energy cut off for the theory, which in the limit of a perfect theory, should extend to infinity. This is known as the hierarchy problem.

Beyond the Standard Model physics is a term that describes extensions of the Standard Model in order to describe the observed phenomenon. For the neutrino oscillations, a solution similar to CKM matrix has been proposed, the Pontecorvo Maki Nakagawa Sakata (PMNS) matrix. This proposes that the mass eigenstates of the neutrino are linear combinations of the weak eigenstates, allowing for the mixing of flavors. Current experiments now seek to measure the free parameters of this model.

Both the dark matter and hierarchy problems suffer in the fact that there is no clearly favored model, such as the PMNS matrix, to provide a theoretical solution. There are many models that describe this phenomenon, just none that are clearly favored. Out of the plethora of theories that attempt to solve these problems, supersymmetry (SUSY) is the most popular in the theoretical and experimental community. It suggests that there is a broken symmetry between fermions and bosons, and introduces a partner to each SM particle with a spin quantum

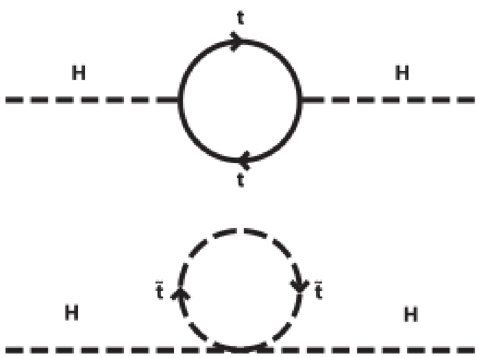

Figure 2.13: The cancellation of the divergent Higgs mass from a loop of top-quarks is cancelled by a loop of supersymmetric top-quarks, stop-quarks [4],

number less 1/2 [78]. For the hierarchy problem, this provides a set of particles to cancel out the divergences in the NLO corrections to the Higgs mass. Figure 2.13 shows the Feynman diagrams for a supersymmetric top-quark, or stop quark, that would cancel the divergent contribution from the SM top quark. Depending on the specific form of the SUSY model, the stop quarks can potentially couple directly or indirectly to the top quark, producing them at a higher rate during pp collisions. This would effect the number of observed events making it into the $t\bar{t}H$ selection.

A number of extensions to the SM also involve introducing new top-like particles into the theory. Vector-like quarks would be spin 1/2 particles that transform as triplets under the $SU(3)$ color group and whose left and right-handed components have the same color and electroweak quantum numbers [79]. These objects are common to several different types of models. Little Higgs models [80] [81] [82], models with extra dimensions [83] [84], top-color models [85], and composite Higgs models [86], include a vector-like top partner,t' that decays to a top-quark and either a Higgs, W, or Z particle. Both $t't'$ pair production and $t't$ production would yield the ttH final state, or at least one indistinguishable detector signature. $t\bar{t}H$ search can provide indirect limits on these models, by observing an excess or lack thereof of $t\bar{t}H$ events, without having to directly construct a t' resonance.

Chapter 3

The Large Hadron Collider

Figure 3.1: Aerial view of the LHC complex, spanning the French-Swiss border [5]

The Large Hadron Collider (LHC), is a superconducting, proton-proton, accelerator and collider operated by the European Center for Nuclear Research (CERN) laboratory in Geneva, Switzerland [8]. Figure 3.1 shows an aerial view of the LHC complex, with the main laboratory campus being labeled as CERN, with four of the detector experiments being labeled as ALICE, ATLAS, CMS, and LHCb. Three smaller experiments, not pictured, also use the LHC ring, and are TOTEM, LHCf, and MOeDAL. It was designed to elucidate the mechanism of electroweak symmetry breaking and explore TeV scale of particle physics. As such, it is required to produce a large number of high center-of-mass energy events. The high center-of-mass energy allows the creation of heavy particles, while a large luminosity allows for the creation of rare processes. The number of events produced at a collider is a product of the luminosity of the collider and the total cross-section for the objects being collided.

$$N_{events} = L\sigma_{event} \tag{3.1}$$

The cross-section, σ_{event}, can be estimated from the theory of the Standard Model as described in section 2.1 and validated by measurement at detectors, such as CMS, as shown in section 2.10. The luminosity is a control of the experiment, and for Gaussian distributed beams, is given by the equation:

$$L = \frac{N_b^2 n_b f_{rev} \gamma_r}{4\pi\epsilon_n\beta^*}F \tag{3.2}$$

The parameters of this equation and their value for the LHC is as follows:

- N_b - Number of of particles per bunch, squared since there are two beams. The mechanism of achieving such high energies is based in Radio-Frequency (RF) cavity technology, which clusters the protons together into packets, which are all accelerated and collided together. For the LHC, $N_b = 1.15 \times 10^{11}$.

- n_b - Number of bunches per beam. The maximum design for the LHC allows for $n_b = 2808$ bunches, however in practice, lower number of bunches have been run with in order to create more time between bunch crossings.

- f_{rev} - Revolution frequency of the protons in the LHC ring. This is determined by ring circumference, and for the LHC, $f_{rev} = 11.2$ kHz.

- γ_r - This is the relativistic gamma-factor, determined by the speed, and thus the center of mass energy of the collisions.

- ϵ_n - This is the normalized transverse emmitance of the beam, which describes the RMS spread of the beam in its transverse plane. For the LHC $\epsilon_n = 3.75$ μm.

- β^* - Is the minimum of the β function, which is defined as the square of the transverse beam-size divided by ϵ_n. It is minimized at interaction regions, where the beams are being squeezed into the smallest region possible, to maximize the probability of protons colliding during each bunch crossing. For the LHC, $\beta^* = 0.55$

- F - This is the efficiency for having the two beams head-on, and is determined by the crossing angle at which the two counter-rotating beams meet each other.

The LHC is designed to deliver a maximum luminosity of L $= 10^{34}\mathrm{cm}^{-2}\mathrm{s}^{-1}$ to the CMS and ATLAS experiments, with a maximum center-of-mass energy of $\sqrt{s} = 14\,\mathrm{TeV}$.

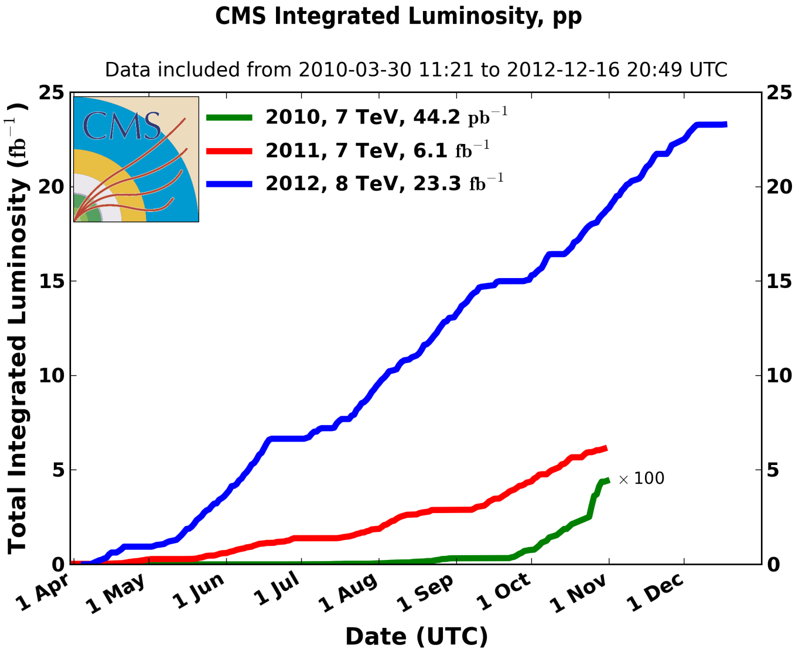

Figure 3.2: Integrated Luminosity delivered to the CMS experiment from 2010-12 [6]

In 2010-11, the LHC ran at center-of-mass energy, $\sqrt{s} = 7\,\text{TeV}$ and delivered $\sim 6\,\text{fb}^{-1}$ of data to the CMS experiment. In 2012, it ran at $\sqrt{s} = 8\,\text{TeV}$ and collected $\sim 23\,\text{fb}^{-1}$. Figure 3.2 shows a diagram of the luminosity collected as a function of time for each year running.

The next sections will describe the LHC accelerator complex, the chain of events leading up to collisions of protons at the LHC, and the associated technologies that allow for the control and operation of the high-energy, high-luminosity beams that allow the CMS and ATLAS experiments to search for heavy particles and rare-processes.

3.1 The LHC Accelerator Complex

The main LHC ring is a 26.7 km tunnel, that is 45 m to 170 m underneath the surface of the earth, with 1.4% slope towards Lake Leman. It extends across the French-Swiss border, into the French countryside. The tunnel was originally constructed between 1984 and 1989 for the Large Electron Positron (LEP) experiment that is famous for it's precision measurements of several Standard Model parameters [8]. The choice to build the ring underground was driven by real estate costs, but the underground setting also provides natural radiation shielding from the beam-line and greatly reduces the impact of cosmic radiation on the detectors.

The LHC also utilizes the existing accelerator complex from the LEP experiment, which is shown in figure 3.3. The complex is composed a series of increasingly powerful accelerators that gradually increase the energy of the protons.

Protons are initially accelerated by the Linac2 linear accelerator up to 50 MeV [93] [94]. A

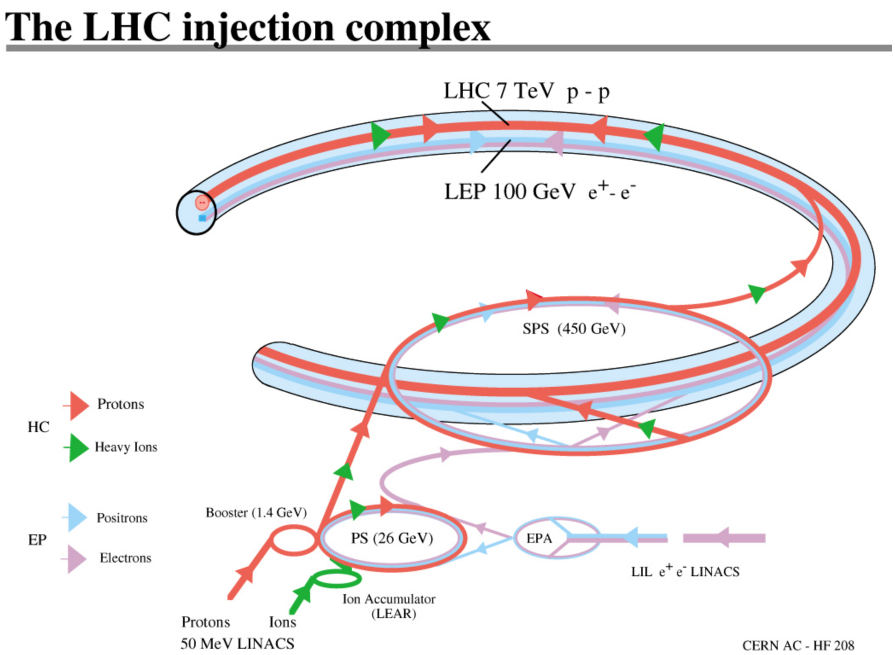

Figure 3.3: The LHC accelerator complex, taking protons from a bottle of Hydrogen at the Linac2, all the way to the LHC ring [7]

bottle of Hydrogen is attached to a duoplasmatron source. This device ionizes the Hydrogen, and creates a 300 mA beam of protons, through a high-voltage anode, and a geometry designed to focus and collimate the beam as it leaves the device. Figure 3.4(a) shows a schematic for this device, showing the gas input on the left, and proton beam leaving to the right. Figure 3.4(b) shows the actual device used in the Linac2 at CERN. The proton beam then enters the Radio-Frequency Quadrupole (RFQ) system, which accelerates and bunches the protons up to 750 keV. The RFQ is a waveguide with four flanges, which have been machined with a sinusoidal modulation in the longitudinal direction, which creates an standing electric wave in this direction, accelerating the protons. Figure 3.4(c) shows a schematic of this modulation, and figure 3.4(d) is a close-up image of this modulation in an actual RFQ. The last stage of acceleration is provided by three Alvarez tanks. Each Alvarez tank holds a series of electrically isolated cylinders, known as drift tubes, coaxial with the main tank, with gaps in between them. An alternating electric field is present in the gaps, and space between each drift tube and the walls of the tank. Protons passing through the center of the drift tubes feel no electric field, but the gaps are located such that, a proton will always see an accelerating field in the gap, and are thus receive a boost of energy from each gap as it traverses the length of the three tanks. Figure 3.4(e) shows an image of the inside of an Alvarez tank, and figure 3.4(f) shows the tanks at the Linac2 at CERN. The final product is a 180 mA, 50 MeV proton beam, which is steered to the Proton Synchrotron Booster for the next stage of acceleration.

The Proton Synchrotron Booster (PS booster) complex accelerates the protons up to 1.4

h

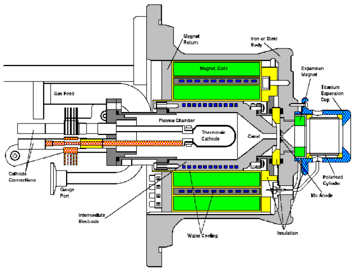

(a) Schematic of the duoplasmatron ion source, which creates a proton beam from source bottle of Hydrogen [87]

(b) The Duoplasmatron used in the Linac2 at CERN, the source of the LHC proton beam [88]

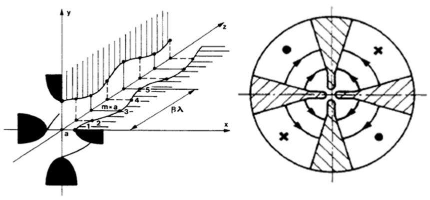

(c) A schematic of a RFQ, showing the modulation of the flanges in the longitudinal direction [89]

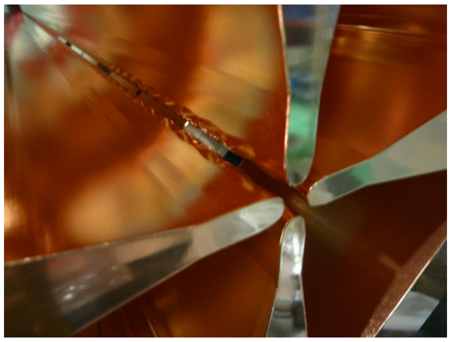

(d) A close-up image of a RFQ, showing the precise machining of the longitudinal modulation of the flanges [90]

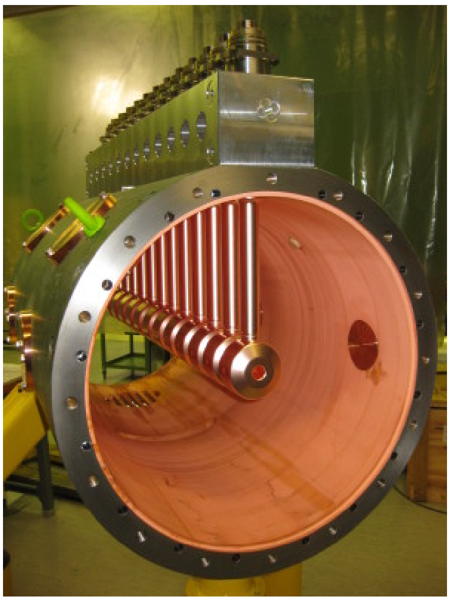

(e) The inside of an Alvarez tank, showing the central drift tubes, where the protons are accelerated at each gap between successive drift tubes [91]

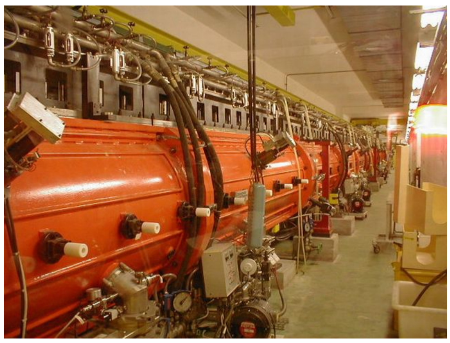

(f) The Alvarez tanks at the Linac2 [92]

Figure 3.4: Features of the Linac2, the first stage of acceleration in the LHC injection chain

h 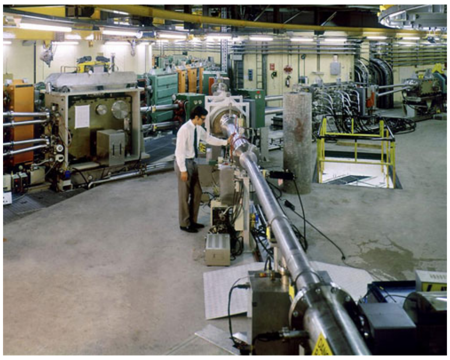

(a) The Injection site from the Linac2 into the PS booster [95]

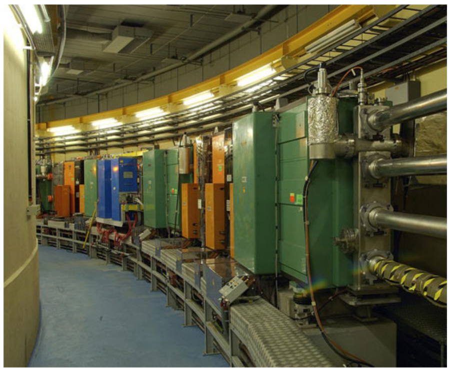

(b) A section of the PS booster, with the four stack synchrotron beam-lines shown in the lower right hand side of the picture [96]

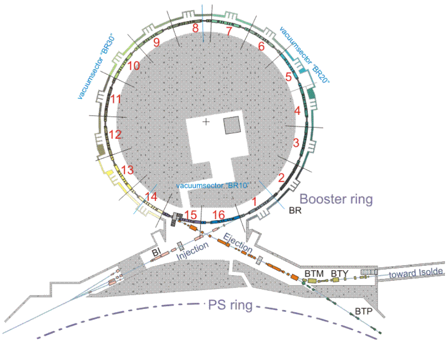

(c) A drawing of the 16 sections of the PS booster [97]

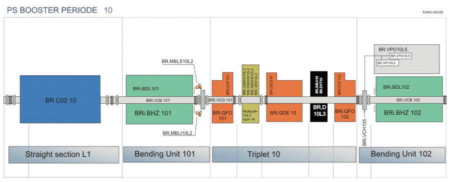

(d) Section 10 of the PS booster. This begins with the CO2 cavity, the main driver of the acceleration; followed by a dipole magnet, a triplet of focusing magnets, and a second dipole magnet [98]

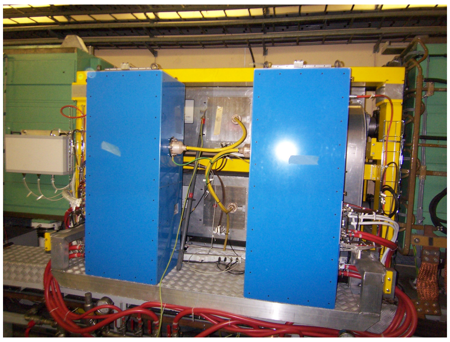

(e) A picture of the CO2 RF Cavity, which provides the principle acceleration for the protons in the PS booster [99]

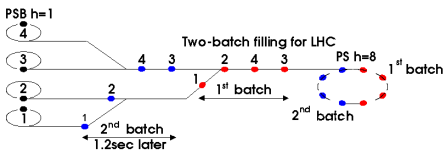

(f) The two batch filling scheme for the PS. It takes 1.2 s for each batch to be accelerated from 50 MeV to 1.4 GeV [100]

Figure 3.5: Features of the PS booster, the second stage of the LHC injection chain

GeV [93]. The complex takes the proton beam from the Linac2 and splits the beam into four separate, synchrotrons, stacked on top of one another. Figure 3.5(a) shows the injection site of the proton beam from the Linac2 into the PS booster. The right side of figure 3.5(b) shows the four synchrotron beam pipes stacked vertically on top one another. The splitting of the beam is done in order to reduce the effect of the space charge of the proton beam, which would increase the transverse emmitance beyond a tolerable degree. The PS booster uses thirty-two 0.87 T dipole magnets to bend the beams, and fourty-eight quadrupoles to focus the beam as it makes its way around each of the 50 m diameter rings. Each magnet is composed of a vertical stack of four magnets, one for each of the synchrotrons, and share a common yoke, allowing one power supply to provide the current to all of them in series [101]. The booster is divided into 16 arcs, as shown in figure 3.5(c). Each arc contains a bending dipole, 3 focusing quadrupoles, and a second bending dipole, followed by a straight section containing beam diagnostic, injection and ejection systems, and in three sections, the Radio-Frequency (RF) cavities, which is the mechanism of accelerating the beam [102]. Figure 3.5(d) shows the layout of the tenth arc, which also contains one of the RF cavities in the first section.

An RF cavity is a specially shaped, hollow conductor, that the beam passes through [103]. The shape of the cavity determines the resonant frequency and harmonics (integer multiples of the fundamental frequency), of the standing electromagnetic fields that result when the cavity is driven by an alternating voltage source. The idea is to choose a resonant frequency such that the proton will always experience a positive electric field, and thus an acceleration, each time it passes through the RF cavity. This means that the revolution frequency of the proton must be equal to the fundamental frequency or harmonic of the RF cavity, $f_{RF} = n \times f_{rev}$, with $n = 1, 2, 3....$ Eventually, the proton is accelerated up to an equilibrium speed and will enter the cavity just as the standing electric field is alternating through it's zero point. If arrives too early for this (moving too fast), then it will experience a negative electric force, a deceleration, which will eventually bring it back to the equilibrium revolution frequency, where it experiences zero net force. A diffuse beam of protons will be bunched into groups of protons through this effect as well, as the faster protons in the beams are decelerated, and the slower ones accelerated, until they all reach the same equilibrium revolution frequency. Driving the RF cavity with a harmonic, n, of the proton's revolution speed will thus create n bunches of protons. Each one of the potential n bunch positions is referred to as a bucket. In the case where a proton has to be accelerated through a wide range of energies, the frequency of the cavity must also increase to maintain synchronization with the proton revolution frequency.

Three types of RF cavities are used to accelerate the beam during each revolution. The first of the three types of RF cavities is the CO2, with frequency range of 0.6 to 2.0 MHz and is used to drive the $h = 1$ harmonic of the synchrotron, and is pictured in figure 3.5(e). The second type of cavity is the CO4 chamber, with a frequency range of 1.2 to 3.9 MHz, and drives the $h = 2$ mode of the synchrotron. This second mode is capable of splitting the beam and creating two separate bunch structures. However, for LHC running, only one bunch is used, and is driven primarily by the $h = 1$ mode. The $h = 2$ mode is supplemental and is used to shape the beam. A third type of RF cavity, CO16, has a frequency range of 5 to 16 MHz, and is used to control the longitudinal shape of a bunch during acceleration. The beam leaves the PS booster and enters the PS in a two-batch filling scheme, taking only 1.2 s to accelerate a second batch of protons from 50 MeV to 1.4 GeV. This second batch enters just as the first batch has traveled to the opposite side of the PS ring. A schematic of this process is shown in figure 3.5(f). To achieve the 25 ns bunch spacing design of the LHC, only 6 bunches of proton beam need to be delivered to PS. This is achieved by either using a 4+2 or 3+3 filling scheme, in terms of the number of proton bunches delivered from the four possible synchrotrons.

The next stage is the Proton Synchrotron (PS), which will boost the protons up to 25 GeV [93]. The layout is shown in figure 3.6(a). The ring has a circumference of 628 m, and uses 100 dipole magnets and 177 higher-order focusing magnets, to steer the beam around the ring. Figure 3.6(b) shows a picture of one of the dipole magnets used at the PS. In addition to providing acceleration up to 25 GeV, the PS forms the basis of the bunch structure that is eventually used in the LHC. The $h = 7$ harmonic is used to capture the 6 bunches of protons delivered from the PS booster, leaving a gap in the place of a seventh bunch. The beam is then split into three, by using three different RF cavities tuned to the $h = 7, 14, 21$ modes of the PS. Figure 3.6(c) shows a simulation of a proton bunch being divided into three over the course of 25 ms. The $h = 21$ mode is then used to accelerate the protons to from 1.4 to 25 GeV using the 20 MHz RF cavity. Each bunch is then split twice, using the $h = 21, 42, 84$ synchrotron modes, to create 72 bunches, spaced 25 ns apart, with a 320 ns gap for the 12 unused buckets of the $h = 84$ harmonic. This process is simulated in figure 3.6(d), over the course of 125 ms. The 320 ns gap is created to account for the rise time of the kicker magnet, which ejects the beam out of the PS into the SPS. The entire splitting process is summarized in figure 3.6(e). For the case of 50 ns bunch spacing, the final stage of splitting is not performed, and the $h = 21, 42$ modes are used to split the beam. Finally, in order to fit the bunches into the 200 MHz RF acceleration scheme of the SPS, the bunch length must be compressed from 11 ns to 4 ns. This is achieved by rotating the beam in the energy vs time phase space by sequential increases in voltage to the 40 MHz $h = 84$ mode, followed by an increase to the 80 MHz $h = 168$ mode. Figure 3.6(f) shows the result of this rotation - a distortion free ellipse with a smaller 4 ns spread, but a larger spread in the energy spectrum of the proton beam.

h

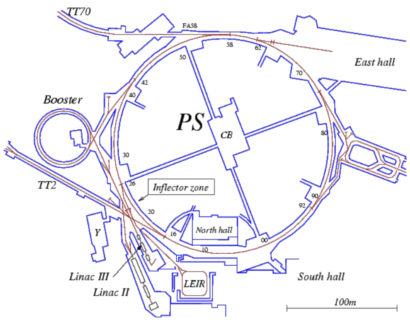

(a) A diagram of the PS layout [104]

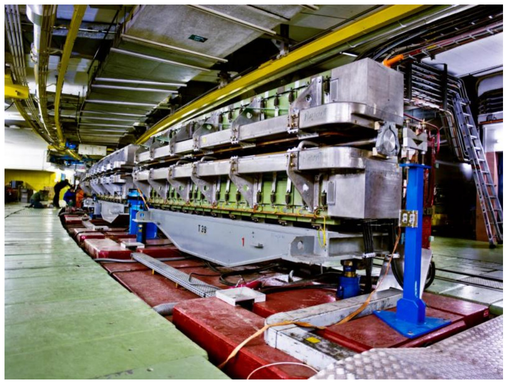

(b) Dipole magnets used to steer the beam around the 100 m radius PS ring [105]

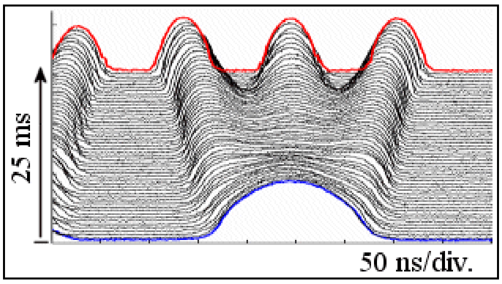

(c) A simulation of the PS using the $h = 7, 14, 21$ modes of to split the beam into 3 bunches [93]

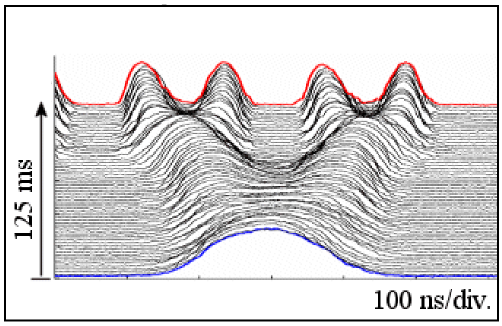

(d) A simulation of the splitting each bunch into two, and two again [93]

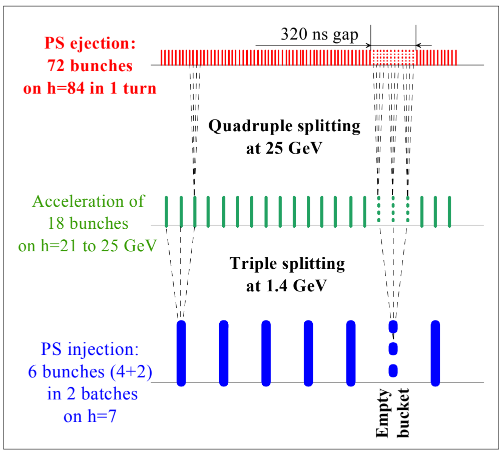

(e) An overview of the splitting procedure [93]

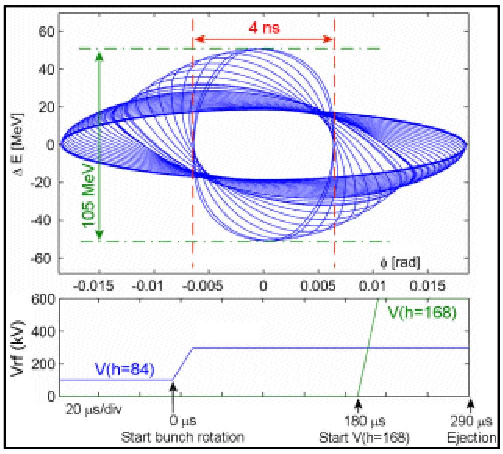

(f) Rotation in phase space of the 25 GeV proton beam, compressing the bunch lengths from 11 ns to 4 ns [93]

Figure 3.6: Features of the PS, the third stage of the LHC injection chain

h

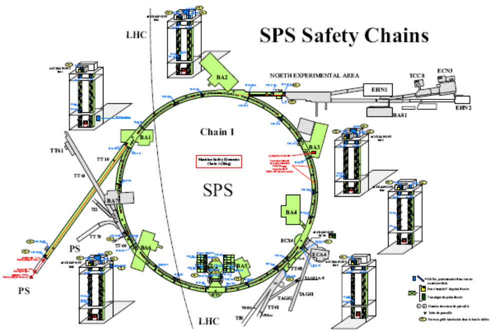

(a) The layout of the SPS facility [106]

(b) A section of dipole magnets used in the SPS [107]

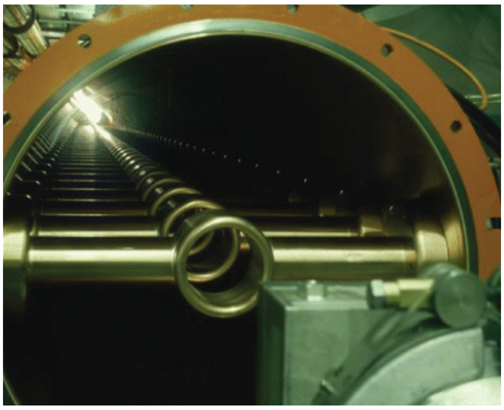

(c) The inside of the traveling wave guide structure, for the 200 MHz RF cavity in the SPS [108]

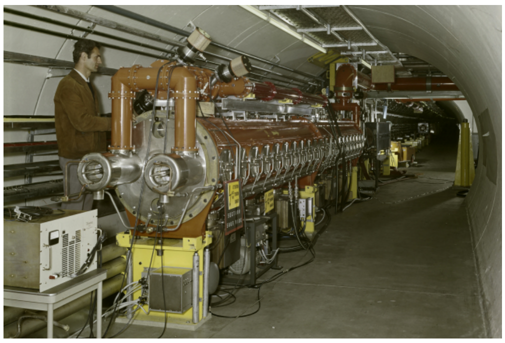

(d) The outside of the 200 MHz RF cavity used to accelerate protons from 25 to 450 GeV [109]

Figure 3.7: Features of the SPS, the fourth and final stage of the LHC injection chain

Next, the protons arrive at the Super Proton Synchrotron (SPS), where they will be accelerated to 450 GeV. The SPS is the last stage of acceleration before the protons are injected into the LHC. The layout is show in figure 3.7(a). It has a circumference of 7 km, and steers the proton beam with 744 dipole magnets, with 573 higher-order focusing magnets [110]. Figure 3.7(b) shows one of the dipole magnets in the SPS tunnel. Like all the other synchrotrons in the injection chain, the acceleration is provided by RF cavities. A 200 MHz system of RF cavities capture and fill the SPS by using 2-4 batches of 72 bunch proton beams from the PS [93]. Although the relative change in frequency is small, the large degree of acceleration necessitates the use of a tunable RF cavity. The 200 MHz system has 2 sections of 4 traveling wave cavities in series, and another 2 sections of 5 cavities in series. Figure 3.7(c) shows the inside of this structure, which uses drift tubes to accelerate protons in the gaps between tubes, with horizontally mounted bars, spaced 374 mm [111] apart, determining the periodicity of the resonant RF field that builds up inside. The outside of the structure is shown in figure 3.7(d). An additional 800 MHz system is used to control the transverse emmitance. It is also used to stabilize the beam-line and prevent coupled-bunch instabilities [93].

Finally, protons are injected into the LHC ring in one clockwise, and another counter-clockwise rotating beams. In order to work in the limited space of the existing LEP tunnel, the two beams are contained within a single mechanical and cryostat structure, with a dual-bore design for each of the beams. Here, each proton beam is accelerated to their final energy of 7 TeV, moving at 99.9999991% the speed of light, before they meet head on, producing 14 TeV center-of-mass collisions.

The LHC ring itself is divided into eight octants, with eight straight sections that are located in front and behind each of the eight collision points, where the beams are made to cross and collide, as shown in figure 3.8. These crossings are known as interaction regions (IRs). Four of these points are currently being used by experiments. TOTEM has detectors on either side of the CMS experiment at one interaction region, known as point 5 (P5). LHCf has detectors on either side of ATLAS at point 1 (P1). MOeDAL has detectors near LHCb at point 8 (P8) and the ALICE detector is located at point 2 (P2). The following sections will cover the RF, magnet, cryogen, and vacuum technologies used in the LHC ring.

3.2 LHC Magnets

Several types of magnets are used in order to properly circulate and focus the proton beam as it makes its way around the 26.7 km long tunnel. A complete list of all types, can be found in the technical design report [112], as well as through CERN's outreach web resources [113].

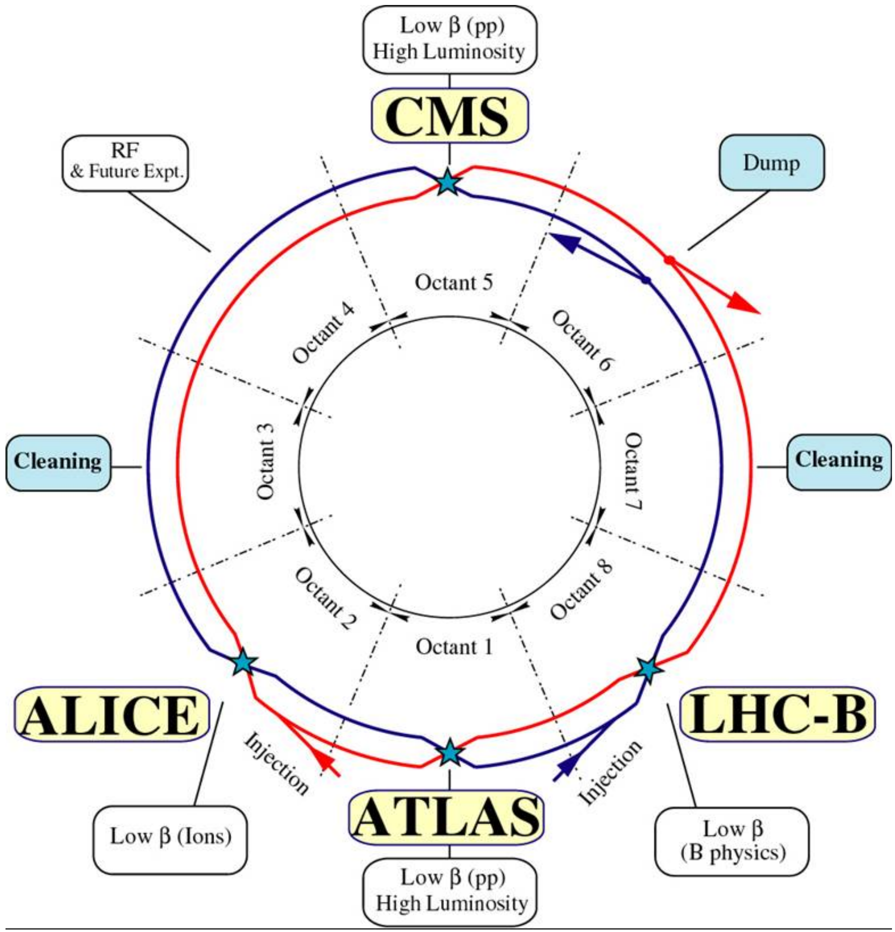

Figure 3.8: The LHC ring is divided into eight octants [8]

This section will give an overview of the a few of the critical subsystems: the septum and kicker magnets used for injection from the SPS, the dipole magnets used for bending the beam around the circumference of the ring, and the higher-order-pole magnets that are used for focusing the beam.

The injection and extraction of proton beams from one synchrotron to another involves three types of magnets, septums, kickers, and bumpers. Septum magnets contain a partition, or a septum, that provides a boundary between a high magnetic field region and a near-zero magnetic field region and are operated in DC or a slow-pulsed mode [114]. In case of injecting a beam of protons into a synchrotron, the target beam-pipe of the synchrotron passes through the low-field region, so the trajectory is unaffected by the high-field region, which bends the injection beam towards the synchrotron aligning it horizontally, with the target beam. The kicker magnet, is a fast-pulsed magnet and provides the timing selection in order to make a final vertical bend into the synchrotron orbit, and into the correct basket of the synchrotron bunch train [9]. Finally, bumper magnets make small bends to the beam and align it with the injection site. Figure 3.9 shows a schematic for this process, where a transfer line brings protons to a septum, which bends the beam to a kicker, which makes the final corrections to match the synchrotron orbit. For

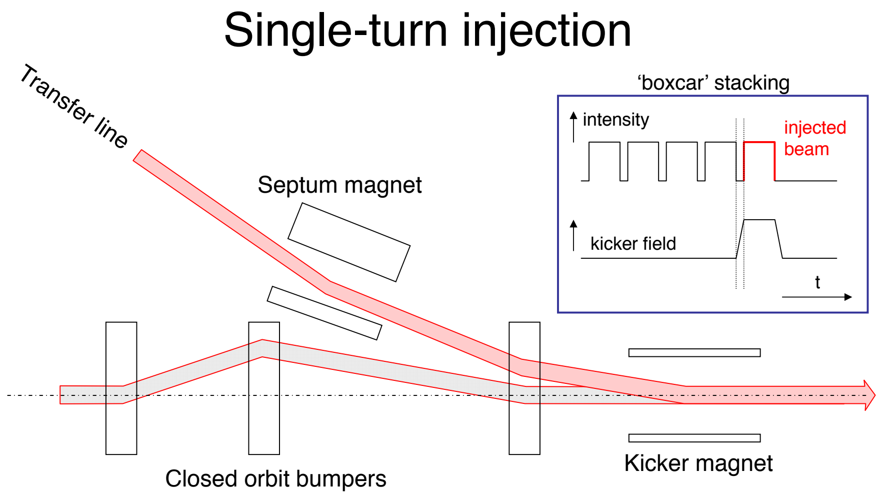

Figure 3.9: The single turn injection scheme. A septum magnet makes the initial alignment. The kicker magnet times the injection and makes the final alignment. Bumper magnets align the LHC beam with the injected beam [9]

extraction, the kicker magnet quickly displaces a portion of the beam, which is steered away by the septum, while the original beam passes through it's low-field region unaffected.

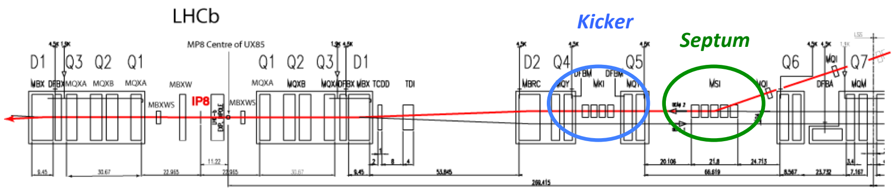

Figure 3.10: Layout of Interaction Region 8, where one proton beam is injected into the LHC ring. A transfer line from the SPS bring a proton in from the right. In green, a septum magnet aligns the beam horizontally with the LHC. In blue, a kicker magnet makes the final vertical alignment into the LHC, and is timed to fill one of the 400 MHz buckets of the RF capture system [8]

At the LHC, beam is injected at Interaction Regions (IR) 2 and 8 [8]. Two transfer lines bring the beam extracted from the SPS to $\sim$ 150 m of the LHC ring. Five Labertson-type septum magnets, of field strength $\sim$ 1 T, are used to deflect each of the transfer line beams 12 mrad to align the transfer beam horizontally with the LHC orbit. Then, four $\sim$ 0.12T MKI kicker magnets quickly deflect the beam 0.85 mrad to close the orbit with the LHC ring. Figure 3.10 shows the layout of the injection point at IR 8. The green circle encloses the septum structure, which provides the horizontal alignment, and the blue encloses the kicker structure, which makes the final vertical alignment and synchronizes the injection of the beam into the LHC. The rise time for the field provided by the kicker magnets in the LHC and SPS determine the final bunch structure of the LHC. Figure 3.11 extends figure 3.6(e) showing how the rise times of the kickers that inject, or eject beam create gaps in the bunch structure of the LHC. The initial filling of the PS with 6 batches of protons from the PSB, leaves one initial bucket unused in the PS. After

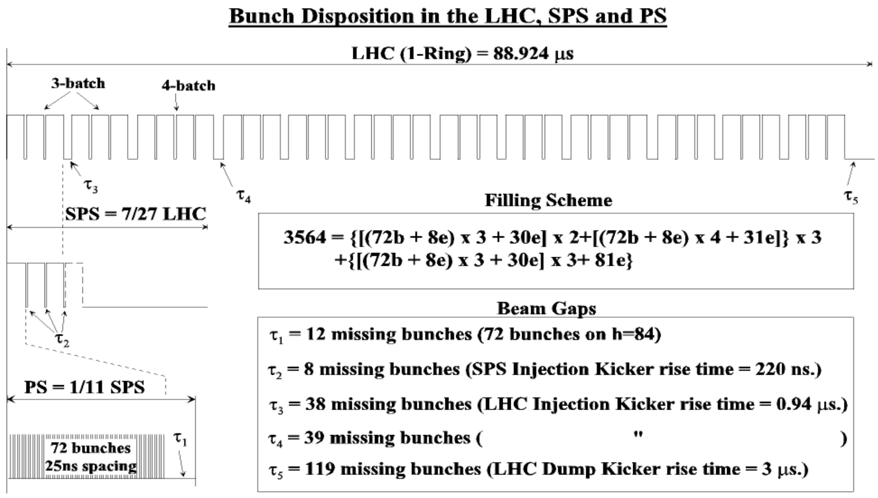

Figure 3.11: The initial filling of 6 batches of protons from the PSB to the PS, leaves 12 empty buckets in the PS bunch structure. The rise time of the SPS magnet creates an additional gap in the SPS bunch structure. Additional gaps emerge due to the rise time of the LHC injection and dumping kicker magnets [8]

the splitting of the beam into the 25 ns bunches, there 12 empty buckets at the of the PS bunch train. The SPS is filled with three to four of these trains, leaving an additional 8 25 ns buckets unfilled due to the 220 ns rise time of the SPS kicker magnet. These three to four trains are then injected into the LHC, where there are 38 or 39 bunch gaps due to the LHC injector 0.94 μs rise time. At the end of a full LHC orbit, 119 buckets are left empty to allow for the rise time of the beam dumping kicker magnet, used to remove beam from the LHC.

Once the beam is injected, the curved path around the circumference of the LHC is maintained via 1232 superconducting dipole magnets. The superconducting material niobium-titanium, NbTi, is cooled to 1.9 K in order to produce the 8.33 T field. Figure 3.12(a) shows a cross-section view of one of the LHC dipoles. The dual-bore design of the beam-pipe is enclosed by an iron yoke, that serves as the cold mass to maintain the superconducting temperature, and provides a 195 mm gap between each beam. A close up picture of the non-magnetic collar and superconducting coils are shown in figure 3.12(b). A simulation of the magnet in figure 3.12(c) shows the homogenous, vertical magnetic field produced in the center of the coil. Diagram 3.12(d) shows an exaggerated view of the 2812 m radius curvature of each dipole. However, since each dipole is only $\sim$ 14 m in length, this curvature is hardly noticeable, as shown in a photo of an actual dipole magnet in a staging area at CERN, awaiting installation in figure 3.12(e).

Quadrupole, sextupole, octupole, and other multipole magnets are used to focus a single beam, as well as squeeze the two beams together. There are 392 quadrupole magnets on the LHC ring, each controlling the height and width of the beam. Figure 3.13(a) shows a schematic of a dual-bore quadrupole magnet, and figure 3.13(b) shows an actual quadrupole in a staging area before installation. Quadrupole magnets use four sets of coils to create a magnetic field that

h

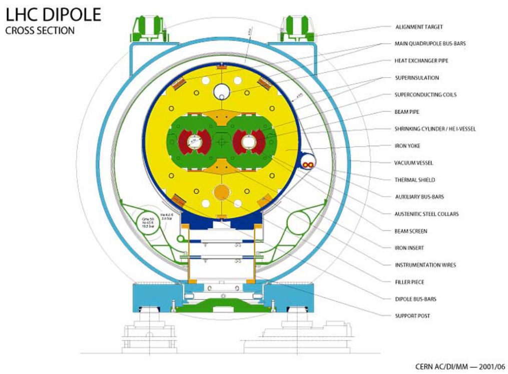

(a) Cross Section of a LHC dipole magnet [8]

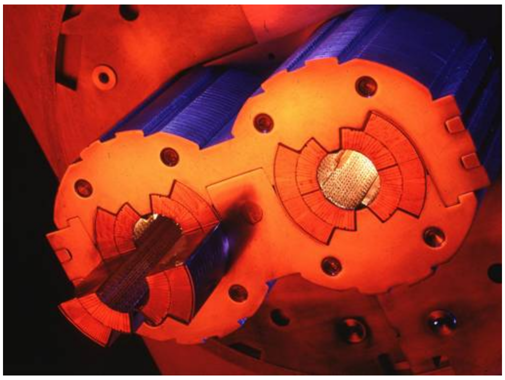

(b) A close-up picture of the non-magnetic collar and superconducting coils of an LHC dipole magnet [115]

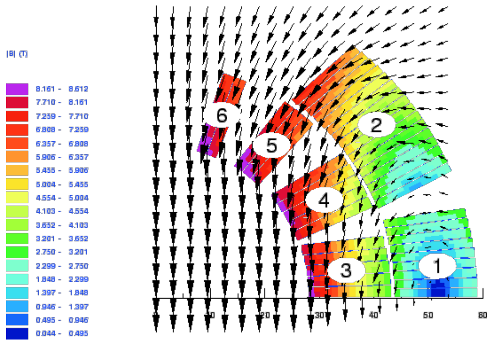

(c) A simulation of the homogenous, vertical magnetic field lines of the dipole [116].

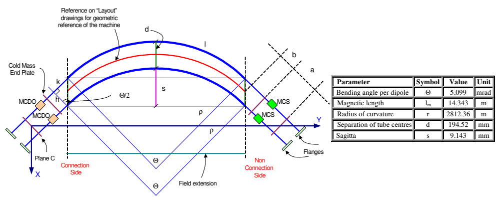

(d) A diagram showing the exaggerated curvature of a dipole magnet, with measurements for some of it's most important features [117].

(e) A ~15 m long dipole magnet, in a staging area at CERN, awaiting installation [118]

Figure 3.12: Features of the dipole magnets used in the LHC

h

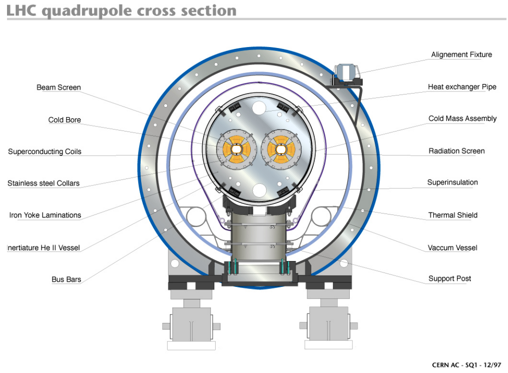

(a) Cross Section of a LHC quadrupole magnet [119]

(b) A dual-bore quadrupole magnet, in a staging area prior to installation [120]

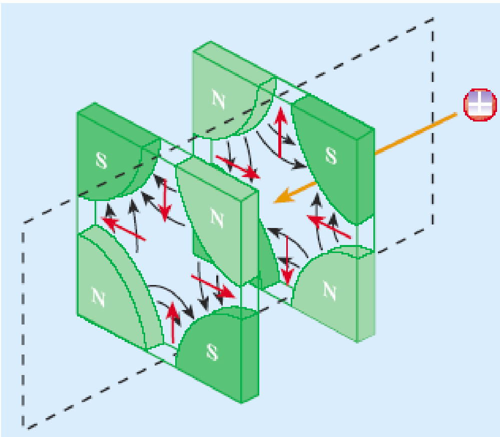

(c) A quadrupole magnet can provide focusing either in the horizontal or vertical direction [121]

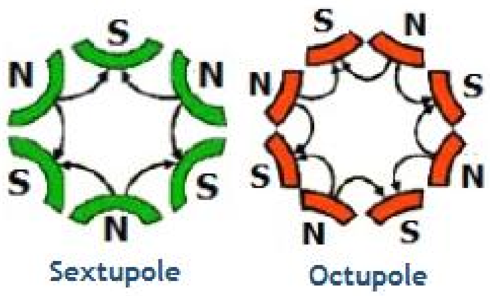

(d) Multipole fields from a sextupole and an octupole magnet [122]

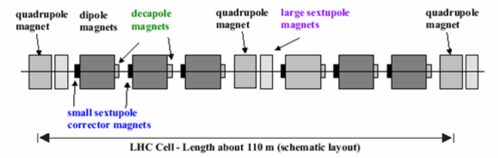

(e) A typical 110m long magnetic cell at the LHC featuring several types of multipole magnets [123]

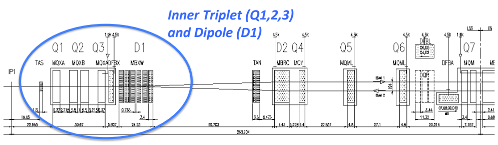

(f) Schematic of the Inner triplet structure that brings the two separate beams together in the interaction region [8]

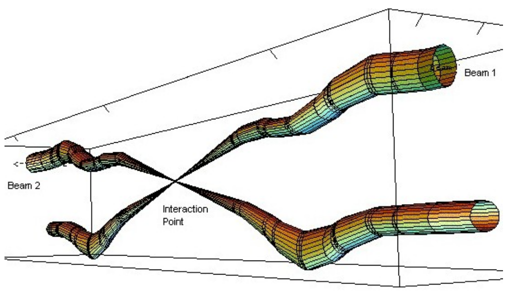

(g) A simulation of two beams being squeezed together by the inner triplet [124]

Figure 3.13: Features of the dipole magnets used in the LHC

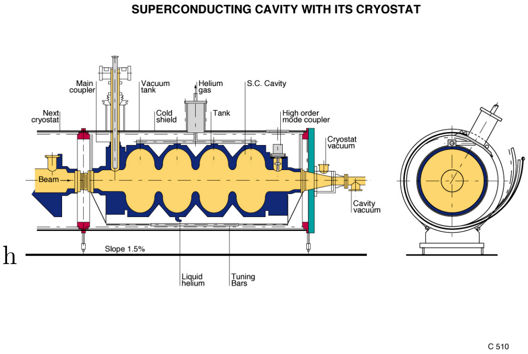

(a) Cross section of a LHC superconducting Radio Frequency cavities, which accelerates the beam by imparting 275 kW of power through a 400 MHz, 16 MV electric field resonating in the cavity [125].

(b) A picture of a four chamber RF cavity in a staging area, prior to installation [126]

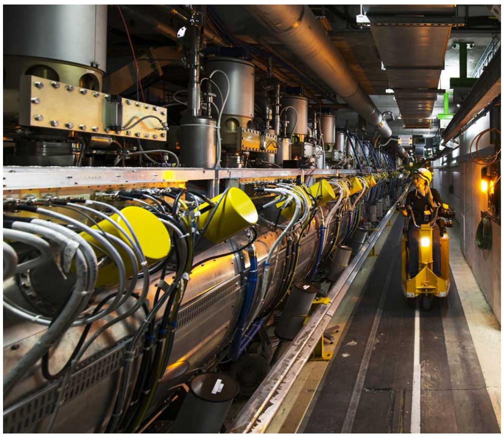

(c) The four chamber RF cavity installed at Point 4 of the LHC [127]

Figure 3.14: Features of the 400 MHz superconducting RF system used in the LHC

either squeezes the beam horizonally or vertically, as shown in figure 3.13(c). Finer corrections to the beam shape are made with the multipole magnets, since they are able to compress the beam from more than two axes. Figure 3.13(d) shows the fields lines of a sextupole and octupole magnet. A typical cell of magnets, 110 m long, in the LHC octant is shown in a diagram in figure 3.13(e), where the dipole, quadrupole and higher order magnets work in series to confine the protons to the LHC ring. Finally, a set of single bore magnets, known as an inner triplet, bring the two beams together into an interaction region. Figure 3.13(f) shows the arrangement of magnets that squeeze the beam together, while figure 3.13(g) shows a simulation of the beams being brought together to collide in the interaction region.

3.3 LHC RF Technology

The LHC uses a 400 MHz superconducting RF cavity system to capture and accelerate the beam from 450 GeV to 7 TeV [8]. Two independent system are used to provide 8 MV of RF voltage at injection at 16 MV during equilibrium at 7 TeV and deliver 275 kW of power to each beam. This is provided by 16 niobium sputtered cavities, housed in 4.5 K refrigeration units, known as cryo-modules, at Point 4 of the LHC octant. The superconducting material covering the inside of the cavity has near-zero resistivity, which dissipates much less power and has a much narrower resonance width, or Q-factor, than a cavity made from normally conducting material. Figure 3.14(a) shows a schematic of a four cavity cryo-module. The beam pipe passes through the center of each chamber and longitudinal (left to right in the diagram) electric fields accelerate the protons each time they circulate the LHC ring. Figure 3.14(b) shows an actual four cavity module in a staging area prior to installation. In this picture, the resonance cavities are concealed underneath the cylindrical housing of the vacuum tank and cryostat. Figure 3.14(c) is a picture of the module installed at Point 4. The thin cylindrical structures extending off the top is the LHe intake valve and quench system. The thicker cylindrical structures are the waveguides that couple the cavities to the source of the electric field, the klystrons.

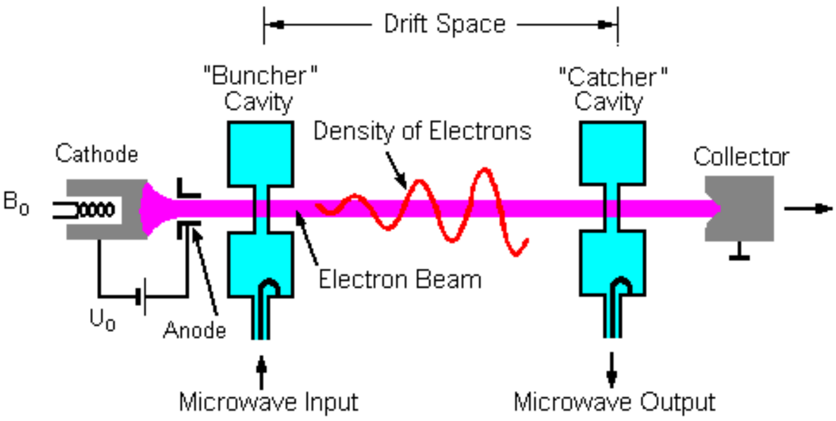

Figure 3.15: A klystron uses a weak RF signal coupled to a resonance cavity to bunch an electron beam, which in turn creates an amplified RF signal as it passes through a second resonance cavity tuned to the same frequency [10].

A Klystron is the source of RF power that builds up as a resonance in the cavities that accelerate the protons. Figure 3.15 shows a diagram of the basic operating principle. The device uses an anode to accelerate the thermionic emission of electrons off of a cathode material into one or more bunching cavities tuned to the frequency the device is designed to produce. This cavity is driven with a weak RF source, that groups electrons into bunches. Just as discussed for protons earlier, when electrons arrive at the entrance of the cavity at just the right time, it will experience the zero-point of the oscillation of the resonating electric field. If it arrives early or late, it is accelerated or decelerated and thus bringing it closer to its neighbors, and increasing the density of the beam. After passing through multiple chambers, the tightly bunched electrons enter a catcher cavity tuned to the same resonance frequency. As the electrons pass through at this resonance frequency, standing electric waves are excited and quickly build up in the catcher cavity. The electron beam is thus used to amplify the original RF signal in the catcher cavity, which is then transported via waveguide to power the RF cavity used to accelerate the proton beam-line.

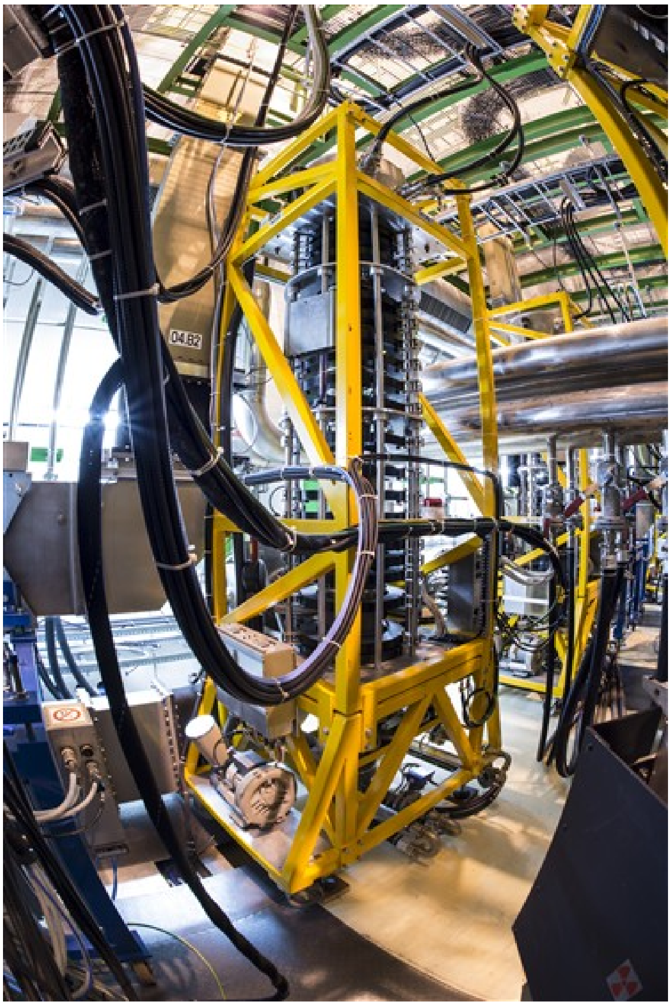

Figure 3.16: One of sixteen 300 kW, 400 MHz klystrons that power the superconducting RF cavities that accelerate the proton beam [11].

At the LHC, 16 400 MHz, 300 kW klystrons, work together to provide 4800 kW of power to the superconducting RF cavities [8]. They are also located at Point 4, in the UX45 service cavern adjacent to the RF cavities, about 6 m below the beam-line. An average of 22 m of waveguide is used to transport the power generated by the klystrons to the RF cavities. Figure 3.16 shows a klystron installed at the LHC, and like most modern klystrons, it also utilizes a multi-bunching chamber design.

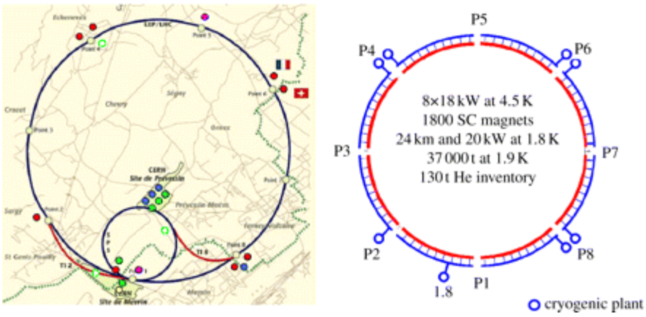

Figure 3.17: Layout of the five cryogenic islands, which are home to the eight facilities that provide liquid helium to the LHC [12]

h

(a) The compressor station for the 4.5 K refrigeration system

(b) The 4.5 K refrigeration system cold box, containing heat exchanging fins and turbines to cool the He

Figure 3.18: Features of the 4.5 K refrigeration system [13]

3.4 The LHC Cryogen System

The LHC is the largest cryogenic system in the world [128], as its operating temperature is 1.8 K, in order to produce the high-magnetic fields needed by the dipole magnets. Additionally, the acceleration mechanism, the RF cavities, are also superconducting, and must be cooled to 4.5 K. Over 120 tons of Helium are used as the cryogenic medium, since once it is cooled below 2.17 K, it becomes a superfluid, a phase of matter with a high thermal conductivity, making it ideal for refrigeration. Cryogenic and auxiliary equipment are concentrated into 5 ”cryogenic islands” at Points 1,2,4,6, and 8 [8]. As shown in figure 3.17, Points 4,6, and 8 house two facilities each, making a total of eight, one for each octant of the LHC arc.

At each cryogenic plant, He is cooled to 80 K by circulating it through refrigeration equipment with liquid nitrogen in the heat exchangers[128]. Next, the He is brought to 4.5 K with refrigerators recovered from the LEP experiment [129]. The He gas is first compressed and allowed to expand, where it is cooled by losing energy through mechanical turbo-expanders that run at up to 140,000 rpm on helium-gas bearings, as shown in figure 3.18(a). The He is then liquified after passing through a vacuum sealed box containing heat exchangers and more turbo-expanders [13]. The compressor for this system is pictured in figure 3.18(b). Finally, the liquified He is brought to 1.8 K with a refrigeration unit that uses a cold compression train to decrease the saturation pressure, and thus temperature as well.

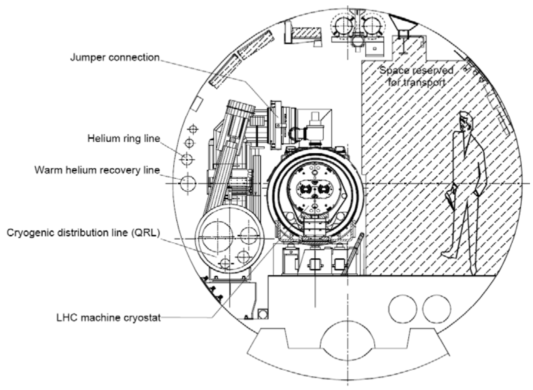

Figure 3.19: Cross section schematic of the cryogenic distribution system in the LHC tunnel [8]

In the LHC tunnel, a cryogenic distribution line runs parallel to the machine [129]. It consists of eight 3.2 km long cryostats, that contain the equipment to supply and recover helium with temperatures ranging from 4 K to 75 K. A total of 310 service modules, are used to control the system and provide safety mechanisms against pressure buildup and magnet quenching. Figure 3.19 shows a cross section of the cryogen distribution system in the tunnel.

3.5 The LHC Vacuum System

The LHC is also the largest operational vacuum system in the world and is capable of achieving pressures lower than outer space [130]. Three different types of vacuum systems are used: one for insulating the helium distribution lines, another for insulating the dipole magnets, and a final ultra-high vacuum system for the beam pipe [8].

The vacuum systems for insulating the helium distribution and dipoles involves some 104 km of piping an over 250,000 welding joints [130]. Pressure here is required to be kept at 10^{-1} mbar, but at cryogenic temperatures, pressures tend to equalize at a much lower level, to 10^{-6} mbar ($\sim 10^{-9}$ atm) [8].

The most stringent requirements come on the vacuum of the beam-pipe. The beam must minimize the number of interactions it has with any particles outside of the interaction region. A pressure of 10^{-10} to 10^{-11} mbar are maintained in the 54 km of beam-pipe [130]. Weeks of cryogenic pumping, eventually condenses gas trapped in the beam-pipe into a liquid that can be absorbed by the walls of the beam-pipe. The inside beam-pipe is also coated with a thin layer

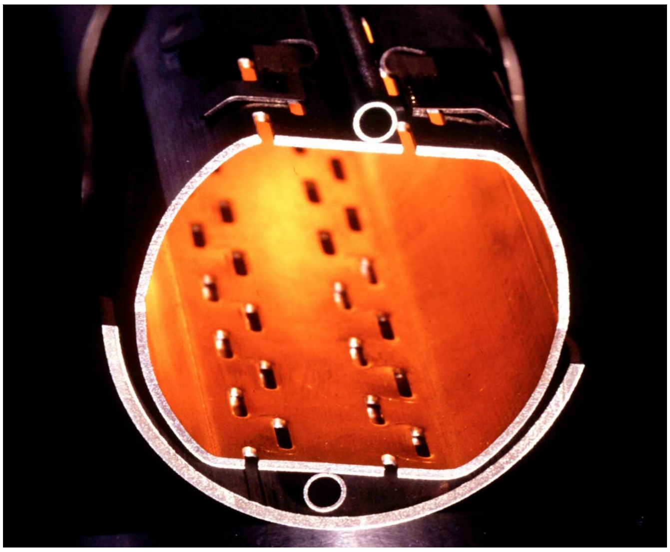

Figure 3.20: Beam screen for the LHC, with slits to allow for easy pumping of residual gas molecules in the beam-pipe [14].

of a special substance developed at CERN, a titanium-zirconium-vanadium alloy, which absorbs residual particles when heated. 780 ion pumps are used to remove the noble gases and methane, which do not interact with the substance, which acts as its own distributed pumping system. Room-temperature sections of the beam-pipe are also heated to 300^{deg} to be baked-out from the outside. This is done to periodically remove any material which may have settled and become trapped. Additionally, the beam-pipe is designed with a racetrack shape, which optimizes the available aperture while leaving space for the cooling tubes, as shown in figure 3.20. Slits also allow for gas molecules to be easily pumped out from inside its volume.

Chapter 4

The Compact Muon Solenoid

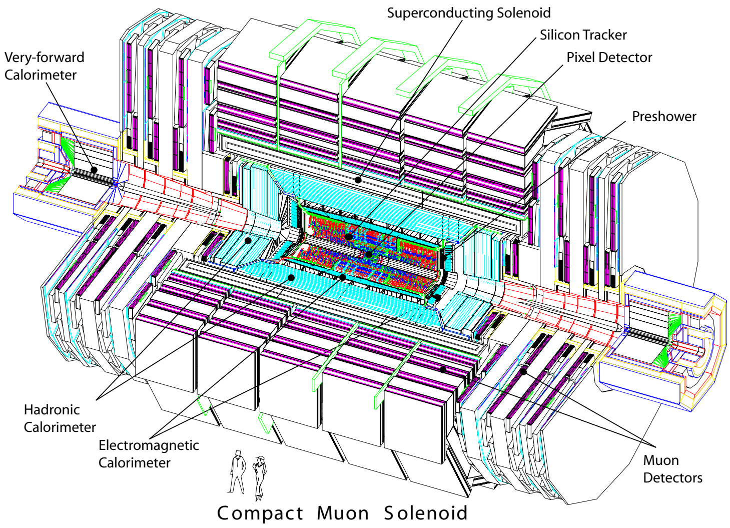

Figure 4.1: A cutaway diagram of the CMS detector. Two humans are present at the bottom of the image to provide scale [15].

The Compact Muon Solenoid (CMS) experiment is a general-purpose particle detector capable of performing a wide range of physics measurements at the TeV energy scale. It provides hermetic, 4π, coverage surrounding the interaction region on Point 5 of the LHC octant, and is capable of identifying and reconstructing charged and neutral hadrons, photons, electrons, and muons directly. Tau leptons, are measured indirectly through a careful reconstruction of its decay products. The hermetic coverage allows the detection of neutrinos by measuring a momentum imbalance in a given collision. The detector is assembled in five sections and weighs over 14,000 tons. The "Compact" part of the experiment's name comes from its relatively small volume for a modern particle detector, with length of 28.7 m and a diameter of 15.0 m. Ironically, this is as tall as most 4-5 story buildings and weights as much as ~7000 cars. Figure 4.1 shows a cutaway drawing of the CMS detector. Unless otherwise stated, all technical information on the CMS detector is taken from [15].

A right-handed coordinate system is used to measure particle positions within the detector. The origin is centered at the nominal interaction point with the $\hat{x}$ direction pointed towards the center of the LHC ring, the $\hat{y}$ direction towards the sky, and the $\hat{z}$ direction pointed counter-clockwise along the LHC ring towards Point 2 and the ALICE experiment. In the much more natural polar coordinates, $\hat{r}$, points radially outward from the interaction point, the azimuthal angle $\hat{\phi}$ is measured as the angle relative to the $\hat{x}$ axis, and the polar angle, $\hat{\theta}$, is measured as the angle relative to the $\hat{z}$ axis. An important Lorentz invariant position variable is the rapidity, y, and its approximation in terms of the polar angle, the pseudorapidity, η:

$$\begin{aligned} y &= \frac{1}{2}\ln\left(\frac{E + p_z c}{E - p_z c}\right) \\ \eta &= -\ln\left(\tan\frac{\theta}{2}\right) \end{aligned} \tag{4.1}$$

The psuedorapidity is useful since it is an approximately Lorentz invariant version of polar angle, which allows for a more intuitive understanding of the distribution of particles when boosting into different measurement reference frames. The component of the momentum transverse to the beam-line, p_T is the most common form of measuring the momentum, and is defined as $p_T = |p|\cos\phi$.

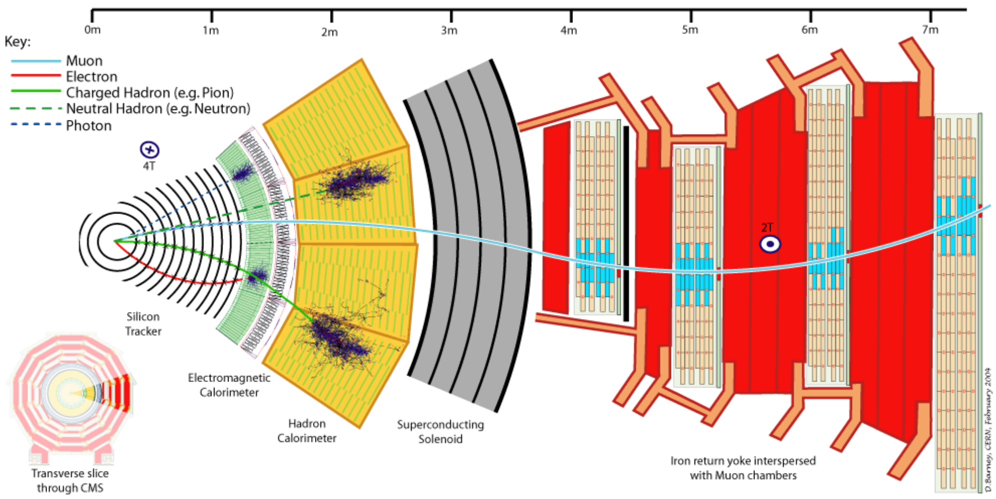

Figure 4.2: A slice of the CMS detector showing how various particles interact and deposit energy. The trajectory of charged particles is measured in the tracker; electrons and photons deposit most of their energy in the ECAL; charged and neutral hadrons deposit most of their energy in the HCAL; the muon chambers measures the trajectory of muons or long-lived charged particles [16].

CMS is composed of a system of sub-detectors, each specialized in measuring a certain type or characteristic of a particle. They are arranged approximately as concentric cylinders of increasing radius, wrapped around the interaction region of the pp collisions and an analogy is often made between the layers of sub-detectors being similar to the layers of an onion. The closest sub-detector to the interaction region is the tracker system. It is an all silicon pixel and strip detector, with a high precision position resolution, which is used to identify the trajectory of charged particles close to the primary vertex of a collision. The Electromagnetic Calorimeter (ECAL) is the next layer, and is used to absorb energy of electromagnetically interacting particles. It uses lead-tungstate ($PbWO_4$) crystals which act as both the absorbing and scintillating medium for energy deposited by charged particles and photons as they pass through this sub-detector. The Hadronic Calorimeter (HCAL) uses brass and steel tiles to absorb energy and induce hadronic interactions, while a plastic scintillator material layered between the absorber tiles samples the energy of hadrons. The tracker, ECAL, and HCAL systems are all contained in the bore of the 3.8 T solenoid from the CMS namesake. This device bends the trajectory of charged particles as they traverse the detector, and the curvature of this bend is used to obtain information on the charge and momentum of the measured particle. The muon system sits outside of the solenoid structure, and uses three types of detection systems: drift tubes (DTs), resistive strip chambers (RPCs) and cathode strip chambers (CSCs), which provide excellent timing and position resolution. The return yoke structure of the magnet also provides the mechanical support for the muon chambers. Figure 4.2 shows a slice of the CMS experiment showing how various particles interact and traverse the different sub-detector regions, as described above.

At center-of-mass energy of $\sqrt{s} = 14\,\text{TeV}$, the expected event rate is approximately 10^9 events/second. This is too much information to store and analyze, and is mainly dominated by Standard Model QCD multi-jet production, a background for searches for new particles or physics. An online event selection, or trigger, must by used to reduce this rate to a manageable 100 events/second. This is achieved through a combination of hardware, firmware, and software that provides a rough reconstruction of events in near real-time, and makes a decision about whether it meets a minimum set of criteria to be used in an analysis.

4.1 The Tracker

The innermost sub-detector is an all silicon pixel and strip tracker designed to provide precise and efficient measurement of the trajectories of charged particles and reconstruction secondary vertices necessary for identification of b-jets and τ leptons.

At peak LHC design luminosity of $10^{34}\text{cm}^{-2}\text{s}^{-1}$, and bunch spacing of 25 ns, there will be $\sim$1000 particles from 20 overlapping pp collisions for each bunch crossing. This corresponds to a hit rate density of 1 MHz/mm^2 at a radius of 4 cm, 60 kHz/mm^2 at 22 cm, and 3 kHz/mm^2 at 115 cm from the beam line. This large particle flux will also cause intense radiation damage to detector components. These conditions necessitate the use radiation-hard silicon, with a high-granularity to create a low occupancy for each detector element, which are read out by fast electronics. Additional mitigation of the effects of radiation damage is taken by cooling and operating the entire detector to -10° C in order to maintain a signal to noise ratio of 10:1 for the sensors. After 10 years of running, it is anticipated that this will need to decrease to -27° in order to compensate for the accumulated damage.

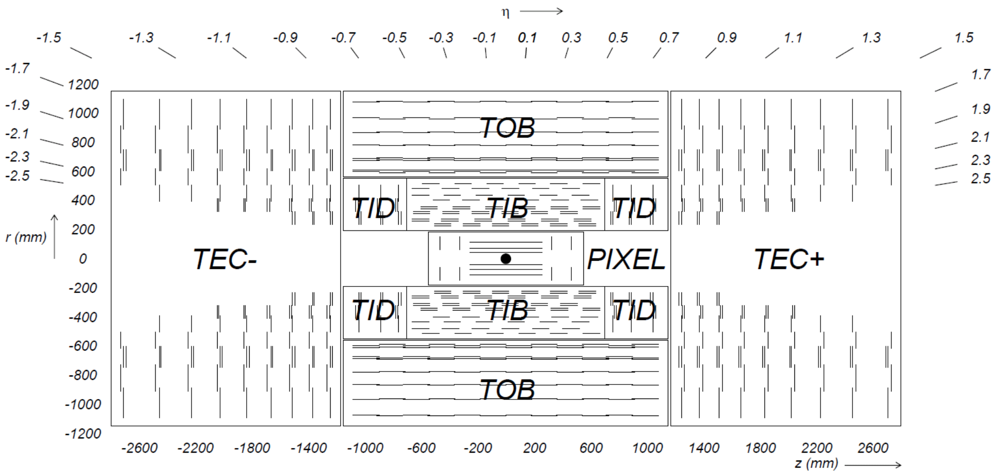

Figure 4.3: A side view of the tracker. The pixel detector is the innermost sub-system, with three concentric rings of detectors in the barrel, and two in the endcap. The tracker inner barrel (TIB) is a silicon strip detector, with four concentric rings. The tracker inner disks (TID) are three layers deep. The tracker outer barrel (TOB) is six concentric rings and the tracker end caps (TEC) are nine layers deep [15].

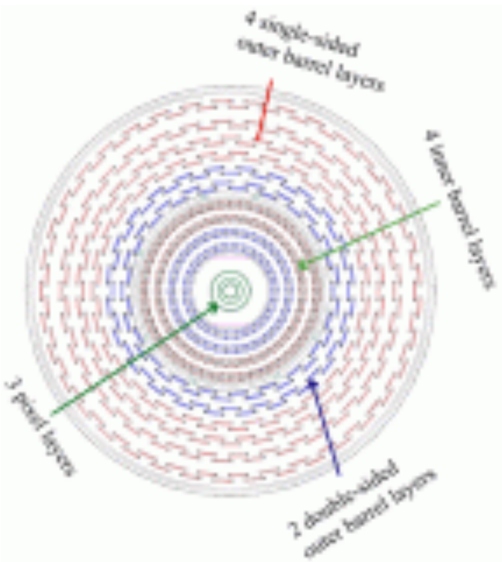

Figure 4.4: A head-on view of the beam-line and barrel components of the tracker [17].

The tracker has a cylindrical shape that surrounds the interaction region, with a length of 5.8 m and a diameter of 2.5 m. The large particle flux close to the beam-line requires the use of a pixel detector sub-system in the innermost region, from radius 4.4 cm to 10.2 cm from the beam-line. The particle flux drops off sufficiently at larger radii to use silicon strip detectors, arranged into four different sub-systems: the tracker inner barrel (TIB), tracker inner disks (TID), tracker outer barrel (TOB) and tracker end caps (TEC), which extend to a radius of 1.2 m from the beam-line. Figure 4.3 shows a side view of the tracker layout and figure 4.4 shows a view down the beam-line of the barrel sections. The tracker has a total acceptance of $|\eta| < 2.5$.

There are competing factors for the radial length of the tracker. More layers allow for more samples of a particle's trajectory, giving a higher spatial precision, but more material means photons and hadrons are more likely to decay, and create a shower of particles that would better measured through the absorption of energy via calorimeters. The depth of the tracker varies from 0.4 to 1.8 radiation lengths, resulting in small degradation of the ECAL performance, since approximately half the photons will be converted to e^+e^- pairs.

4.1.1 The Silicon Pixel Detector

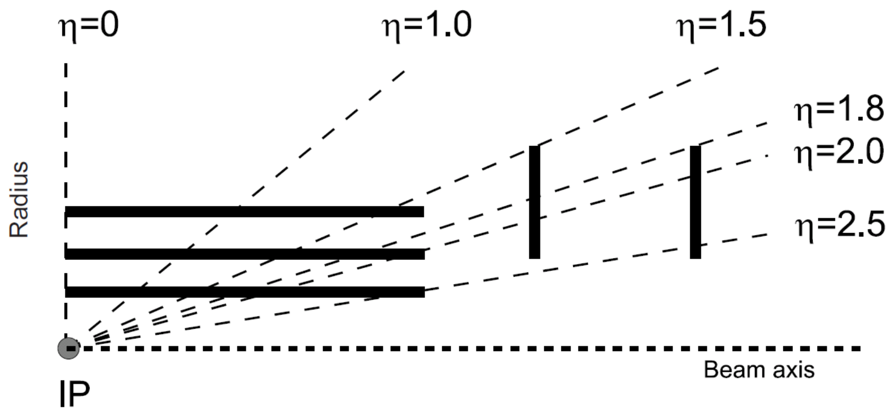

Figure 4.5: The three barrel and two disk layers of the silicon pixel tracker provide coverage of $|\eta| < 2.5$ [15].

The pixel detector consists of 66 million 100×150 μm pixels, arranged in three concentric cylindrical layers of radius of 4.4, 7.3, and 10.2 cm from the beam line and two disc layers on either side of the barrel detectors. Figure 4.5 shows the eta coverage of the detector out to $|\eta| < 2.5$.

The sensor technology uses a n-on-n concept, where a high-dose n-implant is introduced onto a n-substrate with large resistance. A $p-n$ junction is made by the placement of a p-type semiconductor on the back side of the substrate. When a charged particle passes through the face of the substrate, between the $p-n$ junction, it liberates electrons from the silicon atoms, creating electron-hole pairs. The p-side has a voltage bias of 150 V in the barrel, and 300 V in the disks, that sweeps the pair apart, creating a current. Pixels are isolated from one another using a moderated p-spray in the barrel region, and open p-stops in the disks in order to create an additional $p-n$ structure that acts like a diode to limit current flow between pixels. The 3.7 T magnetic field of the CMS solenoid also induces a Lorentz drift of the current in the $\hat{\phi}$ direction. This results in the current produced in one pixel being shared among multiple neighboring pixels. The charge collected by each of the multiple pixels are read-out, using an interpolation between pixels, resulting in a 15-20 μm spatial resolution on the trajectory of the charged particle - much smaller than the size of an individual pixel. In order to induce this effect in the disks (where the pixels are orientated perpendicular to the barrel), the pixels are angled 20° in the $\hat{y}$ direction.

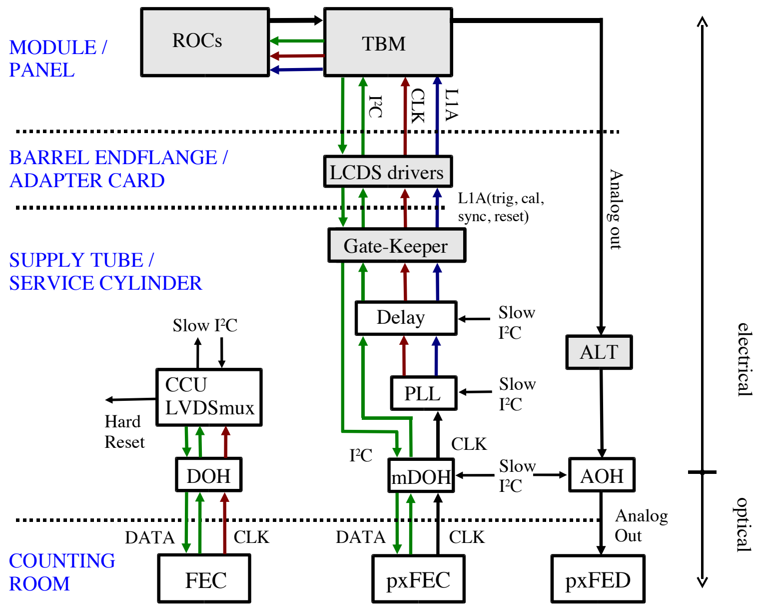

Figure 4.6: The readout electronics chain for the pixel detector [15].

The current created by the charged particle is collected by a readout chip (ROC) that is soldered with a bump bond type connection to the pixel. The ROC is a custom ASIC chip, that processes the signals for a grid of 52x80 pixels. It provides amplification, buffering, and zero suppression (threshold) of the charge from each pixel. Depending on the layer, 8-16 ROCs in the barrel, and 21-24 ROCs in the disks are connected and read-out by a single token bit manager (TBM) chip. This chip communicates information from the sensors to the trigger system, which is used to determine whether a given event is stored as data for analysis later. The pixel front end controller (pxFEC) interfaces with the ROC and TBM and provides central clocking and communicates to the CMS data acquisition system. The pixel front end digitizer (pxFED) converts the analog signals from the ROC and TBMs. A total of 40 pxFED (32 in the barrel and 8 in the disks) modules are used to read-out the entire pixel detector, and figure 4.6 shows a schematic of the pixel read-out chain.

The resolution of the pixel detector was measured in 2012 with $\sqrt{s} = 8\,\text{TeV}$ pp collision. The

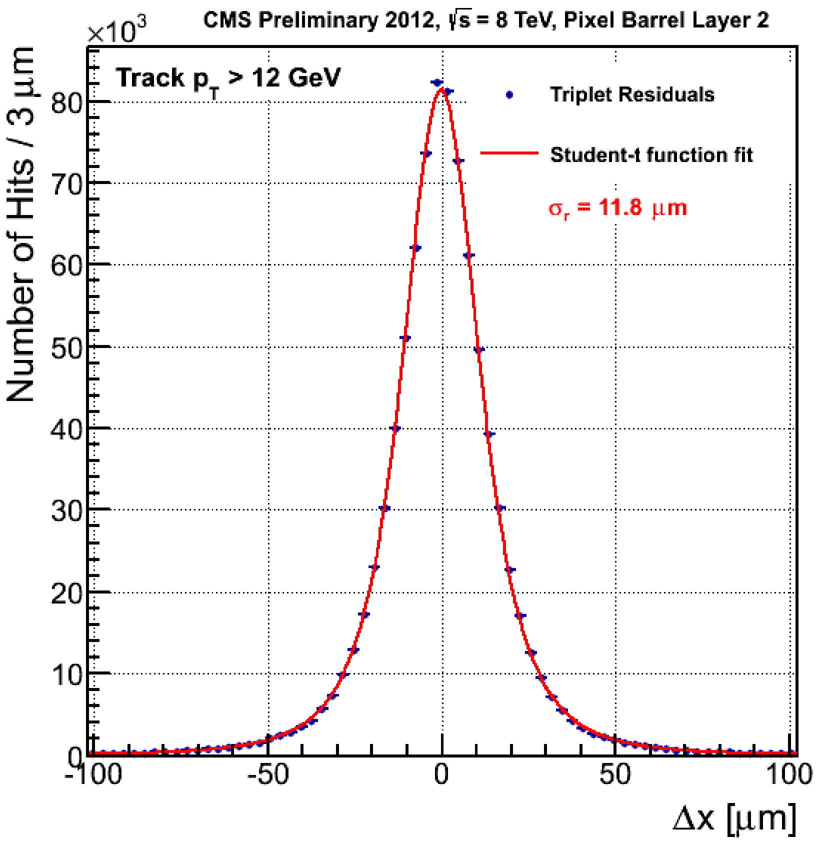

Figure 4.7: In 2012 pp collisions at $\sqrt{s} = 8\,\mathrm{TeV}$, the pixel detector performed with a resolution of 11.8 μm. The above is a plot of the residual difference between a pixel and the results of a fit to a particle track [18].

residual distance between the hit position recorded by a pixel, and an interpolated track that uses that hit is plotted and fit with a student-t function in figure 4.7. For tracks with p_{T} >12 GeV, the pixel detector was found to have a spatial resolution of 11.8 μm.

4.1.2 The Silicon Strip Detector

As shown in figure 4.3, the silicon strip tracking system has four components: the tracker inner barrel (TIB), tracker inner disks (TID), tracker outer barrel (TOB) and tracker end caps (TEC). A total of 15,148 detector modules are distributed among these systems, each with either one 320 μm thick sensor, or two 500 μm thick sensors, making 24,244 sensors with an active area of 198 m^2 of silicon. A module with two sensors is shown in figure 4.8. Each sensor has either 512 or 768 strips since they are read out by two multiplexed 128-channel front end chips, making it possible to only read out sensors in groups of 256. Each strip has a pitch that varies between 80 and 200 μm and lengths that vary between 10 and 25 cm. All in all, 9.3 million strips are used in the silicon tracker.

The TIB and TID provide radial coverage from 20 to 55 cm. The TIB has four barrel layers,

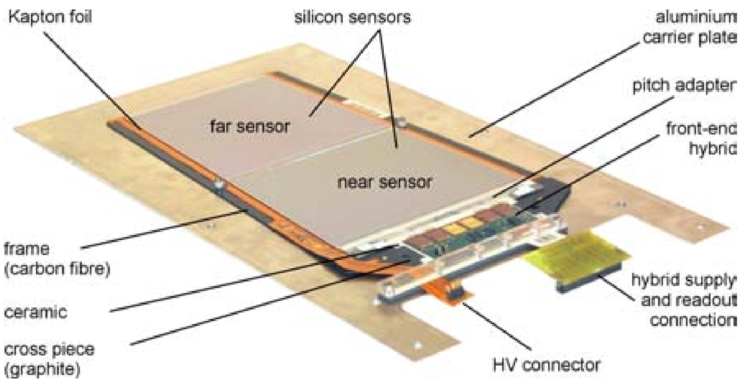

Figure 4.8: A silicon strip module, with two 500 μm thick sensors [15].

with 80 μm pitch strips on the first two layers, and 120 μm strips on the outer two, giving a single point resolution of 23 and 35 μm respectively. The strip pitch varies between 100 and 141 μm in the three discs of the TID. The TOB surrounds the TIB/TID and is composed of six barrel layers that extend the tracker radius to 116 cm. It is composed of 500 μm thick strip sensors, with pitches of 183 μm in the first four layers and 122 μm in the outer two layers. It provides 6 measurement points of the particle trajectory with a single point resolution of 53 (35) μm in the first four (last two) layers. Each TEC is made of 9 discs, each with 7 rings of strip detectors. The inner four rings of each disk use the single, 320 μm thick strip modules, while the outer three rings use the double, 520 μm thick strip modules. The average pitch varies between 97 to 184 μm in each of the rings. In the first two layers of the TIB, the first two rings of the TID, the first two layers of the TOB, and rings 1, 2, and 5 in each disk of the TEC contain modules mounted back-to-back, with an angle of 100 mrad between them to provide a two-dimensional measurement of a particle's trajectory.

Each of the strips is a single sided p-on-n type silicon sensor manufactured on 6 inch wafers, with a base material of n doped silicon. The front side of the wafer is implanted with a p^+ type semiconductor. A uniform n^+ implantation on the back forms the ohmic contact to 500 V. This forms a pn junction and when a charged particle passes through the face of the wafer, atoms in the junction are ionized and the 500 V potential difference creates a current out of the resulting electron/hole pairs. This current is collected and processed through the read-out system.

A custom integrated circuit, the APV25, is used to amplify, shape, and buffer the signals produced from the silicon strips. It has 128 read-out channels, and samples the detector signals at the 40 MHz, suitable for the 25 ns collisions. It is able to store data for up to 4 μs to account

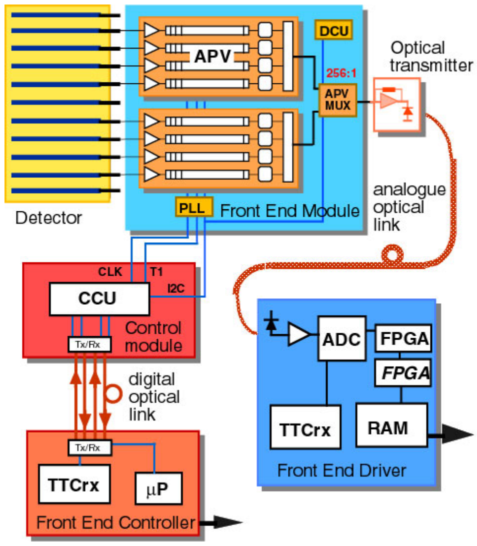

Figure 4.9: Schematic of the readout sequence of the silicon strip detector [15].

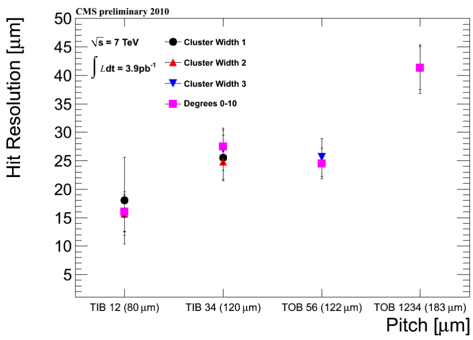

h

(a) Measurement of the resolution on charged particle tracks in the TIB and TOB [131].

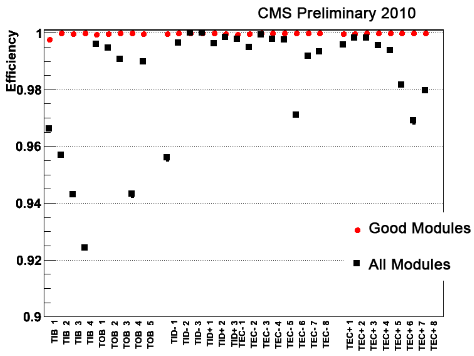

(b) Strip tracker efficiency for identifying charged tracks [132]

Figure 4.10: Measurements of the performance of the silicon strip track using pp collisions from 2011 at $\sqrt{s} = 7\,\text{TeV}$

for trigger latency. Two APV25 chips are linked with fiber optics to the Front End Driver (FED) system. Each FED receives data from 94 optical fibers, and digitizes them in parallel. The Front End Controller (FEC) transmits clock, trigger, and control data to the APV25s. The entire readout chain is shown in figure 4.9.

In 2011, the strip efficiency and resolution were measured from data in center-of-mass energy, $\sqrt{s} = 7\,\text{TeV}$ pp collisions. Figure 4.10(a) shows the resolution varying between 15-40 μm for the TIB and TOB detectors. Figure 4.10(b) shows the efficiency for reconstructing tracks with the strip tracker, which is well above 99% when only considering operational modules.

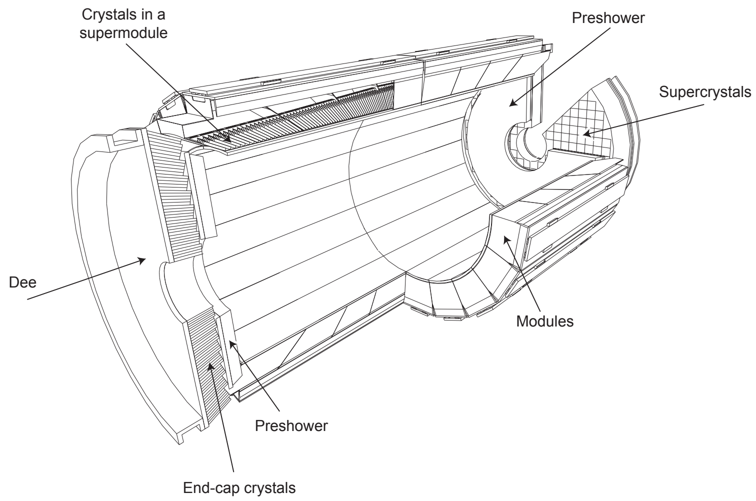

Figure 4.11: Layout of the ECAL sub-detector [15]

4.2 The Electromagnetic Calorimeter

The Electromagnetic Calorimeter (ECAL) surrounds the inner tracker with 61,200 high density lead tungstate ($PbWO_4$) crystals in the central barrel section, and 7,324 crystals in each of the two endcaps. The crystals have a fast response, provide fine granularity, and are radiation resistant, making them ideal for the LHC environment and the physics goal of observing the Standard Model Higgs boson decay to two high energy photons. The primary background for this process comes from neutral pions decaying to two photons, which is especially difficult when the photons are close together and can potentially be reconstructed as a single high-energy photon. This occurs most frequently in the endcaps, so an additional detector, the preshower, provides additional spatial resolution with silicon microstrip detectors, similar to those in the tracker. Figure 4.11 shows the layout of the ECAL.

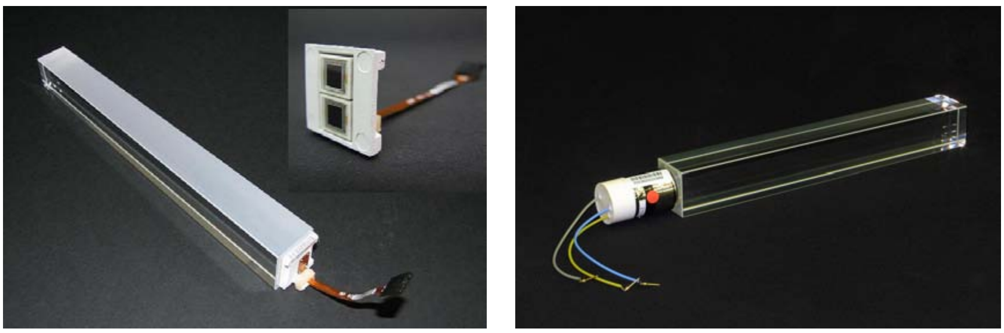

Figure 4.12: Typical Lead Tungstate crystal, with APD attached to the rear face in the left frame, and a VPT attached in the right frame [15].

Lead tungstate is in ideal material for electromagnetic calorimetry. Figure 4.12 shows a typical crystal, with photomultipliers attached to the rear faces, which will be discussed later.

The material has a high density, 8.28 g/cm^3, giving it a large electromagnetic cross-section, making it much more likely for a particle traversing the crystal to interact with one of the atoms in its structure. When a particle interacts with the crystal, it does so by depositing energy into its atoms, which excite the electrons that are bound to it. The atoms then relax by emitting photons, in a process known as scintillation and the $PbWO_4$ crystals release 80% of their light in the 25 ns LHC bunch crossing time. This light is collected by photomultipliers attached to the rear face of the crystal and converted into an electrical signal. Read-out electronics amplify, digitize, and buffer the signal until it can be stored as data or discarded.

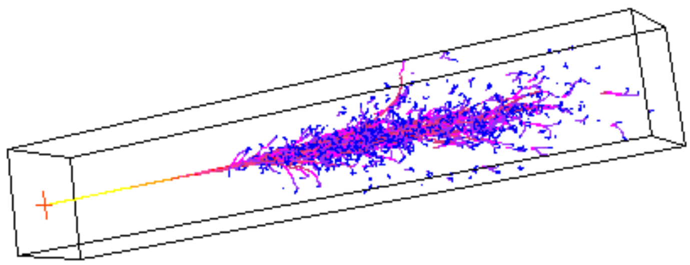

Figure 4.13: A simulation of the evolution of a electromagnetic shower being initiated by an electron entering the center of the front face [19].

As a charged particle or photon begins to deposit energy, it begins a decay chain into many lower energy photons and electrons, known as an electromagnetic shower. Electrons, being bent by the CMS magnetic field, and multiple scattering off of the $PbWO_4$ crystals, create bremsstrahlung photon radiation. Since the intensity of bremsstrahlung is inversely proportional to the mass of the particle squared, particles heavier than electrons such as muons and hadrons do lot leave a large signature in the ECAL. Photons convert to e^+e^- pairs, which in turn create additional bremsstrahlung. The crystals have a short radiation length, X_0=0.89cm, which is the distance it takes an electron to deposit 1/e of it's energy through bremsstrahlung, and 7/9 of the mean free path of a high energy photon before it converts to an e^+e^- pair. A corollary of the crystal's short radiation length is its small Moliere radius, 2.2cm, which is the radius of a cylinder that encloses of 90% of the electromagnetic shower's energy deposition. A typical crystal has a front face that is 22$\times$22 mm^2, a rear face of 26$\times$26 mm^2, and a length of 230 mm, or 25.8 X_0 radiation lengths. This means that a relatively small grid of crystals can be used to fully collect the energy deposited by a high energy electron or photon. As previously mentioned, heavier charged particles will not bremsstrahlung as much as electrons, and will travel through the entire ECAL, depositing only a moderate fraction of their energy in the crystals. Figure 4.13 shows a simulation of an electromagnetic shower produced by an electron entering the front face of a crystal.

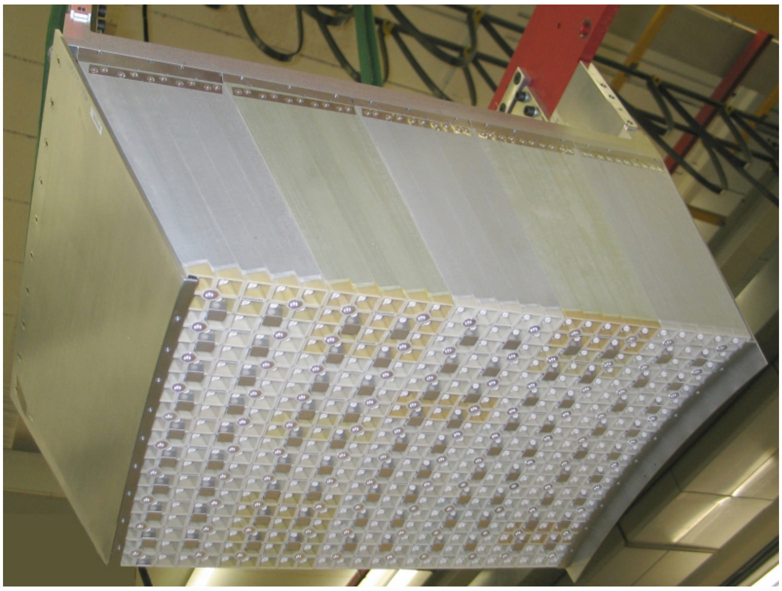

Figure 4.14: A module of 500 crystals (25 crystals wide by 20 crystal tall) [15].

The barrel of ECAL (EB) covers a psuedorapidity range of $|\eta| < 1.479$ with 61,200 crystals at a radius 1.29 m from the beam-line. The crystals are positioned in a quasi-projective geometry, such that their axes make a 3° angle with respect to the vector pointing to the nominal interaction point. This ensures that particles will not pass through the cracks and spaces between crystals, and are forced to interact with a portion of the ECAL. Crystals are assembled in groups of 400 or 500 into modules, as shown in figure 4.14 . Four of these modules are assembled into a supermodule contain 1700 crystals, and 36 supermodules make up the barrel region.

The crystals in the EB are read out by Avalanche Photo-Diode (APD) photomultipliers, shown in the left frame of figure 4.12. The APDs were manufactured by Hamamatsu and are a bulk n-type silicon material, with a p-type implanted on its surface to form a pn-junction. The operation principle is similar to that of tracker. When scintillation light from the lead tungstate crystals enters the face of the APD, it creates electron-hole pairs in the intrinsic region between the p implantation and the n bulk material. The APD is biased with 45 V, which creates a current from the electron-hole pairs and is the signal that a particle has created scintillation in the crystal. The APD provides a gain of 50 and has a quantum efficiency of 75%. Both the APDs and the $PbWO_4$ exhibit a strong temperature dependence, so the entire system is kept at 18° C with a water-based cooling system distributed throughout the barrel and end-caps.

The ECAL readout electronics are designed to read-out a 5×5 array of crystals, known as a trigger tower, in the EB, and a single supercrystal in the EE. Each trigger or tower or supercrystal consists of 5 Very Front End (VFE) boards, each connected to 5 APDs (VPTs), one Front End (FE) board, two (EB) or six (EE) Gigabit Optical Hybrids (GOHs), one Low Voltage Regulator (LVR) and a motherboard. Once triggered, the APD (or VPT in the EE) is sampled 10 times, at

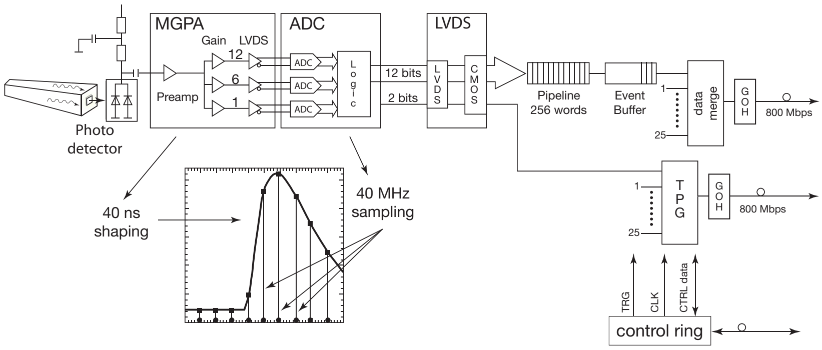

Figure 4.15: Schematic of the On-Detector Readout for the ECAL [15].

a 40 MHz sampling rate, and amplified by a multi-gain amplifier (MGPA), with nominal gains of 1, 6, and 12 contained on the VFE. These digitized samples are sent to the FE, where they are buffered until receiving a Level-1 trigger, where they are sent to the off-detector electronics Data Concentrator Card (DCC) via the GOHs. Figure 4.15 shows a schematic of the on-detector read-out.

In the barrel, the 5×5 trigger towers are divided in the 5 strips in the $\hat{\phi}$ direction. The energy deposits in these strips is summed by the FE cards and define the transverse energy of the tower. In the endcaps, supercrystals are divided into groups of five contiguous crystals of variable shape, known as psuedo-strips. The energy of these strips is performed by the FE, and the off-detector electronics use these to compute the transverse energy deposition.

The preshower detector sits in front of the ECAL end-caps and provides coverage from $1.653 < |\eta| < 2.6$. It is a two-layer sampling calorimeter. Lead radiators initiate electromagnetic showers from electrons and photons, and silicon strips are placed behind them to measure trajectories and deposited energy of passing particles. The total thickness is 20cm, which corresponds to a 2 radiation lengths in the first layer, and another radiation length in the second layer. 95% of photons are converted to e^+e^- pairs after the first layer. Each silicon sensor is composed of 31 strips, with thickness of 320 μm and are 1.9 mm in pitch. A front-end ASIC performs pre-amplification, shaping, voltage sampling, and communicates information to the trigger system to determine if data is stored or discarded. The structure is formed into Dees, and two Dees form a disk with a hole for the beam-line to pass through.

Behind the preshower is the ECAL end-cap (EE). It covers the psuedorapidity range of $1.479 < |\eta| < 3.0$, and sits a longitudinal distance of 315.4 cm from the nominal interaction point. Crystals are grouped into 5×5 modules known as supercrystals (SCs). Like the preshower, each endcap is divided into two sections, Dees, which form a disk with an inner bore for the beam line to pass through, as shown in figure 4.16. Each Dee holds 3,662 crystals, which are divided

Figure 4.16: A section of the ECAL end-cap, a Dee. Two Dees form a disk with an inner bore for the beam-line to pass through. 5x5 modules, or supercrystals, are mounted in preparation for installation at CMS [15].

h

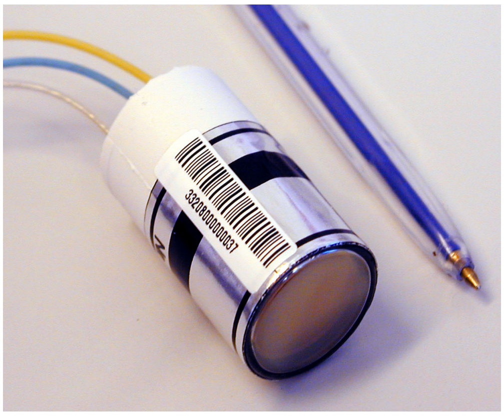

(a) A picture of a VPT next to a standard size pen for scale [133]

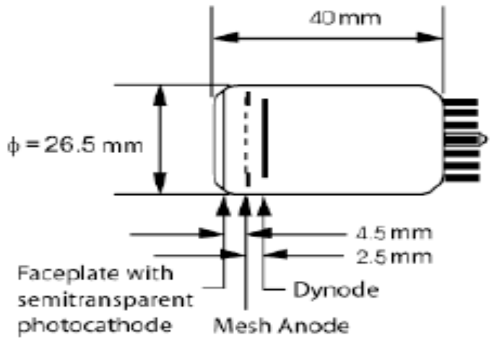

(b) Schematic of a VPT showing characteristic dimensions [134]

Figure 4.17: Vacuum Photo-Triode devices used in the ECAL end-caps (EE)

into 138 supercrystals, and 18 special partial-supercrystals for the inner and outer sections of the Dee.

4.2.1 Vacuum Photo-Triodes

The photomultiplier used to readout the lead tungstate crystals in the EE is the Vacuum Photo-Triode (VPT), shown in the right frame of figure 4.17(a). Each device is 26.5mm in diameter and 40mm in length as shown in figure 4.17(b). It is a gain stage device. Photons from the lead tungstate scintillation light enter the front face of the VPT and liberate electrons from the grounded bi-alkali photocathode (SbKCs) via the photoelectron effect. The cathode material has a quantum efficiency of $\sim 20-25\%$. The photo-electrons are accelerated towards the mesh anode grid, which is held at 800 V. Approximately half the photo-electrons pass through the mesh and encounter a dynode plate held at 600 V. Electrons either collide with the dynode, liberating secondary electrons from the collision, or are turned around by the 200 V difference between anode an dynode. Electrons are thus constantly accelerated towards the anode, and create secondary electrons as they collide with the anode. The process repeats with the secondary electrons, creating an avalanche of charge near the anode. As these charges eventually recombine with the anode over the course of a few nanoseconds, the voltage of anode drops, signaling the device has detected a photon from the $PbWO_4$ crystals.

The performance of the VPT is degraded over time by two effects associated with exposure to the scintillation light from the crystals. The first is loss of the vacuum inside the tube. Molecules from the air become ionized by the large voltages and the positive ions are accelerated towards the photo-cathode, which is damaged through the resulting collision. The second effect is the gradual depletion of photo-electrons from the bi-alkali cathode material. The result is a decrease in the current, and thus signal, produced by the anode. Both of these effects can be effectively modeled as the sum of two falling exponential functions. The University of Virginia has studied the performance of VPTs with respect to their light exposure rates over the course of several years in order to characterize the device's response and long-term behavior.

4.2.2 Test Rig at UVa

The University of Virginia (UVa) has continuously monitored four production VPTs operated at 800 V anode and 600 V dynode, in a 3.8 T field, at 15° to the tube axis, with photocathode currents of approximately 10 nA. This was done to simulate light exposure from the lead tungstate crystals in the forward regions of the ECAL end-caps, as well as provide an accelerated simulation of photocurrents that would be experienced in the larger eta regions. As described above, the light exposure is theorized to be the most significant cause of the loss of response in the VPT, known as burn-in. The amount of light that the device has been exposed to is measured in terms of the total number amount of charge liberated from the cathode, measured from the cathode current draw, and is known as the integrated charge. By operating at such high photocurrents, UVa is able to probe this burn-in effect in an attempt to understand the long term behavior of the VPT response to light.

The University of Virginia is well suited to test these devices, since it operates a 3.8 T solenoid magnet, with a sufficiently large inner bore to accommodate a rig containing five (5) VPTs, LEDs, LED driving hardware, and amplifying equipment. The magnet itself was built by Oxford instruments and has an inner bore diameter of 0.4 m and an outer bore diameter of 1.5 m. The inner bore is 0.13 m in height from the ground, and the magnet has a length of 1.5m along its z-axis, which is perpendicular to the normal of the floor.

The VPTs were supplied with high voltage (800 V anode, 600 V cathode) from a CAEN High Voltage supply. This manufacturer also provides high voltage supplies for the VPTs used in CMS. They are preferable due to their stability, programmable user interface, and capacity to drive multiple VPTs simultaneously. A voltage separation between anode and cathode much larger than this is not recommended due to its potential do damage the device.

The VPTs were pulsed with blue and orange LEDs at rates of 10 kHz, and 20 kHz, to capture the same features (frequency and rate) that light from the lead tungstate crystals would produce while collisions were occurring in the detector. The driving circuits are the same as those used in the LED system in the end-caps at point 5 (the location of CMS at CERN), with the exception that the current limiting resistors are larger. The driving circuits are Dallas Semiconductor DS1040Z-D70 Programmable One-Shot Pulse Generators. The TTL signals from the FPGA serve as a trigger for a Dallas Semiconductor pulse generator chip on the board that generates a 30 nSec pulse, so there is no overlap in pulses generated by the VPT. The pulsing was also run in an on/off cycle of 16 hrs on, 8 hrs off to be consistent with the LHC beam fill cycle.

The LED pulsing and data acquisition was automated via a PXI unit manufactured by National Instruments, which contains a FPGA card, a digital oscilloscope, and computer running Windows XP. The FPGA card was programmed with LabVIEW software which controlled LED pulse rate, low voltage power, and measurements of VPT signals. The data acquisition was triggered by means of a PIN diode placed next to the VPT. This served the dual purpose of independent data triggering and also provided the means to correct fluctuations in the illumination provided by the LEDs.

The current from the VPTs anode and cathode are ultimately routed to the PXI Crates switches, and then on to the crates DMM or oscilloscope via a preliminary amplification stage. The VPTs anode is connected directly to a Stephenson amplifier, which connects to a high-frequency switch. The PIN diode signal passes unmodified to that same high-frequency switch. The cathode signal cables connect to a distribution box near the PXI Crate. The distribution box then routes their signals to the terminal block on a low-frequency switch. All of these signals leave the rig over BNC cables before terminating at or adjacent to the PXI Crate. Figure 4.18 highlights different components of the test stand at UVa.

4.2.3 Results of UVa Tests

The University of Virginia rig ran three sets of 5 VPTs for approximately 30 wks each in a 3.8 T magnetic field under high light conditions from blue and orange frequencies to simulate a large light yield found in large eta regions of the end-cap. The large photocurrents allowed

h

(a) The 3.8 T superconducting solenoid magnet used at UVa to study VPT performance

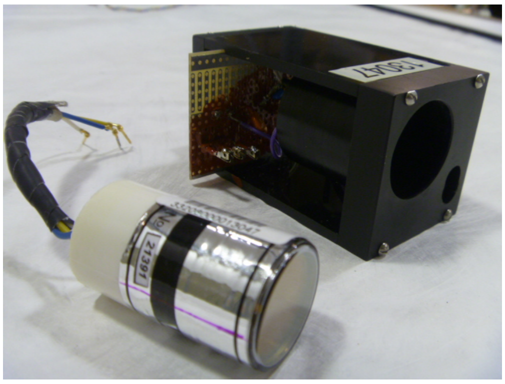

(b) A VPT before being installed in the rig and the housing that provides mechanical support and high voltage connections

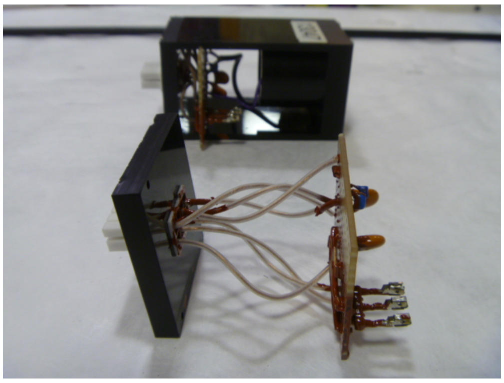

(c) The housing for the VPT also provides simple HV filtering to provide stable power to the device

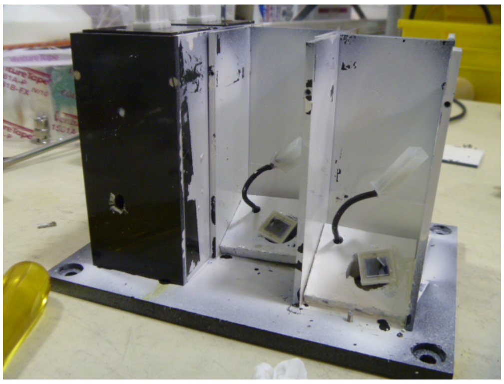

(d) The structure which holds 5 vpts in their housing. A PIN diode is used to measure the LED light and make corrections for fluctuations in brightness

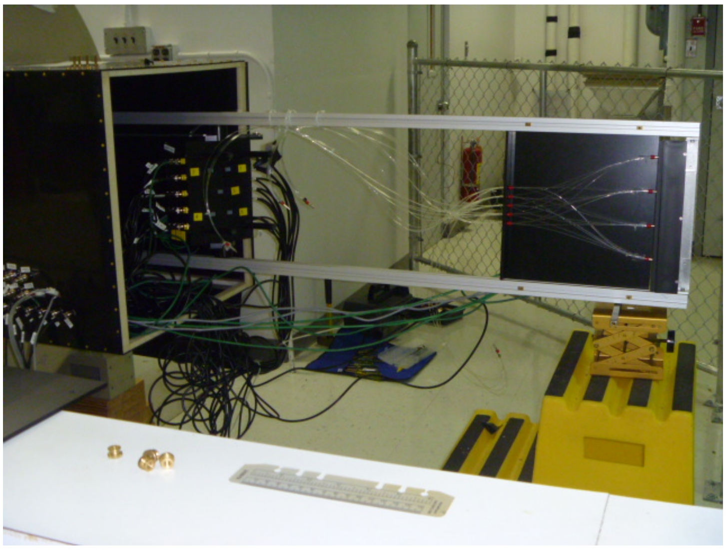

(e) The VPT rig in maintenance position outside of the bore of magnet (during operation the rail is inserted into the bore such that the vpt housing is at the center). Fiber optics feed from the left into the VPT and amplifier housing.

Figure 4.18: Features of the UVa VPT test stand

the collection of an integrated charge of ∼48 mC for the largest gain VPT, and ∼16 mC for the other three. All VPTs were characterized by an initial steep decline followed by a plateau region, which was fit with a double exponential function of the form

$$f(x) = A + B\exp(Cx) + D\exp(Ex) \tag{4.2}$$

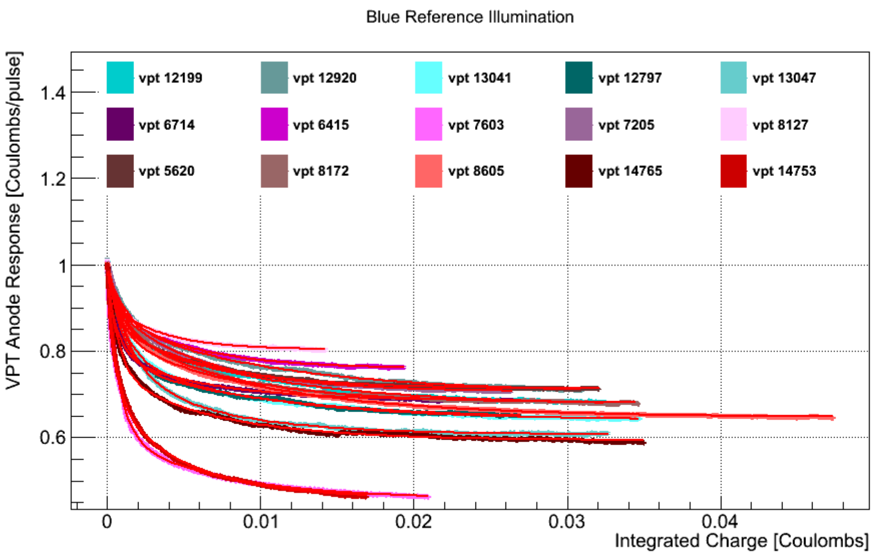

Figure 4.19: 3 runs of 5 VPTs, exposed to blue LED light, and fit to a sum of two exponentials.

Table 4.1: Fit Results for VPT Conditioning Studies at U.Va. and Brunel, Blue Reference LED

RIE Number	% Drop	χ^2/NDF	Pedestal	Fast exp Amplitude	Fast exp τ	Slow exp Amplitude	Slow exp τ
12199	30.1	1.20e+00	1.51e-09	3.42e-10	-8.84e-04	3.85e-10	-1.00e-02
12920	27.0	7.27e-01	1.72e-09	3.16e-10	-1.16e-03	4.03e-10	-1.05e-02
13041	33.5	8.46e-01	1.09e-09	3.43e-10	-1.20e-03	2.46e-10	-9.31e-03
12797	33.6	1.07e+00	6.39e-10	2.18e-10	-9.72e-04	1.31e-10	-9.87e-03
13047	38.1	1.06e+00	5.48e-10	1.98e-10	-1.40e-03	1.49e-10	-6.19e-03
6714	29.3	8.37e-01	1.55e-09	4.10e-10	-6.66e-04	2.48e-10	-6.11e-03
6415	23.6	1.28e-01	1.19e-09	1.54e-10	-6.55e-04	2.20e-10	-5.16e-03
7603	50.3	3.25e+00	1.44e-09	1.02e-09	-8.22e-04	4.87e-10	-6.72e-03
7205	29.4	4.53e-01	1.41e-09	2.14e-10	-5.68e-04	3.94e-10	-5.96e-03
8127	19.6	1.97e-01	1.71e-09	1.82e-10	-3.12e-04	2.35e-10	-3.30e-03
5620	27.4	4.57e+00	1.68e-09	2.85e-10	-5.20e-04	3.68e-10	-6.19e-03
8172	30.3	8.75e+00	8.32e-10	1.52e-10	-1.06e-03	2.27e-10	-6.87e-03
8605	32.1	6.94e+00	1.36e-09	3.33e-10	-8.97e-04	3.94e-10	-1.03e-02
14765	38.9	2.78e+01	3.47e-10	1.37e-10	-7.46e-04	9.24e-11	-6.77e-03
14753	52.9	2.53e+01	1.19e-09	7.45e-10	-5.86e-04	6.10e-10	-4.77e-03
Average	31.0	4.62e+00	1.17e-09	2.94e-10	-1.09e-03	1.66e-10	-3.07e-01

where A is a pedestal parameter, B is the amplitude of the fastest dropping exponential, C is the time constant of the fast dropping exponential, D is the amplitude of the slow dropping exponential, and E is the time constant of the fast exponential. The summary of the fit parameters for blue LED light is shown in table 4.1 and the summary of fit parameters for the orange LED light is shown in table 4.2. Plots of the VPT anode response versus integrated charge, and the associated fit for each of the devices is shown in figure 4.19 for blue LED exposure and in figure 4.20 for orange LED exposure. Based on these findings, it can be concluded that the VPT "burn-in" eventually reaches a plateau at about $\sim 70\%$ for blue LED exposure and $\sim 50\%$ for orange LED exposure.

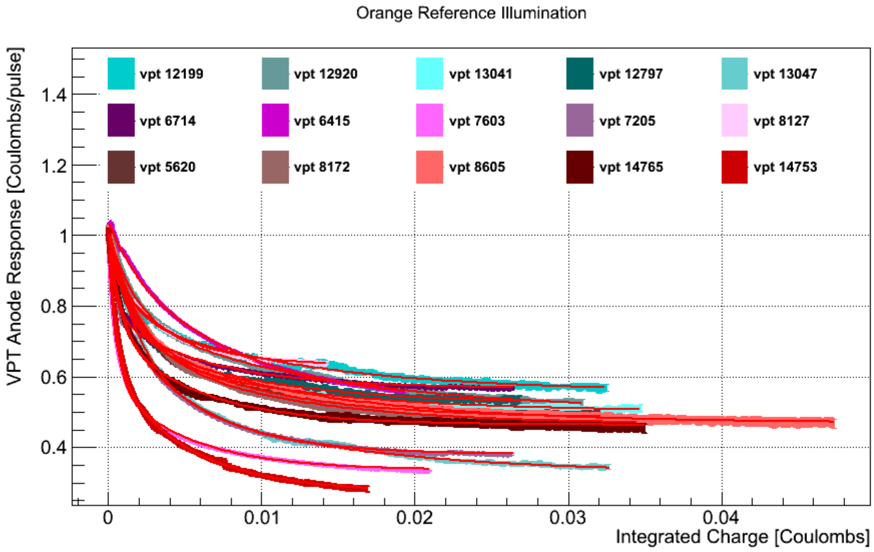

Figure 4.20: 3 runs of 5 VPTs, exposed to orange LED light, and fit to a sum of two exponentials.

Table 4.2: Fit Results for VPT Conditioning Studies at U.Va., Orange LED

RIE Number	% Drop	χ^2/NDF	Pedestal	Fast exp Amplitude	Fast exp τ	Slow exp Amplitude	Slow exp τ
12199	41.9	6.23e-01	4.23e-10	1.79e-10	-1.10e-03	1.76e-10	-1.10e-02
12920	45.3	1.84e-01	6.73e-10	3.24e-10	-1.67e-03	3.72e-10	-1.26e-02
13041	48.3	7.42e-01	2.75e-10	1.81e-10	-1.63e-03	1.04e-10	-1.02e-02
12797	46.4	5.05e-01	2.05e-10	1.14e-10	-1.23e-03	7.87e-11	-8.77e-03
13047	63.0	1.09e+00	1.34e-10	1.73e-10	-2.18e-03	1.07e-10	-1.16e-02
6714	43.4	1.43e+01	7.73e-10	3.29e-10	-4.49e-04	2.84e-10	-6.11e-03
6415	46.5	2.34e+01	4.41e-10	8.75e-11	-1.80e-03	3.47e-10	-7.95e-03
7603	64.8	3.20e+01	3.01e-10	3.42e-10	-5.42e-04	2.24e-10	-5.04e-03
7205	63.2	6.52e+01	1.94e-10	1.29e-10	-4.49e-04	2.16e-10	-5.13e-03
8127	39.4	2.24e+01	7.09e-10	1.54e-10	-2.08e-04	3.10e-10	-3.75e-03
5620	50.3	2.30e-01	4.07e-10	2.13e-10	-1.16e-03	2.37e-10	-7.79e-03
8172	51.7	1.56e-01	4.01e-10	2.73e-10	-1.91e-03	2.08e-10	-9.48e-03
8605	49.6	1.83e-01	2.39e-10	1.46e-10	-1.45e-03	1.33e-10	-1.12e-02
14765	53.3	3.08e-01	2.07e-10	1.27e-10	-8.55e-04	1.17e-10	-5.66e-03
14753	72.2	2.22e-01	1.94e-10	2.76e-10	-6.01e-04	2.47e-10	-5.06e-03
Average	52.0	1.08e+01	3.72e-10	2.03e-10	-1.15e-03	2.11e-10	-8.10e-03

4.3 The Hadronic Calorimeter

The Hadronic Calorimeter (HCAL) is is divided into four sub-systems: the barrel (HB), the endcap (HE), the outer calorimeter (HO), and the forward calorimeter (HF). It is especially important for measuring hadronic jets and neutrinos by measuring an imbalance in energy trans-

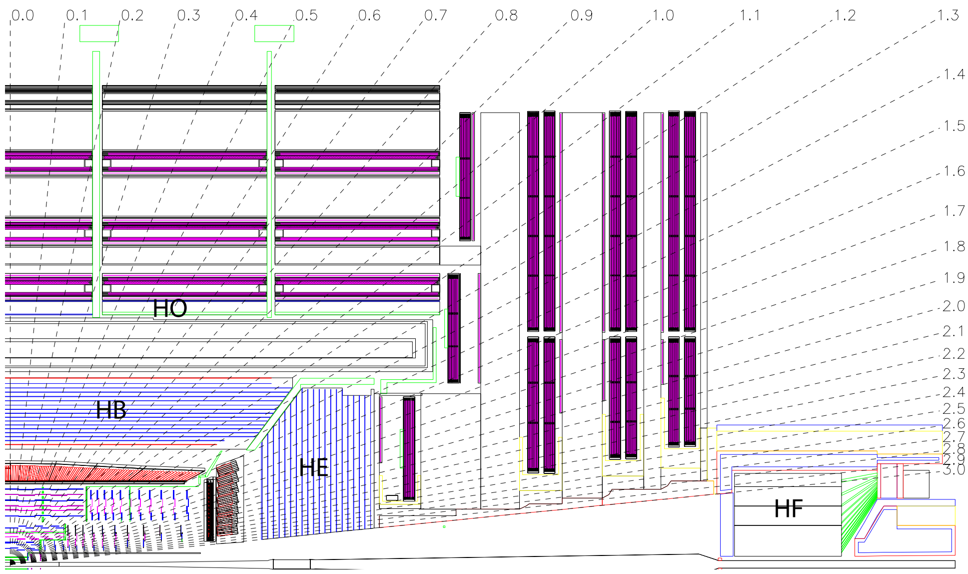

Figure 4.21: Longitudinal cross-section of the HCAL with the four sub-systems labeled [15].

verse to the beam-line. It provides coverage from $|\eta| < 3$ from the HB, HE, and HO, and the HF extends the coverage out to $|\eta| < 5.2$. A diagram of the longitudinal cross section is shown in figure 4.21.

The barrel section of the HCAL, the HB, is divided into two sections longitudinally, each with 18 identical azimuthal wedges wrapped around the beam-line. Each wedge has four azimuthal sections, with the center two sections aligned and each edge piece angled and staggered in a configuration that creates no projective dead material for the full radial extent of the HCAL. Figure 4.22 shows a closeup photograph of four wedges, where optical fibers are laid out across the seam that joins the staggered edge layers to the two aligned center layers, and blue lines highlight the four azimuthal divisions for a single wedge.

The HB is a sampling calorimeter, with each azimuthal section composed of 14 alternating layers of brass absorber plates, and layers plastic scintillator tiles, with steel plates on the top and bottom layers for structural support. Each quarter-barrel section of scintillator has 16 η divisions, giving a segmentation of $(\Delta\eta, \Delta\phi) = (0.087, 0.087)$. The brass absorber plates are C26000/Cartridge Brass. The material was chosen since the absorber material could not be distorted or bend under the stress of its own weight for at least 15 years of experimental running. Much of the material was purchased, but over a million Russian WW2 brass shell casings, designed to withstand the stresses of travel aboard 1940s Navy vessels, were melted down and processed into absorber tiles. Figure 4.23 shows members of the Russian Navy posing with some of the shells.

When a hadron passes through a wedge, the brass and steel plates absorb energy and ini-

Figure 4.22: Closeup of the HCAL barrel section. The center section of each of the 18 wedges are labeled, optical cables lay across the joint of the center and staggered edge sections of each wedge. The blue lines show the approximate azimuthal division of the wedge [15].

tiates the decay of the hadron into a number of lighter particles. These particles pass through the scintillator layer, which absorb energy from the interactions or collisions with the passing particles. The electrons of the scintillator become excited and relax by emitting a number of photons in the blue-violet range of the visible spectrum proportional to the amount of energy absorbed by the scintillator. These photons are absorbed by wavelength shifting fibers (WSFs), which re-emit the light in the green part of the visible spectrum. The WSFs are spliced into four clear fiber optical cables. These fibers transport the light from each of the layers to an optical decoding unit (ODU), which arranges the fibers into readout towers. A hybrid photodiode (HPD) converts this light into electric signals and is digitized by an ADC contained on the front-end electronics. The HPD is a photo-cathode, which converts light to electrons via the photoelectric effect, that sits above a silicon diode that amplifies the signal of the cathode. The HPD provides a gain of 2000 to the light signals received from the scintillator trays. The on-detector electronics communicate to the HCAL trigger/readout (HTR) boards, which communicate with the trigger system to decide whether the store the event as data or discard it.

The brass absorbing material has a nuclear interaction length, or the length necessary to reduce the number of charged particles in a hadron shower by 1/e, of 16.42 cm, and a radiation length of 1.49 cm. This means that the HB will be able to contain a large part of most hadron showers produced at LHC energies, but a portion will still pass through the entire radial distance. The outer barrel layer, HO is designed to measure the remnants of the hadron shower. It sits

Figure 4.23: Over 1 million Russian shells of military artillery were re-processed in the construction of the HCAL [20]

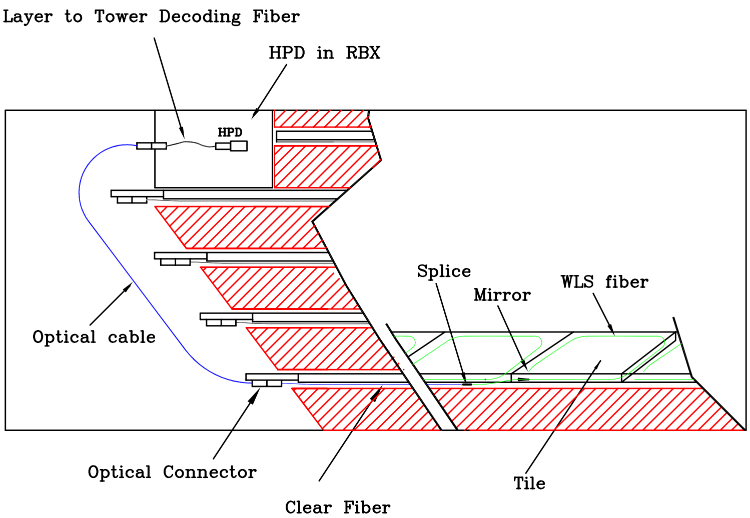

Figure 4.24: Optical readout chain of the HCAL scintillator tiles [15].

outside of the solenoid magnet, using it as an absorber layer $1.4/\sin\theta$ interaction lengths. It consists of 5 sections along the z-axis, which form rings around the beam-line. Each ring is a layer of scintillator tiles at radial distance of 4.07m, except for the center ring. Since it corresponds the the $\eta = 0$ ring, there is a minimum amount of absorber material in front of it. The central ring is thus two layers of scintillator at radial distances 3.82 and 4.07 m, which sit on either side of a 19.5cm thick piece of iron absorber.

The endcap system, the HE, provide a substantial portion of the total η coverage, from $1.3 < |\eta| < 3.0$, and contains $\sim$1/3 of the final state particles in a collision. Like the HB, it is a sampling calorimeter with alternating layers of brass and plastic. The demand for radiation hardness, and the need for a non-magnetic material, lead to the same choice of C26000 cartridge

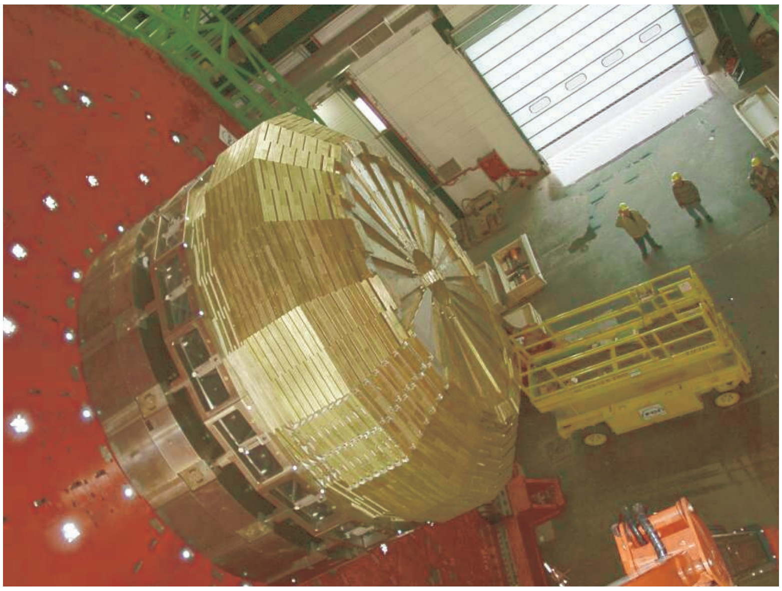

Figure 4.25: HCAL endcap, 18 azimuthal divisions of alternating layers of brass and plastic scintillator [15].

brass found in the HB. It is also divided into 18 azimuthal wedges, and 16 η divisions, giving it the same $(\Delta\eta, \Delta\phi) = (0.087, 0.087)$ segmentation. Figure 4.25 shows an image of a partially assembled endcap before being installed.

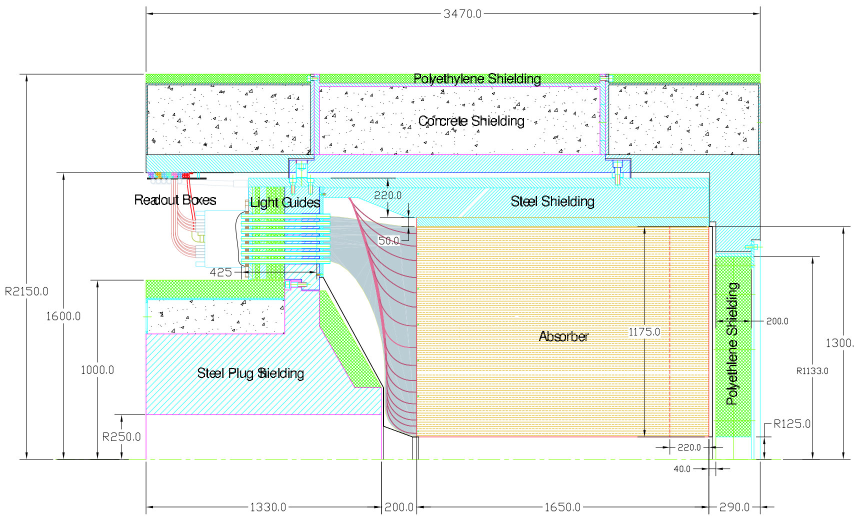

Figure 4.26: Longitudinal cross-section of the HCAL forward calorimetry, the HF [15].

The forward calorimetry, HF, extends the HCAL coverage from $3.0 < |\eta| < 5.0$, and necessarily must sit in the region of the detector with the largest particle fluxes and thus radiation exposure. The HF is a cylindrical steel structure with an inner bore 12.5 cm from the beam line, and a outer radius of 130.0 cm. It sits 11.2 m away from the nominal interaction point in the

$\hat{z}$ direction. Like the HE, it has 18 azimuthal divisions on either side of the interaction point. Relativistic particles that move through the steel generate Cherenkov light, which is collected by radiation hard quartz fibers, which transport the light to HPDs which are readout in the manner as described above. Since the detection mechanism is Cherenkov light, this sub-system is primarily sensitive to the electromagnetic component of the hadronic shower. Figure 4.26 shows a cross-sectional view of the HF detector.

4.4 Muon Chambers

In pp collisions, muons are only created through electroweak or exotic physics processes, making the detection of this particle an invaluable tool for reducing the large hadronic backgrounds produced at the LHC. The muon chambers, positioned furthest from the beam-line, sit behind the ECAL and HCAL detectors, which absorb almost all of the hadronic activity from a collision. They operate in a relatively low flux environment, allowing for robust measurement of their kinematics, making it an excellent trigger system. One of the most important discovery channels for the Higgs boson, involved the decay of the Higgs into two Z bosons, which decay to two pairs of muons. Only 25 events were needed for a statistically significant observation in that channel, since the backgrounds had been reduced to only 5 expected events and the muons had provided high resolution on the invariant mass of the Higgs.

The muon chambers are composed of three types of gaseous detector technology: drift tubes (DTs), cathode strip chambers (CSCs), and resistive plate chambers (RPCs). In the muon barrel system (MB), where the magnetic field is uniform DTs provide η coverage, for $|\eta| < 1.4$, and are supplemented by a system of RPCs that provide an independent trigger source and faster timing resolution. In the muon endcap system (ME), where the magnetic field would degrade the performance of DTs, a system of CSCs and RPCs provide η coverage from $1.4 < |\eta| < 2.4$.

The DTs are located in the MB system, which is divided into 5 longitudinal, cylindrical sections around the beam-line, known as wheels. In each wheel there there 4 concentric layers of drift tube stations, one on either side of the magnet return yoke, and two interspersed inside of it. Each wheel is divided into 12 azimuthal section, making 48 stations in the barrel, as shown in figure 4.27. Each station on the first three (fourth) layers contain 3(2) superlayers, where each superlayer is made of a stack of 4 layers of rectangular drift cells, which are staggered by half a cell each. Two of the superlayers are oriented such that they are parallel to the beam, measuring the muon in the $r-\phi$ plane. The first three layers contain a third superlayer, orientated perpendicular to the beam, measuring a z component of the muon trajectory. Each drift cell is a hollow 13×42 mm tube, with a relatively thick 1.5mm wall to provide isolation

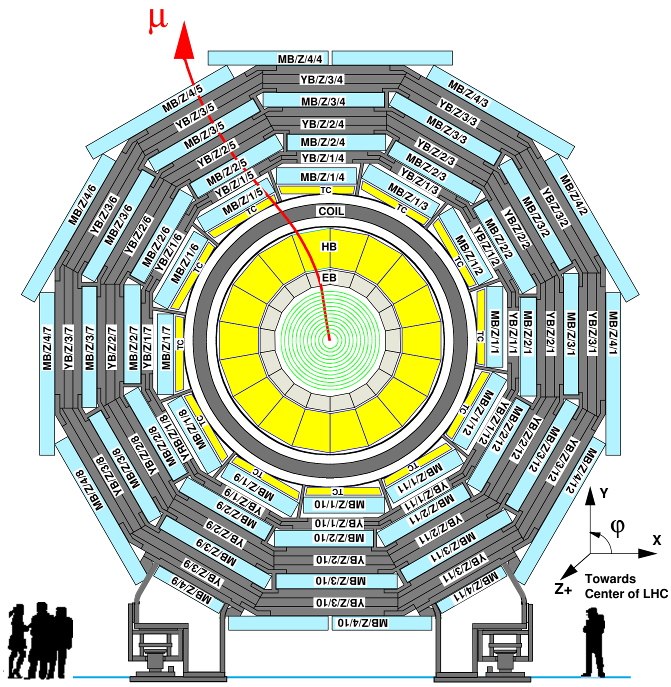

Figure 4.27: Longitudinal cross-section of one of the 5 wheels of the muon system. Drift tubes are placed in 4 concentric layers, with 2 being placed inside the return yoke of the magnet, and 12 azimuthal divisions [15].

between adjacent cells. Each cell is filled with a mixture of 85% argon + 15% CO_2 gas mixture, and contains an anode wire that is held at 3600 V that runs down the axis of the cell. The walls of the cell are held at 1800 V or -1200 V depending on the wall. When a muon passes through the chamber, it's charge ionizes molecules of the CO_2 gas, causing the electrons to drift towards the anode wire, and the CO_2 ions drift towards the wall. As the electrons approach the anode, they are accelerated and liberate secondary electrons from other CO_2 molecules, creating an avalanche of electrons near the wire, resulting in a drop in voltage as they are collected. The voltage drop is read out by front end electronics as a signal that a muon has passed through the chamber. The Argon gas quenches the avalanche reaction, and the maximum drift time for electrons in the gas is 380 ns. This long time scale necessitates the use of an additional, fast-timing system, the RPCs. Figure 4.28 shows a cross-section view of a drift cell, including electric field lines produced by the potential difference between the anode wire and the walls of the drift cell.

The resistive place chambers (RPCs) are the fast timing system chosen to supplement the DTs in the barrel, and the CSCs in the endcaps. In the barrel, they are adhered to the top and bottom of the first two layers of drift stations. In the outer two layers, they are only adhered to the bottom of each station. Figure 4.29(a) shows the layout of the barrel RPC system. The muon endcap system is composed of three disks on either side of the interaction point, and is

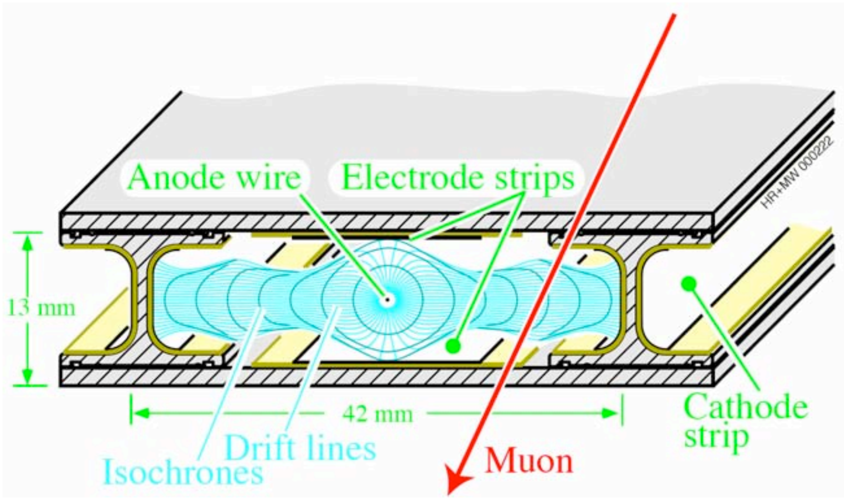

Figure 4.28: A cross-section view of a drift cell. The anode wire is held at 3600 V, creating a potential difference with the walls. Electric field lines are shown in blue [15].

shown in figure 4.29(b). RPCs are mounted on the back of the CSC stations of the innermost and outermost disks, and on the front of the CSC for the middle disk. Each RPC consists of two plates of high resistance material, one held at a positive voltage, the anode, and the other held at a negative voltage, the cathode. The volume between the plates is filled with a gas similar to the drift tubes. When a muon passes between the plates, it ionizes the gas molecules, and the electrons are accelerated towards the positive plate, creating an avalanche of secondary electrons that combine with the positive plate creating a voltage drop that is read out as a signal. The timing resolution achieved from the RPCs is less than the 25 ns LHC bunch

h

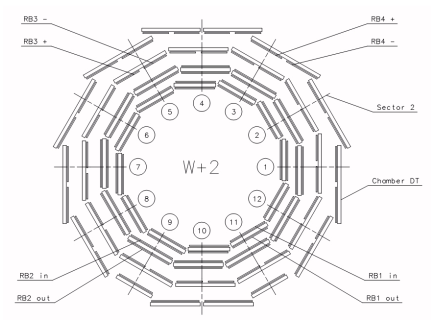

(a) A longitudinal cross-section of the muon barrel RPC system. RPCs are attached to the top and bottom of the first two layers of drift stations, and to the bottom of the outer two layers [15]

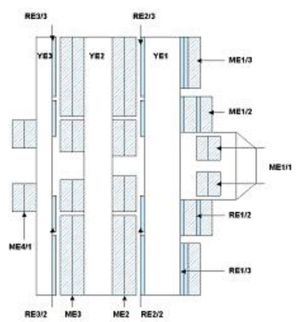

(b) Cross-section of muon endcap system. It is composed of three disks, with RPCs mounted on the back of CSC system on the first and last disks, and on the front of the CSC in the middle disk [15]

Figure 4.29: RPC layout for the barrel and endcaps

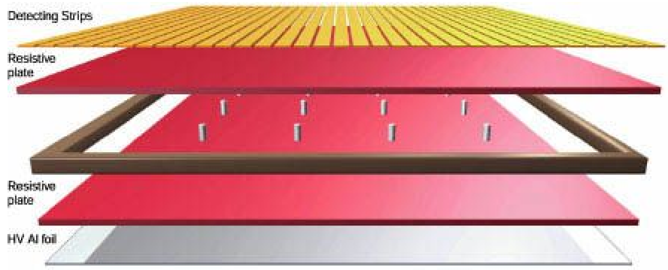

Figure 4.30: Exploded diagram of an RPC [21]

crossing, supplementing the spatial resolution provided by the DTs in the barrel, and the CSCs in the endcap.

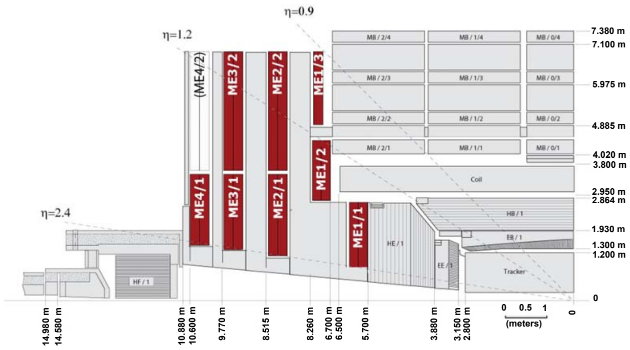

Figure 4.31: Cross-section of one quarter of the muon endcap system, with the 4 disks of CSC systems shown in red [15].

In addition to RPCs, the muon endcap (ME) system, uses cathode strip chambers (CSCs) to provide additional spatial resolution on muons. Each endcap has 4 layers of CSCs, with a trapezoidal shape, with 468 cathode strip chambers distributed on each. Three groups of 72 are located on the inner disk, a group of 36 and a group of 72 in the second and third disk, and a group of 36 in the outer disk. Figure 4.32 shows the layout of a quarter section of the CSC system in the ME. A CSC station consists of 6 layers of gas chambers, where each chamber is an array of anode wires, held at a positive voltage, arranged perpendicular to cathode strips, held at negative voltage. The volume of the chamber is filled with a gas that is 40% Argon, 50% CO_2, and 10% CF_4. When a muon passes through the volume, the gas is ionized, and now, since the anode and cathode strips are perpendicular, when the electrons and gas ions combine with the anode and cathode respectively, a 2-D measurement of the muon's position is recorded. Figure 4.32 shows a diagram of a CSC chamber with 7 layers to create the 6 gas chambers.

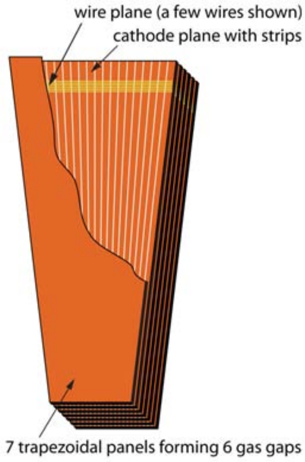

Figure 4.32: A CSC station with 7 layers, making 6 gas chambers. Cathode strips are shown in yellow, perpendicular to the vertical anode wires in orange [15].

4.5 Data Collection Overview

The LHC is designed to deliver protons at 40 MHz, corresponding to a bunch crossing every 25 ns. The majority of the interactions will be glancing, low-energy collisions, which do little to reveal new phenomenon, and would be impossible to store for analysis. A trigger system is designed to select interesting events with a large potential of revealing new physics. The rate is reduced in two steps through the Level-1 (L1) trigger, and the High-Level Trigger (HLT). The L1 trigger is composed of programmable electronics and hardware that buffers the data and perform simple calculations on tracks and calorimeter energy deposits to determine whether an event should be kept for analysis. This reduces the event rate from 40 MHz to 10 kHz. The HLT is a computer farm of $\sim$1000 computer processors, that perform a more sophisticated reconstruction of the tracks and energy deposits, as well as more complicated calculations between reconstructed objects. This stage reduces the rate to a much more manageable 100 Hz.

The L1 trigger is composed of local, regional, and global components. The process of determining whether to accept or reject the event begins by calculating Trigger Primitive Generators (TPGs) based on calorimeter energy deposits, and tracks in the muon chambers. The entire process has a latency time of 3.2 μs, which corresponds to the length of the LHC abort gap. Sufficiently large data buffers allow the storage of all the events processed during a bunch train, meaning that CMS is capable of running with zero dead time due to detector readout latency.

In the ECAL a trigger tower consists of a 5$\times$5 array of crystals. Front-end electronics on the crystals receive ADC counts on the amplitudes of the photomultipliers, and uses information encoded in the electronics to convert this sum to the transverse energy, E_{T} deposited in the crystals. The EB TPG also encodes information about the distribution of energy, and thus the

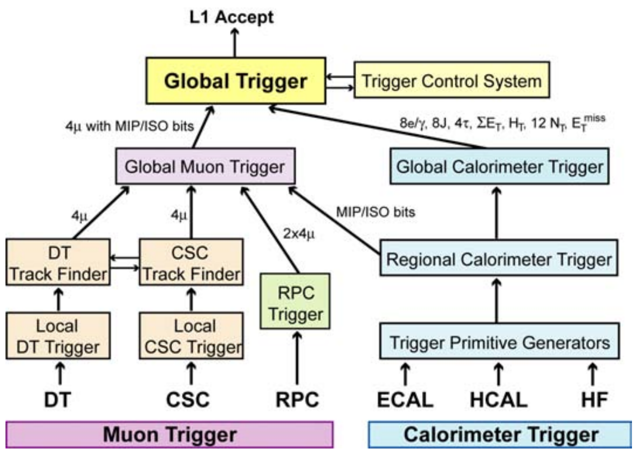

Figure 4.33: A block diagram of the L1 trigger [15]

shower shape in the 5×5 array, which is used to veto anomalous signals. In the HCAL, a trigger tower consists of one of the 16 azimuthal wedges, with segmentation $(\Delta\eta, \Delta\phi) = (0.087, 0.087)$, in the barrel and endcap. Similarly to the ECAL, front-end electronics digitize the signal from the HCAL HPDs, and convert the ADC counts into sums of transverse energy. These calorimeter TPGs are sent to a Regional Calorimeter Trigger (RCT) that is composed of a 4×4 array of trigger towers, with the exception of the HF, which is formed by a single trigger tower.

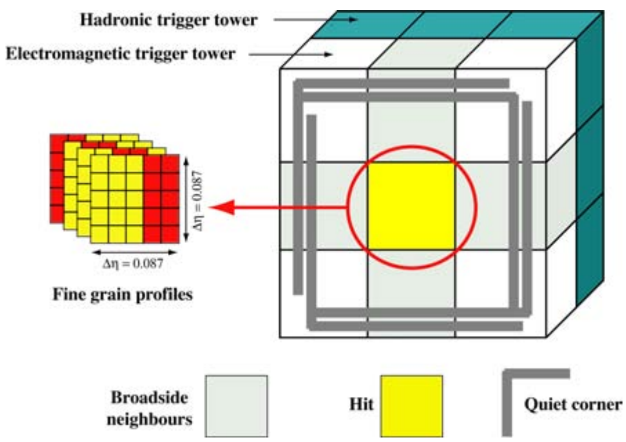

Figure 4.34: A schematic of the e/γ trigger algorithm [15].

The RCT determines electron and photon candidates from the calorimeter sums. The e/γ trigger searches for the highest energy trigger tower in the ECAL. Within that trigger tower, it checks that the EM shower is contained in a 2×5 array of crystals and that the ratio of ECAL to HCAL energies is less than 5%. It is considered an isolated electron if all eight of its nearest neighbors pass these requirements, and a corner of five neighbors has energy below a threshold requirement. It is considered a non-isolated electron if only the second highest E_{T}

broadside neighbor trigger tower passes these criteria. Up to four isolated, and four non-isolated e/γ candidates per RCT are passed to the Global Calorimeter Trigger (GCT).

The GCT determines jets, total transverse energy, missing transverse energy, jet counts, and H_{T} (scalar sum of transverse momentum), in addition to the highest rank isolated and non-isolated *egamma* candidates. Jets are found in a clustering algorithm that looks for large energy deposits in 2×12 cells of ϕ or η that span 40° and half the detector in each of the coordinates, respectively. Up to four jets, and four tau jets from the HCAL and four jets from the HF are forwarded to the Global Trigger (GT).

The non-calorimeter based triggers are based on measurements of the DTs, CSCs, and RPCs in the muon drift chambers. The barrel DTs look for hit patterns among neighboring tubes in successive layers, and fits a track segment in the η and ϕ coordinates. The endcap CSCs provide 3-dimensional track segments and are combined with the DTs to form tracks that are passed to the Global Muon Trigger (GMT). The RPCs provide an independent set of tracks and timing hits to the GMT. Each bunch crossing the GMTs receive up to four muon candidates in the barrel RPCs, four from the barrel DTs, four from the endcap RPCs, and four from the endcap CSCs. The GMT records the candidate's p_{T}, charge, η, and ϕ position, as well as a quality code related to the fit of the track to the hit positions of the detector. The GMT sends then sends these muon candidates to the GT.

The Global Trigger can execute up to 128 trigger algorithms in parallel to analyze the p_{T}, charge, η, and ϕ position, and associated quality codes for muons, electrons, photons, jets, and missing transverse energy. Most algorithms compare single object characteristics to thresholds to determine if they pass minimally interesting criteria. If any of the algorithms return a passing decision, the L1 trigger issues an accept statement that allows the data stored in buffers to be readout by the CMS Data Acquisition (DAQ) system.

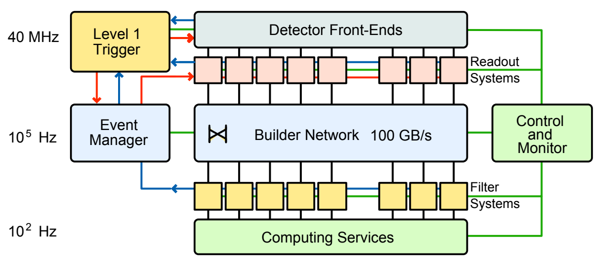

Figure 4.35: Layout of the CMS DAQ [15]

The CMS DAQ collects information from 626 sub-detector Front End Drivers (FEDs), which extract the buffered information from the various front-end systems, upon the arrival of a L1 trigger accept. An event builder algorithm assembles the fragments from the various sub-systems into a single coherent event, and transmits the information to the HLT computing farms. Figure 4.35 shows a schematic of the DAQ system.

The HLT computer farm performs the final reduction of data rate, from 100kHz from the L1 to 100Hz. The computer farm performs basic consistency checks to ensure the quality of the data, then performs calculations based on topology of the HLT path. Typically, a more sophisticated reconstruction of an object takes place, and kinematic cuts are applied to the object or in relationship to other objects in the event. Each HLT path forms its own data set, thus creating single muon, single electron, electron+jets, etc. type datasets. The unpacked detector information read by the DAQ is composed of ADC counts for each readout channel, TPGs, and the L1 decision. This is known as the RAW dataset. Reconstructed physics objects are stored RECO data tier, and finally an analysis object data (AOD) tier is created containing only information about the reconstructed objects without having to store detector information. This last format requires the least amount of data per event for storage, and contains the reconstructed physics objects, such as electrons, muons, jets, etc. which are be used to search for new physics phenomenon.

Chapter 5

Particle Reconstruction at CMS

Charged and neutral hadrons in the form of jets, missing transverse energy (MET), photons, electrons, muons, and tau leptons are reconstructed at CMS using the particle-flow event-reconstruction algorithm [24]. The algorithm is based on on a three-step process of identifying charged particle tracks using the muon chambers and silicon tracker, identifying clusters of energy in the ECAL and HCAL, and linking the tracks to the calorimeter clusters. The calorimeter energy deposits were calibrated with test beam sources, data from cosmic rays and beam dumps, and finally from collision data. The algorithm constructs muons by fitting the tracks formed between the muon chambers, pixel and silicon trackers. Electrons have tracks from the pixel and silicon tracker matched to the ECAL, with a minimum energy deposited in the HCAL. Jets are formed from tracks, ECAL, and HCAL clusters falling within a conical angle. The identification of one, three, or larger odd number of tracks, and the majority of the energy contained in a small cone size, allows a jet to be tagged as a hadronically decaying tau lepton. Additional algorithms are also used to identify a jet as coming from the decay of a b-quark, primarily by looking for secondary vertices in the pixel and silicon tracker.

5.1 Iterative Tracking

Since approximately two-thirds of the energy of a jet is carried by charged hadrons, the tracker is the cornerstone of the particle-flow algorithm [24]. The path of a charged particle in a magnetic field follows a helical pattern, described by 5 parameters. The extraction of these requires three 3-dimensional measurements of the particle, or two 3-dimensional measurements and a constraint on the origin [135]. The pixel detector is ideal for this since each pixel provides a 3-dimensional measurement of the particle's location. Track reconstruction is the process of using hits in the pixel and silicon detector elements to estimate the momentum and trajectory of the charged particle responsible for the hit [135]. The tracking software at CMS is known as the Combinatorial Track Finder (CTF), which is based on producing tracks over multiple iterations of the reconstruction sequence, removing the tracks with the largest p_{T} closest to the interaction region first, reducing the combinatorial complexity over each iteration.

Each iteration begins by identifying a seed for the particle tracks, which is a minimum combination of pixel or silicon tracker hits that is used as an initial estimate of the trajectory of the particle [135]. Then, tracks are found by applying the Kalman filter [136]. This method is based on applying a small Gaussian uncertainty to the location of the seed hits, fitting an initial track to these hits, then looking for additional hits that fall within the error of the initial estimate, deeper in the tracker. These hits are added to the fit with their own uncertainties, and the fit is re-calculated, each time attempting to minimize the mean-square estimation of the error. The 5 helical trajectory parameters are extracted, and tracks with poor fits are discarded.

A total of six iterations are used, each with a different starting seed or kinematic requirement on the p_{T} of the tack, as well as the transverse and longitudinal distance from the reconstructed vertex [136]. The first iteration is seeded by three hits in the pixel detector. The second, is seeded by two hits in the pixel detector and a pixel vertex, which occurs when at least four pixel tracks point back to a common origin. The third iteration is seeded once again by three hits in the pixel detector, except with a looser minimum p_{T} cut. The fourth iteration uses seeds from any three hits in the pixel detector or silicon tracker, with at least one hit coming from the pixel detector. In the fifth iteration seeds are formed from the inner two rings of the TIB, TID, and TEC. The final iteration begins with seeds from the first two rings of the TOB and the fifth ring of the TEC.

5.2 Calorimeter Clustering

The clustering algorithm is used to detect the energy and direction of stable, neutral particles such as photons and neutral hadrons [24]. It also separates the energy contributions from the neutral and charged hadrons, and provides an additional energy measurement for charged hadrons with very low or high p_{T} tracks, both cases that degrade the energy resolution. Finally, the clustering algorithm properly accounts for bremsstrahlung energy losses from electrons. The algorithm is performed independently for the ECAL barrel, ECAL endcaps, HCAL barrel, and HCAL endcaps. In the HF, no clustering algorithms are used, as each cell is used as its own cluster in an event.

The clustering algorithm begins by identifying "cluster seeds", which are the highest p_{T} cells above a defined energy threshold [24]. Then, "topological clusters" are formed by grouping adjacent cells together with energy above 80 MeV in the ECAL barrel, 300 MeV in the ECAL endcaps, and 800 MeV in the HCAL. As a new cell is added, the total cluster energy and position is updated until no new cells are able to be added. Each cluster seed thus gives rise to a "particle-flow cluster". Each of these clusters is used as a candidate to be associated with tracks during the third stage of the algorithm, the linking step.

5.3 Calorimeter Energy Calibration

One of the most critical steps in reconstructing particles is the calorimeter energy calibration, which is the conversion of calorimeter scintillator light and photodetector current to the energy deposited in the calorimeter by the particle traversing it. This is done by exposing the crystals to particles of a known energy, using large samples of cosmic ray muons, by measuring minimum-bias events assuming a ϕ symmetry, the of π^0 and η^0 meson resonances decaying into photons, and W and Z bosons into electrons.

Before installation at P5, the ECAL and HCAL were pre-calibrated using a dedicated "test beam" of known energy. In 2006, the ECAL was exposed to an electron beam with energies between 15 and 250 GeV [137] at CERN. Additionally, intercalibrations between crystals were performed with 90 and 120 GeV beams. Also at CERN in 2006, the HCAL was calibrated, prior to installation, using a beam of 50 GeV pions [138].

Once both calorimeters were installed, the detectors were calibrated with cosmic ray muon events in 2007 with the CMS magnet de-energized during the CRUZET (Cosmic RUn at ZEro Tesla) data taking campaign, and again with the CMS field on in 2008 during the CRAFT (Cosmic Run At Four Tesla) campaign. Shortly after the CRAFT campaign, the LHC delivered 450 GeV proton beams to collimator targets upstream of the CMS detector, creating accelerated muons that were additionally used to calibrate the detector response. The ECAL endcap energy resolution was improved from 7.6% to 6.3%, and in the barrel, the intercalibrations from the test beam were validated at a 2% level of agreement [139]. The HCAL energy calibration resulted in 5% energy resolution in the HB, 10% in the HE, 12% in the HF, and 5% in the HE[140].

After an initial set of data collection three independent calibration methods are combined to determine the absolute energy scale and intercalibration coefficients for the crystals [22]. The first method uses a large amount of data collected from minimum-bias trigger events, events which are dominated by glancing collisions and QCD jet production. The processes that contribute to these events have final state particles symmetrically distributed in the ϕ coordinate. By grouping the crystals into rings of η, and the response of each crystal can be determined and modified such that it matches the average crystal response in that η ring, with the uncertainty on

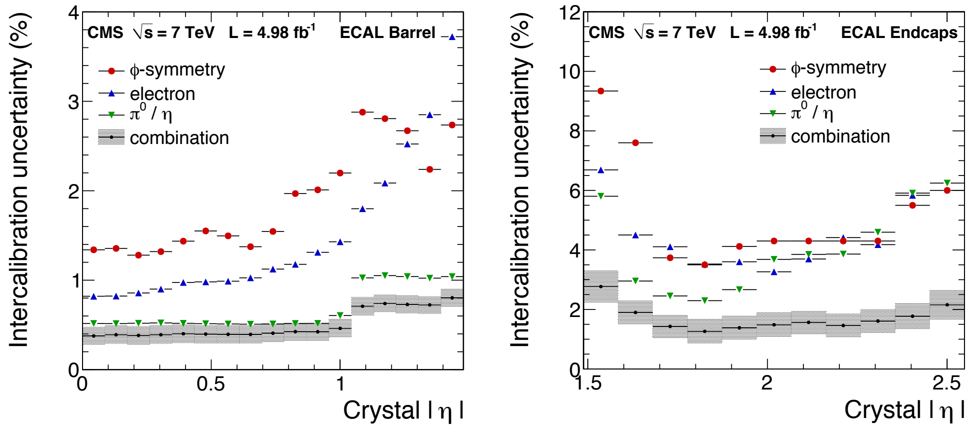

Figure 5.1: Results of the uncertainty on the ECAL intercalibration coefficients for the barrel (left) and endcaps (right) [22].

the average representing the uncertainty on the intercalibration coefficient. The second method involves reconstructing the resonances of the π^0 and η^0 mesons decaying to two photons and relying on the high-precision measurements from other experiments to determine the exact mass of the resonance. Events near the resonance of these two particles are once again divided into rings of η, and averaged over the ϕ coordinate. Decays of the Z boson to an electron pair are also used to determine the absolute scale (ADC counts/GeV) of the crystals, once again relying on the higher-precision measurements of previous experiments for the location of the mass peak. Finally, comparisons between the energy measured in the tracker and that measured in the ECAL are made from W and Z boson decays to a electrons. Figure 5.1 shows the results of combining all three methods, to determine the uncertainty of the intercalibration coefficients.

The ECAL also has a strong dependence on the rate of instantaneous luminosity that the crystals are exposed to. It is therefore necessary to perform additional crystal calibrations as a function of time during a run of data collection. Blue and orange LED light, and blue laser light is fed through a network of optical fibers to each crystal. A known amount of light is injected and the crystal response is measured. Figure 5.2 shows a plot of the crystal response versus time. Rings of η are formed and crystals within the same η ring are used to calculated an average response, as is done in the intercalibration procedures described above.

The performance of the HCAL calibration to the 50 GeV pion beam is validated by comparing energy measurements in the tracker to energy deposits in the HCAL [141]. Since neutral hadrons contribute approximately 10% of the energy contained in a jet, it is necessary to recalibrate the measured energy in the HCAL using simulated events where the true hadronic energy is known. The equation for the total calorimeter energy is given by:

$$E_{\text{calib}} = a + b(E,\eta)E_{ECAL} + c(E,\eta)E_{HCAL} \tag{5.1}$$

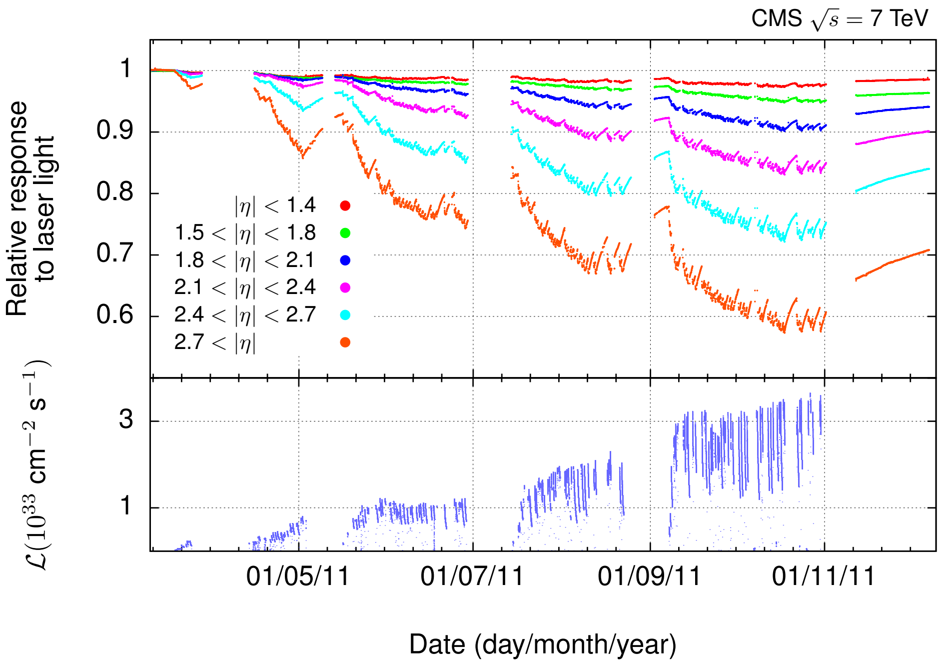

Figure 5.2: Instantaneous luminosity response to the crystals as measured by the laser and LED system. Additional crystal calibration constants are derived to normalize the crystal response over the range of collected data [23]

The coefficients, a, b, and c are determined through a χ^2-minimization procedure over each bin of energy, minimizing the difference between the reconstructed and true energies and solving for the parameters a, b, and c. Figure 5.3 shows the resulting HCAL energy resolution as a function of energy, and the values of the coefficients a, b, and c.

5.4 Linking

Once clusters are formed in the ECAL and HCAL barrels and endcaps, they are associated with nearby tracks in the pixel and silicon tracker in the step of the particle-flow algorithm known as linking [24]. Single particles are formed out of the tracks and calorimeter clusters without double counting contributions from different detectors, forming "blocks" of linked elements. Due to the high granularity of each sub-detector, blocks of two to four elements are typical.

The linking procedure between pixel and silicon strip tracks and the calorimeter deposits occurs in three steps: extrapolating the track to the ECAL preshower (PS); then to the ECAL to a depth corresponding to the maximum longitudinal shower profile; and finally to the HCAL to a depth corresponding to one interaction length. A track is then linked to a cluster if it falls within the cluster boundaries. One HCAL cluster may be associated to many tracks, but each track can only be associated with a single cluster, determined as the track with the shortest

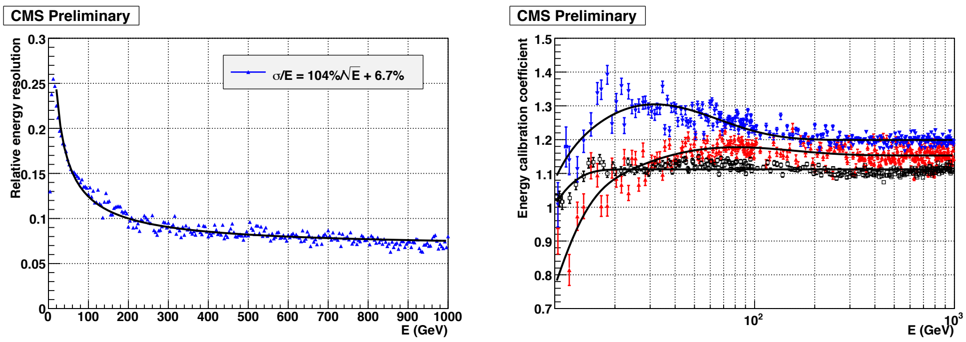

Figure 5.3: Results of using a χ^2 minimization procedure to estimate the neutral hadron energy contribution in the HCAL using simulated events[24]

distance to the center of the HCAL cluster in the case of many candidates. For the ECAL, one track may be associated with many energy clusters, since they may have originated from hadronic shower fluctuations, so links to tracks should be preserved to avoid double counting the hadron energy. In order to account for the bremsstrahlung energy losses of electrons, tangent lines to the tracks are linked to the ECAL. If this extrapolated, tangent track falls within the ECAL cluster boundaries, it becomes a candidate for a bremsstrahlung photon from an electron. Since the ECAL has a finer granularity than the HCAL, clusters of the ECAL are linked to HCAL clusters if an ECAL cluster falls within the boundary of the HCAL cluster. Finally, linking between the muon chambers and the inner tracker occurs via a χ^2 fit to a muon trajectory that would traverse the entire detector.

5.5 Physics Object Reconstruction

Once tracks have been formed from the muon chambers, pixel, and silicon tracker detectors and linked to clusters in the ECAL and HCAL, particles can be reconstructed. The process begins by reconstructing muons, then electrons and photons, finishing with charged and neutral hadrons. The charged and neutral hadrons are then clustered together to make jets, which can be tagged as τ or b-jets. After each object is formed, the tracks and calorimeter energy depositions associated with it are removed from the collection of blocks that are used to form the particle-flow candidates, ensuring that no double counting of energy contributions is taking place.

5.5.1 Muon Reconstruction

The reconstruction of physics objects in the particle-flow algorithm begins by identifying muons [24]. The algorithm begins by identifying tracks in the pixel and silicon strip detectors that have

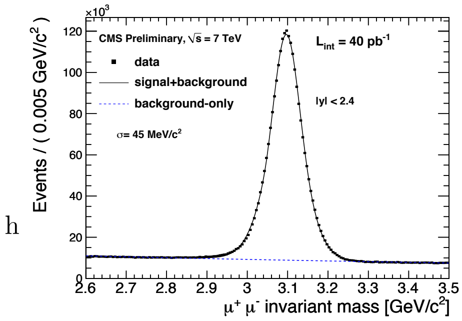

(a) Reconstructed JΨ mass peak from di-muon events in 7 TeV data, used to commission low p_{T} muons reconstructed with the particle flow algorithm [142].

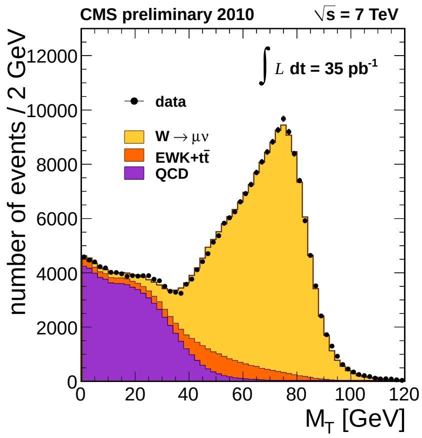

(b) Transverse mass peak of W boson events reconstructed from single muon events in 7 TeV data, used to commission high p_{T} muons reconstructed with the particle flow algorithm [142].

Figure 5.4: Muon validation plots for the particle-flow reconstruction

been linked to tracks in the muon chambers, and fit with a muon trajectory with a minimum χ^2. Additionally, it is required that muon track that is fit with both muon chambers, pixel, and silicon tracker information is compatible, within 3 sigma, to a track fit with the pixel and silicon tracker information alone. When the "particle-flow" muon is removed from the collection of candidate blocks, 3 (0.5) GeV $\pm 100\%$ is removed from the HCAL (ECAL) cells that the muon traverses, based on studies from the CRAFT data run.

In 2010, 7 TeV data was collected [143] in order to commission the reconstruction of muons. The J/Ψ resonance at 3.1 GeV provides a large number of low p_{T} di-muon pairs. Figure 5.4(a) shows the reconstructed J/Ψ mass with 40 pb^{-1} of data. High p_{T} muons are commissioned by reconstructing the W boson mass. Figure 5.4(b) shows the results the first 35 pb^{-1} of 7 TeV data.

5.5.2 Electron Reconstruction

The next stage in particle-reconstruction is the identification of electrons [24]. Electrons leave hits in the tracker and deposits most of their energy into the ECAL, with the clustering widest in the ϕ direction due to bremsstrahlung. Electron tracks tend to be shorter and lose energy in the tracker due to bremsstrahlung, a highly non-linear process, that the Kalman fitter used in the track identification phase is not optimized for. These tracks are re-fit using the Gaussian Sum Filter (GSF) algorithm [144]. This algorithm accounts for the change in trajectory of the electron due to bremsstrahlung, extending the linking to ECAL clusters in the ϕ direction. Blocks that have GSF tracks linked to ECAL clusters, including clusters identified as bremsstrahlung

h

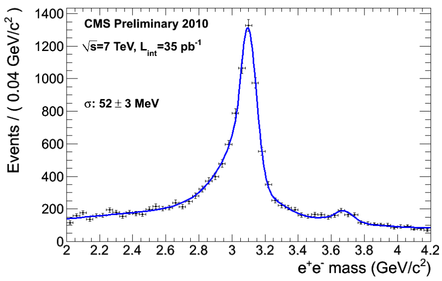

(a) Reconstructed JΨ mass peak from di-electron events in 7 TeV data, used to commission low p_{T} electrons reconstructed with the particle flow algorithm [145].

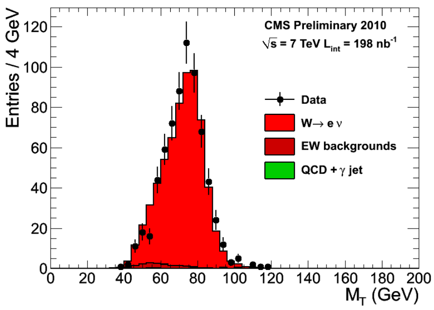

(b) Transverse mass peak of W boson events reconstructed from single electron events in 7 TeV data, used to commission high p_{T} electrons reconstructed with the particle flow algorithm [146]

Figure 5.5: Electron validation plots for the particle-flow reconstruction

photons, and additionally linked to an HCAL cluster with a much smaller energy deposition than in the ECAL are then identified as a "particle-flow electron".

Similarly to the muons, the electron identification from the particle-flow algorithm was commissioned using 7 TeV data collected in 2010. Low p_{T} electrons were commissioned from the J/Ψ mass peak, shown in figure 5.5(a) and high p_{T} electrons were commissioned from W boson decays, shown in figure 5.5(b).

5.5.3 Charged Hadron Reconstruction

Charged hadrons are reconstructed next in the particle flow algorithm [24]. Tracks linked to both ECAL and HCAL energy deposits give rise to "particle-flow charged hadrons" if calorimeter energy is compatible to what is measured from the curvature of the tracks in the pixel and silicon detector. A fit is then performed between all of the tracks and the HCAL energy clusters to determine an optimally-measured momentum. In the case where there is only one track, this fit reduces to a weighted average between the track and HCAL energy clusters.

5.5.4 Photon and Neutral Hadron Reconstruction

The next step in the algorithm is to identify ECAL and HCAL energy clusters that aren't linked to tracks or clusters that are linked to tracks, but have a much larger energy measurement . In the latter case, blocks are kept if the excess energy in the calorimeter clusters is larger than the energy resolution of the calorimeter. In both cases, if the total energy excess in the HCAL is larger than the energy measured in the ECAL, than a "particle-flow photon" is created using the energy in the ECAL and the remaining HCAL energy forms a "particle-flow neutral hadron", with calibrations performed in the manner described in section 5.3. In the case where the ECAL energy is larger than the HCAL energy, both cluster energies form a particle-flow photon. This is justified by the observation that, in jets, the neutral component of the hadronic energy only deposits 3% of the total jet energy in the ECAL, compared to 25% of the jet energy from photons.

5.5.5 Jet Reconstruction

After the formation of photons, charged and neutral hadrons, and jets can be formed by clustering groups of these objects together based on their momentum weighted, spatial separation from one another. This clustering procedure is performed with the anti-k$_T$ algorithm [25]. The momentum weighted spatial separation function between two particles, i and j, is defined as:

$$d_{ij} = \min(\frac{1}{p_{iT}^2}, \frac{1}{p_{jT}^2})\frac{\Delta_{ij}^2}{\mathrm{R}^2} \tag{5.2}$$

where $\Delta_{ij}^2 = (y_i - y_j)^2 + (\phi_i - \phi_j)^2$ and $y_{i,j}$ is the rapidity, and ϕ is the azimuthal angle in the CMS detector. R is is the distance parameter, which is a user-defined quantity for the algorithm.

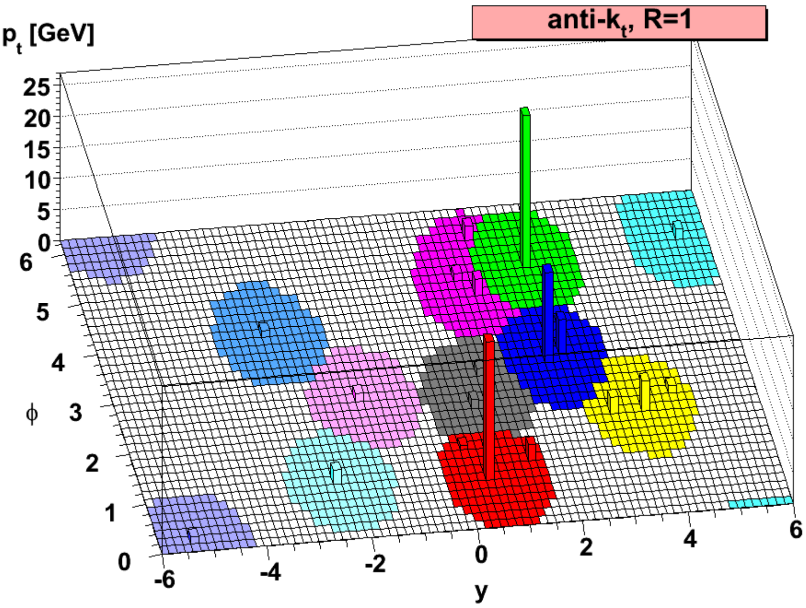

Figure 5.6: The anti-kt jet clustering algorithm with distance parameter R=1.0 [25]

The algorithm proceeds by looping over all of the particle-flow candidate objects that have been formed and calculates the quantity d_{ij}, and combines the two objects with smallest value, into a single object. The process is repeated until the smallest value, d_{ij} has a value $d_{ij} > \frac{1}{p_{Ti}^2}$ for all remaining pairs. The parameter, d_{ij}, will be larger for two small p_{T} objects, when compared to a pair of equally spatially separated high p_{T} objects. Thus, softer particles will cluster around harder objects before clustering amongst themselves. If no hard particles are present within the distance parameter, then the object will accumulate soft particles in a circle of radius R. The tendency is to produce circular jets, but in the case where a soft p_T cluster intersects with a hard p_T cluster, the $1/p_T^2$ weighting will tend to favor clustering around the harder p_T object. Figure 5.6 shows an example of the results of an anti-kt algorithm with distance parameter R = 1.0, in the azimuthal-rapidity coordinate system. An example of the preferential grouping around harder p_T objects can be seen at $\phi = 5, y = 2$.

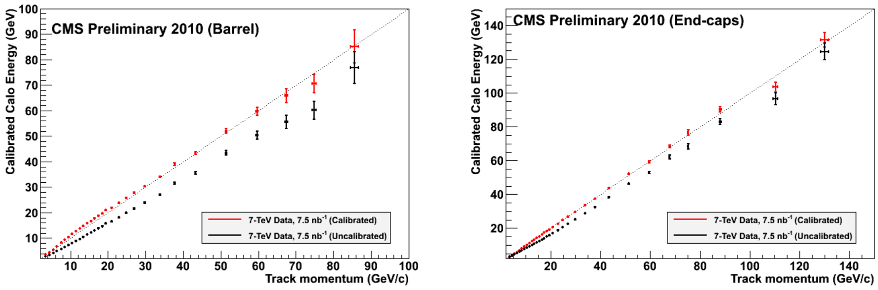

Figure 5.7: Commissioning of the particle-flow algorithm on jets, involved comparing the energy measured from charged hadron tracks, to energy measured in calorimeter clusters linked to the tracks [26].

In 2010, the particle-flow algorithm for jet reconstruction was commissioned with 7 TeV data [26]. The calibration procedure involved selecting charged hadrons from tracks in the pixel and silicon strip detector, and comparing the energy measured there to the energy measured in the calorimeter. After calibration, the measurements between tracker and calorimeter agree within error bars up to 100 GeV, as shown in figure 5.7.

Hadronic Tau Reconstruction

Tau leptons are unstable particles which decay via the weak interaction. If the resulting W boson decays hadronically to two quarks, the tau lepton can be reconstructed by analyzing the resulting jets that are clustered by the anti-kt algorithm. Tau jets are characterized by the number of charged hadrons produced in the decay. Since charge must be conserved, this results in one charged hadron being produced $\sim$ 85% of the time, known as a "one-pronged" decay, and three charged hadrons being produced $\sim$ 15% of the time, known as a "three-pronged" decay. Thus, a tau jet is identified as a jet with only 1 or 3 tracks associated with the calorimeter cluster. Additionally, the jets from hadronic tau decays tend to have their energy more collimated than jets produced from quarks or gluons. Jets are clustered twice, using two different distance-parameters. The ratio of energies of the smaller to the larger of the distance parameter jets is used to determine how collimated a jet is. If the ratio is within a given threshold, determined by the analyst in terms of the reconstruction efficiency and fake rate, the jet is tagged as a hadronic tau jet.

b-Tagging

Jet that originate from b-quarks have unique characteristics that allow them to be distinguished from jets originating from other quarks or gluons. This identification process is known as b tagging. Several algorithms exist to identify b jets, since there are many kinematic variables that distinguish them from other jets. Due to the heavier nature of the b quark, b jets have a larger transverse momentum compared to lighter-flavor quarks. Since it belongs to the third quark generation, it is much more likely to find a non-prompt lepton embedded in the jet. Muons are especially useful to tag b jets since the information they leave in the tracker can used to easily identify if it came from prompt decay or not.

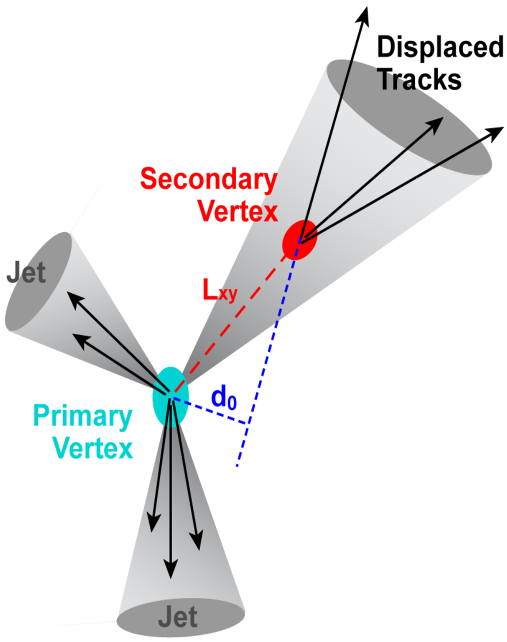

Figure 5.8: A b-meson will travel a distance L_{xy} before decaying and creating a secondary vertex. The impact parameter, d_0 measures the longitudinal displacement of the two vertices [27].

The most important characteristic of the b quark is its relatively long lifetime compared to light-flavor quarks. The consequence is that a B-hadron will travel a very small, but observable distance within the tracker before it decays, forming a secondary vertex. The distance and uncertainty measured on the distance between the primary and secondary vertex is then used as discriminating variables to tag b-jets. Figure 5.8 shows a cartoon of a b jet creating a secondary vertex after traveling some distance from the primary vertex.

5.5.6 Missing Transverse Energy Reconstruction

CMS has a hermetic design to ensure that all particles produced in a collision would pass through the detector. Only long-lived, neutral particles avoid detection, such as neutrinos in the standard model. Many BSM theories, such as SUSY, are also characterized by stable, neutral particles. These particles can only be detected by measuring a momentum imbalance after measuring all of the particles in the event.

The missing transverse energy (MET), $\not{E}_{\mathrm{T}}$, is the vector sum of all of particle-flow candidates reconstructed in the event. It is defined as

$$\not{E}_{\mathrm{T}} = | - \sum_{i=1}^{nPF} \vec{p_{Ti}}| \tag{5.3}$$

where nPF is the number of partice-flow candidates in the event, and $\vec{p_{Ti}}$ is the vector sum of their transverse momentum.

The particle-flow algorithm for reconstructing MET was commissioned in 2010 with 7 TeV data [26]. Minimum-bias collisions and QCD multi-jet production are processes that produce no real MET. Therefore, a sample of these events were collected, allowing for the algorithm to be tuned and calibrated.

Chapter 6

Analysis I: The first 5.08 fb^{-1} of 8 TeV data

The search for $t\bar{t}H$ production begins by identifying pp collisions consistent with the production of a top-quark pair with additional b jets. Top quarks decay $\sim 100\%$ of the time to a bottom quark and a W boson, and the W boson can decay either into a charged lepton and a neutrino or into a pair of quarks. Since there are two W bosons in the event, the decays of the W bosons determine the specific top-pair signatures recorded in the detector. The decay of the two W bosons define the categorizations of $t\bar{t}$-like events as either all-hadronic, in the case of zero charged leptons; semi-leptonic, in the case of one charged lepton; and di-leptonic in the case of two charged leptons. This analysis describes the Lepton+Jets (LJ) channel, where one of the W bosons has decayed to an electron or a muon and the corresponding neutrino, while the other W boson decays into two quarks. To compensate for the low production rate, the analysis is optimized to search for the Higgs boson decaying to a b-quark pair, since the branching ratio to b-quarks is highest for the mass range favored by the exclusion limits of LEP and the Tevatron, as well as preliminary results by CMS and ATLAS, for a Higgs boson mass of $\sim$ 125 GeV. The final state is then $l\nu qqbbbb$, where l refers to either an electron or a muon. In the case of an ideal reconstruction of the event, the LJ signal events contains six jets, four of which are b-tagged. However, to accommodate jets lost to detector acceptance and merging between separate partons, and the b-tagging efficiency, events with four or more jets and two or more b tags are included in the signal region.

The largest background contribution is $t\bar{t}$+jets production. This process can be decomposed in terms of the flavor of the extra jets produced in the event. For this analysis, the inclusive $t\bar{t}$+jets process is broken into three sub-processes: $t\bar{t}+$ light flavor jets where one or more of

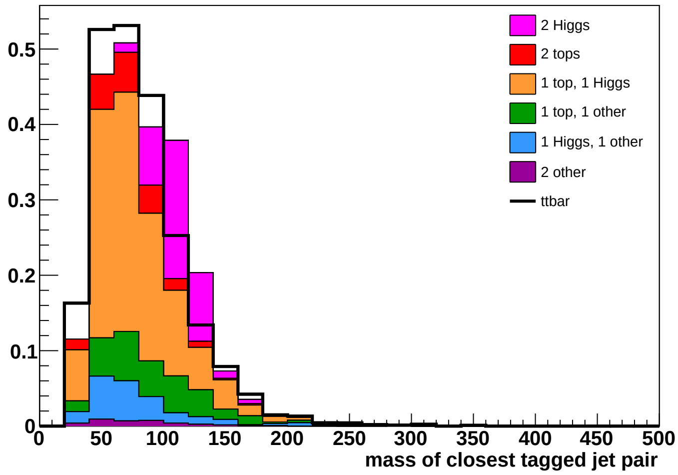

Figure 6.1: This figure shows the breakdown of jet-to-parton assignments for the two jets with the minimum ΔR separation in the event for events with greater or equal 4 b-tagged jets.

the jets is mistagged, $t\bar{t}+c\bar{c}$ and $t\bar{t}+b\bar{b}$. Smaller background contributions come from W+jets, Z+jets, single top quark, diboson, and $t\bar{t}+W/Z$ production.

In other Higgs searches involving the decay to two b-quarks, the most powerful discriminating variable is the invariant mass of the $b\bar{b}$ pair, which has a peak at the mass of the Higgs. However, for $t\bar{t}H$ production, with a final state of four b-quarks, the combinatorics of selecting the quarks coming from the Higgs, instead of the $t\bar{t}$ system, prevents the reconstruction of a clear resonant peak, as shown in figure 6.1. This results in an additional loss of mass resolution, or smearing, on the $b\bar{b}$ invariant mass spectrum.

Although there is poor resolution on the Higgs boson resonance in the b-quark dijet mass spectrum, there are a number of kinematic variables that can be used to discriminate between the $t\bar{t}$+jets background and the $t\bar{t}H$ signal. For example, the recoil of the Higgs off of the $t\bar{t}$ system, the decay products of the top quarks from the $t\bar{t}H$ signal will have, on average, a slightly larger component of momentum transverse to the beam-line. Additionally, the larger number of authentic b-jets in $t\bar{t}H$ events can be exploited through the likelihood value returned by a b-tagging algorithm for all of the jets in the event. By themselves, none of these variables provide a large degree of discriminating power to separate the $t\bar{t}H$ signal from the large, and kinematically-similar background. Therefore, the discriminating power of several variables is combined using a multivariate analysis technique (MVA), which is used to set upper limits on $t\bar{t}H$ production in the data set.

The following sections will describe the analysis that was carried out on the first 5 fb^{-1} of data collected by the CMS detector at 8 TeV. This includes definitions of the simulated samples used to estimate the expected backgrounds in data, the event selection used to isolate the $t\bar{t}H$

signal, the application of MVA techniques, evaluation of systematic uncertainties, and upper limit setting on the production rate of $t\bar{t}H$.

6.1 Data and Simulated Samples

pp collision data is collected by the CMS detector, as described in previous chapters. The signal and background signatures are estimated using Monte Carlo simulation techniques. The simulation involves the combination of the most current theoretical and empirical information about the interactions of the known particles. The simulation of an event is decomposed into a sequence of calculations and each signal and background process is calculated separately. Information about Monte Carlo event simulation techniques is taken from reference [147].

The first stage of event simulation for a given signal or background process is to calculate the probability that some set of initial state particles with a certain momentum will create a final state of particles with a certain momentum. For example, in the case of the $t\bar{t}H$ signal, this is the probability that two protons traveling towards each other along the z-axis (beam-line), each with a given energy and momentum, will produce a top-quark pair and a Higgs boson, each with some momentum vector, $\hat{p}_t$, $\hat{p}_{\bar{t}}$, $\hat{p}_H$, which points into the hermetic CMS detector. As discussed in section 2.1, this probability is calculated by examining the Lagrangian of the theory describing the process and calculating its scattering amplitude, to some order in perturbation theory, using the Feynman rules derived from the Lagrangian. The scattering amplitude is a multi-dimensional probability function, which depends on the initial- and final-state momenta of the particles in the process. Thus, given some initial state momentum, p_i, it tells you the probability to produce a final state particle with momentum p_f. It is understandable that the scattering amplitude is often referred to as a matrix element, since given a vector of initial state particles with a certain momentum, the scattering amplitude would be a matrix, whose elements would give the probability of creating the vector of final state particles.

Since protons are composite objects, when they collide, it is their quarks or gluons which are actually interacting. The momentum distribution of each of the valence quarks, the gluons, and the sea quarks, which account for quantum fluctuations that temporarily create all other quark flavors inside the proton, is described by a Parton Distribution Function (PDF). The PDF describes what fraction of the proton's momentum is distributed among each of its constituents. Due to the large strength of the QCD interactions that bind the quarks together, the PDF cannot be calculated perturbatively from QCD. It has been measured empirically, and is a composition of the results of several experiments over the past decades.

Event generator algorithms are computer programs that, given a Lagrangian of particle theory, will calculate the matrix element for a given process. Then, the generator is provided with values of the momenta of the initial state particles. For protons, this would the beam energy of the LHC. To assign momentum values to the constituent quarks or gluons that actually participate in the interaction, random values are sampled from the probability distributions described by a PDF that is provided to the algorithm. Given a choice of momentum for the input particles, a value and direction of the momentum for each of the final state particles is sampled from the probability function provided by the calculated the matrix element (ME). The process of randomly sampling a probability function, in order to conduct a calculation, is known as a Monte Carlo sampling technique.

In the case where final-state particles are quarks or gluons, also known as partons, an additional calculation is necessary to create the physical hadron states. First, the decay sequence of each parton is calculated until the decay products reach a user-defined value, known as the hadronization scale. This decay sequence is referred to as the parton shower (PS), since each parton creates a multitude, or a shower, of additional partons. Once the parton shower is calculated, each of the colored partons are transformed into color-singlet primary hadrons, which themselves decay, and form secondary hadrons. This process, known as hadronization, results in a collimated spray of hadrons, each with a component of momentum along the original parton's direction. These hadrons are clustered together and referred to as a hadron jet.

Once the hadronization is completed, the next stage of the event generation is to simulate the response of the CMS detector when this process occurs at the interaction point where the LHC beams are made to collide. The Geant 4 detector simulation framework is used to create a model of each and every detector element, electronic readout, and mechanical support structures that compose CMS [148]. Geant 4 also describes how energy is deposited into the different types of material as a particle passes through each detector element, simulating the response of each element to the presence of a particle in the detector. The digitization and signal acquisition of the electronics that read-out the detector elements is also simulated.

The final stage the generation of an event is the reconstruction of the simulated detector signals into physics objects. This process is described in detail in the previous chapter. It proceeds with simulated, instead of real, detector signals.

The entire event simulation, reconstruction, and subsequent analysis is implemented in a software framework that is known as CMS Software (CMSSW).

6.1.1 Data Samples

The results presented here are based on the first $5.08\,\mathrm{fb}^{-1}$ of the 2012 CMS dataset. Data-sets are collected through HLT triggers and stored offline for analysis. Table 7.1 lists the datasets used for this analysis, which is composed of two runs of data collection triggered on the presence of one muon or electron in an event. The luminosities are quoted from a calculation performed with minimum-bias events measured with the HF detector and have been determined to have a 2.2% uncertainty.

Dataset	Run Range	Integrated Luminosity
SingleMu, Run2012A, PromptReco	190645–193621	0.87 fb^{-1}
SingleMu, Run2012B, PromptReco	193834–196531	4.21 fb^{-1}
Total SingleMu	**190645–196531**	**5.08 fb^{-1}**
SingleElectron, Run2012A, PromptReco	190645–193621	0.87 pb^{-1}
SingleElectron, Run2012B, PromptReco	193834–196531	4.21 pb^{-1}
Total SingleElectron	**190645–196531**	**5.08 fb^{-1}**

Table 6.1: The datasets analyzed for this analysis.

6.1.2 Signal Samples

The $t\bar{t}H$ signal is modeled using the leading order Pythia Monte Carlo generator. Signal events were generated privately using the same conditions and configuration as the "Summer" MC campaign, which generated the background samples used in this analysis and is a central effort by a dedicated team of collaborators within the CMS experiment. The samples and associated cross sections used are listed in Table 7.2.

Mass	Dataset	Cross Sect.
110 GeV/c^2	TTH, Inclusive Decays, $M_H = 110$, Pythia6	0.1887 pb
115 GeV/c^2	TTH, Inclusive Decays, $M_H = 115$, Pythia6	0.1663 pb
120 GeV/c^2	TTH, Inclusive Decays, $M_H = 120$, Pythia 6	0.1470 pb
122.5 GeV/c^2	TTH, Inclusive Decays, $M_H = 122.5$, Pythia 6	0.1383 pb
125 GeV/c^2	TTH, Inclusive Decays, $M_H = 125$, Pythia 6	0.1302 pb
127.5 GeV/c^2	TTH, Inclusive Decays, $M_H = 127.5$, Pythia 6	0.1227 pb
130 GeV/c^2	TTH, Inclusive Decays, $M_H = 130$, Pythia 6	0.1157 pb
135 GeV/c^2	TTH, Inclusive Decays, $M_H = 135$, Pythia 6	0.1031 pb
140 GeV/c^2	TTH, Inclusive Decays, $M_H = 140$, Pythia 6	0.09207 pb

Table 6.2: List of signal MC datasets and cross sections used to determine the SM expectation.

6.1.3 Background Samples

In order to estimate the rate and kinematic behavior of the backgrounds, this analysis primarily uses Monte Carlo (MC) samples from the "Summer12" MC campaign, based on leading order event generators. Most of the samples are generated either with the Madgraph tree-level matrix element generator matched to Pythia for the parton shower, or with the NLO generator Powheg combined with Pythia. These samples are reconstructed with the same CMSSW version as the data samples listed above. Table 7.3 lists the background MC samples and associated cross sections.

Sample	Dataset	Cross Sect.
$t\bar{t}$+jets	TTJets, Madgraph	225.197 pb
$t\bar{t}+W$	TTWJets, Madgraph	0.249 pb
$t\bar{t}+Z$	TTZJets, Madgraph	0.208 pb
W+jets	WJets to Leptons, Madgraph	36257.2 pb
$Z/\gamma^{*}+$ jets		
$M_{\ell\ell}$ >50 GeV/c^2	DYJets to Leptons $M_{\ell\ell}$ >50, Madgraph	3503.17 pb
10 GeV/c^2 $< M_{\ell\ell}$ <50 GeV/c^2	DYJets to Leptons 10 $< M_{\ell\ell} <$ 50, Madgraph	860 pb
Single t		
s-channel	T, schannel, Powheg	3.79 pb
t-channel	T, tchannel, Powheg	56.4 pb
tW	T, tWchannel, Powheg	11.1 pb
Single $\bar{t}$		
$s$channel	$\bar{T}$, schannel, Powheg	1.76 pb
$t$channel	$\bar{T}$, tchannel, Powheg	30.7 pb
tW	$\bar{T}$, tWchannel, Powheg	11.1 pb
WW	WW, Pythia6	54.8 pb
WZ	WZ, Pythia6	32.3 pb
ZZ	ZZ, Pythia6	7.7 pb

Table 6.3: List of background MC datasets and cross sections used for normalization.

6.1.4 MC pileup reweighting

During 2012 data collection, the LHC provided increasingly large instantaneous luminosities to the CMS experiment. Consequently, the average number of overlapping events reconstructed in single detector readout window also increased. When these overlapping events, known as pileup events, occur within the same bunch crossing, this is referred to as "in-time" pileup. Alternatively, "out-of-time" pileup, comes from energy deposits in the detector from previous bunch crossings and from very early arrivals of particles from the forthcoming bunch crossing. Pileup events can affect many aspects of the reconstruction of a more interesting event, such as the degradation of lepton isolation and jet energy resolution. The simulated samples used in the analysis must also have the same distribution of pileup events as what was measured in the data.

During the generation of the simulated samples used in the analysis, the average amount of expected pileup was unknown. Events were thus simulated with a conservatively large estimate of the pileup distribution, so that if the measured data revealed a smaller average value, the simulation could be reweighted to match the data. For the simulation, the number of interactions is a user-defined value added to every generated event. For the data, the number of pileup interactions for each unit of time depends on the instantaneous luminosity for each bunch pair and the total inelastic cross section, $\sigma_{inelastic}$, of the proton. The value of $\sigma_{inelastic} = 69.4$ mb was found to describe the data well. To estimate the effect of the systematic uncertainty of this choice, the value was varied by $\pm 7\%$.

To gauge the accuracy of the calibration of the pileup distribution used in the simulated samples, a comparison of the number of reconstructed vertices between data and the simulated $t\bar{t}$ MC sample is shown in figure 7.1. The unweighted MC distribution is shown in blue, the reweighted distribution in red, and the measured data in black points. After reweighting, there is a good level of agreement between the data and MC distributions.

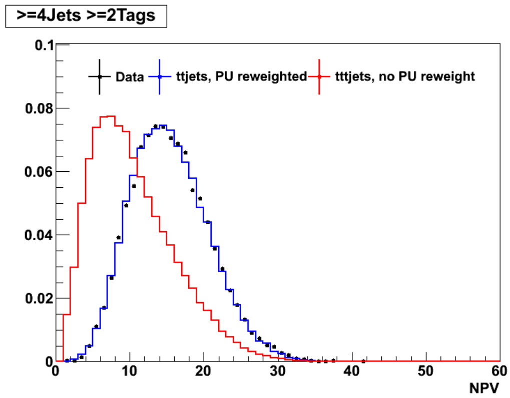

Figure 6.2: Comparison of number of reconstructed vertices for data (black) and the $t\bar{t}$ MC sample before (blue) and after (red) pileup reweighting. After pileup reweighting, the MC matches the data well.

6.1.5 Additional Pileup Corrections

Studies comparing the Monte Carlo simulations to observed data revealed that the jet p_T spectra was not well modeled. Many sources of this discrepancy were investigated, but the clearest correlations arises when the 8 TeV data events are divided into three categories according to their amount of pileup:

- Low PU, number of primary vertices ≤ 10
- Medium PU, number of primary vertices from 11 to 15
- High PU, number of primary vertices ≥ 16

The modeling of jet p_T was worse for events with a larger number of pileup events overlapping in the detector. The same effect was present for the majority of the jets in the event, evidenced by the discrepancy in the H_T distribution, shown in figure 6.3, where H_T is defined as the scalar sum of the transverse momentum for reconstructed jets in the event:

$$H_T = \sum_i^{jets} p_T^i \tag{6.1}$$

The effect makes the data have a softer p_T spectrum than the simulations. The same effect was observed in 7 TeV data as well. It was present even after employing several sophisticated reconstruction techniques designed to mitigate pileup effects. These techniques included the removal of charged hadrons in the particle-flow algorithm, not associated with the primary vertex and re-weighting the simulated samples to match the pileup distribution measured in the data.

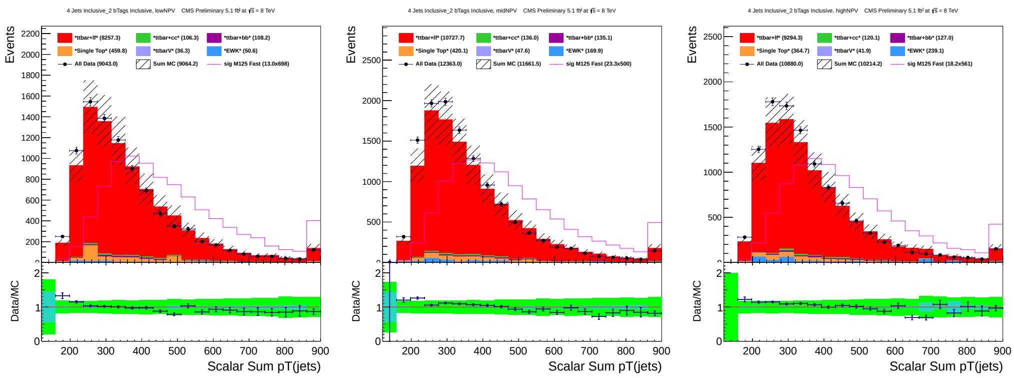

Figure 6.3: H_T distribution for 8 TeV lepton plus jet events with ≥ 4 jets and ≥ 2 tags shown for different amounts of pileup. The left-hand plot shows low pileup, the middle plot shows medium pileup, and the right-hand plot shows high pileup.

Although the exact underlying cause of the jet mis-modeling effect was not able to be identified, the magnitude of the effect seemed to be related to the number of pileup events. As such, an additional correction factor is needed to account for the remaining difference in pileup effects between data and Monte Carlo. The correction factor was calculated from data that was dominated by background events, with a single lepton, ≥ 4 jets, and ≥ 2 tags. The expected signal-to-background ratio in this sample is 0.002, which is low enough that the correction factor will not be biased by signal events. The correction factor is based on the H_T distribution for data and Monte Carlo for Low pileup (PU), Medium PU, and High PU events. The correction factor is the bin-by-bin ratio of the data and the Monte Carlo H_T distributions in each PU category. By preparing a separate correction factor for each PU category smaller adjustments were made to well-modeled Low PU events and larger adjustments to the poorly modeled High PU events. H_T shows the same mis-modeling as each of the jet p_Ts and it effects all of the jet p_Ts. This makes it a natural choice for a correction factor.

In order to evaluate the systematic shape uncertainty introduced by the correction factor, the uncorrected simulated distributions are used as -1σ systematic uncertainty and the $+1\sigma$ uncertainty is determined by doubling the correction factor. The factor of two for the $+1\sigma$ variation is motivated by the desire to provide a large enough systematic uncertainty to cover any possible over-correction of the simulations. This is a reasonable choice because it creates a deviation that is the same size as the original observed difference between data and simulations.

The correction factor and uncertainty improved the agreement between data and Monte Carlo. Figure 6.4 compares the H_T distributions before and after reweighting. The data-to-MC ratio plots are the clearest indicators of the improvement from the correction factor. Before the correction, the H_T ratio plot forms a line with a slope. After the correction the slope is gone.

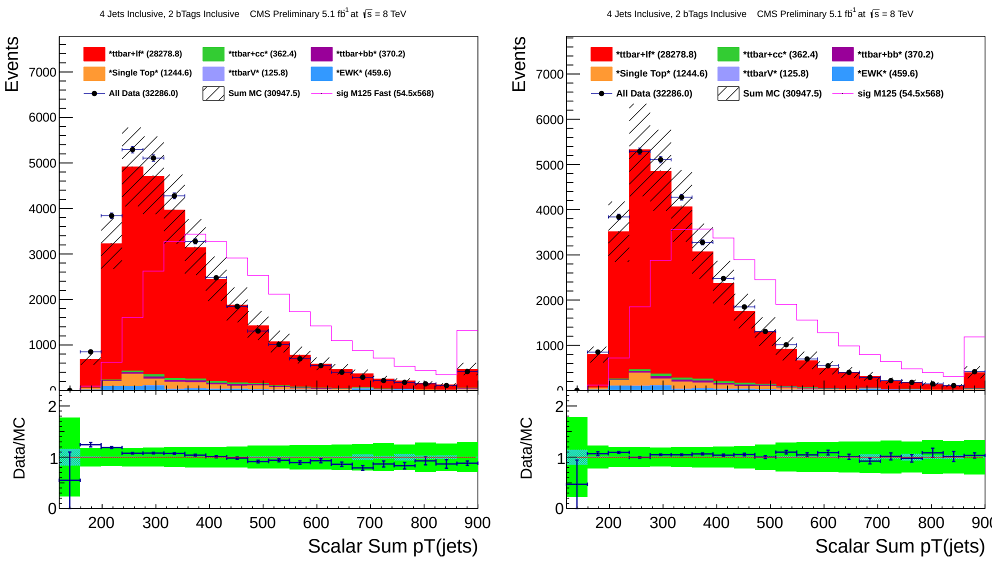

Figure 6.4: H_T distribution for 8 TeV lepton plus jet events with ≥ 4 jets and ≥ 2 tags. The left-hand plot shows the distribution before correction. The right-hand plot shows the distribution after correction. Note that the ratio in the right-hand plot is flatter than the left-hand plot.

6.2 Event Selection

This section defines the common physics objects and event selection requirements. Leptons are classified into two categories, tight and loose, defined for muons in section 6.2.3 and for electrons in 6.2.4. For this analysis, exactly one tight muon or exactly one tight electron is required and events with any additional loose leptons are rejected.

6.2.1 Event cleaning

For data and MC events, certain cuts are applied to remove events that are either non-physical or that come from non-collision events, such as instrumental noise or beam backgrounds. In the data, every event is required to pass the following filters:

- CSC tight beam halo filter - Secondary particles are produced in showers which are initiated by collisions of the beam with residual gas inside the LHC vacuum chamber or by interactions of the particles with a large transverse emmitance with limiting apertures.

- HBHE noise filter with isolated noise rejection - this filters spurious signals from the HCAL barrel and endcap sub-detectors which are not associated with particles measured in a collision event.

- HCAL laser filter - ensures that data is not taken simultaneously with the laser calibration system
- ECAL dead cell trigger primitive (TP) filter - removes dead or noisy ECAL cells from being used in the reconstruction, these compose $< 1\%$ of the total crystals in the ECAL
- Tracking failure - designed to catch events with too-few tracks
- Noisy SCs in EE - new filter from the ECAL Detector Performance Group (PDG), and validated by the MET Physics Object Group (POG)

which are described in [149].

Additionally, beam-scraping events are filtered based on the fraction of good tracks. At least 25% of tracks are required to be of high purity. Finally, every data event must contain at least one primary vertex (PV) that passes the following selection:

- The number of degrees of freedom used to find the PV must be larger than 4,
- The absolute value of the z-coordinate of the PV must be smaller than 24 cm,
- The absolute value of the ρ-coordinate of the PV must be smaller than 2 cm,
- The PV must not be identified as fake.

6.2.2 Trigger

Each data and MC event is required to pass passes one of the triggers in Table 6.4, which are a subset of the total number of SingleMu and SingleEle HLT triggers available. Muon+jet events must pass the SingleMu trigger, while electron+jet events must pass the SingleEle trigger.

Dataset	Trigger Name
SingleMu	HLT_IsoMu24_eta2p1_v*
SingleEle	HLT_Ele27_WP80_v*

Table 6.4: List of lepton+jets triggers

6.2.3 Muon Selection

In this analysis, muons are selected from the set of "particle-flow' muon" objects that have been reconstructed in the event. Muons are classified into two categories: tight and loose, according to the quality of their reconstruction. This is ensured by applying the selection cuts shown in Table 6.5. The cuts are defined as follows:

- p_T - the component of the momentum transverse to the beam-line.

- PFRelIso - this is the quantity known as relative isolation, computed by the particle flow algorithm. It is a ratio of the energy deposits remaining in the calorimeter and tracker, after the contribution from the muon has been removed, in a cone size ΔR = 0.3, around the muon track.
- $|\eta|$ - the absolute value of the psuedorapdity of the muon
- ID - This refers to whether the muon was reconstructed with a χ^2 fit to the tracks from the tracker only (tracker muon), the tracker and the muon chambers (global muon), or if the particle was reconstructed from the particle-flow algorithm (PFmuon)
- N_{layers}(tracker) - the number of layers in the tracker with hits used in the muon track reconstruction
- X^2 of track fit - the reduced χ^2 (raw χ^2/Number of Degrees of Freedom in the fit), typically a value of 1 indicates the fit describes the data well
- N_{layers}(pixel) - the number of hit-containing layers in the inner pixel detector used in the muon track reconstruction
- $N_{segments}(\mu)$ - the number of segments in the muon chambers used to the reconstruct the muon tracks
- $|d_0(\text{BS})|$ - the absolute value of the transverse distance of the extrapolated muon track to the primary vertex, as calculated from the beam spot (BS)
- $|d_Z(\text{BS})|$ - the absolute value of the longitudinal distance of the extrapolated muon track to the primary vertex

Cuts	Tight μ	Loose μ
p_T	>30 GeV/c	>10 GeV/c
PFRelIso(0.4)	0.12	<0.2
$\|\eta\|$	<2.1	<2.5
ID	Global Muon	Global Muon or Tracker Muon
ID	PFMuon	PFmuon
N_{layers}(tracker)	>5	
X^2 of track fit	<10	
N_{layers}(pixel)	>0	
$N_{segments}(\mu)$	>1	
$\|d0(\text{BS})\|$	<0.2 cm	
$\|dZ(\text{BS})\|$	<0.5 cm	

Table 6.5: Tight and loose muon definition

6.2.4 Electron Selection

Electrons are selected from the set of "particle-flow electron" objects reconstructed in the event. Similarly to muons, electrons are classified into two categories: tight and loose, according to the quality of their reconstruction. The selection cuts are shown in the Table 6.6. The definitions are identical to the ones provided in section 6.2.3. Additional variables not described are:

- E_T - the transverse energy of the electron, which due to its relatively light mass, is approximately equal to its p_T
- ID - electron ID is passed on a multivariate analysis (MVA) technique, which provides a discriminant value to separate fake from real electrons, and is trained with events that are required to pass a HLT trigger (mvaTrigV0), or not (mvaNonTrigV0). The "passConversionVeto" ID ensures that the electron has not been reconstructed from a photon which has converted to an electron positron pair

Cuts	Tight e	Loose e
E_T	>30 GeV/c^2	>15 GeV/c^2
PFRelIso(0.3)	<0.1	<0.2
$\|\eta\|$	<2.5	<2.5
ID	MVA ID("mvaTrigV0") >0.0	MVA ID("mvaNonTrigV0") >0.0
ID	passConversionVeto	passConversionVeto
$\|d0(BS)\|$	<0.02 cm	
$\|dZ(PV)\|$	<1 cm	

Table 6.6: Tight and loose muon definition

6.2.5 Lepton selection and trigger efficiencies

The cumulative reconstruction efficiency of ID+isolation+trigger has been calculated from data, as a function of p_T and η, as shown in figure 6.5 for electrons and muons. In order to reproduce the same the same response in the simulations as found in data, an event-by-event scale factor is applied to correct for this difference in efficiency.

The efficiency in data was measured by selecting events with two tight muons, or two tight electrons with an invariant mass in a range between 70 and 130 GeV. This is centered on the Z-boson resonance, and ensures that the selected leptons are authentic. The two leptons are additionally required to have opposite charge, which is measured by the direction of the curvature of their tracks in the magnetic field. A "tag" lepton is selected if has $p_T > 30$ GeV, and passes the appropriate muon or electron trigger. The second lepton, the "probe" lepton, since selected as a pair coming from a Z boson, should be identical to the tag lepton, and thus should be identically reconstructed. The efficiency is then the ratio of the number events where both tag and probe leptons pass the p_T and trigger requirements over the number of events where only the tag lepton passes the p_T and trigger requirements. This study is repeated in bins of p_T and η to remove any kinematic dependence on lepton efficiency.

The combined ID, isolation, and trigger scale factor uncertainty is evaluated by looking at the variation of the scale factor as a function of parameters besides p_T and η, such as pileup and

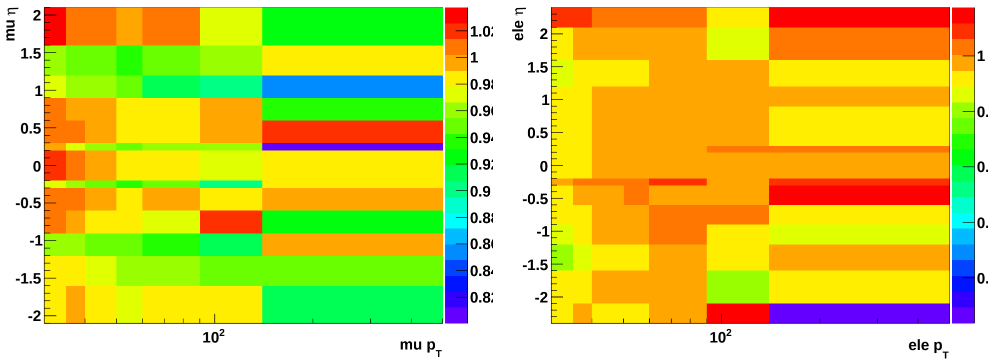

Figure 6.5: Muon and electron ID, isolation selection and trigger efficiency scale factors in bins of p_T and η.

b-tag scale factor reweighting (described below). A flat uncertainty of 4% covers the variations that are observed, and is thus adopted as a conservative estimate of the uncertainty on the combined lepton reconstruction efficiency.

6.2.6 Jet selection

As described in the previous chapter, jets are reconstructed with the anti-kt clustering algorithm [25], with a distance parameter of of 0.5, starting from the set of objects reconstructed by the particle flow algorithm [24]. Non-isolated leptons, not associated with the decay of a W boson, are allowed to be clustered into the jets. The selection cuts defining our jets can be found in Table 6.7. The cuts use the following variables to ensure the reconstruction of authentic hadronic jets:

- p_T - component of the momentum transverse to the beam-line
- η - the psuedorapidity of the reconstructed jet
- CEF - Charged Electromagnetic Fraction: the ratio of charged particles to the total number of particles in the jet
- NHF - Neutral Hadron Fraction: the ratio of neutral particles to the total number of particles in the jet
- NEF - Neutral Electromagnetic Fraction: the ratio of photons to the total number of particles in the jet
- CHF - Charged Hadron Fraction: the ratio of charged hadrons to the total number of particles in the jet
- NCH - Number of Charged Hadrons: raw charged hadron multiplicity

- $N_{constituents}$ - Number of constituents, which can be charged and neutral hadrons, as well as non-prompt photons and leptons.

Cuts	Jet
p_T	>30 GeV/c
$\|\eta\|$	<2.4
CEF, NHF, NEF	<0.99
CHF, NCH	>0
$N_{constituents}$	>1

Table 6.7: Jet definition

Additional correction factors are required such that the measured energy of the jet correctly reproduces the energy of the initial parton. This is done in four stages. The L1 Charged Hadron Subtraction (CHS) correction, is implemented in the particle-flow algorithm, and involves subtracting the energy contributions from charged hadrons that are not associated with the jet from the energy cluster. The next stage, L2 correction is a relative correction to make the measured jet response flat in η. The third stage, L3, is an absolute correction to the measured p_T of a jet in order to match the simulated jet p_T created using generator-level input and a similar jet-clustering algorithm. The L2 and L3 corrections are calculated using Monte Carlo, and thus an fourth correction factor, the L2L3 residual correction is applied that fixes the discrepancies between Monte Carlo and data. The correction factors are described in reference [150], and are derived from 2011 7 TeV data, with a selection of dijet events near the Z-boson mass peak. A "tag-and-probe" procedure similar to the lepton scale factors is applied to jets to determine the kinematic dependence (p_T and η) of the detector in both simulations and data. Additionally, a scale factor is needed to adjust for the difference in jet energy resolution as measured in data and predicted in simulation. Table 6.8 gives the scale factors, and uncertainties, as derived from dijet events [150] as a function of η only, since no significant p_T dependence was observed.

6.2.7 b-tagging selection

The algorithm used to perform b-tagging in this analysis is the combined secondary vertex (CSV) algorithm [151]. It relies on the superior ability of the inner tracker to reconstruct secondary

$\|\eta\|$	Data/MC Ratio
	(factor +-stat. +syst.- syst.)
0.00.5	1.052±0.012+0.062-0.061
0.51.1	1.057±0.012+0.056-0.055
1.11.7	1.096±0.017+0.063-0.062
1.72.3	1.134±0.035+0.087-0.085
2.35.0	1.288±0.127+0.155-0.153

Table 6.8: Jet Energy Resolution (JER) scale factors

vertices, which are the characteristic signature of B-hadron decays. Tracks are selected if they meet the following requirements:

- At least 8 hits in the pixel and silicon tracker, with at least 2 hits in the pixel detector
- tracks must have p_T >1 GeV
- χ^2/NDF of the fitted track < 10
- $|d0|$ - transverse impact parameter $<$ 2mm, since b-quarks will on average travel 0.45 mm in the detector before decaying

Additionally, the following cuts are required:

- The transverse distance between the primary and secondary vertices, L_T, is between 100 μm and 2.5 cm
- The ratio of L_T and the uncertainty on it's measurement, L_T/σ_{L_T} >3
- The invariant mass formed by adding the four-vectors of all the tracks forming the secondary vertex $<$ 6.5 GeV
- The invariant mass falls outside a window near 50 MeV, corresponding to the K^0_S resonance

Secondary vertices are decomposed into three categories. If a secondary vertex is found meeting the above criteria, it is a "reco vertex". If no secondary vertex is found meeting all the above criteria, the event can be classified as a "pseudo vertex" if more than two tracks have a signed transverse impact parameter significance, relative to the primary vertex, greater than 2. "No vertex" is found if neither of the prior two classification criteria can be met.

For each of the vertex categories, a set of variables is used to create a single discriminating variable, using a likelihood ratio technique. The following input variables are used:

- The invariant mass of the charged particles associated with the secondary vertex
- The multiplicity of charged tracks associated with the primary vertex
- The distance between the primary and secondary vertex in the transverse plane, divided by its error (only used in reco vertex category)
- The pseudorapidities of the charged particle tracks associated with the secondary vertices
- The track impact parameter significance of the highest p_T track with invariant mass larger than the charm quark threshold, 1.5 GeV.

The likelihood function is split to separate between the charm and light-flavor backgrounds and is defined as:

$$\mathcal{L}^{b,c,q} = f^{b,c,q}(\alpha) \times \prod_i f_\alpha^{b,c,q}(x_i) \quad (6.2)$$

where α = 1,2,3, denotes the different vertex categories, x_i are the individual variables, q stands for the light flavor quarks, while b and c stand for the bottom and charm quarks respectively. $f^{b,c,q}(\alpha)$ is the probability for a quark flavor b, c, or q, to fall into category α. $f_\alpha^{b,c,q}(x_i)$ is the probability density function of the variable x_i in category α for quark flavor b, c, or q. The combined discriminant is defined as

$$d = f_{BG}(c) \times \frac{\mathcal{L}^b}{\mathcal{L}^c + \mathcal{L}^b} + f_{BG}(q) \times \frac{\mathcal{L}^b}{\mathcal{L}^q + \mathcal{L}^b} \quad (6.3)$$

where $f_{BG}(c)$, and $f_{BG}(q)$ are the a-priori probabilities for the content of charm and light flavor quarks in non-b jets.

A jet is considered b-tagged if the CSV discriminant is greater than 0.679, which is the medium working point defined by the BTag Physics Object Group (POG) [152], defined in order to produce a light-flavor mistag rate at $\sim 1\%$, with the reconstruction efficiency for real b jets at $\sim 70\%$.

Additionally, it is necessary to account for differences in the measured efficiency for b-tagging jets between data and simulation [153]. An event weight scale factor is used to correct the MC b-tagging efficiency ($SF_{tag} = \epsilon_{tag}^{data}/\epsilon_{tag}^{MC}$). The scale factor is measured for three different cuts, or working points, on the CSV discriminant value, and it is binned in terms of the p_T and η and flavor of the jet.

In addition to providing jet flavor identification for event classification, the discriminant value of the algorithm will be used to separate between $t\bar{t}H$ signal and $t\bar{t}+jets$ background. Therefore, a correction value for the efficiency difference between data and MC over the whole range of discriminator values is needed, not just for three working points. This procedure was developed in the context of the search for the standard model Higgs boson produced in association with a W or Z boson, with the Higgs decaying to bottom quarks [154].

For each of the three operating points and for each of the data/MC SFs, an equivalent cut on the CSV value is determined, CSV_{equiv}, such that

$$\epsilon_{CSV>CSV_{\mathrm{orig}}}^{data} = SF_{CSV>CSV_{\mathrm{orig}}} \cdot \epsilon_{CSV>CSV_{\mathrm{orig}}}^{MC} = \epsilon_{CSV>CSV_{\mathrm{equiv}}}^{MC} \quad (6.4)$$

where the SFs are measured in data and the MC efficiency measurements are calculated for each sample.

In order to correct or "reshape" the CSV discriminator output values, a function is applied to the MC to produces a corrected CSV value: $CSV_{\text{corr}} = f(CSV_{\text{orig}})$. Given that there are three b-tag efficiency measurements, there are three pairs of $(CSV_{\text{orig}}, CSV_{\text{equiv}})$. The reshaping function must satisfy $f(CSV_{\text{equiv}}) = CSV_{\text{orig}}$ for each of the operating points and for the upper and lower values of the CSV discriminant to make sure those values do not change (e.g., $CSV = 0.0$ and $CSV = 1.0$). The whole range of CSV discriminant values is found by linearly interpolating between these five points (the three working points, and upper and lower limit of the discriminate range).

6.2.8 Lepton + Jets Selection

The final Lepton+Jets (LJ) selection is carried out by requiring that events have exactly one tight lepton (e or μ), and at least four jets. Events with any additional loose or tight leptons are vetoed so this analysis can later be combined with a diLepton final state, without double counting events. Additionally, each event must have at least three jets with $p_T > 40$ GeV/c.

Events are further categorized by the reconstructed jet, and b-tagged jet multiplicities as follows:

- ≥6 jets, ==2 b-tags: At least 6 jets, 2 of which are b-tagged
- ==4 jets, ==3 b-tags: Exactly 4 jets, 3 of which are b-tagged
- ==5 jets, ==3 b-tags: Exactly 5 jets, 3 of which are b-tagged
- ≥6 jets, ==3 b-tags: At least 6 jets, 3 of which are b-tagged
- ==4 jets, ==4 b-tags: Exactly 4 jets, 4 of which are b-tagged
- ==5 jets, ==4 b-tags: Exactly 5 jets, 4 of which are b-tagged
- ≥6 jets, ≥4 b-tags: At least 6 jets, with at least 4 of which are b-tagged

Events with either 4 or 5 jets, where 2 of the those jets are b-tagged, make up two categories, which are used only as a control region to validate comparisons between collected data and simulations. The number of $t\bar{t}H$ events increases with the number of jets and tags because the largest branching fraction is H to $b\bar{b}$. Data to Monte Carlo comparisons of the jet and b-tag multiplicities are shown in figure 6.6. The event yields for the μ+jets and e+jets channels are shown in tables 6.11 and 6.10 respectively.

Table 6.9: Expected event yields in 5 fb^{-1} for signal and backgrounds in the μ+jets channel.

	≥6 jets 2 tags	4 jets 3 tags	5 jets 3 tags	≥6 jets 3 tags	4 jets 4 tags	5 jets ≥4 tags	≥6 jets ≥4 tags
$t\bar{t}H(125)$	6.1 ± 1.1	2.1 ± 1.9	3.2 ± 2.7	3.6 ± 3.3	0.3 ± 0.3	0.8 ± 0.9	1.3 ± 1.4
$t\bar{t}$+lf	1750 ± 480	680 ± 150	460 ± 110	270 ± 84	9.5 ± 3.2	13.0 ± 4.2	20.6 ± 7.8
$t\bar{t}+b\bar{b}$	34 ± 19	21 ± 12	24 ± 14	17.3 ± 10.0	1.5 ± 1.1	5.1 ± 3.2	8.6 ± 5.6
$t\bar{t}+c\bar{c}$	29.5 ± 8.7	10.0 ± 2.9	13.2 ± 3.9	11.1 ± 3.5	0.2 ± 0.2	0.2 ± 0.1	1.1 ± 0.8
$t\bar{t}V$	18.7 ± 3.9	2.3 ± 0.6	3.3 ± 0.8	4.1 ± 1.1	0.1 ± 0.0	0.4 ± 0.2	0.8 ± 0.2
Single t	42.6 ± 9.8	25.8 ± 6.0	14.3 ± 3.8	4.3 ± 1.3	0.2 ± 0.3	1.6 ± 1.8	0.7 ± 0.5
V+jets	39 ± 32	1.0 ± 0.9	0.0 ± 0.0	0.0 ± 0.0	0.0 ± 0.0	0.0 ± 0.0	0.0 ± 0.0
Diboson	0.6 ± 0.2	0.9 ± 0.4	0.3 ± 0.1	0.1 ± 0.1	0.0 ± 0.0	0.0 ± 0.0	0.0 ± 0.0
Total bkg	1910 ± 500	740 ± 160	520 ± 120	307 ± 90	11.4 ± 3.8	20.3 ± 6.1	32 ± 11
Data	1780	861	585	362	15	32	37

Table 6.10: Expected event yields in 5 fb^{-1} for signal and backgrounds in the e+jets channel.

	≥6 jets 2 tags	4 jets 3 tags	5 jets 3 tags	≥6 jets 3 tags	4 jets 4 tags	5 jets ≥4 tags	≥6 jets ≥4 tags
$t\bar{t}H(125)$	5.6 ± 1.0	1.8 ± 1.2	2.9 ± 1.8	3.2 ± 2.1	0.3 ± 0.2	0.7 ± 0.6	1.2 ± 1.0
$t\bar{t}$+lf	1720 ± 470	640 ± 140	410 ± 94	293 ± 85	8.6 ± 2.9	14.5 ± 5.2	20.7 ± 7.8
$t\bar{t}+b\bar{b}$	27 ± 15	14.3 ± 7.9	19 ± 11	18 ± 10	1.0 ± 1.0	3.3 ± 2.6	6.7 ± 4.3
$t\bar{t}+c\bar{c}$	32.8 ± 9.4	9.6 ± 2.9	11.8 ± 3.5	14.8 ± 4.8	0.4 ± 0.3	0.6 ± 0.6	2.6 ± 1.4
$t\bar{t}V$	17.0 ± 3.6	2.1 ± 0.6	2.8 ± 0.7	4.5 ± 1.1	0.0 ± 0.0	0.3 ± 0.1	0.6 ± 0.2
Single t	35.9 ± 8.9	30.5 ± 6.4	11.3 ± 3.4	6.0 ± 2.0	0.1 ± 0.3	1.4 ± 1.2	0.4 ± 0.4
V+jets	14 ± 14	4.8 ± 5.8	0.8 ± 0.9	0.0 ± 0.0	0.0 ± 0.0	0.0 ± 0.0	0.0 ± 0.0
Diboson	0.7 ± 0.3	1.0 ± 0.3	0.2 ± 0.1	0.1 ± 0.0	0.0 ± 0.0	0.0 ± 0.0	0.0 ± 0.0
Total bkg	1850 ± 490	700 ± 150	460 ± 110	336 ± 93	10.1 ± 3.2	20.2 ± 6.6	31 ± 11
Data	1723	785	531	324	13	24	37

Table 6.11: Expected event yields in 5 fb^{-1} for signal and backgrounds in the μ+jets channel.

	≥6 jets 2 tags	4 jets 3 tags	5 jets 3 tags	≥6 jets 3 tags	4 jets ≥4 tags	5 jets ≥4 tags	≥6 jets ≥4 tags
$t\bar{t}H(125)$	11.7 ± 1.9	3.9 ± 1.9	6.1 ± 3.1	6.9 ± 3.5	0.6 ± 0.3	1.5 ± 0.8	2.5 ± 1.3
$t\bar{t}$+lf	3460 ± 940	1320 ± 280	870 ± 210	570 ± 170	18.0 ± 5.1	27.6 ± 8.6	41 ± 15
$t\bar{t} + b\bar{b}$	61 ± 34	35 ± 19	43 ± 24	35 ± 20	2.5 ± 1.7	8.4 ± 5.4	15.4 ± 9.4
$t\bar{t} + c\bar{c}$	62 ± 17	19.6 ± 5.2	25.0 ± 6.9	25.9 ± 7.7	0.6 ± 0.4	0.8 ± 0.9	3.7 ± 1.8
$t\bar{t}V$	35.7 ± 7.5	4.5 ± 1.1	6.1 ± 1.4	8.6 ± 2.1	0.1 ± 0.1	0.7 ± 0.2	1.5 ± 0.4
Single t	79 ± 18	56 ± 11	25.6 ± 6.3	10.3 ± 2.9	0.3 ± 0.6	3.1 ± 2.2	1.0 ± 0.6
V+jets	53 ± 40	5.9 ± 5.9	0.8 ± 0.9	0.0 ± 0.0	0.0 ± 0.0	0.0 ± 0.0	0.0 ± 0.0
Diboson	1.2 ± 0.4	1.8 ± 0.6	0.5 ± 0.2	0.2 ± 0.1	0.0 ± 0.0	0.0 ± 0.0	0.0 ± 0.0
Total bkg	3760 ± 980	1440 ± 300	970 ± 230	650 ± 190	21.5 ± 6.1	41 ± 12	63 ± 21
Data	3503	1646	1116	686	28	56	74

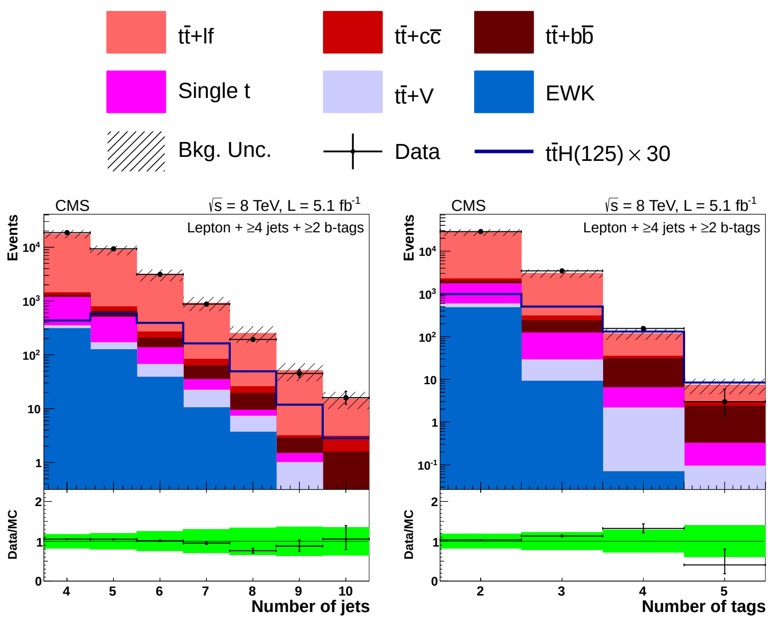

Figure 6.6: Number of jets (left) and number of b-tagged jets (right) in data and simulation for events with $\geq$4 jets + $\geq$2 b-tags in the lepton+jets channel at 8 TeV. The background is normalized to the SM expectation; the uncertainty band (shown as a hatched band in the stack plot and a green band in the ratio plot) includes statistical and systematic uncertainties that affect both the rate and shape of the background distributions. The $t\bar{t}H$ signal ($m_H = 125\,\mathrm{GeV}/c^2$) is normalized to 30 $\times$ SM expectation.

6.3 Multivariate Analysis

As discussed in the chapter introduction, no single variable offers sufficient discriminating power, to separate the $t\bar{t}H$ signal from the $t\bar{t}+jets$ background. Instead, the combined power of several input variables is utilized through a multivariate analysis (MVA) technique. For this analysis, the MVA algorithm chosen from the sub-class of artificial neural network (ANN) algorithms, known as multi-layer perceptrons (MLPs). The specific algorithm is the Clermond-Ferrand Multi-Layer Perceptron Artificial Neural Network (CFMlpANN). It was first developed at the Universitye Blaise Pascal in Clermont-Ferrand, for the ALEPH experiment at the LEP collider to search for the Standard Model Higgs and has also been utilized by the BABAR experiment to search for rare B meson decays [155]. It has been implemented in the ROOT TMVA framework, available in all CMSSW releases. A CFMlpANN is trained for each jet-tag category listed in section 6.2.8. A total of 10 input variables is used in each category, with the exception of the $\geq$6 jets, $\geq$4 $b$tags category, where the full reconstruction of the $t\bar{t}H$ system is possible, features an additional variable that is the invariant mass of the di-jet system of b-jets selected by a χ^2 minimization algorithm.

6.3.1 Artificial Neural Network Overview

An artificial neural network (ANN), most generally speaking, is any collection of interconnected, simulated "neurons" which produce a certain response to a set of input variables [155]. A simulated neuron is some independent function which takes several input variables, performs a mathematical operation, and passes the result to one or more other neurons. In the most general case, a set of n input variables, connected to a single output, will produce on the order of n^2 connections. For case of using the network to discriminate between signal from background (a yes or no answer on whether an event is signal-like), the ANN is mapping an n-dimensional space onto a one-dimensional space.

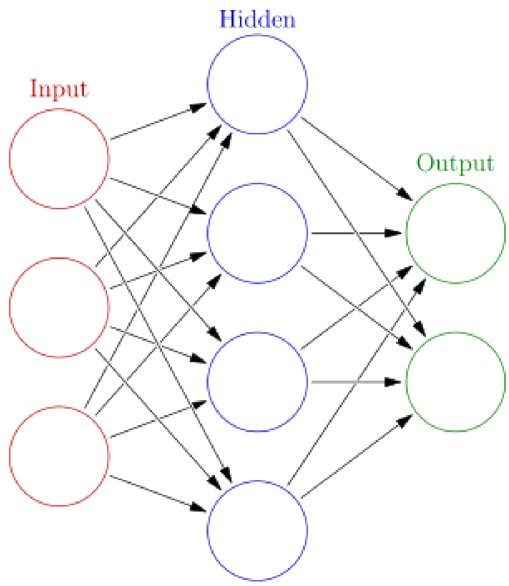

Figure 6.7: A simple example of a MLP type ANN, with one layer of input neurons that make connections to a hidden layer, which is connected to the output layer [28]

The multi-layer perceptron (MLP) is a specific type of arrangement of neurons. Any number of neurons are arranged into a single layer, and connections to other neurons are only made if they are arranged in a successive layer [155]. This is known as feed-forward network, and a simple example with one input layer, one hidden layer, and one output layer is shown in figure 6.7. This limits the complexity of the connections formed by the neurons and allows for simplified calculations.

This analysis uses an architecture that consists of two hidden layers, with N and $N-1$ variables respectively, where N is the number of input variables for the given jet/tag category. An example diagram is shown in figure 6.8. The output of the CFMlpANN algorithm is one-dimensional discriminant with range from 0 to 1, for background-like and signal-like events. Each neuron response is the based on an activation function $A(\alpha)$, and a synapse response, α.

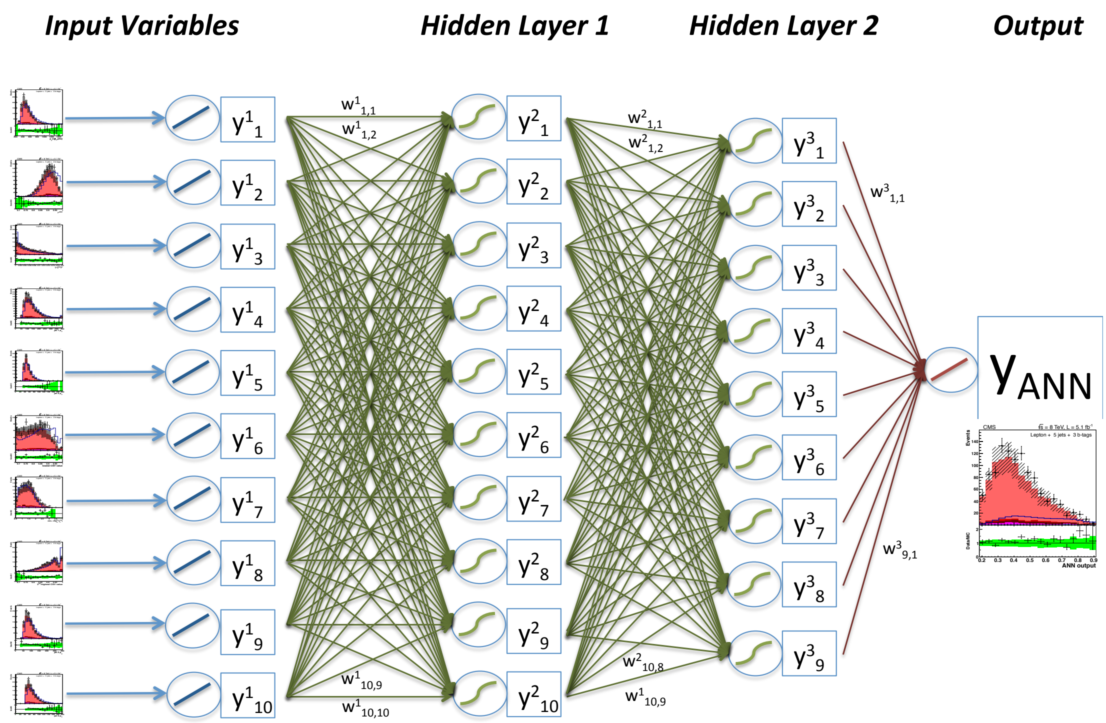

Figure 6.8: The CFMlpANN architecture used in this analysis features two hidden layers, and 10 input variables for each jet/tag category (11 variables for the $\geq$6jets, $\geq$4b-tags category)

In this case, a sigmoid function is used as the activation function:

$$A(\alpha) = \frac{1}{1 + e^{-x}} \tag{6.5}$$

and the synapse response is a simple weighted sum:

$$\alpha = w_{0j}^{(l)} + \sum_{i=1}^{n} y_i^{(l)} w_{ij}^{(l)} \tag{6.6}$$

The entire CFMlpANN response is then

$$y_{ANN} = \sum_{k=1}^{n-1} y_k^{(3)} w_{k1}^{(3)} = \sum_{k=1}^{n-1} A\left(\sum_{j=1}^{n} y_j^{(2)} w_{jk}^{(2)}\right) w_{k1}^{(3)} = \sum_{k=1}^{n-1} A\left(\sum_{j=1}^{n} A\left(\sum_{i=1}^{n} x_i w_{ij}^{(1)}\right) w_{jk}^{(2)}\right) w_{k1}^{(3)} \tag{6.7}$$

where n is the number of input variables for that jet tag category and A is the sigmoid function described in equation 6.5.

The CFMlpANN is trained with $t\bar{t}H$ signal events and inclusive $t\bar{t} + jets$ background events in order to optimize the weights $w_{ij}^{(l)}$ that are used for each neuron connection such that the output, y_{ANN} is closest to 1 for signal-like events, and closest to 0 for backgorund-like events. This process involves sending the CFMlpANN an event from a known source (either signal or background), calculating the response, y_{ANN}, and computing an error function associated with the answer, given by:

$$E(x_1, ..., x_N|w) = \sum_{a=1}^{N} E_a(x_a|w) = \sum_{a=1}^{N} \frac{1}{2}(y_{ANN} - \hat{y}_a) \tag{6.8}$$

where $\hat{y}_a$ is the correct response (either 0 or 1), knowing that the event was either signal or background, and N is the number of events used to train the CFMlpANN. The optimized set of weights is the set that minimizes this error function. This is done by the method of steepest descent, where a random set of weights is moved a small distance in the direction that gives the largest change in minimizing the error function.

$$w^{t+1} = w^t - \eta \nabla_w E \tag{6.9}$$

where ∇_w is the direction that reduces the error function the most, and η is a parameter that determines how large of an adjustment is made. After the weights are adjusted, the CFMlpANN makes another iteration over the training events, re-calculating the CFMlpANN output for each event and the error function. For this analysis a total of 2000 iterations were used to train the CFMlpANN.

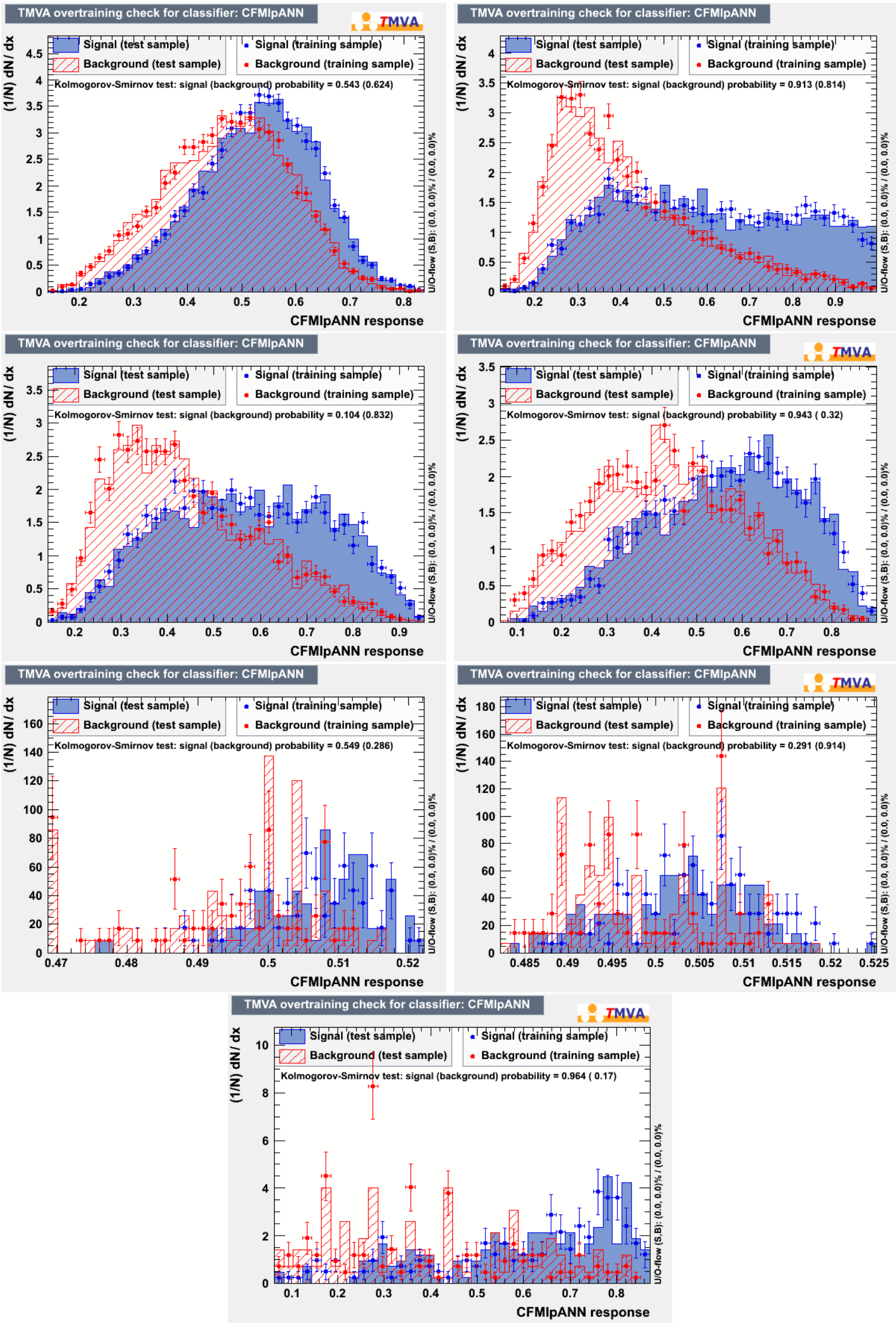

Figure 6.9: Comparisons of the testing and training samples used to optimize the CFMlpANN weights for each jet/tag category

It is possible to bias the CFMlpANN response by overtraining it. This is the case where the weights are over-adjusted to correctly classify events in the training sample. If overtrained, small fluctuations in the input variable distributions of authentic signal events can lead to incorrect classification of the signal events when the CFMlpANN attempts to classify the data. To avoid this, half of the simulated events for $t\bar{t}H$ signal and $t\bar{t}+jets$ background are used during training. After training, the other half are used to test the response of the algorithm. If properly trained, the testing and training samples should have identical CFMlpANN responses. The figure of merit used to assess this is the Kolomogrov-Smirnoff test, which computes the probability that two distributions have been sampled from the same underlying probability distribution. The results of the training and testing for each of the jet/tag categories is shown in figure 6.9. No signs of overtraining are observed.

6.3.2 MVA Input Variables, Data to Monte Carlo Comparisons

As mentioned in the previous section, each jet/tag category has been trained with its own CFMlpANN. Each category uses ten input variables, except for the ≥6j, ≥4t category, which uses eleven. A total of 24 unique input variables are used in the 7 different jet/tag categories and are listed in table 6.12. The most discriminating variable for each category is denoted by a ★. The inputs are selected from a ranked list based on initial separation between signal and background. The separation of the individual variables is evaluated using a separation benchmark $\langle S^2 \rangle$ [155] defined as follows:

$$\langle S^2 \rangle = \frac{1}{2} \int \frac{\left(\hat{y}_S(y) - \hat{y}_B(y)\right)^2}{\hat{y}_S(y) + \hat{y}_B(y)} dy, \tag{6.10}$$

where y is the input variable, and $\hat{y}_S$ and $\hat{y}_B$ are the signal and background probability density functions for that input variable in the signal and background samples, respectively. The maximum number of input variables used in each category is limited by the statistics in the simulated samples used for the CFMlpANN training. The number of variables per category is determined by reducing the number of variables until the minimum number of variables needed to maintain roughly the same ANN performance is reached. In this case, 10 input variables yields stable and approximately identical performance to using 15, while using 5 variables degraded discrimination power significantly.

The input variables used in the CFMlpANN can be broken down into several classes. The first is related to jet, and multi-object kinematics. The b-jets produced by the Higgs boson tend to have a harder p_T spectrum compared to b-jets produced from gluon radiation. Additionally, the recoil of the Higgs off of the top-system produces small differences in the p_T and invariant

Table 6.12: The ANN inputs for the nine jet-tag categories in the 8 TeV $t\bar{t}H$ analysis in the lepton+jets and dilepton channels. The choice of inputs is optimized for each category. Definitions of the variables are given in the text. The best input variable for each jet-tag category is denoted by ★.

	Lepton+Jets						
Jets	≥6	4	5	≥6	4	5	≥6
Tags	2	3	3	3	4	≥4	≥4
Jet 1 p_{T}		✓	✓		✓		
Jet 2 p_{T}		✓	✓				
Jet 3 p_{T}	✓	✓	✓			✓	
Jet 4 p_{T}	✓	✓	✓			✓	
$p_{\mathrm{T}}(\ell, E_{\mathrm{T}}^{\mathrm{miss}}, \mathrm{jets})$		★	✓		✓	✓	
$M(\ell, E_{\mathrm{T}}^{\mathrm{miss}}, \mathrm{jets})$	✓	✓		✓	✓		✓
Average $M((\mathrm{j}_m^{\mathrm{untag}}, \mathrm{j}_n^{\mathrm{untag}}))$	✓			✓			
$M((\mathrm{j}_m^{\mathrm{tag}}, \mathrm{j}_n^{\mathrm{tag}})_{\mathrm{closest}})$							✓
$M((\mathrm{j}_m^{\mathrm{tag}}, \mathrm{j}_n^{\mathrm{tag}})_{\mathrm{best}})$							✓
Average $\Delta R(\mathrm{j}_m^{\mathrm{tag}}, \mathrm{j}_n^{\mathrm{tag}})$				✓	✓	✓	✓
Minimum $\Delta R(\mathrm{j}_m^{\mathrm{tag}}, \mathrm{j}_n^{\mathrm{tag}})$			✓				
$\Delta R(\ell, \mathrm{j}_{\mathrm{closest}})$						✓	✓
Sphericity	✓			✓			✓
Aplanarity	✓				✓		
H_0	✓						
H_1	✓				✓		
H_2				✓			✓
H_3	★			✓			✓
μ^{CSV}	✓	✓	★	★	★	★	★
$(\sigma_n^{\mathrm{CSV}})^2$		✓	✓	✓	✓	✓	
Highest CSV value						✓	
2^{nd}-highest CSV value		✓	✓	✓	✓	✓	✓
Lowest CSV value		✓	✓	✓	✓	✓	✓

mass of the reconstructed $t\bar{t} + jets$ system.

- Jet 1 p_{T} - the highest value of transverse jet momentum in the event
- Jet 2 p_{T} - the second highest value of transverse jet momentum in the event
- Jet 3 p_{T} - the third highest value of transverse jet momentum in the event
- Jet 4 p_{T} - the fourth highest value of transverse jet momentum in the event
- $p_{\mathrm{T}}(\ell, E_{\mathrm{T}}^{\mathrm{miss}}, \mathrm{jets})$ - the transverse momentum of the four-vector formed by summing the four-vectors of the lepton, MET, and all selected jets in the event
- $M(\ell, E_{\mathrm{T}}^{\mathrm{miss}}, \mathrm{jets})$ - the invariant mass of the four-vector formed by summing the four-vectors of the lepton, MET, and all selected jets in the event
- Average $M((\mathrm{j}_m^{\mathrm{untag}}, \mathrm{j}_n^{\mathrm{untag}}))$ - the average di-Jet mass formed by all combinations of jets that have not been b-tagged in the event
- $M((\mathrm{j}_m^{\mathrm{tag}}, \mathrm{j}_n^{\mathrm{tag}})_{\mathrm{closest}})$ - the invariant di-Jet mass of the two b-tagged jets that are closest to one another in the detector

- $M((\mathrm{j}_m^{\mathrm{tag}}, \mathrm{j}_n^{\mathrm{tag}})_{\mathrm{best}})$ - the invariant mass constructed from the two tagged jets least likely to be a part of the $t\bar{t}$ system as determined by a minimum χ^2 search among all the jet, lepton, and $E_{\mathrm{T}}^{\mathrm{miss}}$ combinations in the event, using the W boson and top masses as kinematic constraints.

The next class of input variables describe the angular relationship between reconstructed objects in the event. These are event shape variables. Production of a relatively massive object, in addition to top quarks, such as the Higgs, tends to make $t\bar{t}H$ events more spherically distributed in the detected, while the background events are more collimated. Variables in this class include angular correlations, like the opening angle between the tagged jets

- Average $\Delta R(\mathrm{j}_m^{\mathrm{tag}}, \mathrm{j}_n^{\mathrm{tag}})$ - the average ΔR spatial separation between all combinations of b-tagged jets in the event
- Minimum $\Delta R(\mathrm{j}_m^{\mathrm{tag}}, \mathrm{j}_n^{\mathrm{tag}})$ - the smallest value of ΔR measured between a pair of b-tagged jets
- $\Delta R(\ell, \mathrm{j}_{\mathrm{closest}})$ - the ΔR spatial separation of the lepton and the closest reconstructed jet
- Sphericity - Event shape variable equal to $\frac{3}{2}(\lambda_2 + \lambda_3)$, where λ_2 and λ_3 are the second and third eigenvalues of the sphericity tensor as described in[156]
- Aplanarity - Event shape variable equal to $\frac{3}{2}(\lambda_3)$, where λ_3 is the third eigenvalue of the sphericity tensor as described in
- H_0 - the zeroth Fox-Wolfram moment [157]
- H_1 - the first Fox-Wolfram moment
- H_2 - the second Fox-Wolfram moment
- H_3 - the third Fox-Wolfram moment

where $\Delta R = \sqrt{\Delta\eta^2 + \Delta\phi^2}$. The sphericity tensor is given by the equation:

$$S^{a,b} = \frac{\sum_i p_i^a p_i^b}{\sum_i |\hat{p}_i|^2} \tag{6.11}$$

where $a, b = x, y, z$ coordinates. This tensor is diagonalized, and solved for its eigenvalues, which are used to compute the sphericity and aplanarity variables. The Fox-Wolfram moments are defined are momentum weighted spherical harmonics, defined as:

$$H_\ell = \sum_{i,j=1}^{N_{Jets}} \frac{|\hat{p}_i||\hat{p}_j|}{|\hat{p}|_{tot}^2} P_\ell(\cos\Omega_{ij}) \tag{6.12}$$

where $P_\ell(\cos\Omega_{ij})$ is the ℓ^{th} spherical harmonic, with polar angle calculated between jets i and j.

The final class of variables is based on the discriminant output from the b-tagging algorithm. For many of the categories, the average b-tag discriminant of all of the jets in the event tends to be the most powerful single variable. This is due to the high multiplicity of authentic b-jets in a $t\bar{t}H$ event. Additionally, since the b-quarks are coming from high mass sources, such as the top-quark and the Higgs boson, they will, on average, have a higer momentum in the transverse plane than b-jets originating from gluon radiation, as in $t\bar{t}+b\bar{b}$ events. This allows for this high transverse momentum b-jets to travel a further distance inside the detector before decaying, making the significance of impact parameter of the secondary vertex much higher, increasing the probability it will be tagged as a b-jet by the CSV algorithm. Thus, variables related to the value b-tagging discriminant provide the greatest signal extraction power.

- μ^{CSV} - the average value of the output of the CSV algorithm for all b-tagged jets in the event.
- $(\sigma_n^{\text{CSV}})^2$ - the variance of the average value of the output of the CSV algorithm for all b-tagged jets in the event.
- Highest CSV value - the highest value of the CSV discriminant for any b-tagged jet in the event
- 2^{nd}-highest CSV value - the second highest value of the CSV discriminant for any b-tagged jet in the event
- Lowest CSV value - the lowest value of the CSV discriminant for any b-tagged jet in the event

The modeling of the input variables is compared against data for each of the jet/tag diagrams in the the following figures:

- $\geq$6 jets, ==2 b-tags: Figure 6.10, and Figure 6.11
- ==4 jets, ==3 b-tags: Figure 6.12, and Figure 6.13
- ==5 jets, ==3 b-tags: Figure 6.14, and Figure 6.15
- $\geq$6 jets, ==3 b-tags: Figure 6.16, and Figure 6.17
- ==4 jets, ==4 b-tags: Figure 6.18, and Figure 6.19
- ==5 jets, ==4 b-tags: Figure 6.20, and Figure 6.21
- $\geq$6 jets, $\geq$4 b-tags: Figure 6.22, and Figure 6.23

Below each histogram is a ratio of the yields for data over the simulated sample prediction. The green band is the total uncertainty estimated for the simulation, and the error bars on the points are determined by the statistical error on the data collected.

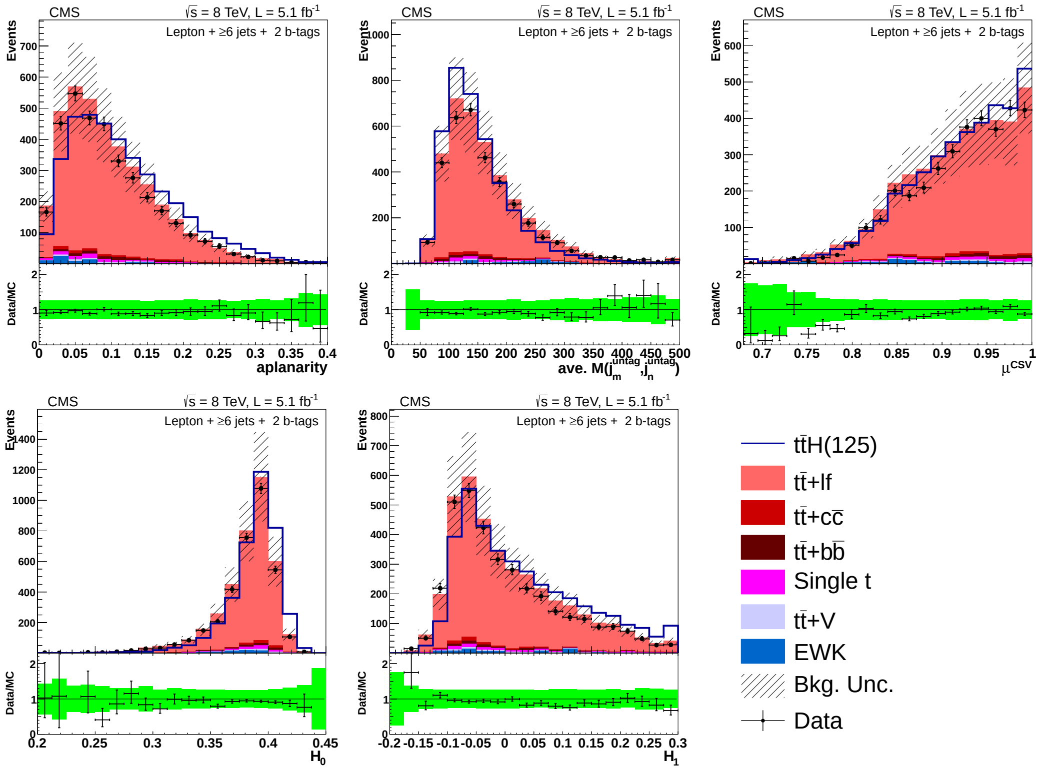

Figure 6.10: Lepton + jets data/MC comparison for the ≥6 jets + 2 tag category. The uncertainty band includes statistical and systematic uncertainties that affect both the rate and shape of the background distributions.

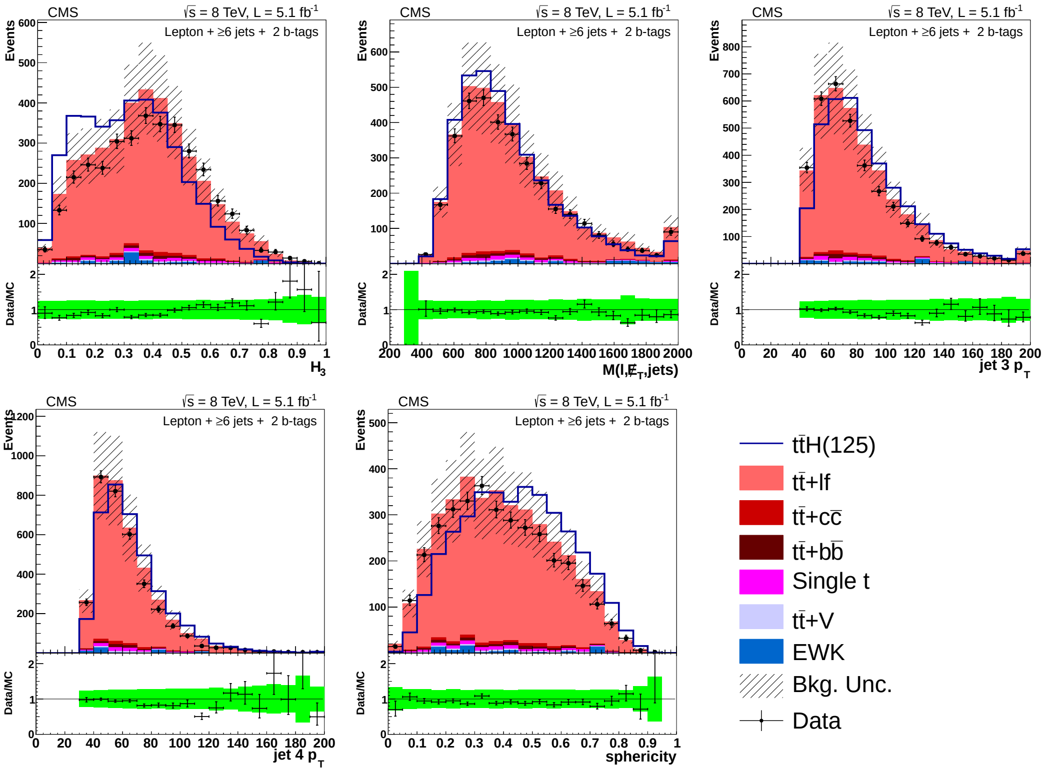

Figure 6.11: Lepton + jets data/MC comparison for the $\geq$ 6 jets + 2 tag category. The uncertainty band includes statistical and systematic uncertainties that affect both the rate and shape of the background distributions.

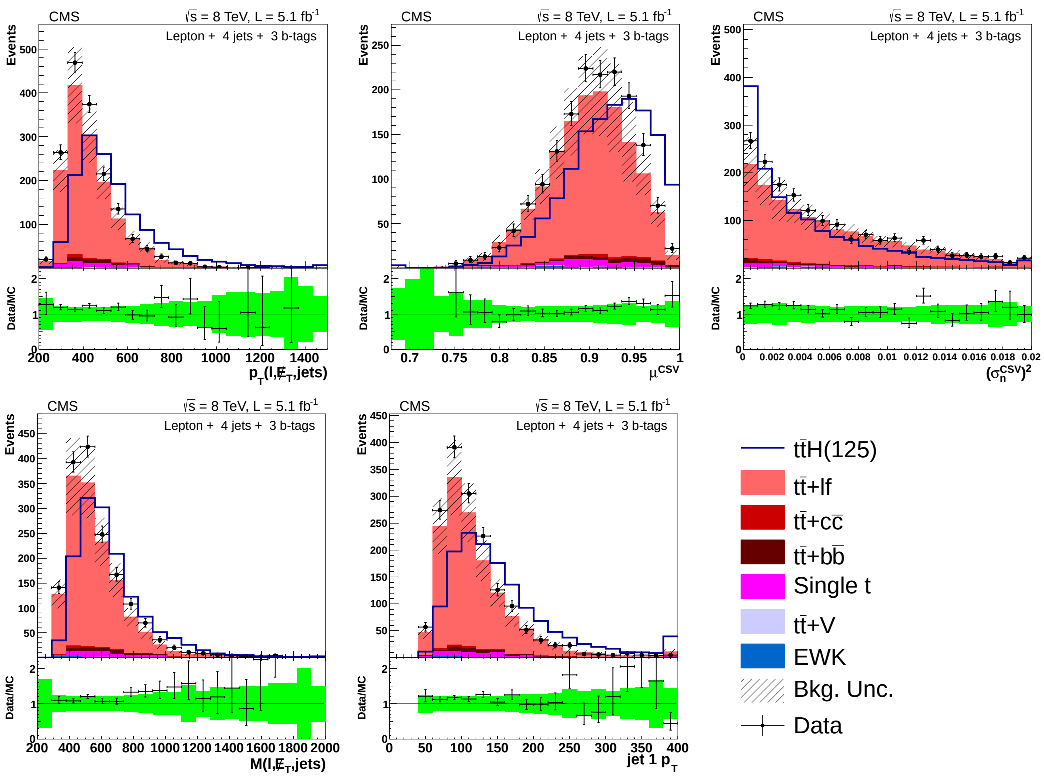

Figure 6.12: Lepton + jets data/MC comparison for the 4 jets + 3 tag category. The uncertainty band includes statistical and systematic uncertainties that affect both the rate and shape of the background distributions.

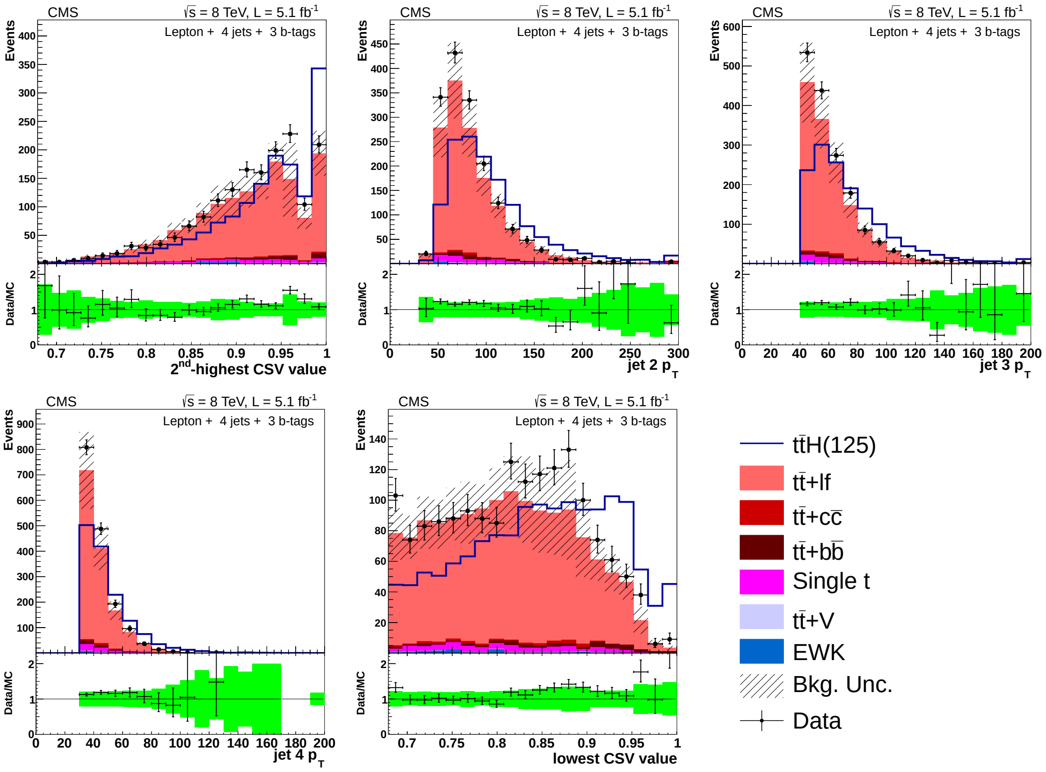

Figure 6.13: Lepton + jets data/MC comparison for the 4 jets + 3 tag category. The uncertainty band includes statistical and systematic uncertainties that affect both the rate and shape of the background distributions.

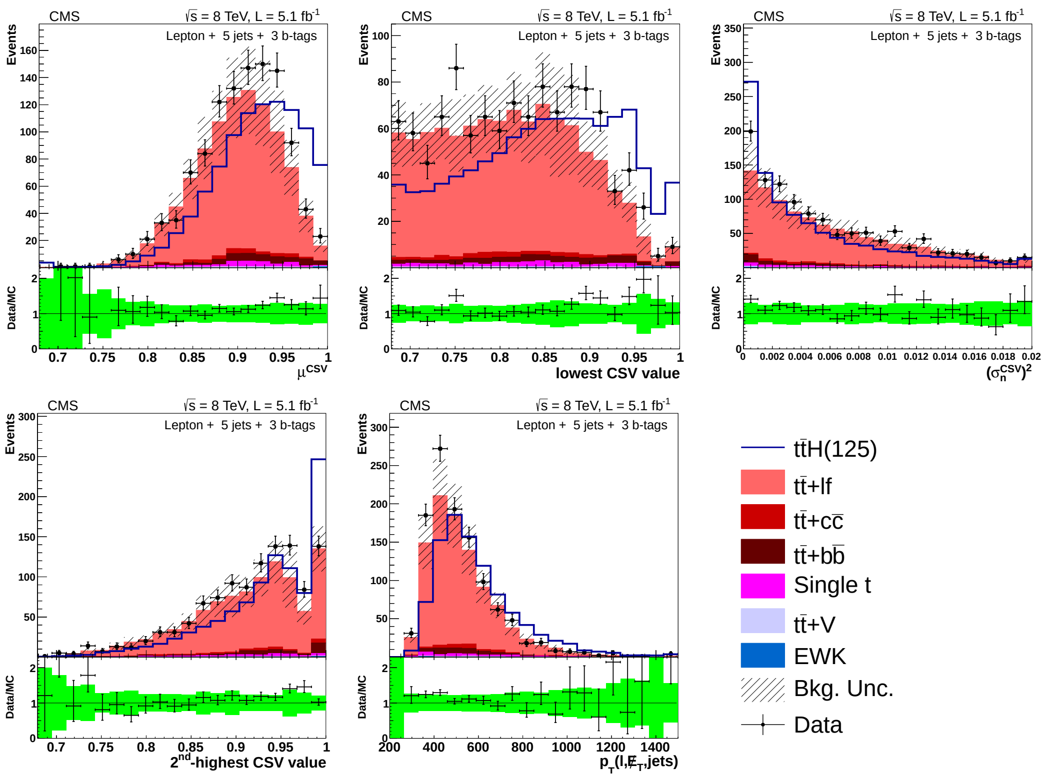

Figure 6.14: Distributions of the five ANN input variables with rankings 1 through 5, in terms of separation, for the 5 jets + 3 b-tags category of the lepton+jets channel at 8 TeV. Definitions of the variables are given in the text. The background is normalized to the SM expectation; the uncertainty band (shown as a hatched band in the stack plot and a green band in the ratio plot) includes statistical and systematic uncertainties that affect both the rate and shape of the background distributions. The $t\bar{t}H$ signal ($m_H = 125\,\mathrm{GeV}/c^2$) is normalized to the total background yield, for easier comparison of the shapes.

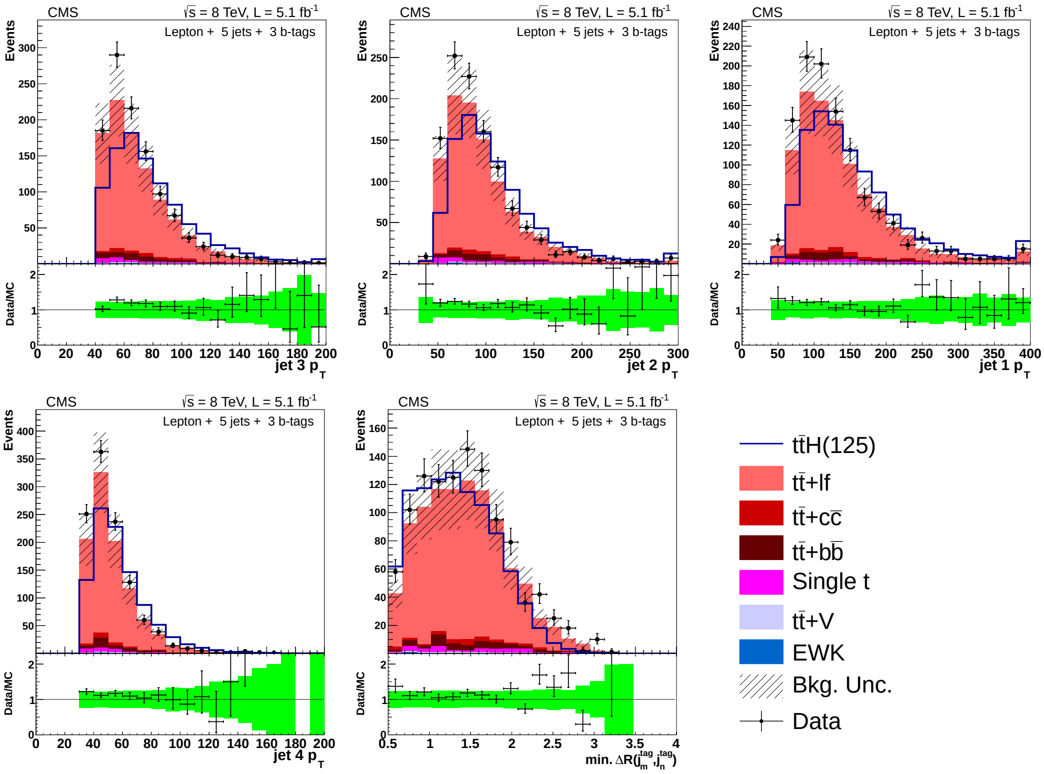

Figure 6.15: Distributions of the five ANN input variables with rankings 6 through 10, in terms of separation, for the 5 jets + 3 b-tags category of the lepton+jets channel at 8 TeV. Definitions of the variables are given in the text. The background is normalized to the SM expectation; the uncertainty band (shown as a hatched band in the stack plot and a green band in the ratio plot) includes statistical and systematic uncertainties that affect both the rate and shape of the background distributions. The $t\bar{t}H$ signal ($m_H = 125\,\mathrm{GeV}/c^2$) is normalized to the total background yield, for easier comparison of the shapes.

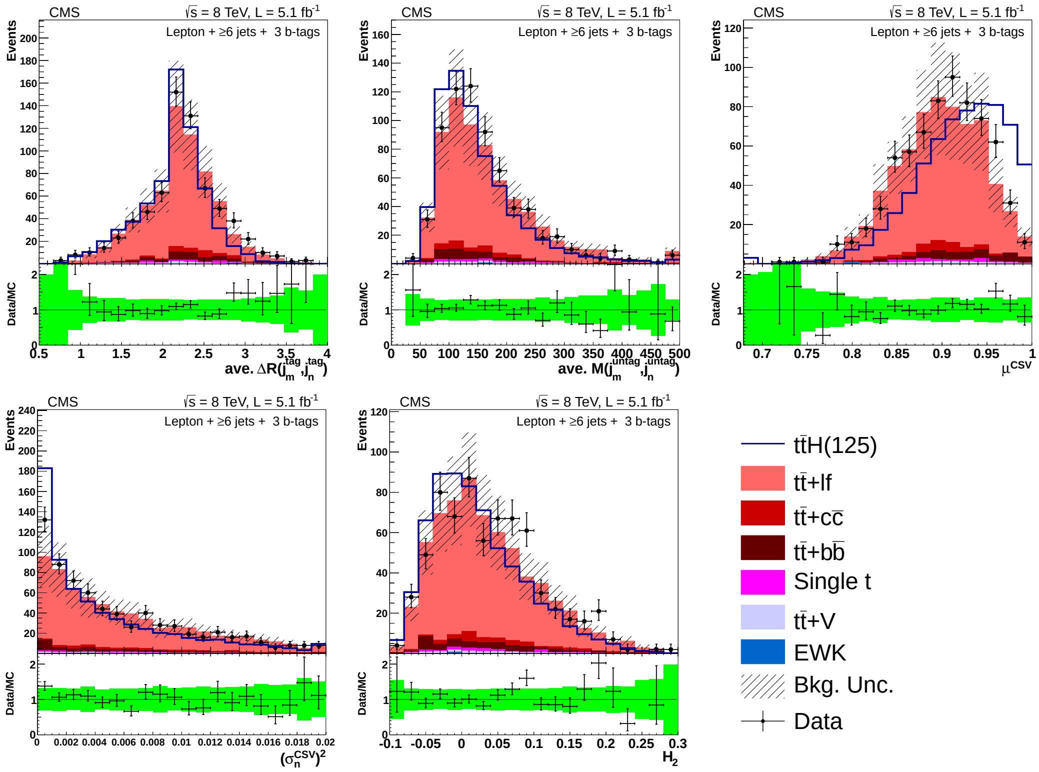

Figure 6.16: Lepton + jets data/MC comparison for the ≥6 jets + 3 tag category. The uncertainty band includes statistical and systematic uncertainties that affect both the rate and shape of the background distributions.

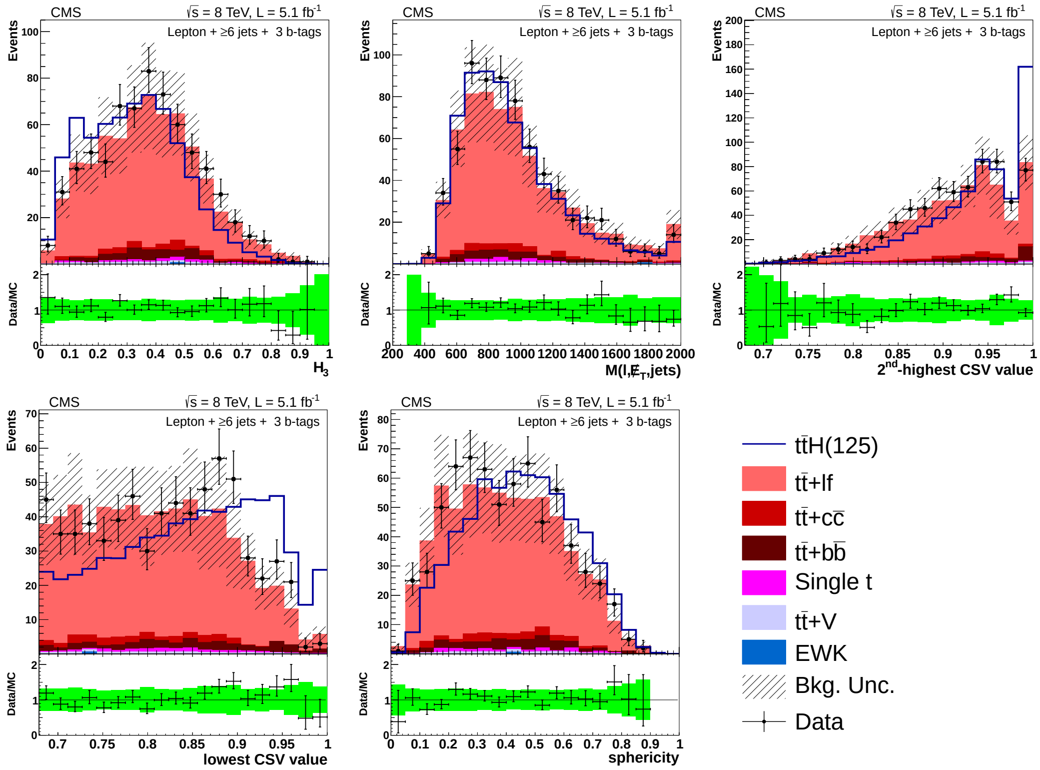

Figure 6.17: Lepton + jets data/MC comparison for the ≥6 jets + 3 tag category. The uncertainty band includes statistical and systematic uncertainties that affect both the rate and shape of the background distributions.

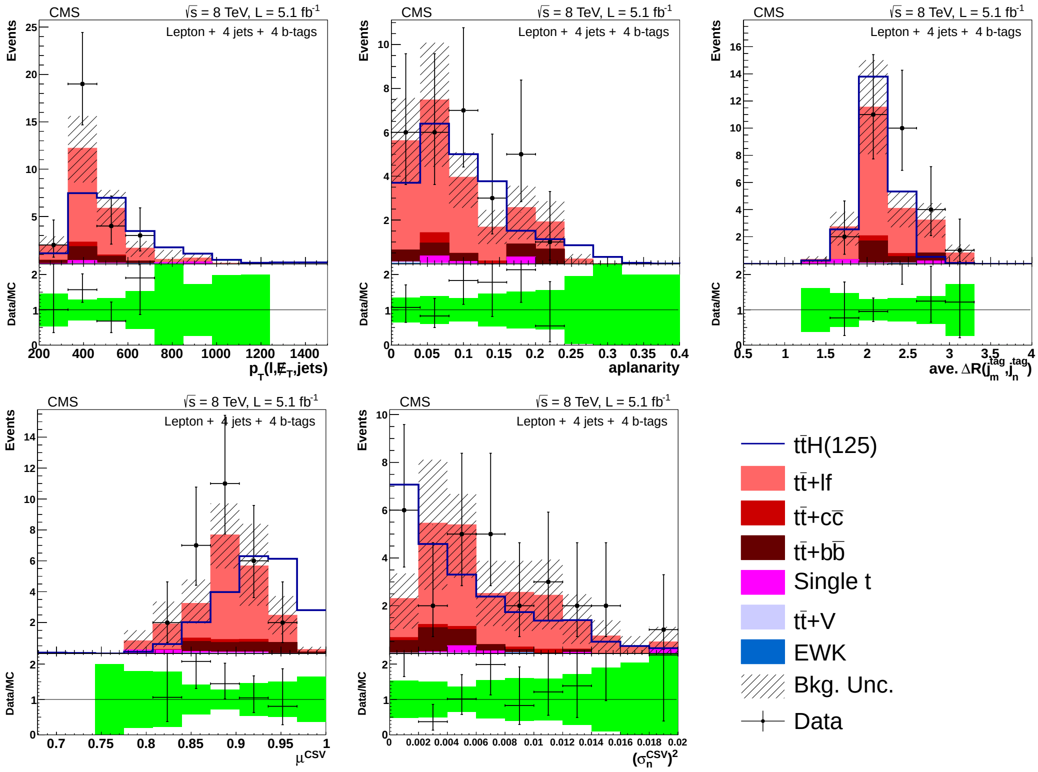

Figure 6.18: Lepton + jets data/MC comparison for the 4 jets + 4 tag category. The uncertainty band includes statistical and systematic uncertainties that affect both the rate and shape of the background distributions.

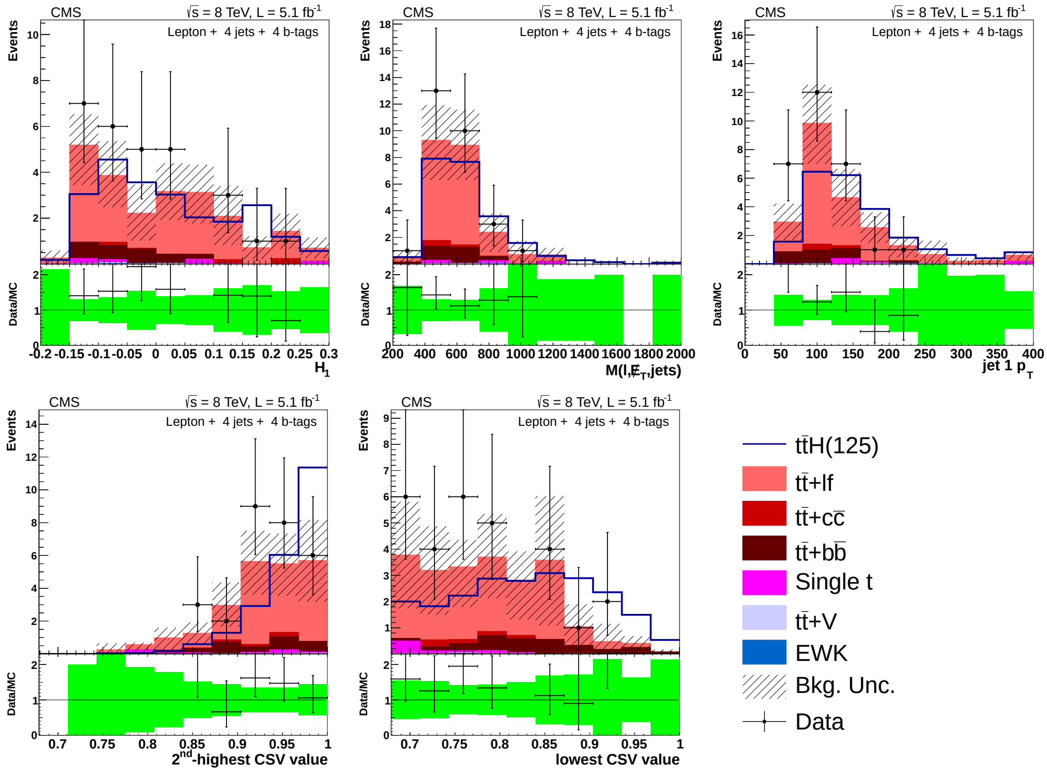

Figure 6.19: Lepton + jets data/MC comparison for the 4 jets + 4 tag category. The uncertainty band includes statistical and systematic uncertainties that affect both the rate and shape of the background distributions.

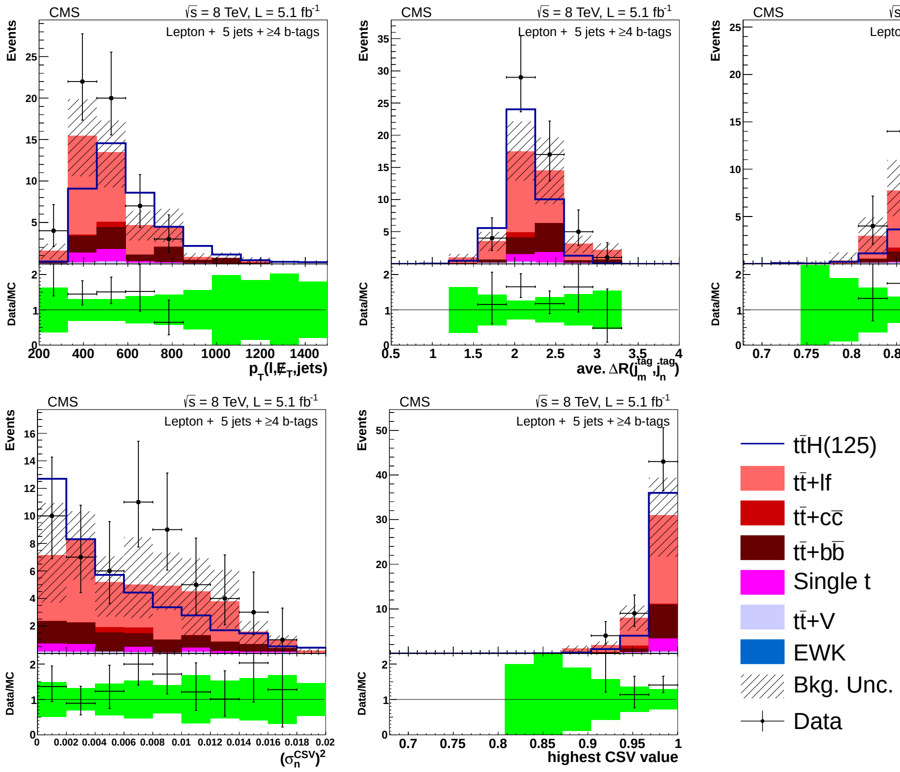

Figure 6.20: Lepton + jets data/MC comparison for the 5 jets + 4 tag category. The uncertainty band includes statistical and systematic uncertainties that affect both the rate and shape of the background distributions.

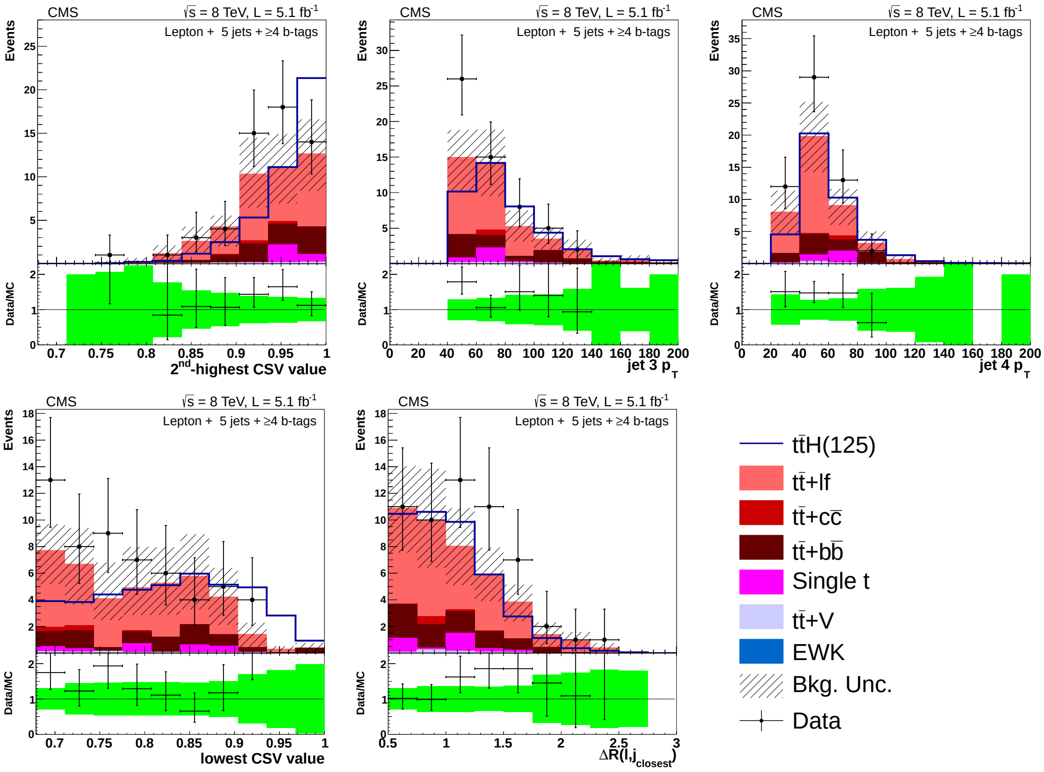

Figure 6.21: Lepton + jets data/MC comparison for the 5 jets + 4 tag category. The uncertainty band includes statistical and systematic uncertainties that affect both the rate and shape of the background distributions.

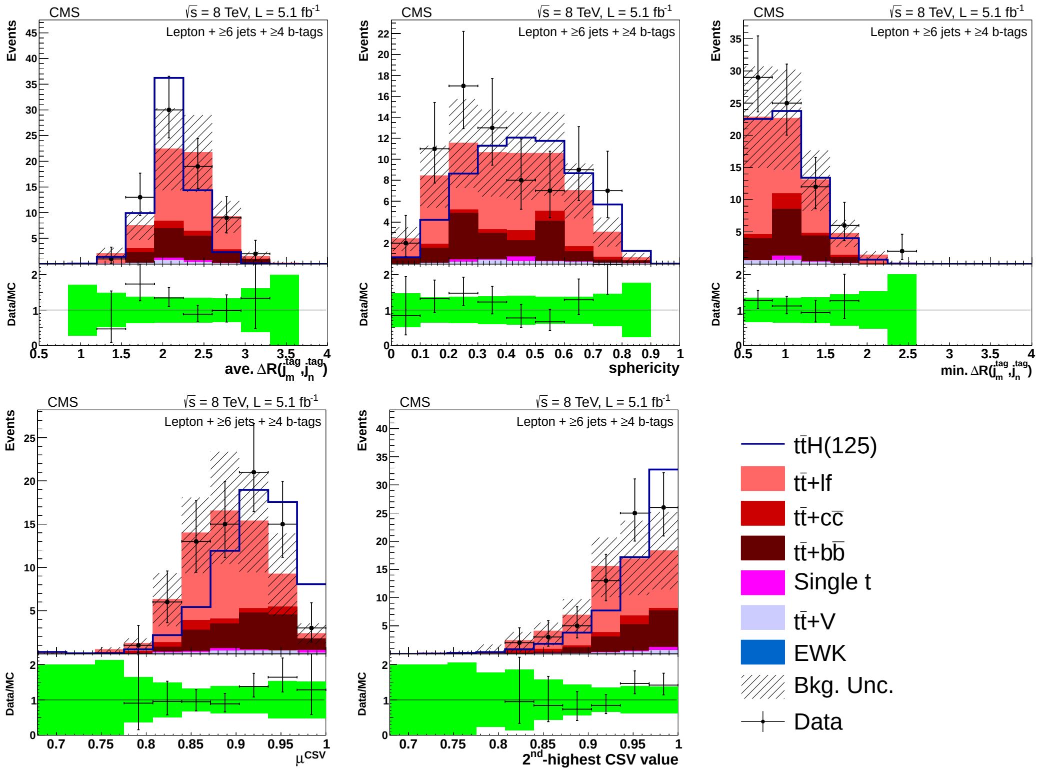

Figure 6.22: Lepton + jets data/MC comparison for the $\geq$ 6 jets + 4 tag category. The uncertainty band includes statistical and systematic uncertainties that affect both the rate and shape of the background distributions.

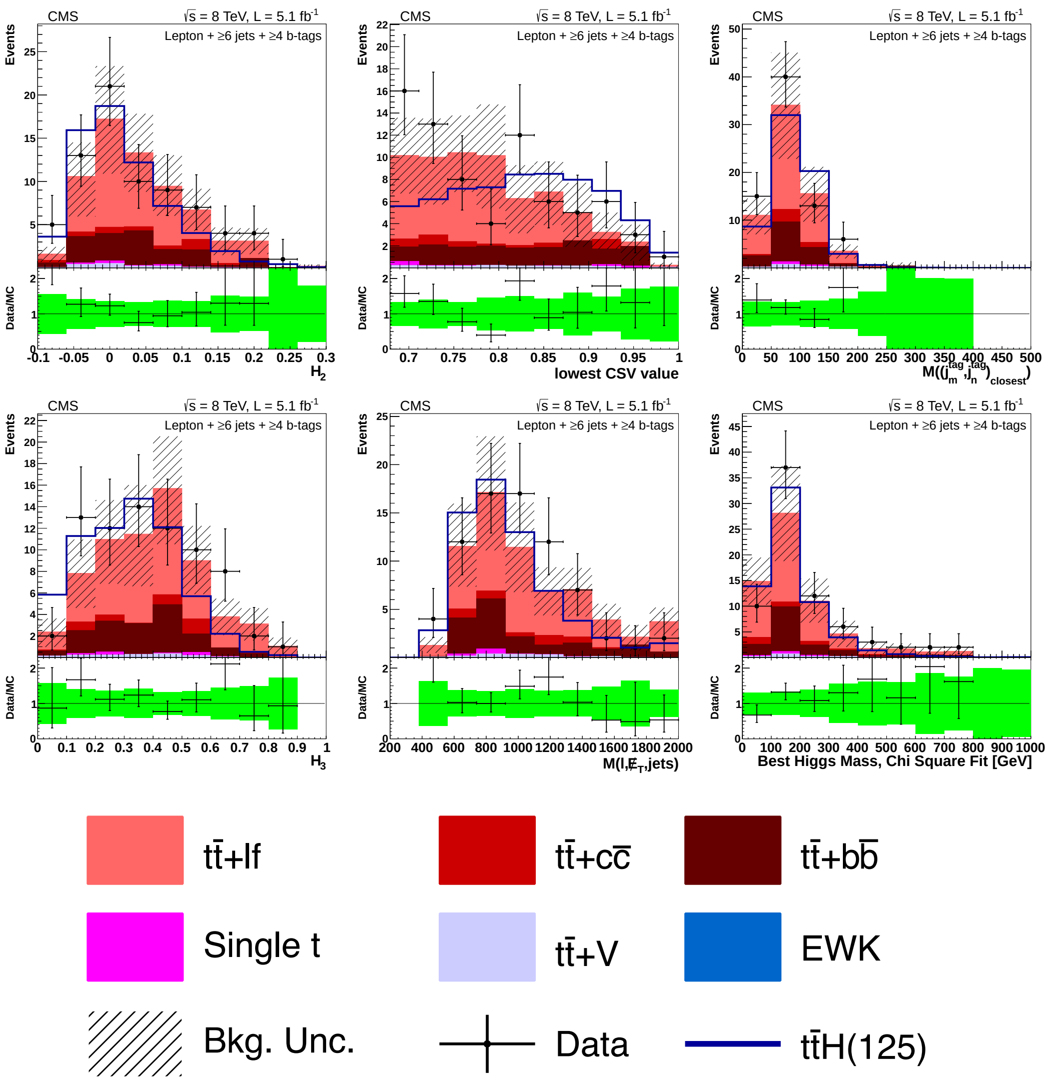

Figure 6.23: Lepton + jets data/MC comparison for the $\geq$ 6 jets + 4 tag category. The uncertainty band includes statistical and systematic uncertainties that affect both the rate and shape of the background distributions.

6.3.3 MVA Output, Data to Monte Carlo Comparisons

Data to Monte Carlo comparisons for the CFMlpANN output can be seen on figure 6.24. In the plots, the signal shape has been multiplied by a factor of 30 in order to make its shape visible, and in order to gauge a scale of the expected size of signal to background in each jet/tag category.

h

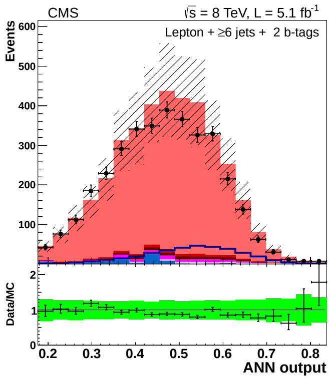

(a) ≥6 jets, 2 b-tags

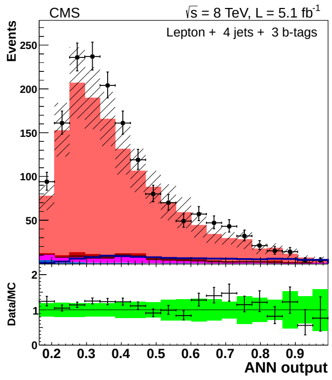

(b) 4 jets, 3 b-tags

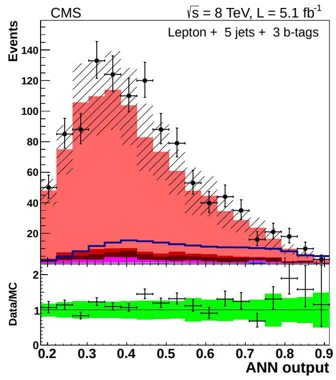

(c) 5 jets, 3 b-tags

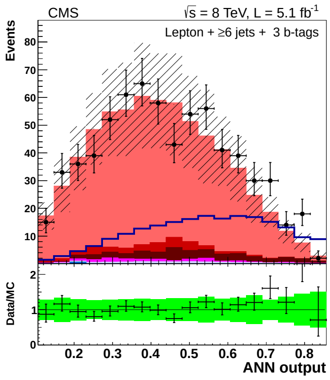

(d) ≥6 jets, 3 b-tags

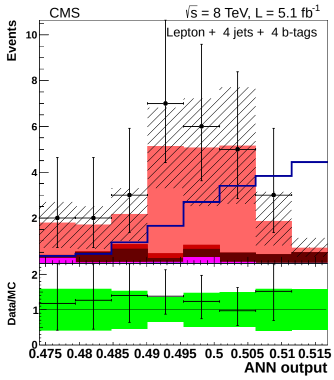

(e) 4 jets, 4 b-tags

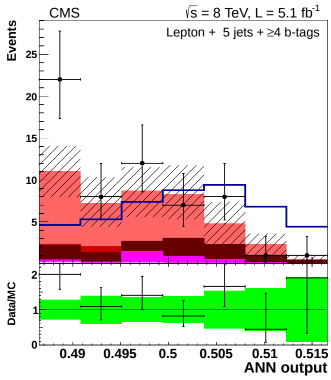

(f) 5 jets, ≥4 b-tags

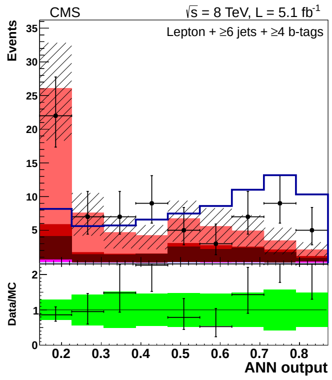

(g) ≥6 jets, ≥4 b-tags

(h) Legend

Figure 6.24: The distributions of the CFMlpANN output for lepton+jets events at 8 TeV in the various analysis categories. Background-like events have a low CFMlpANN output value. Signal-like events have a high CFMlpANN output value. The background is normalized to the SM expectation; the uncertainty (shown as a hatched band in the stack plot and a green band in the ratio plot) includes statistical and systematic uncertainties that affect both the rate and shape of the background distributions. The $t\bar{t}H$ signal ($m_H = 125\,\mathrm{GeV}/c^2$) is normalized to 30 $\times$ SM expectation.

6.4 Systematic Uncertainties

There are three types of systematic effects considered in this analysis: those that affect only the rates of signal or background processes, those that affect only the shapes of the CFMlpANN discriminants for signal or background processes, and those that affect both the rate and the shape. In the last case, the rate and shape effects are treated simultaneously so that they are considered completely correlated. Unless otherwise noted, all of the uncertainties listed here apply equally to signal and background and are treated as 100% correlated between the two. Below is a list of systematic effects considered for this analysis:

Table 6.13: Summary of the systematic uncertainties considered on the inputs to the limit calculation. Except where noted, each row in this table will be treated as a single, independent nuisance parameter.

Source	Rate Uncertainty	Shape	Remarks
Luminosity (8 TeV)	2.2%	No	All signal and backgrounds
Lepton ID/Trig	4%	No	All signal and backgrounds
Pileup	1%	No	All signal and backgrounds
Additional Pileup Corr.	–	Yes	All signal and backgrounds
Jet Energy Resolution	1.5%	No	All signal and backgrounds
Jet Energy Scale	0-60%	Yes	All signal and backgrounds
b-Tag SF (b/c)	0-33.6%	Yes	All signal and backgrounds
b-Tag SF (mistag)	0-23.5%	Yes	All signal and backgrounds
MC Statistics	–	Yes	All backgrounds
PDF (gg)	9%	No	For gg initiated processes ($t\bar{t}$, $t\bar{t}$ Z, $t\bar{t}H$)
PDF ($q\bar{q}$)	4.2-7%	No	For $q\bar{q}$ initiated processes ($t\bar{t}\,W$, W, Z).
PDF (qg)	4.6%	No	For qg initiated processes (single top)
QCD Scale ($t\bar{t}H$)	15%	No	For NLO $t\bar{t}H$ prediction
QCD Scale ($t\bar{t}$)	2-12%	No	For NLO $t\bar{t}$ and single top predictions
QCD Scale (V)	1.2-1.3%	No	For NNLO W and Z prediction
QCD Scale (VV)	3.5%	No	For NLO diboson prediction
Madgraph Scale ($t\bar{t}$)	0-20%	Yes	$t\bar{t}$ +jets/$b\bar{b}$/$c\bar{c}$ uncorrelated. Varies by jet bin.
Madgraph Scale (V)	20-60%	No	Varies by jet bin.
$t\bar{t}$ $+ b\bar{b}$	50%	No	Only $t\bar{t} + b\bar{b}$.

Jet Energy Scale (JES): The Jet Energy Scale systematic is based on the uncertainty on the L1, L2, L3, and L2L3 residual corrections to the reconstructed jet energy, as described in section 6.2.6. To evaluate the effect on the CFMlpANN output, the jet energy scale is shifted by one standard deviation up and down using the standard JetMET procedure [158]. For each variation, the jet energies are recalculated, allowing for new jets to pass the selection where once they failed, or fail the selection where once they passed, resulting in a migration of events across jet/tag categories. Finally, the CFMlpANN response is recalculated, and the effect for signal and the $t\bar{t} + jets$ background is shown in figure 6.25.

Jet Energy Resolution (JER): The jet p_T resolution in MC differs from that observed in data by approximately 10% in a η dependent way, as described in table 6.8, as per the recommendations of the JetMET group [159]. The value of the jet p_T is adjusted according

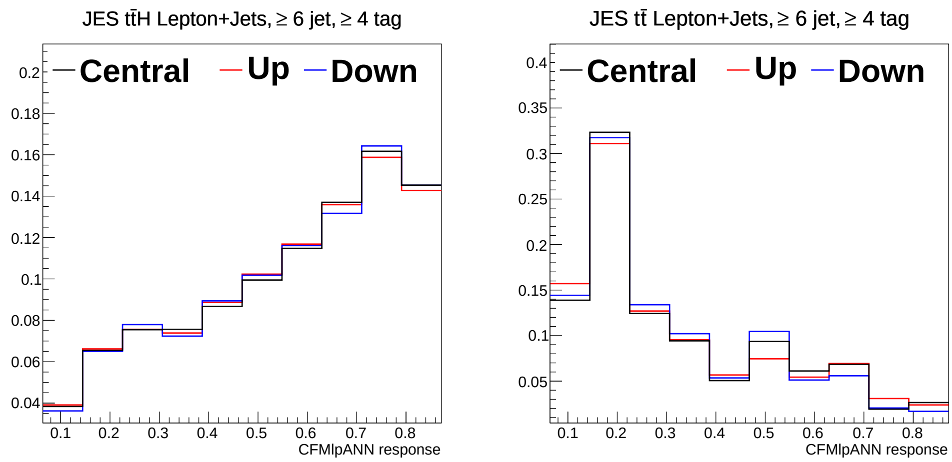

Figure 6.25: Comparison of the MVA discriminator for JES shift upwards (red) and downwards (blue) relative to the nominal (black) shape for the $t\bar{t}H(120)$ signal (left) and the main background sample $t\bar{t}+$ light flavor (right). The plots shown are from the ≥6 jet ≥4 tag category in the lepton+jets channel. All plots are normalized to unit area.

JES systematic yield change			
		lepton+jets	
sys	shift	$t\bar{t}H(120)$	$t\bar{t}$
JES	up	+8.6%	+12.1%
	down	-8.4%	-7.3%

Table 6.14: Relative yield change due to JES shift up/down for the ≥ 6 jets + ≥ 4 tags category in the lepton+jets channel.

to the formula:

$$p'_T = \max\left[0, p_T^{gen} + c(p_T^{reco} - p_T^{gen})\right] \tag{6.13}$$

The correction factor c is taken from table 6.8. To assess the effect of the systematic uncertainty on the JER, the value of c is shifted up and down by standard deviation, the JER correction is applied to the jets using this new c value, and the event rates and ANN shapes are recalculated. The effect of the JER on the shape variation is negligible, so it is treated as a rate-only effect in limit setting.

b-tag Scale Factor: The uncertainty in the b-tagging scale factor is assessed according to the prescriptions developed by the BTag POG [160]. Each per-jet b-tag scale factor is shifted up or down by its uncertainty, and the new CSV output value corresponding to that uncertainty is recalculated This new CSV value is used to determine both the number of tags associated with that systematic and the new shape of variables that use the CSV output, such as the average CSV value for b-tagged jets. This uncertainty effects both rate and shape estimates. The effects of the b-tag scale factors on the ANN shape and event yields are summarized in Fig. 6.26 and Table 6.15 respectively.

Lepton ID and Trigger Scale Factors: As discussed previously, an uncertainty of 4% covers

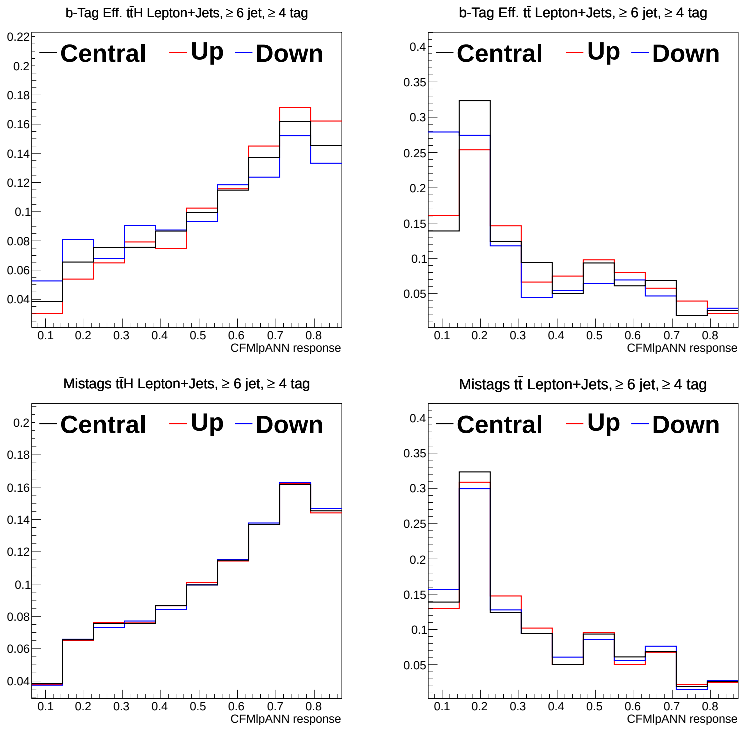

Figure 6.26: Comparison of the MVA discriminator for b-tag scale factor shift upwards (red) and downwards (blue) relative to the nominal (black) shape for the $t\bar{t}H(120)$ signal (left) and the main background sample $t\bar{t}$ + light flavor (right). The plots are from the ≥6 jets + ≥4 tags category in the lepton+jets channel. All plots are normalized to unit area.

b-tag systematic yield change			
		lepton+jets	
sys	shift	$t\bar{t}H(120)$	$t\bar{t}$
heavy flavor SF	up	+14.9%	+23.7%
	down	-15.3%	-16.0%
light flavor SF	up	+0.7%	+5.7%
	down	-1.1%	-4.2%

Table 6.15: Relative yield change due to b-tag scale factor shift up/down for the ≥6 jets + ≥4 tags category in the lepton+jets channel.

variations of the combined trigger, ID, and isolation scale factor.

Pileup Reweighting: The uncertainty on the pileup reweighting comes from changing the minimum bias cross section used to calculate the pileup reweighting by $\pm 7\%$ from the default value of 69.4 mb. The pileup reweighting is calculated using the shifted cross sections and the new weights are applied to determine the uncertainty on both the rate and shapes. Since the effect of the pileup on the shape variation is negligible, the effects of pileup are accounted through a rate-only uncertainty for the limit calculations.

Additional Pileup Correction The uncertainty associated with the additional pileup correction, described in section 6.1.5, is applied as a pure shape uncertainty to all processes. Fig. 6.27 shows the effects of the additional pileup correct uncertainty on the CFMlpANN shape.

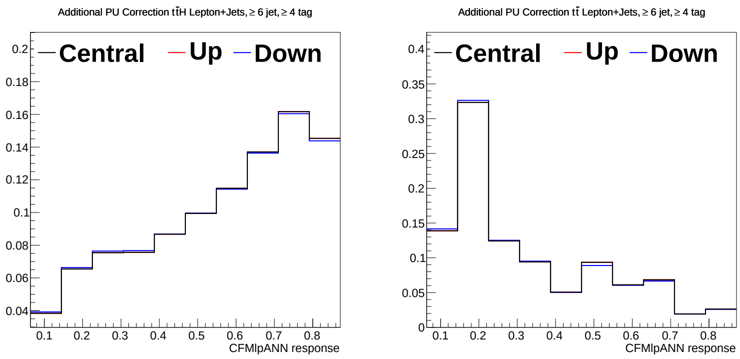

Figure 6.27: Comparison of the MVA discriminator for additional PU correction systematic upwards (red) and downwards (blue) relative to the nominal (black) shape for the $t\bar{t}H(120)$ signal (left) and the main background sample $t\bar{t}$ + light flavor (right). The plots are from the $\geq$6 jets + $\geq$4 tags category in the lepton+jets channel. All plots are normalized to unit area.

Cross Sections: The expectation for signal and background yields are derived from theoretical predictions of at least NLO accuracy. Uncertainties affecting these normalizations are summarized in table 6.16. Where appropriate, factors contributing to these uncertainties that are common to multiple processes are treated as 100% correlated. Note that for the $t\bar{t}$+jets (including $t\bar{t} + b\bar{b}$ and $t\bar{t} + c\bar{c}$ processes, as well as the V+jets processes, there is an additional uncertainty coming from the scale choice in Madgraph that effects these channels in a jet-bin specific way. This uncertainty is not included in the table 6.16, but is detailed in the next point.

Luminosity: The uncertainty on the luminosity estimate is 2.2%. This affects all rates.

Madgraph Q^2 Uncertainty: Although that backgrounds are normalized using NLO accurate theoretical calculations, these are only applicable to inclusive distributions. To extrap-

Process	pdf			QCD Scale			
	gg	qb	qg	$t\bar{t}$	V	VV	$t\bar{t}H$
$t\bar{t}H$	9%						12.5%
$t\bar{t}$+jets	9%			12%			
$t\bar{t}+W$		7%		15%			
$t\bar{t}+Z$	9%			15%			
Single top			4.6%	2%			
W+jets		4.8%			1.3%		
Z+jets		4.2%			1.2%		
Dibosons						3.5%	

Table 6.16: Cross section uncertainties used for the limit settings. Each column in the table is an independent source of uncertainty, except for the last column which represents uncertainties uncorrelated with any others. Uncertainties in the same column for two different processes (different rows) are completely correlated.

olate these inclusive predictions to exclusive rates in particular jet bins requires the use of a Monte Carlo sample. The MADGRAPH generator is used at the matrix element level and includes tree-level calculations for processes with multiple additional jets, matched to the PYTHIA parton shower to model additional soft and collinear radiation. Since the MADGRAPH + PYTHIA is tree-level, the choice of the renormalization and factorizations scales in this calculation has a significant impact. To include the effects of this uncertainty, the factorization and renormalization scales are varied by a factor of two. The ideal way to study this effect would be to generate dedicated samples with the varied scale choice, however the required statistics to get a precise determination of the systematic effect is computationally prohibitive. Therefore, as an alternative, we reweight the samples, dividing by the appropriate power of α_s and the *pdf* values at the original scale, and multiplying by the values at the new scale choice. This reweighting procedure is supported by the CMS Monte Carlo Generators group, and has been validated against dedicated scale-varied samples and has been shown to produce consistent results [161]. This reweighting procedure provides both a rate and a shape uncertainty, separately for $t\bar{t}$+light flavor, $t\bar{t}+c\bar{c}$, and $t\bar{t}+b\bar{b}$ components of the $t\bar{t}$ sample. Figure 6.28 shows the shape and rate variations for selected event categories. To prevent the strength of the $t\bar{t}$+jets constraint from over-constraining the $t\bar{t}+b\bar{b}$ and $t\bar{t}+c\bar{c}$ components, we allow the Madgraph scale to vary independently for these three components.

MC Statistics Uncertainty: To account for the effect of limited MC statistics in the analysis, a method described by Barlow and Beeston, is used to select regions of the CFMlpANN output that should have additional nuisance parameters applied [162, 163]. For the CFMl-pANN shapes of every MC process in all different categories, each bin is allowed to float within statistic uncertainty and a corresponding nuisance parameter is added. To make

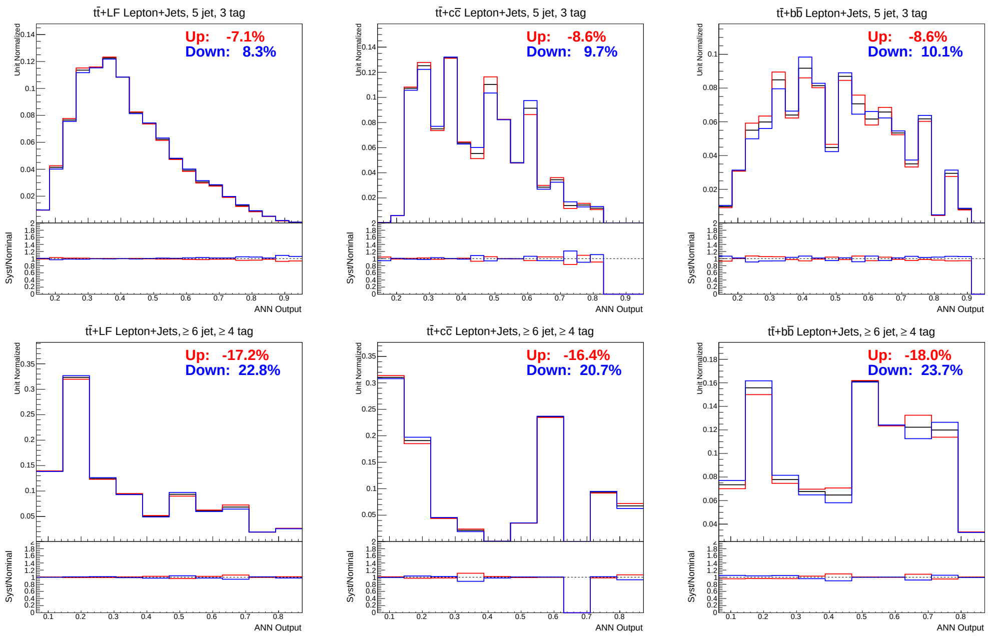

Figure 6.28: The rate and shape variations for selected categories due to the Q^2 uncertainty.

the limit computation more efficient and stable, bins are removed as nuisance parameters if the MC statistics uncertainty is negligible compared to the data statistics uncertainty or where there is no appreciable contribution from signal. In total, there are 60 nuisance parameters used to describe the MC statistics for this analysis. Tests show that the effect of neglecting bins as described above is smaller than 5%.

Additional $t\bar{t}+b\bar{b}$ Rate Uncertainty: $t\bar{t}+b\bar{b}$ background is very similar to our signal, the uncertainty on its rate and shape will have a big impact on our search. Due to the lack of more accurate next leading order(NLO) theoretical predication for this process, we obtained this background and assessed its uncertainty based on the inclusive 8 TeV $t\bar{t}$ sample. Since the inclusive $t\bar{t}$ sample is generated with Madgraph + Pythia, we need to apply a K-factor to the Madgraph cross section. According to calculations done in [164], the K-factor from leading order(LO) to NLO ranges between 1.2 and 1.8, depending on the scale choice. To be conservative, an extra 50% rate uncertainty is assigned to $t\bar{t}+b\bar{b}$ which corresponds to a K-factor of 1.7 for $\sigma_{NLO}/\sigma_{Madgraph}$. Studies also showed consistently that $t\bar{t}+b\bar{b}$ rate is correct to within factor of 2 in control regions dominated by $t\bar{t}$+light flavor statistics. The extra 50% rate uncertainty should possibly include additional uncertainty beyond the 20% from Q^2 scale to account for the differences between NLO and Madgraph.

In order to validate this assessment further, a dedicated CFMlpANN was trained to separate $t\bar{t}+b\bar{b}$ from the $t\bar{t}+jets$ background. In order to have sufficient statistics, two jet/tag categories are used: 5jets, $\geq 3b$-tags, and $\geq$6jets, $\geq 3b$-tags. The nominal $t\bar{t}+b\bar{b}$ cross section

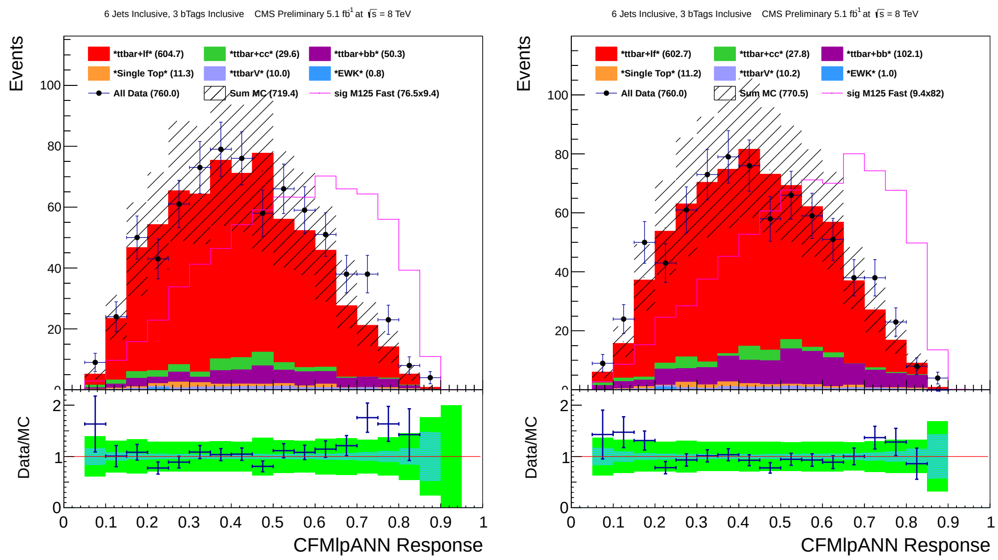

Figure 6.29: A dedicated CFMlpANN trained to isolate $t\bar{t}+b\bar{b}$ from $t\bar{t}+jets$. The left plot shows is for the case of nominal $t\bar{t}+b\bar{b}$ cross-section, the right plot shows the case for x2 $t\bar{t}+b\bar{b}$ cross-section. The left-most region of both plots is the most sensitive to the $t\bar{t}+b\bar{b}$ normalization, and shows no significant improvement in data to MC agreement, justifying the reasoning that an uncertainty larger than 50% is needed.

was doubled, in an attempt to observe an improvement in the range of the discriminant that was enriched in $t\bar{t}+b\bar{b}$. However, as figure 6.29 shows, no significant improvement was seen, justifying the reasoning that an uncertainty much larger than 50% is needed.

6.5 Statistical Methods

In the lack of an observation of any deviation from SM predictions, upper limits are set on the Higgs boson production cross section, with respect to the SM expectation, $\sigma^{95\%}/\sigma^{SM}$. Although the analysis has been optimized for Higgs decays to b-quarks, there is still acceptance from WW and ZZ decays. As such, limits on the inclusive decay of the Higgs boson are set. The statistical method used to report results is the modified frequentist approach, also known as CL_s.

For the CL_s method, the likelihood function $\mathcal{L}(\text{data}|\mu,\theta)$ is defined as

$$\mathcal{L}(\text{data}|\mu,\theta) = Poisson(\text{data}|\mu\cdot s(\theta)+b(\theta))\cdot p(\tilde{\theta}|\theta) \tag{6.14}$$

$$= \prod_i \frac{(\mu s_i+b_i)^{n_i}}{n_i!}e^{-(\mu s_i+b_i)}\cdot p(\tilde{\theta}|\theta) \tag{6.15}$$

where μ is the signal strength modifier which is often reported in the upper limit results as the ratio of the cross-section upper limit over the standard model cross-section and θ represents a full set of nuisance parameters that are used to incorporate systematic uncertainties [165]. The

Probability Distribution Function (*pdf*) of the nuisance parameter $p(\tilde{\theta}|\theta)$, where $\tilde{\theta}$ is the default value, reflects the degree of confidence in what the true value of θ is. For rate uncertainties, this is parameterized by a log-normal distribution given by:

$$\rho(\theta) = \frac{1}{\sqrt{2\pi}\ln\kappa}\exp\left(-\frac{(ln(\theta/\tilde{\theta}))^2}{2ln(\kappa)^2}\right)\frac{1}{\theta} \tag{6.16}$$

where κ is the parameter used to determine the width of the uncertainty, and $\tilde{\theta}$ is the nominal value of the distribution. Shape uncertainties can be taken into account by "vertical morphing" [166]. For each shape uncertainty, two additional histograms of the CFMlpANN output are needed, with $\pm1\sigma$ variations of the systematic uncertainty in question When building the likelihood, the systematic is associated to a nuisance parameter taken from a unit gaussian distribution, which is used to parameterize a quadratic interpolation for shifts below the 1σ value of a given bin, and linear interpolation for values beyond.

To compare the compatibility of the data with the $background-only$ ($\mu = 0$) and $signal + background$ hypotheses, where the signal is allowed to be scaled by some factor μ, the test statistic $\tilde{q}_\mu$ is constructed based on the profile likelihood ratio:

$$\tilde{q}_\mu = -2\ln\frac{\mathcal{L}(\text{data}|\mu,\hat{\theta}_\mu)}{\mathcal{L}(\text{data}|\hat{\mu},\hat{\theta})} \qquad ,0 \leq \hat{\mu} \leq \mu \tag{6.17}$$

where $\hat{\theta}_\mu$ refers to the conditional maximum likelihood estimator of θ, given the signal strength parameter μ and data. The pair of parameter estimators $\hat{\mu}$ and $\hat{\theta}$ correspond to the global maximum of the likelihood.

To perform the full CL_S technique, $pdf's$ of the results of the $background-only$, $f(\tilde{q}_\mu|\mu,\hat{\theta}_\mu^{obs})$, and $signal + background$, $f(\tilde{q}_\mu|0,\hat{\theta}_\mu^{obs})$ test statistics are formed by creating $psuedo-datasets$ of the signal and background CFMlpANN distributions, with the values of $\hat{\theta}_0^{obs}$ and $\hat{\theta}_\mu^{obs}$ fixed, but allowing the shapes and normalizations of the CFMlpANN distributions to vary within the constraints of the nuisance parameter shapes. Once the $pdfs$ for each of the test statistics are constructed, the p-value associated with each hypothesis, p_μ and p_0, are evaluated by the following integrals:

$$p_\mu = P(\tilde{q}_\mu \geq \tilde{q}_\mu^{obs}|signal + background) = \int_{\tilde{q}_\mu^{obs}}^{\inf} f(\tilde{q}_\mu|\mu,\hat{\theta}_\mu^{obs})d\tilde{q}_\mu \tag{6.18}$$

for the $signal + background$ hypothesis, and

$$1 - p_0 = P(\tilde{q}_\mu \geq \tilde{q}_\mu^{obs}|background - only) = \int_{\tilde{q}_0^{obs}}^{\inf} f(\tilde{q}_\mu|0,\hat{\theta}_0^{obs})d\tilde{q}_\mu \tag{6.19}$$

for the *background − only* hypothesis. CL$_s(\mu)$ is calculated as a ratio of these p-values:

$$CL_s(\mu) = \frac{p_\mu}{1 - p_0} \tag{6.20}$$

To quote the 95% upper limit on μ, $\mu^{95\%CL}$, the value of μ is adjusted until CL$_s$ = 0.05.

The frequentist CL$_s$ approach uses a large number of pseudo-experiments to extract the limit results. The "asymptotic" approach makes an analytic approximation of the full CL$_s$ technique and therefore avoids throwing pseudo-experiments [167]. The $pdfs$, $f(\tilde{q}_\mu|\mu, \hat{\theta}_\mu^{obs})$, and $f(\tilde{q}_\mu|0, \hat{\theta}_\mu^{obs})$ are approximated as a falling exponential below $q_{\mu,A}$, and a Gaussian above, where $q_{\mu,A}$ is the test statistic of the Asimov dataset, the background only hypothesis with nominal nuisance value parameters. The asymptotic approach is used for optimization and the results of this analysis. For the limits set from the combined Lepton+Jets and di-Lepton channels, using both 7 and 8 TeV data, the results are calculated using the full CL$_s$ treatment. Comparisons have shown that limits obtained with the two techniques agree at the 10% level.

In the limit calculation, the backgrounds are decomposed into the following distinct categories: $t\bar{t}$+jets, $t\bar{t} + b\bar{b}$, $t\bar{t} + c\bar{c}$, single top (s-channel, t-channel, and tW-channel combined), W+jets, Z+jets, $t\bar{t} + W$, $t\bar{t} + Z$, and dibosons (WW, WZ, and ZZ combined). The rates and shapes of these background processes, as well as the signal are allowed to vary according to a set of nuisance parameters, and the values of these nuisance parameters are constrained according to the uncertainties summarized in Table 7.13. Except where noted below, each row in that table represents a single nuisance parameter, completely correlated across all categories and processes to which it applies. The exceptions to this approach are as follows:

- In the case of the Madgraph Q^2 uncertainty, there are separate nuisance parameters for each of the three components of the $t\bar{t}$ background (+jets, $+b\bar{b}$, and $+c\bar{c}$). Furthermore, for the $t\bar{t}$+jets component, the uncertainty is actually broken into three nuisance parameters for the contributions coming from diagrams with zero extra partons, one extra parton, or at least two extra partons.

- For the b-tagging efficiency and mistag rate uncertainties, the rate and shape components are described by separate, independent nuisance parameters. Furthermore, each event selection category has its own, independent nuisance parameter. This is to prevent the high statistics background rich regions from over-constraining the shape uncertainties in the lower statistics, more signal rich regions.

For systematic effects such as the jet energy scale or the rate component of the b-tagging scale factor that may cause migration between event categories, care has been taken to correlate properly the different categories so that, for example, increasing the jet energy scale will cause the appropriate increases and decreases in the yields in various categories. The binning of the CFMlpANN output is chosen to minimize the impact of MC statistics and, as described in section 6.4 the MC statistics for bins where the MC statistical uncertainty causes a significant impact are accounted for.

6.6 Results and Conclusions

The variable used for signal extraction is the shape of the MVA output discriminator distribution. The fit of the simulated samples to the measured data will test for the presence of signal and, in its absence, it will set upper limits on the Higgs boson cross section. Besides the MVA discriminator shapes for data, background and signal, inputs to the "Higgs Combination" package also include the number of events passing our selection for each of the above processes. Various systematic uncertainties described in section 6.4 have all been taken into account in our limit calculation. The Higgs mass points we set limits for are: 110, 115, 120, 125, 130, 135 and 140 GeV/c^2. The upper limits are shown in Tab. 6.17 and Fig. 6.30.

		Expected		
Higgs Mass	Observed	Median	68% C.L. Range	95% C.L. Range
110 GeV/c^2	5.9	3.1	[2.1,4.6]	[1.6,6.8]
115 GeV/c^2	7.2	3.9	[2.7,5.7]	[2.0,8.1]
120 GeV/c^2	8.8	4.8	[3.4,6.9]	[2.5,9.7]
125 GeV/c^2	9.5	5.4	[3.8,7.9]	[2.8,11.1]
130 GeV/c^2	11.4	6.6	[4.6,9.6]	[3.4,13.7]
135 GeV/c^2	15.0	8.9	[6.3,12.8]	[4.7,18.1]
140 GeV/c^2	17.0	11.0	[7.7,15.9]	[5.7,22.5]

Table 6.17: Expected and observed upper limits for SM Higgs for lepton + jets channel using the first 5.1 fb^{-1} of the 2012 dataset. These limits were extracted using the asymptotic method.

For this first 5.1 fb^{-1} of data collected by the CMS detector, the first search for the Standard Model Higgs boson produced in association with top-quark pairs. Although there have been no observed signs of Higgs production in association with top quarks, upper limits are set on the production cross-section, using the statistical methods described above. If this data set was repeatedly collected, allowing for statistical fluctuations, it should be expected that, for a Standard Model Higgs boson, with mass, $m_H = 125\,\text{GeV}$, that 95% of the results would fail to observe the $t\bar{t}H$ signal unless its cross-section was modified by a factor of 9.5. From simulations alone, this expected factor is 5.4, a difference of less than 2 σ from the observed data.

The results of this analysis were combined with previous results in this channel from 7 TeV data and with a di-lepton final state channel and published in the Journal of High Energy Physics (JHEP) in May of 2013 [168]. The combined analytical power of all of the channels allowed for an upper limit of 5.8 times the predicted Standard Model cross section. This is less than 1σ

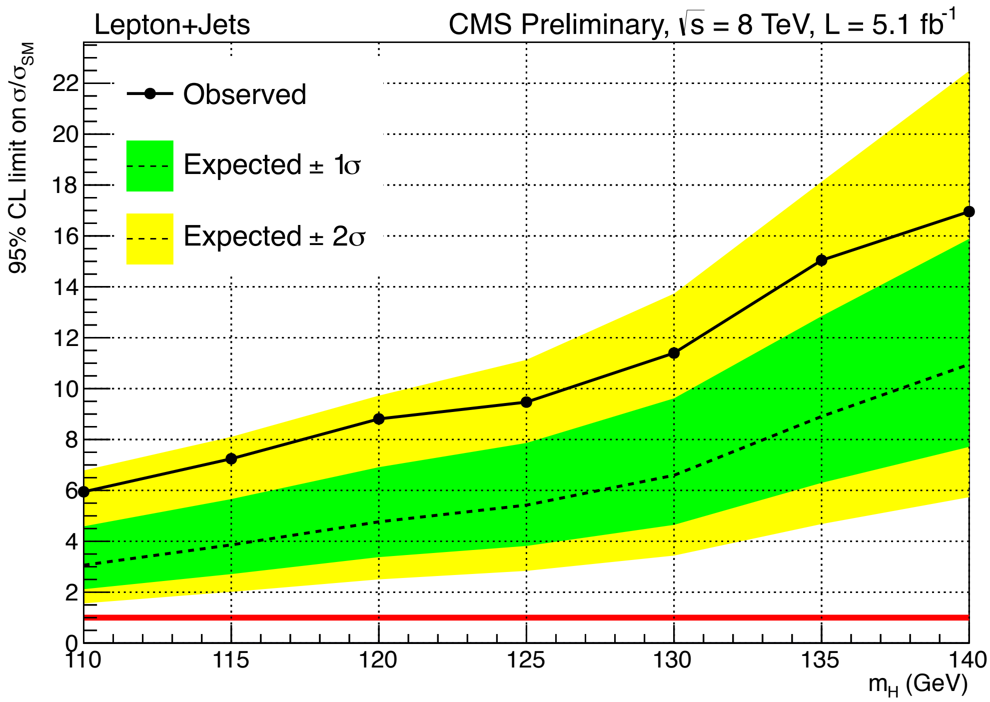

Figure 6.30: The expected and observed 95% CL upper limits on the signal strength parameter $\mu = \sigma/\sigma_{SM}$ for the lepton+jets channel using the 2012 dataset. These limits were extracted using the asymptotic method.

away from the expected factor of 5.2 from simulations alone.

The technique of using a simultaneous fit of the signal and background simulations accross each of the jet/tag categories was developed in the 7 TeV analysis. My specific contributions included the creation of software to identify physics objects with variables and selections optimized for the 8 TeV dataset. The validation of the selection was acheived by synchronization with a $t\bar{t}$ cross-section analysis, careful inspection of the calibration factors used, and the evaluation of the simulations against data in the lower jet and tag multiplicity categories (to avoid signal bias). Additionally, I was responsible for the training, testing, and validation of the CFMlpANN algorithm used in this analysis. Finally, I performed limit calculations and evaluated normalization and pull distributions using the asymptotic limit setting method to validate the performance of the limit setting technique.

Chapter 7

Analysis II: The Complete 19.5 fb^{-1} of 8 TeV data

The CMS experiment recorded 19.5 fb^{-1} of data in the complete 8 TeV run during 2012. The previous analysis was updated with the full dataset. A similar lepton and jet selection is used, with the same classification scheme for events, based on the reconstructed jet and b-tag multiplicity. New signal and background simulations were generated to account for the increased dataset, requiring new calibration factors for the pileup, lepton and jet reconstruction, and b-tagging efficiency. Additionally, a new type of multivariate analysis (MVA) technique was employed, in place of the Clermond-Ferrand Multi-Layer Perceptron Artificial Neural Network (CFMlpANN), a Boosted Decision Tree (BDT) is used for signal extraction and limit setting. The number of input variables that were investigated for use in each jet/tag category, was expanded, and some new variables were found to offer slightly more discriminating power. The discrimant of a specialized BDT, trained to separate $t\bar{t} + b\bar{b}$ from $t\bar{t}H$, was added as an input variable to the BDT trained in the 5 jet, $\geq$4 b-tag; $\geq$6 jet, 3 b-tag; and $\geq$6 jet, $\geq$4 b-tag categories.

7.1 Data and Simulated Samples

As described in the earlier chapters, data is collected through an HLT trigger path and stored offline for analysis later. Simulated samples are generated with the latest theoretical and empirical inputs for the proton PDF, standard model cross sections, and hadronic showering. These events are processed with a simulation of the detector environment, and the subsequent electronic response of each of its elements. Finally, physics objects, such as electrons, and muons are reconstructed with the particle-flow algorithm described in a previous chapter.

7.1.1 Data Samples

The results presented here are based on the full ∼19.5 fb^{-1} of the 2012 CMS dataset. Table 7.1 lists the datasets used for this analysis, based on single muon and single electron triggers used to collect the data. Luminosities are quoted from the HF luminosity calculation and have a 2.2% uncertainty.

Dataset	Run Range	Integrated Luminosity
SingleMu, Run2012A	190456–193621	0.81 fb^{-1}
SingleMu, Run2012A	190782–190949	0.08 fb^{-1}
SingleMu, Run2012B	193834–196531	4.40 fb^{-1}
SingleMu, Run2012C	198022–198523	0.50 fb^{-1}
SingleMu, Run2012C	198941–203746	6.39 fb^{-1}
SingleMu, Run2012D	203768–208686	7.27 fb^{-1}
Total SingleMu	**190645–208686**	**19.5 fb^{-1}**
SingleElectron, Run2012A	190456–193621	0.81 fb^{-1}
SingleElectron, Run2012A	190782–190949	0.08 fb^{-1}
SingleElectron, Run2012B	193834–196531	4.40 fb^{-1}
SingleElectron, Run2012C	198022–198523	0.50 fb^{-1}
SingleElectron, Run2012C	198941–203746	6.40 fb^{-1}
SingleElectron, Run2012D	203768–208686	7.27 fb^{-1}
Total SingleElectron	**190645–208686**	**19.5 fb^{-1}**

Table 7.1: The datasets analyzed for this analysis.

7.1.2 Signal Samples

The $t\bar{t}H$ signal is modeled using the Pythia Monte Carlo generator. The samples and associated cross sections used are listed in Table 7.2.

Mass	Higgs Decay	Dataset	Cross Sect.
110 GeV/c^2	$H \to$ all	TTH, Inclusive Decays $M_H = 110$, Pythia6	0.1887 pb
115 GeV/c^2	$H \to$ all	TTH, Inclusive Decays $M_H = 115$, Pythia6	0.1663 pb
120 GeV/c^2	$H \to$ all	TTH, Inclusive Decays $M_H = 120$, Pythia6	0.1470 pb
122.5 GeV/c^2	$H \to$ all	TTH, Inclusive Decays $M_H = 122.5$, Pythia6	0.1383 pb
125 GeV/c^2	$H \to$ all	TTH, Inclusive Decays $M_H = 125$, Pythia6	0.1302 pb
127.5 GeV/c^2	$H \to$ all	TTH, Inclusive Decays $M_H = 127.5$, Pythia6	0.1227 pb
130 GeV/c^2	$H \to$ all	TTH, Inclusive Decays $M_H = 130$, Pythia6	0.1157 pb
135 GeV/c^2	$H \to$ all	TTH, Inclusive Decays $M_H = 135$, Pythia6	0.1031 pb
140 GeV/c^2	$H \to$ all	TTH, Inclusive Decays $M_H = 140$, Pythia6	0.09207 pb

Table 7.2: List of signal MC datasets and cross sections used to determine the SM expectation.

7.1.3 Background Samples

To model the backgrounds, this analysis primarily uses Monte Carlo (MC) samples from the "Summer12" MC campaign, discussed in the previous chapter. Most of the samples are generated either with the Madgraph tree-level matrix element generator matched to Pythia for the parton shower, or with the NLO generator Powheg combined with Pythia. These samples are reconstructed with the same CMSSW version as the data samples listed above. Similarly to the previous analysis, the pileup distribution in all MC samples is reweighted, using the procedure listed below so that the MC pileup distribution matches the one expected for data. Table 7.3 lists the background MC samples and associated cross sections.

For this analysis, the $t\bar{t}+jets$ background, is decomposed into four components. The $t\bar{t}+b\bar{b}$, background is separated into two classes: $t\bar{t}+b\bar{b}$ events in which both b-quarks are well separated and energetic enough to be reconstructed, and events in which either the two b-quarks are so close together they merge into the same jet or one of the b-quarks is too soft or forward to be reconstructed as a jet. The latter contribution is referred to as $t\bar{t}\ +b$.

Sample	Dataset	Cross Sect.
$t\bar{t}$+ jets		
$t\bar{t} \to$ all	TTJets, Inclusive Decays, Madgraph	245.8 pb
$t\bar{t} \to$ jets	TTJets, Hadronic Decays, Madgraph	112.33 pb
$t\bar{t} \to \ell\nu + 4$ jets	TTJets, Semileptonic Decays, Madgraph	107.66 pb
$t\bar{t} \to \ell\nu\ell\nu + 2$ jets	TTJets, Fully Leptonic Decays, Madgraph	25.81 pb
$t\bar{t} + W$	TTWJets, Madgraph	0.249 pb
$t\bar{t} + Z$	TTZJets, Madgraph	0.208 pb
W+ jets	WJets to Leptons, Madgraph	36257.2 pb
$W + 1$ jet	W+1Jet to Leptons, Madgraph	6440.4 pb
$W + 2$ jets	W+2Jets to Leptons, Madgraph	2087.2 pb
$W + 3$ jets	W+3Jets to Leptons, Madgraph	619.0 pb
$W + 4$ jets	W+4Jets to Leptons, Madgraph	255.2 pb
Z/γ^*+ jets		
10 GeV/c^2 $< M_{\ell\ell} <$50 GeV/c^2	DYJets to Leptons, $10 < M_{\ell\ell} < 50$ GeV, Madgraph	14702 pb
$M_{\ell\ell}\ >\ 50$ GeV/c^2	DYJets to Leptons, $M_{\ell\ell} > 50$ GeV, Madgraph	3505.7 pb
$Z/\gamma^* + 1$ jet	DY+1Jet to Leptons, $M_{\ell\ell} > 50$ GeV, Madgraph	666.7 pb
$Z/\gamma^* + 2$ jets	DY+2Jets to Leptons, $M_{\ell\ell} > 50$ GeV, Madgraph	215.1 pb
$Z/\gamma^* + 3$ jets	DY+3Jets to Leptons, $M_{\ell\ell} > 50$ GeV, Madgraph	66.07 pb
$Z/\gamma^* + 4$ jets	DY+4Jets to Leptons, $M_{\ell\ell} > 50$ GeV, Madgraph	27.38 pb
Single t		
s-channel	T, s-channel, Powheg	3.79 pb
t-channel	T, t-channel, Powheg	56.4 pb
tW	T, tW-channel, Powheg	11.1 pb
Single $\bar{t}$		
s-channel	$\bar{T}$, s-channel, Powheg	1.76 pb
t-channel	$\bar{T}$, t-channel, Powheg	30.7 pb
tW	$\bar{T}$, tW-channel, Powheg	11.1 pb
WW	WW, Pythia6	54.8 pb
WZ	WZ, Pythia6	32.3 pb
ZZ	ZZ, Pythia6	7.7 pb

Table 7.3: List of background MC datasets and cross sections used for normalization.

7.1.4 MC pileup reweighting

As discussed in section 6.1.4, the large instantaneous luminosities provided by the LHC result in the overlap of multiple proton-proton collisions during a single read-out window. These "pileup events" affect many aspects of the reconstruction, including lepton isolation and jet energy resolution, thus the simulated samples must accurately reproduce these effects.

As with the last analysis, for the simulation, it is known how many additional interactions were added to every generated event. For the data, the number of pileup interactions for each unit of time depends on the instantaneous luminosity for each bunch pair and the total inelastic cross section, $\sigma_{inelastic}$. Empirically, it was found that $\sigma_{inelastic} = 69.4$ mb described the data well.

Changing of this value by ±7% are used for the ±1σ variations for the associated systematic uncertainty. Figure 7.1 shows the number of reconstructed vertices for data and for the $t\bar{t}$ MC sample, both before and after pileup reweighting. After reweighting, the data and MC distributions agree very well, indicating that the pileup reweighting is working as expected.

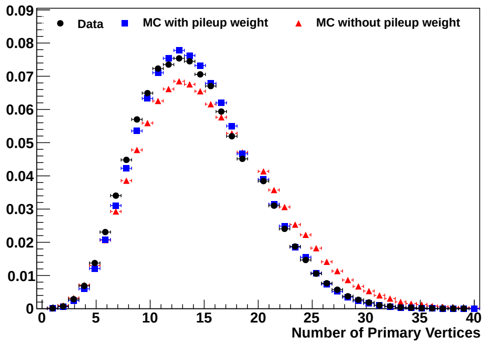

Figure 7.1: Comparison of number of reconstructed vertices for data (black) and the sum of all background MC samples before (red) and after (blue) pileup reweighting. After pileup reweighting, the MC matches the data well.

7.1.5 Top p_{T} Reweighting

It has been observed that the spectra of leptons and jets produced from top quark decays have softer p_{T} distribution than are predicted by the Monte Carlo. Investigations have show that the p_{T} spectra of leptons and jets is softer than data and have traced this expected to the top quark p_{T} distribution [169, 170]. Measurements of the differential cross section for top pair production as a function of the top quark p_{T}, have allowed for the creation of correction factors for this effect. These predictions of the $t\bar{t}$ +jets Monte Carlo are also more consistent with calculations done at approximate NNLO accuracy. This correction factor replaces the additional pileup reweighting factor based on the H_T distribution, binned by number of reconstructed vertices.

The scale factor used to correct the Madgraph top quark p_{T} distributions are shown in figure 7.2. The associated uncertainty is a band shown in green, and corresponds to no correction factor for the down variation, and a doubling of the correction factor for the up variation. The scale factors are taken from a polynomial of the form:

$$SF = 1.18246 + 2.10061 \times 10^{-6} p_{\mathrm{T}} \left(p_{\mathrm{T}} - 2 \times 463.312\right)$$

For $p_{\mathrm{T}} > 463.312\,\mathrm{GeV}/c$, a constant scale factor of 0.732 is used.

The top p_{T} scale factor improves the agreement between data and Monte Carlo. Figure 7.3

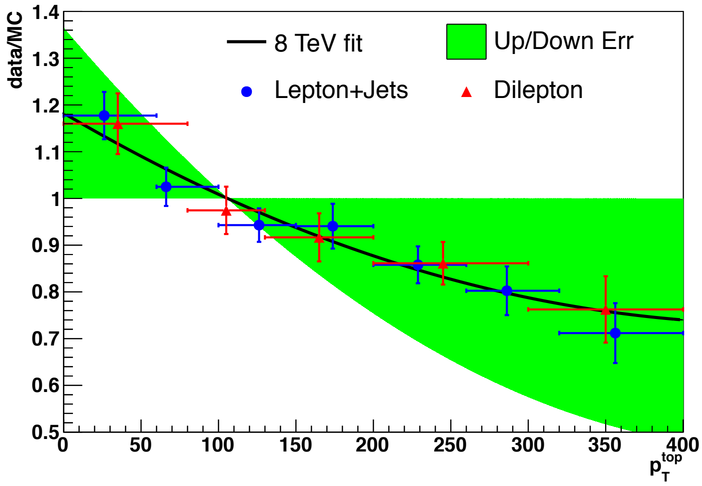

Figure 7.2: The scale factors from top differential crosse section group, the fitting as well as the $\pm 1\sigma$ variations.

compares the leading jet p_{T} distributions before and after reweighting. Before the correction, the leading jet p_{T} ratio plot forms a line with a slope, which is removed after the correction.

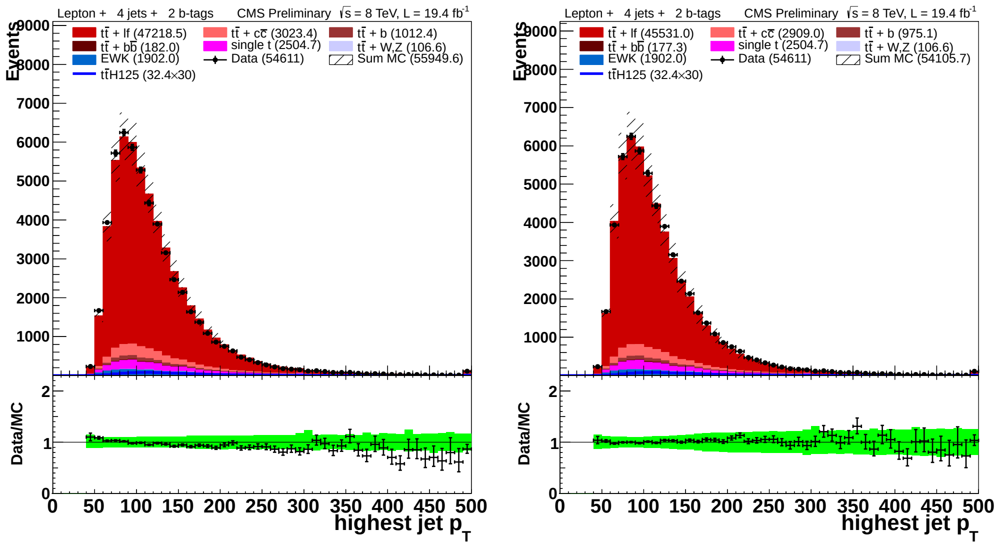

Figure 7.3: Leading jet p_{T} distribution for 8 TeV lepton plus jet events with ≥ 4 jets and ≥ 2 tags. The left-hand plot shows the distribution before top p_{T} reweighting. The right-hand plot shows the distribution after top p_{T} reweighting. Note that the ratio in the right-hand plot is flatter than the left-hand plot.

7.2 Event Selection

This section defines the common physics objects and event selection requirements. Events are required to pass quality filters, ensuring optimal operation of electronics and reconstruction, as described in section 6.2.1. The same lepton selection is used that was employed in the previous analysis, with events being selected by triggers described in section **??**. Leptons are classified into two categories, tight and loose, defined for muons in section 6.2.3 and for electrons in 6.2.4. For this analysis, exactly one tight muon or exactly one tight electron is required and events with any additional loose leptons are rejected. Lepton reconstruction efficiency scale factors are discussed in 6.2.5. The selection for jets is also the same, with the same procedure for correcting the energy as in section 6.2.6. The only significant change to the event selection comes from the b-tag scale factors used to calibrate the differences between efficiency in data and simulation for the CSV algorithm.

7.2.1 b-tag discriminant reweighting

As described in section 6.2.7, the algorithm used to tag jets as coming from a b-quark, is the Combined Secondary Vertex (CSV) algorithm. Differences have been observed in the measured efficiency for b-tagging jets between data and simulation [153]. To account for these efficiency differences, a scale factor to correct the MC b-tagging efficiency. Moreover, we found that the CSV distribution of MC doesn't match that of data, there making it necessary to correct the shape of the discriminant distribution as well.

A b-tag CSV reweighting method has been developed to address not only the difference in efficiency, but the difference in the shape of the discriminant distribution as well [171]. The method is based on a "tag and probe" approach. Events with two leptons, and exactly two jets are initially selected. One jet is required to pass a "tight" working point, characterized by a CSV value with $\sim 90\%$ efficiency and $\leq 1\%$ mistag rate. Then, the other jet is required to pass the analysis working point to assess the efficiency there. The results are binned by p_T, η, jet flavor and CSV value.

For MC the truth is available to assess the efficiency. For data, the full 8 TeV DoubleMu, DoubleElectron and MuEG datasets taken in 2012 are used. The scale factors for heavy flavor jets were derived in the dilepton channel, using a $t\bar{t}$ enriched control sample dominated by events which have two b flavor jets from the top pair decay. The scale factors for light flavor jets in the dilepton channel, using a control sample dominated by Z+jets events where there are two light flavor jets. The scale factors for light flavor jets will account for the mis-tag efficiency discrepancy between data and MC. For events with one jet passing the tag requirements, the CSV distribution for the probe jet in given p_t and η bins. The total MC yields are normalized to the data yields. In order to account for heavy or light flavor contamination, the MC is divided into samples of heavy flavor and light flavor components and then non-relevant part from data is subtracted. The scale factor is then given by the ratio of subtracted data CSV distribution and the relevant MC CSV distribution, as shown below:

$$SF(CSV, p_t, \eta) = \frac{Data - MC_A}{MC_B} \tag{7.1}$$

where A, B = heavy flavor component or light flavor component.

Unlike the last analysis, where scale factors where applied to adjust the value of the CSV distribution, correction factor for this analysis is an event-by-event weight. If the jet is a b flavor jet, a heavy flavor scale factor is assigned to it; if it is a c flavor jet, a flat scale factor of 1.0 is applied, with the same uncertainty as a b flavor jet would receive; otherwise, if it is a light flavor jet, a light flavor scale factor is assigned. The total scale factor for the event is the product of all the scale factors of the jets:

$$SF_{total} = \prod_{i}^{N_{\mathrm{jets}}} SF_{jet_i} = SF_{jet_1} \cdot SF_{jet_2} \cdot ... \tag{7.2}$$

7.2.2 Lepton + Jets Selection

As with the previous analysis, the final selection requires events have exactly one tight lepton (e or μ), and at least four jets. Events with any additional loose or tight leptons are vetoed so this analysis can later be combined with a diLepton final state, without double counting events. Additionally, each event must have at least three jets with $p_T > 40$ GeV/c.

As before, events are further categorized by the reconstructed jet, and b-tagged jet multiplicities:

- $\geq$6 jets, ==2 b-tags: At least 6 jets, 2 of which are b-tagged
- ==4 jets, ==3 b-tags: Exactly 4 jets, 3 of which are b-tagged
- ==5 jets, ==3 b-tags: Exactly 5 jets, 3 of which are b-tagged
- $\geq$6 jets, ==3 b-tags: At least 6 jets, 3 of which are b-tagged
- ==4 jets, ==4 b-tags: Exactly 4 jets, 4 of which are b-tagged
- ==5 jets, ==4 b-tags: Exactly 5 jets, 4 of which are b-tagged
- $\geq$6 jets, $\geq$4 b-tags: At least 6 jets, with at least 4 of which are b-tagged

Table 7.4 gives the event yield for MC backgrounds, both the total and each contribution, the expected event yield for signal $t\bar{t}H$ (m_H = 125 GeV/c^2), and the data observed in each category. Figure 7.4 shows the data/MC comparison for the number of jets and the number of tagged jets distributions for events with one lepton (e or μ), $\geq$ 4 jets and $\geq$ 2 b-tags, it also includes a plot showing the event yields for data and each MC background in each category.

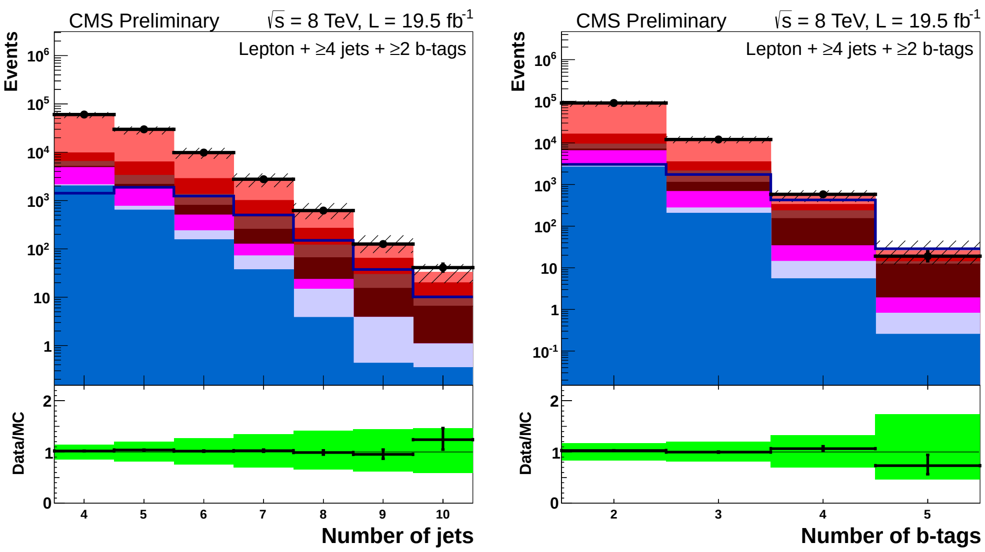

Figure 7.4: Comparison of yields for the different categories (top), number of jets (bottom left), and number of tagged jets (bottom right) in data and Monte Carlo for events with one lepton μ or e, $\geq$ 4 jets and $\geq$ 2 tags.

	≥6 jets 2 tags	4 jets 3 tags	5 jets 3 tags	≥6 jets 3 tags	4 jets 4 tags	5 jets ≥4 tags	≥6 jets ≥4 tags
$t\bar{t}H(125)$	33.4 ± 8.1	14.0 ± 3.0	21.1 ± 4.5	23.1 ± 5.5	1.8 ± 0.5	5.2 ± 1.4	8.3 ± 2.3
$t\bar{t}$+lf	7650 ± 2000	4710 ± 820	2610 ± 530	1260 ± 340	74 ± 30	79 ± 34	71 ± 36
$t\bar{t}+b$	530 ± 300	350 ± 190	360 ± 200	280 ± 160	21 ± 12	29 ± 17	33 ± 20
$t\bar{t}+b\bar{b}$	220 ± 120	99 ± 52	158 ± 85	200 ± 110	13.1 ± 7.3	38 ± 21	78 ± 47
$t\bar{t}+c\bar{c}$	1710 ± 1110	440 ± 230	520 ± 290	470 ± 280	19 ± 11	32 ± 18	52 ± 31
$t\bar{t}V$	99 ± 27	16.2 ± 3.8	23.9 ± 5.7	28.8 ± 7.4	1.1 ± 0.4	2.5 ± 0.7	5.8 ± 1.8
Single t	264 ± 54	235 ± 41	116 ± 22	55 ± 14	3.4 ± 1.6	10.3 ± 5.3	7.3 ± 3.1
V+jets	160 ± 110	122 ± 95	44 ± 38	29 ± 27	2.1 ± 2.4	1.9 ± 1.7	1.2 ± 1.3
Diboson	5.9 ± 1.6	6.3 ± 1.4	2.4 ± 0.7	1.0 ± 0.4	0.3 ± 0.2	0.1 ± 0.1	0.2 ± 0.1
Total bkg	10630 ± 2790	5970 ± 1060	3830 ± 790	2310 ± 620	133 ± 44	193 ± 62	249 ± 90
Data	10724	5667	3983	2426	122	219	260

Table 7.4: Observed data event yields, expected event yields in 19.5 fb^{-1} for signal and backgrounds in the lepton+jets channel.

7.3 Multivariate Analysis

The MVA technique used to analyze the full 8 TeV dataset is a Boosted Decision Tree (BDT). Each jet/tag category is trained with half of the simulated $t\bar{t}H$ events for signal, and half of the simulated $t\bar{t} + jets$ events as background. The top 10 variables, ranked with the separation figure of merit given in equation 6.10, are used as input variables. The BDT distribution of the discriminant is then used for signal extraction and limit setting.

7.3.1 Boosted Decision Tree Overview

A Boosted Decision Tree (BDT) is a code structure that makes a sequence of binary decisions to classify events as either signal-like or background-like [155]. For this analysis, the BDT uses

10 input variables for each jet/tag category. The BDT looks at the distribution of events for signal and background, with 40 bins with a maximum and minimum value determined by the the largest and smallest values respectively for either the signal or the background. Out of these 10 variables, the BDT selects the variable which maximizes the Ginni Index, which is given by the equation:

$$GiniIndex = p \times (1 - p) \tag{7.3}$$

where the purity, $p = s/b$, is the ratio of the integral number of signal, s, events and background, b, events above or below the cut value chosen by the BDT. This effectively tries to find a cut on a variable that maximizes the amount signal in sample afterwards, creating a background-like set of events, and a signal-like set of events. After the first cut is chosen, the distributions for each of the variables above and below the cut value are are re-examined. A second cut on a variable, at a point that maximizes the Ginni Index is found, for each of the signal and background-like regions formed by the first cut. This process continues for a user-defined number of cuts. Since the input events are known to be singal-like or background-like, the purity of the final region that an event is classified as is used as the output for this set of decisions, known as a decision tree. Figure 7.5 shows a diagram of the general process.

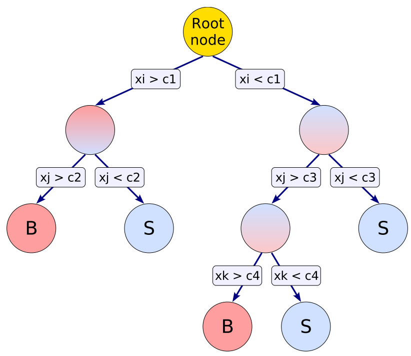

Figure 7.5: Example of a decision tree, which chooses a set of variables to cut on, in order to produce a region of events with high signal purity

The BDT in this analysis uses 5 cuts for a single tree. The reason for using a small number, is that the BDT employs a process known as ”boosting” to enhance its discriminating power.

Boosting is the process of using multiple, or a forest, of individual decision trees to cast a majority vote for the decision to classify the event as signal-like or background-like [155]. Events from the training sample, which were misclassified, are given a larger weight, making their contribution to the distributions of the input variable more prominent, making it more likely for the next decision tree to classify the event correctly. The final discriminant, $F(\hat{x}, P)$, of the forest of decision trees is given by:

$$F(\hat{x}, P) = \sum_{m=0}^{M} \beta_m f(x; a_m); \quad P \in (\beta_m; a_m)_0^M \tag{7.4}$$

where P is the set of parameter, whose values are optimized to create an optimized classification decision. For M trees in the forest, β_m is the weight for the output of a single decision tree, $f(x; a_m)$, which is the purity, s/b of the final region of the tree an individual event is classified into. The set of input variables for a single decision tree, m, is denoted by a_m.

This analysis uses the "Gradient" method of boosting [155]. After the first tree is has been built, the "loss function", $L(F, y)$, is calculated with the function:

$$L(F, y) = ln\left(1 + e^{-2F(\hat{x})y}\right) \tag{7.5}$$

where y is the true value of the classification of the event (1 for signal, 0 for background). This function has a minimum value when all of the events have been classified correctly. The loss function is then minimized by varying the set of parameters, $P \in (\beta_m; a_m)_0^M$, using the steepest-descent method. A random selection of events are reweighted, and the loss-function is re-calculated. The error rate of classifying events for the previous tree is used to calculate the new weight, α, of events for the next tree:

$$\alpha = \frac{1 - err}{err} \tag{7.6}$$

where err is the error rate. After events are re-weighted, a new decision tree is created and the process is repeated, iteratively minimizing the loss function until a desired set of decision trees are created. This analysis uses a forest of 100 decision trees to separate the $t\bar{t}H$ signal from the $t\bar{t} + jets$ background.

Overtraining was checked in a similar procedure that was used in the last analysis. Half the events for the signal and background samples are used to train the BDT, the other half are used to test it. The response to the BDT is calculated for both the testing and training sample, and the Kolomogrov-Smirnoff statistic is used as a figure of merit to judge the compatibility of the two samples. As seen in figure 7.6, there are no significant deviations between the testing and training samples, implying that no overtraining has occurred.

7.3.2 MVA Input Variables, Data to Monte Carlo Comparisons

The set of 10 input variables for each jet/tag category were chosen through their ranking using the separation figure of merit given in equation 6.10. The categories most sensitive to signal, 5

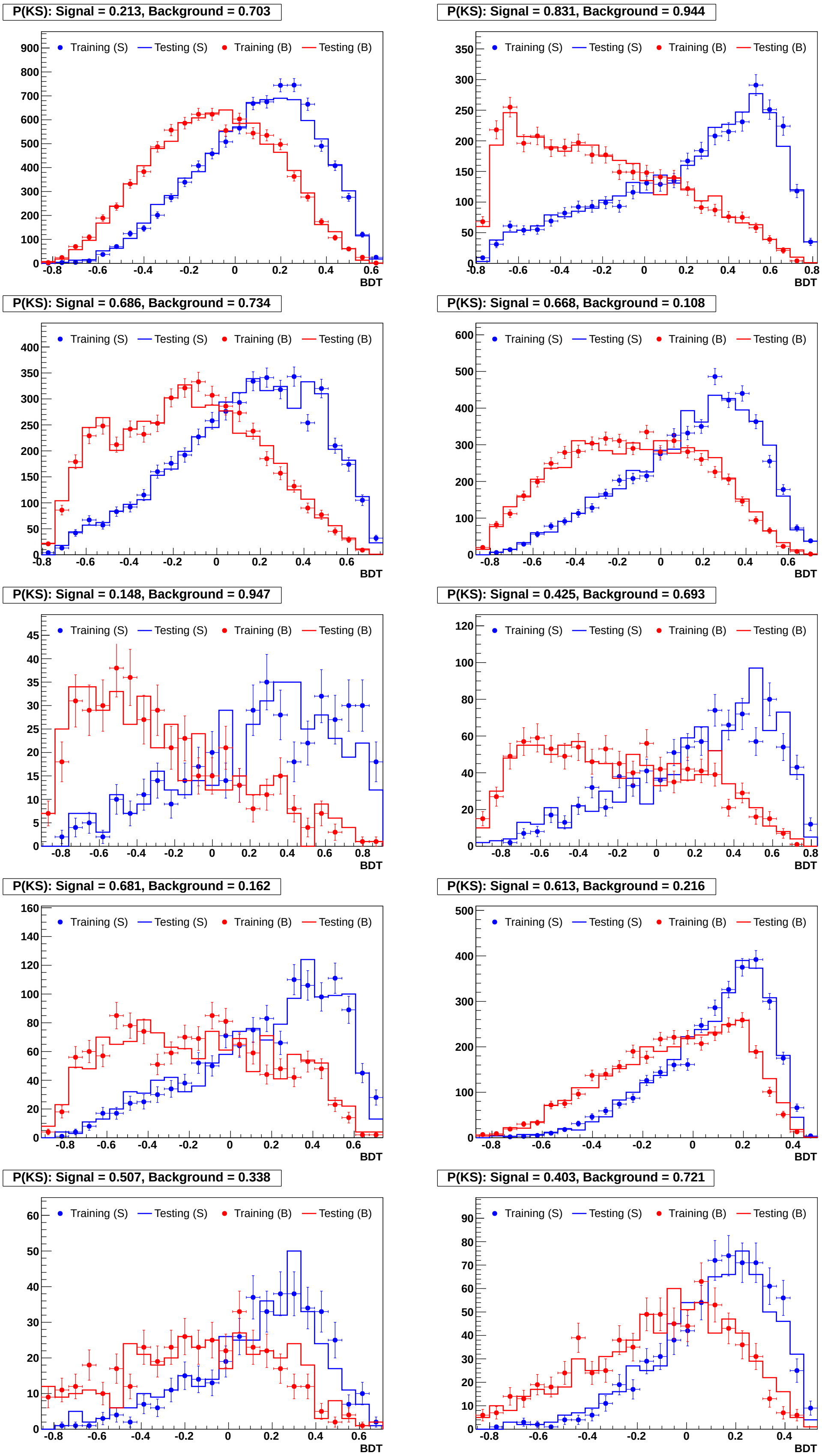

Figure 7.6: Comparisons of the testing and training samples used to optimize the BDT weights for each jet/tag category

jets, $\geq$4 b-tags; $\geq$6 jets, $\geq$3 b-tags; and $\geq$6 jets, $\geq$4 b-tags all include a variable, which is the output discriminant of a dedicated BDT trained to separate $t\bar{t}H$ signal from $t\bar{t}+b\bar{b}$ background. Table 7.5 gives a description of each of the input variables used. Table 7.6 describes which variables are used in each jet/tag category, and table 7.7 lists the variables used in the dedicated $t\bar{t}H$, $t\bar{t}+b\bar{b}$ BDT.

Table 7.5: Event variables used in dilepton and lepton+jets BDT training and their descriptions.

abs $\Delta\eta$ (leptonic top, bb)	Delta-R between the leptonic top reconstructed by the best Higgs mass algorithm and the b-jet pair chosen by the algorithm
abs $\Delta\eta$ (hadronic top, bb)	Delta-R between the hadronic top reconstructed by the best Higgs mass algorithm and the b-jet pair chosen by the algorithm
aplanarity	Event shape variable equal to $\frac{3}{2}(\lambda_3)$, where λ_3 is the third eigenvalue of the sphericity tensor as described in [?].
ave CSV (tags/non-tags)	Average b-tag discriminant value for b-tagged/non-b-tagged jets
ave ΔR(tag,tag)	Average ΔR between b-tagged jets
best Higgs mass	A minimum-chi-squared fit to event kinematics is used to select two b-tagged jets as top-decay products. Of the remaining b-tags, the invariant mass of the two with highest E_t is saved.
best ΔR(b,b)	The ΔR between the two b-jets chosen by the best Higgs mass algorithm
closest tagged dijet mass	The invariant mass of the two b-tagged jets that are closest in ΔR
dev from ave CSV (tags)	The square of the difference between the b-tag discriminant value of a given b-tagged jet and the average b-tag discriminant value among b-tagged jets, summed over all b-tagged jets
highest CSV (tags)	Highest b-tag discriminant value among b-tagged jets
H_0, H_1, H_2, H_3	The first few Fox-Wolfram moments [?] (event shape variables)
HT	Scalar sum of transverse momentum for all jets with $p_T > 30$ GeV/c
$\sum p_T$(jets,leptons,MET)	The sum of the p_T of all jets, leptons, and MET
$\sum p_T$(jets,leptons)	The sum of the p_T of all jets, leptons
jet 1, 2, 3, 4 p_T	The transverse momentum of a given jet, where the jet numbers correspond to rank by p_T
lowest CSV (tags)	Lowest b-tag discriminant value among b-tagged jets
mass(lepton,jet,MET)	The invariant mass of the 4-vector sum of all jets, leptons, and MET
mass(lepton,closest tag)	The invariant mass of the lepton and the closest b-tagged jet in ΔR
max $\Delta\eta$ (jet, ave jet η)	max difference between jet eta and avg delta eta between jets
max $\Delta\eta$ (tag, ave jet η)	max difference between tag eta and avg delta eta between jets
max $\Delta\eta$ (tag, ave tag η)	max difference between tag eta and avg delta eta between tags
median inv. mass (tag pairs)	median invariant mass of all combinations of b-tag pairs
M3	The invariant mass of the 3-jet system with the largest transverse momentum.
MHT	Vector sum of transverse momentum for all jets with $p_T > 30$ GeV/c
MET	Missing transverse energy
min ΔR(lepton,jet)	The ΔR between the lepton and the closest jet (LJ channel)
min ΔR(tag,tag)	The ΔR between the two closest b-tagged jets
min ΔR(jet,jet)	The ΔR between the two closest jets
$\sqrt{\Delta\eta(t^{lep}, bb) \times \Delta\eta(t^{had}, bb)}$	square root of the product of abs $\Delta\eta$ (leptonic top, bb) and abs $\Delta\eta$ (hadronic top, bb)
second-highest CSV (tags)	Second-highest b-tag discriminant value among b-tagged jets
sphericity	Event shape variable equal to $\frac{3}{2}(\lambda_2 + \lambda_3)$, where λ_2 and λ_3 are the second and third eigenvalues of the sphericity tensor as described in [?]
(Σ jet p_T)/(Σ jet E)	The ratio of the sum of the transverse momentum of all jets and the sum of the energy of all jets
tagged dijet mass closest to 125	The invariant mass of the b-tagged pair closest to 125 GeV/c^2
$t\bar{t}b\bar{b}/t\bar{t}H$ BDT	BDT used to discriminate between $t\bar{t}b\bar{b}$ and $t\bar{t}H$ in the LJ $\geq$ 6 jets, $\geq$ 4 tags, $\geq$6 jets + 3 tags, and 5 jets + $\geq$4 tags categories. See text for description and table 7.7 for list of variables.

The modeling of the input variables is compared against data for each of the jet/tag diagrams in the the following figures:

- $\geq$6 jets, ==2 b-tags: Figure 7.7
- ==4 jets, ==3 b-tags: Figure 7.8
- ==5 jets, ==3 b-tags: Figure 7.9

4 jets, 3 tags	4 jets, 4 tags
jet 1 p_T	jet 1 p_T
jet 2 p_T	jet 2 p_T
jet 3 p_T	jet 4 p_T
jet 4 p_T	HT
M3	$\sum p_T$(jets,lepton,MET)
$\sum p_T$(jets,lepton,MET)	M3
HT	ave CSV (tags)
lowest CSV (tags)	second-highest CSV (tags)
MHT	third-highest CSV (tags)
MET	lowest CSV (tags)
5 jets, 3 tags	**5 jets, $\geq$ 4 tags**
jet 1 p_T	max $\Delta\eta$ (tag, ave jet η)
jet 2 p_T	$\sum p_T$(jets,lepton,MET)
jet 3 p_T	(Σ jet p_T)/(Σ jet E)
jet 4 p_T	ave ΔR(tag,tag)
$\sum p_T$(jets,lepton,MET)	ave CSV (tags)
(Σ jet p_T)/(Σ jet E)	dev from ave CSV (tags)
HT	second-highest CSV (tags)
ave CSV (tags)	third-highest CSV (tags)
third-highest CSV (tags)	lowest CSV (tags)
fourth-highest CSV (jets)	ttbb/ttH BDT

$\geq$ 6 jets, 2 tags	$\geq$ 6 jets, 3 tags	$\geq$ 6 jets, $\geq$ 4 tags
$\sum p_T$(jets,lepton,MET)	H_0	(Σ jet p_T)/(Σ jet E)
HT	sphericity	ave ΔR(tag,tag)
mass(lepton,closest tag)	(Σ jet p_T)/(Σ jet E)	product($\Delta\eta$(leptonic top, bb), $\Delta\eta$(hadronic top, bb))
max $\Delta\eta$ (jet, ave jet η)	max $\Delta\eta$ (jet, ave jet η)	closest tag mass
min ΔR(lepton,jet)	$\sum p_T$(jets,lepton,MET)	max $\Delta\eta$ (tag, ave tag η)
H_2	ave CSV (tags)	ave CSV (tags)
sphericity	second-highest CSV (tags)	third-highest CSV (tags)
(Σ jet p_T)/(Σ jet E)	third-highest CSV (tags)	fourth-highest CSV (tags)
third-highest CSV (jets)	fourth-highest CSV (jets)	best Higgs mass
fourth-highest CSV (jets)	ttbb/ttH BDT	ttbb/ttH BDT

Table 7.6: BDT input variable assignments for the lepton+jets categories.

5 jets, $\geq$ 4 tags	$\geq$ 6 jets, 3 tags	$\geq$ 6 jets, $\geq$ 4 tags
ave ΔR(tag,tag)	tagged dijet mass closest to 125	H_3
max $\Delta\eta$ (tag, ave tag η)	(Σ jet p_T)/(Σ jet E)	ave ΔR(tag,tag)
(Σ jet p_T)/(Σ jet E)	$\sqrt{\Delta\eta(t^{lep}, bb) \times \Delta\eta(t^{had}, bb)}$	closest tagged dijet mass
tagged dijet mass closest to 125	H_1	sphericity
H_1	H_3	max $\Delta\eta$ (tag, ave jet η)
H_3	M3	max $\Delta\eta$ (tag, ave tag η)
$\sum p_T$(jets,lepton,MET)	max $\Delta\eta$ (tag, ave tag η)	mass(lepton,jet,MET)
fourth-highest CSV (tags)	max $\Delta\eta$ (tag, ave jet η)	(Σ jet p_T)/(Σ jet E)
aplanarity	max $\Delta\eta$ (jet, ave jet η)	abs $\Delta\eta$ (leptonic top, bb)
MET	abs $\Delta\eta$ (hadronic top, bb)	abs $\Delta\eta$ (hadronic top, bb)
	abs $\Delta\eta$ (leptonic top, bb)	$\sqrt{\Delta\eta(t^{lep}, bb) \times \Delta\eta(t^{had}, bb)}$
	sphericity	ave CSV (tags)
	aplanarity	best ΔR(b,b)
	min ΔR(tag,tag)	best Higgs mass
	jet 3 p_T	median inv. mass (tag pairs)

Table 7.7: List of variables used as inputs in each of the ttbb/ttH BDTs. See table 7.5 for definitions.

- $\geq$6 jets, ==3 *b*-tags: Figure 7.10, and Figure 7.11
- ==4 jets, ==4 *b*-tags: Figure 7.12
- ==5 jets, ==4 *b*-tags: Figure 7.13, and Figure 7.14
- $\geq$6 jets, $\geq$4 *b*-tags: Figure 7.15, and Figure 7.16

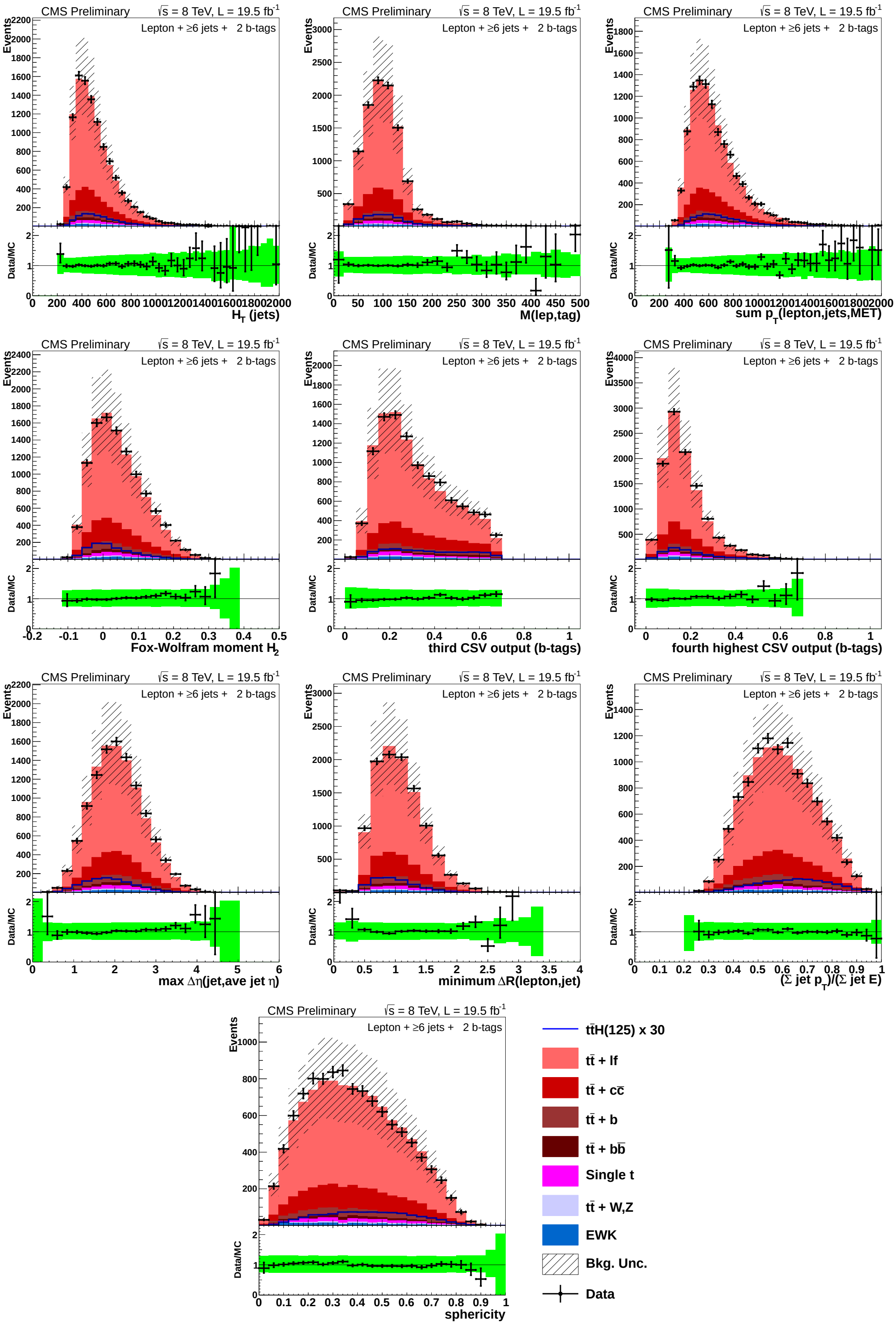

Figure 7.7: Data/MC comparisons for events with one lepton and ≥6 jets + 2b- tags. The uncertainty band includes statistical and systematic uncertainties that affect both the rate and shape of the background distributions.

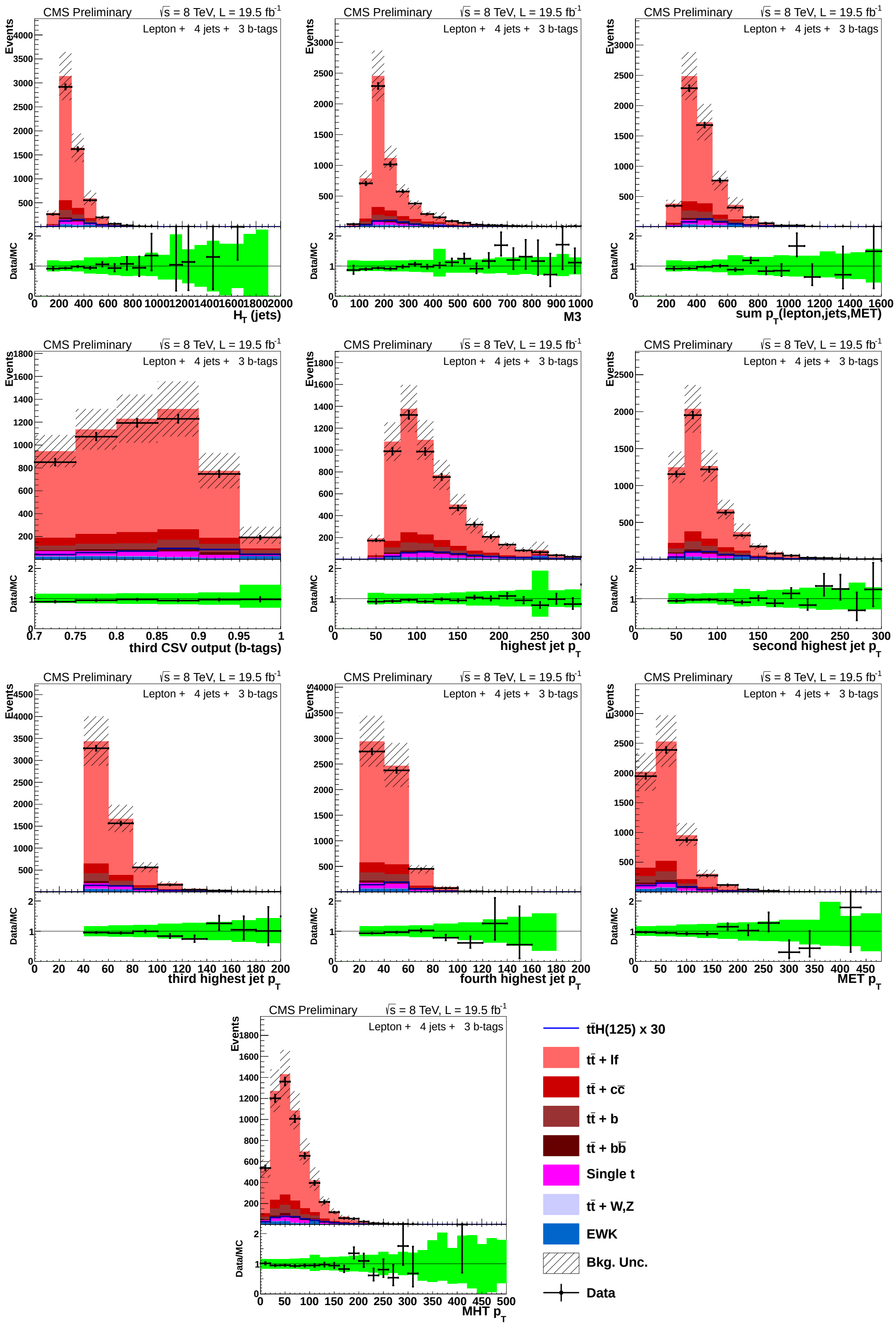

Figure 7.8: Data/MC comparisons for events with one lepton and 4 jets + 3 b-tags. The uncertainty band includes statistical and systematic uncertainties that affect both the rate and shape of the background distributions.

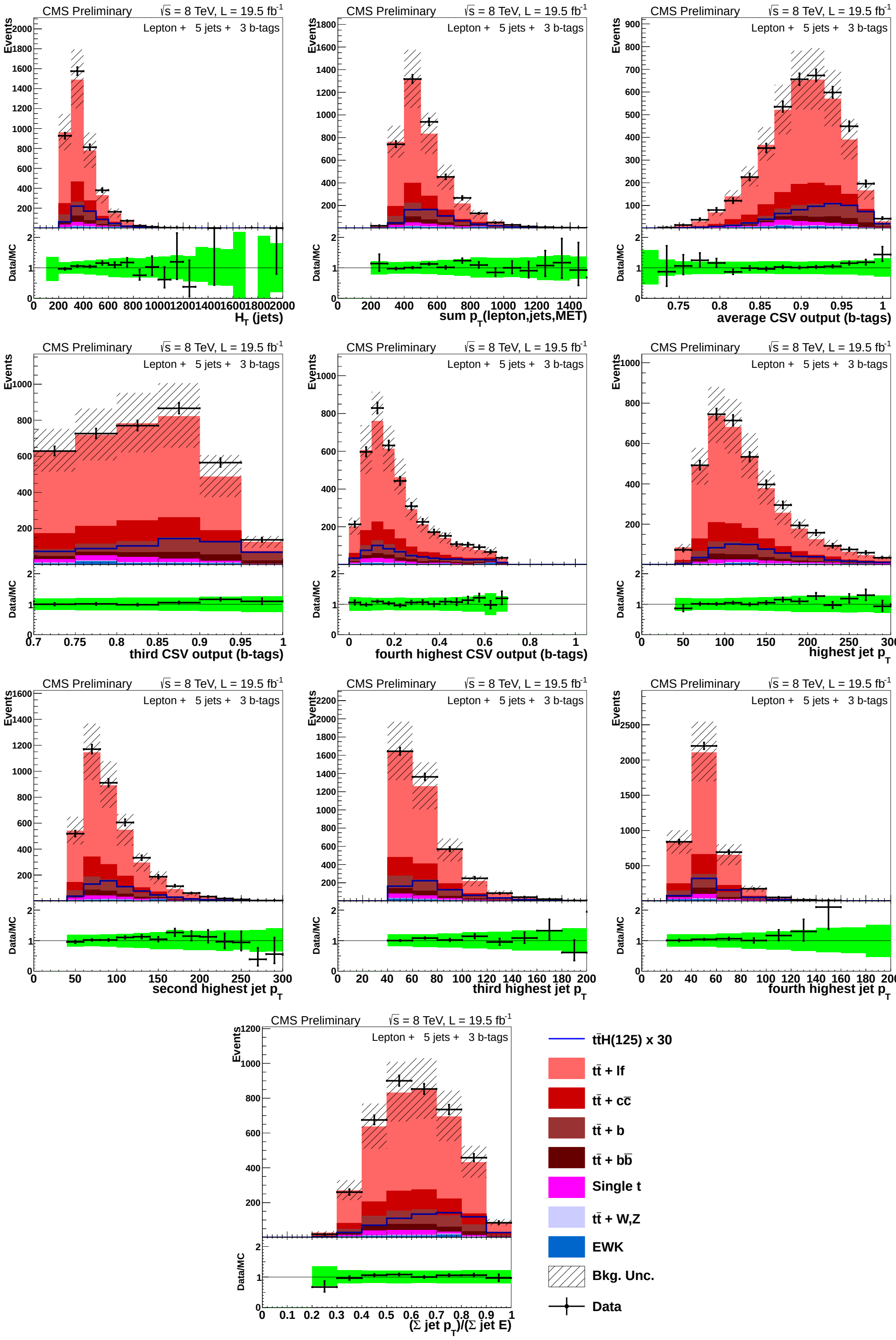

Figure 7.9: Data/MC comparisons for events with one lepton and 5 jets + 3 b-tags. The uncertainty band includes statistical and systematic uncertainties that affect both the rate and shape of the background distributions.

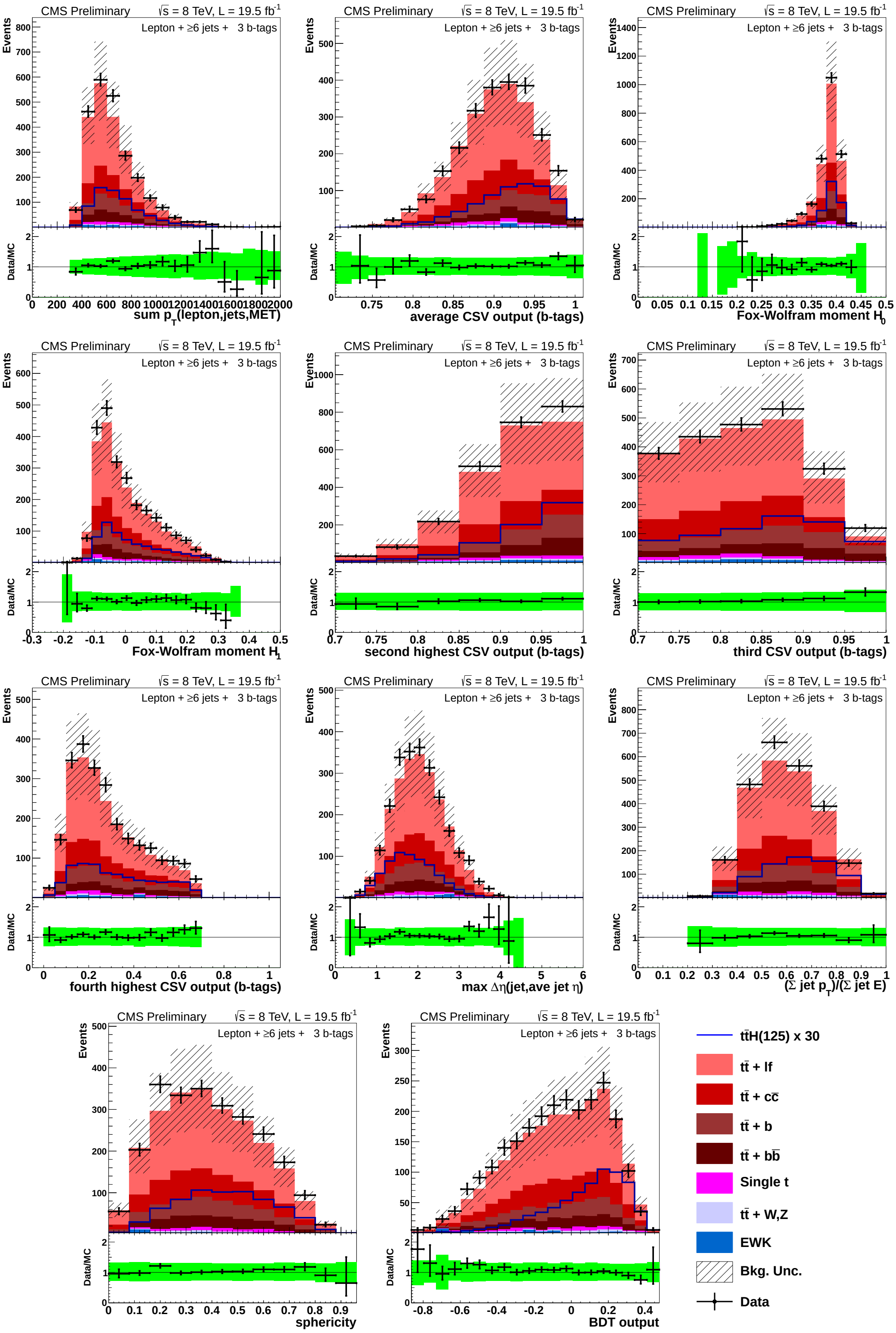

Figure 7.10: Data/MC comparisons for events with one lepton and ≥6 jets + 3 b-tags. The uncertainty band includes statistical and systematic uncertainties that affect both the rate and shape of the background distributions.

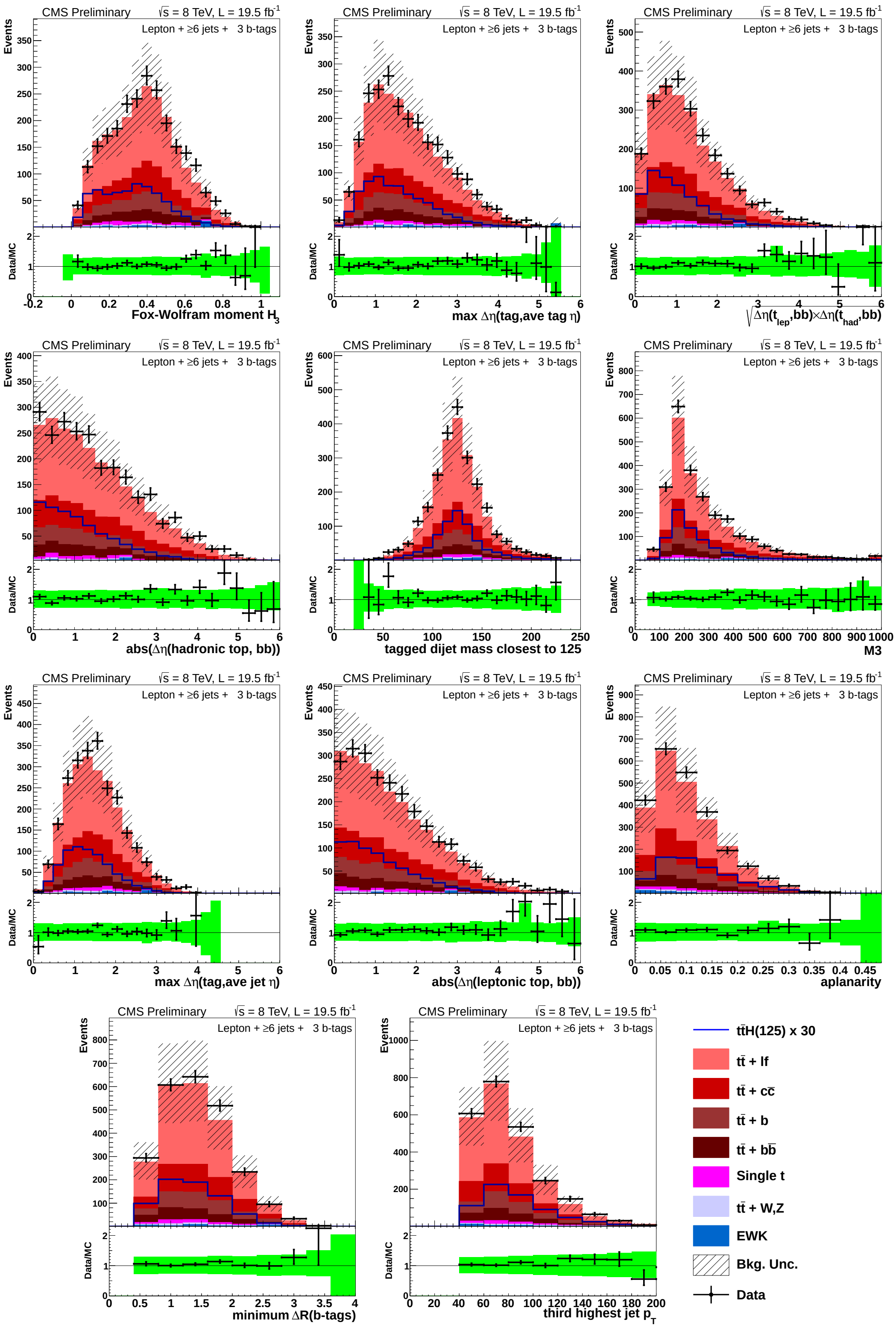

Figure 7.11: Data/MC comparisons for events with one lepton and ≥6 jets + 3 b-tags. The uncertainty band includes statistical and systematic uncertainties that affect both the rate and shape of the background distributions.

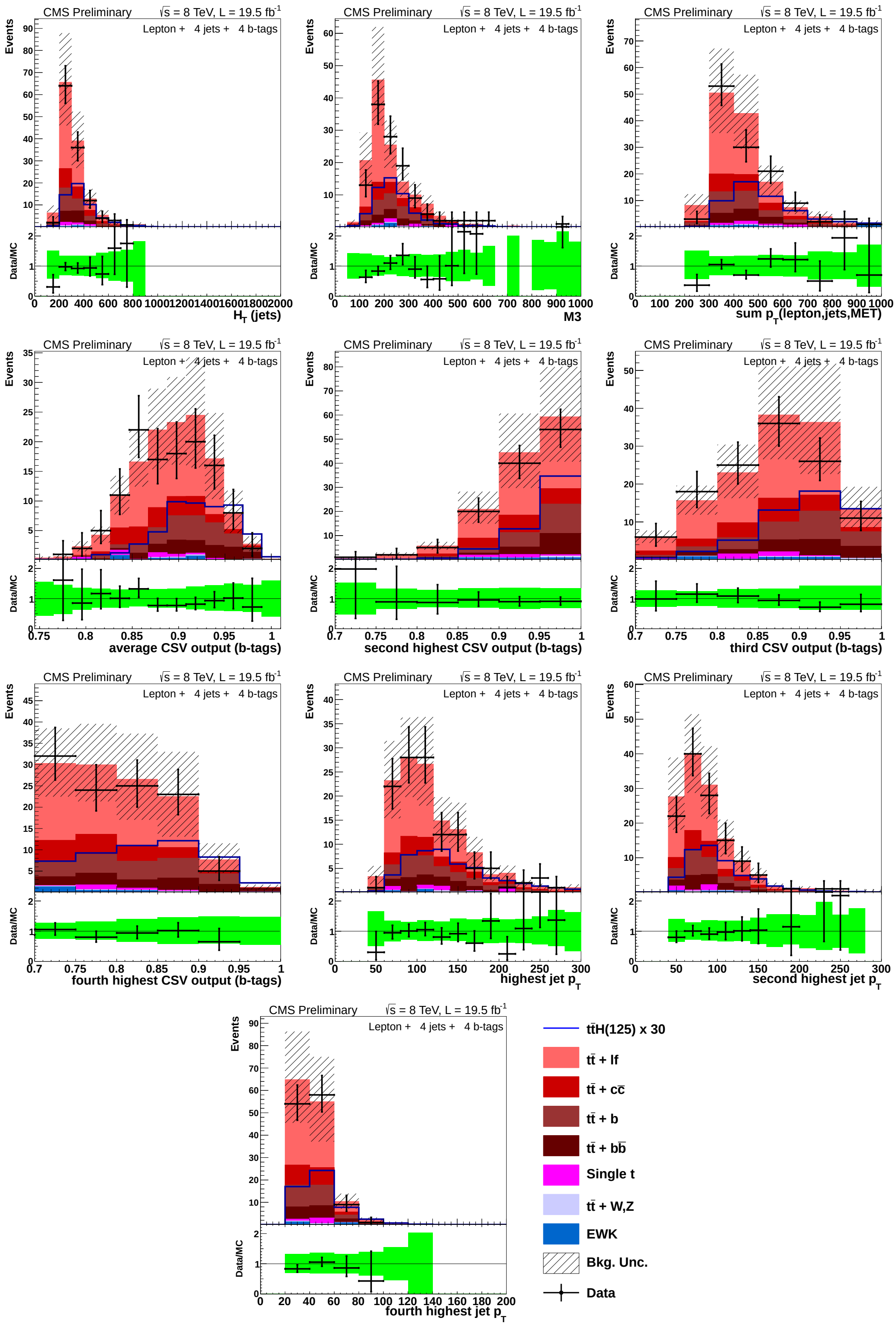

Figure 7.12: Data/MC comparisons for events with one lepton and 4 jets + 4 b-tags. The uncertainty band includes statistical and systematic uncertainties that affect both the rate and shape of the background distributions.

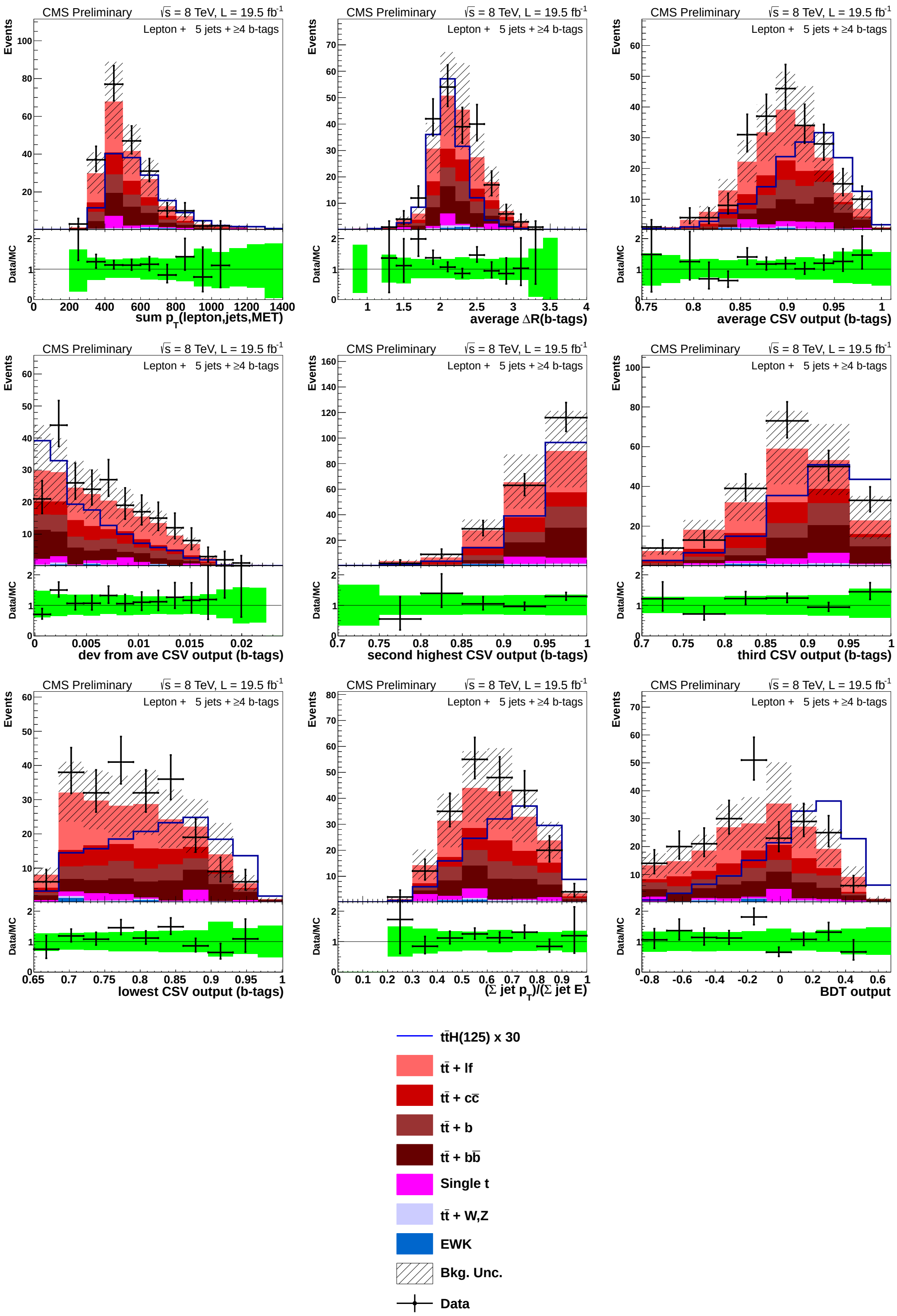

Figure 7.13: Data/MC comparisons for events with one lepton and 5 jets +≥4 b-tags. The uncertainty band includes statistical and systematic uncertainties that affect both the rate and shape of the background distributions.

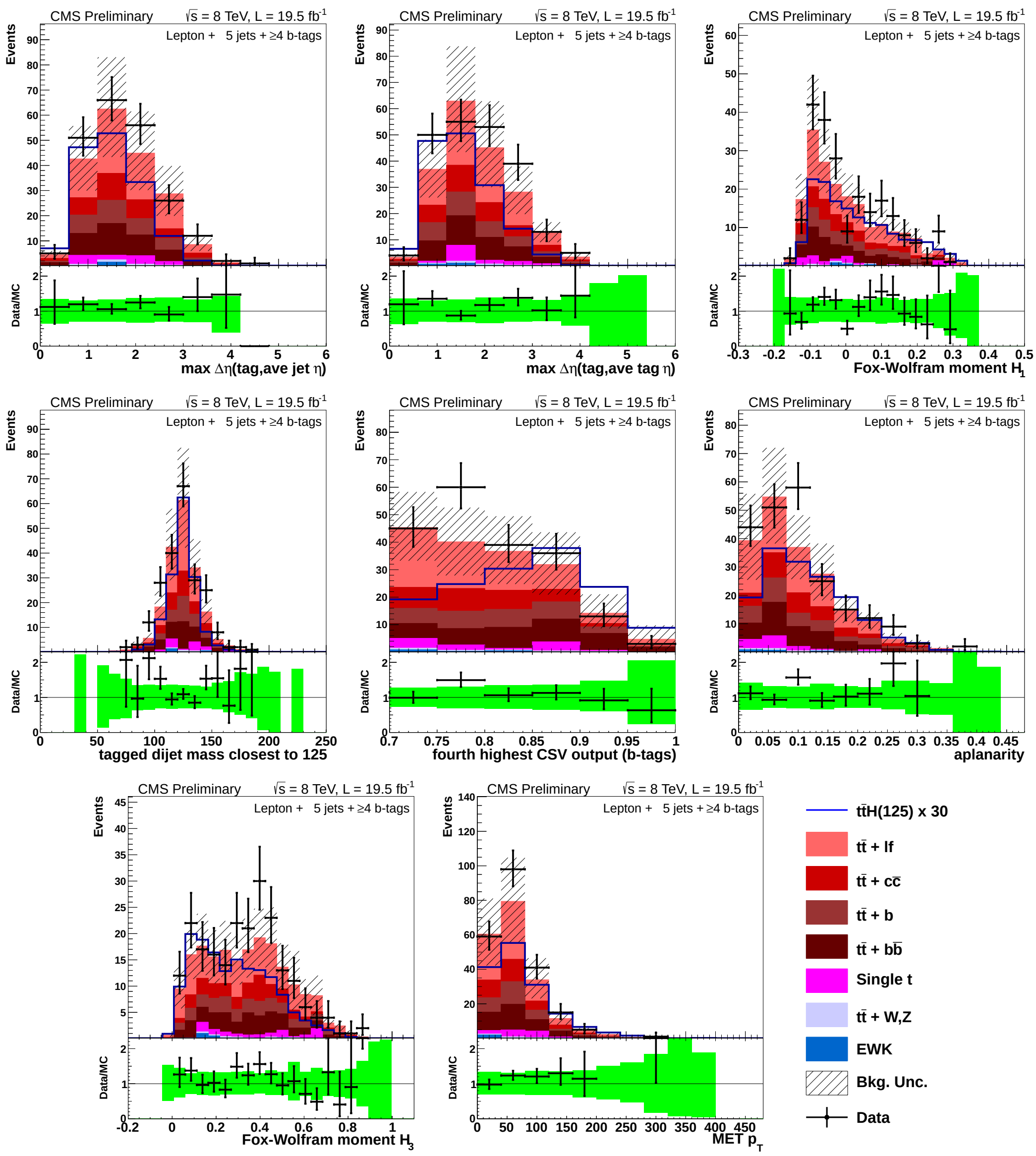

Figure 7.14: Data/MC comparisons for events with one lepton and 5 jets +≥4 b-tags. The uncertainty band includes statistical and systematic uncertainties that affect both the rate and shape of the background distributions.

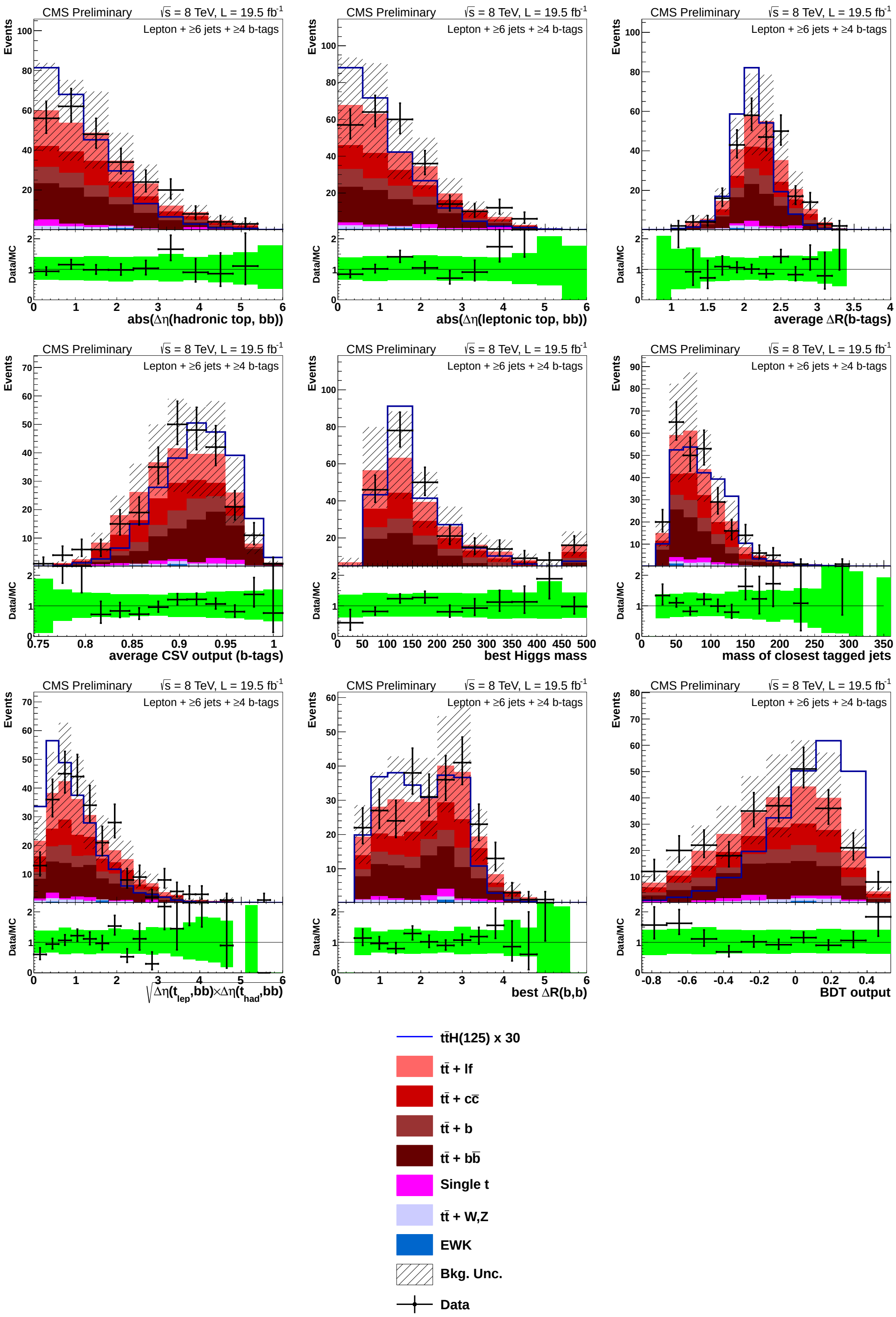

Figure 7.15: Data/MC comparisons for events with one lepton and ≥6 jets + ≥4 b-tags. The uncertainty band includes statistical and systematic uncertainties that affect both the rate and shape of the background distributions.

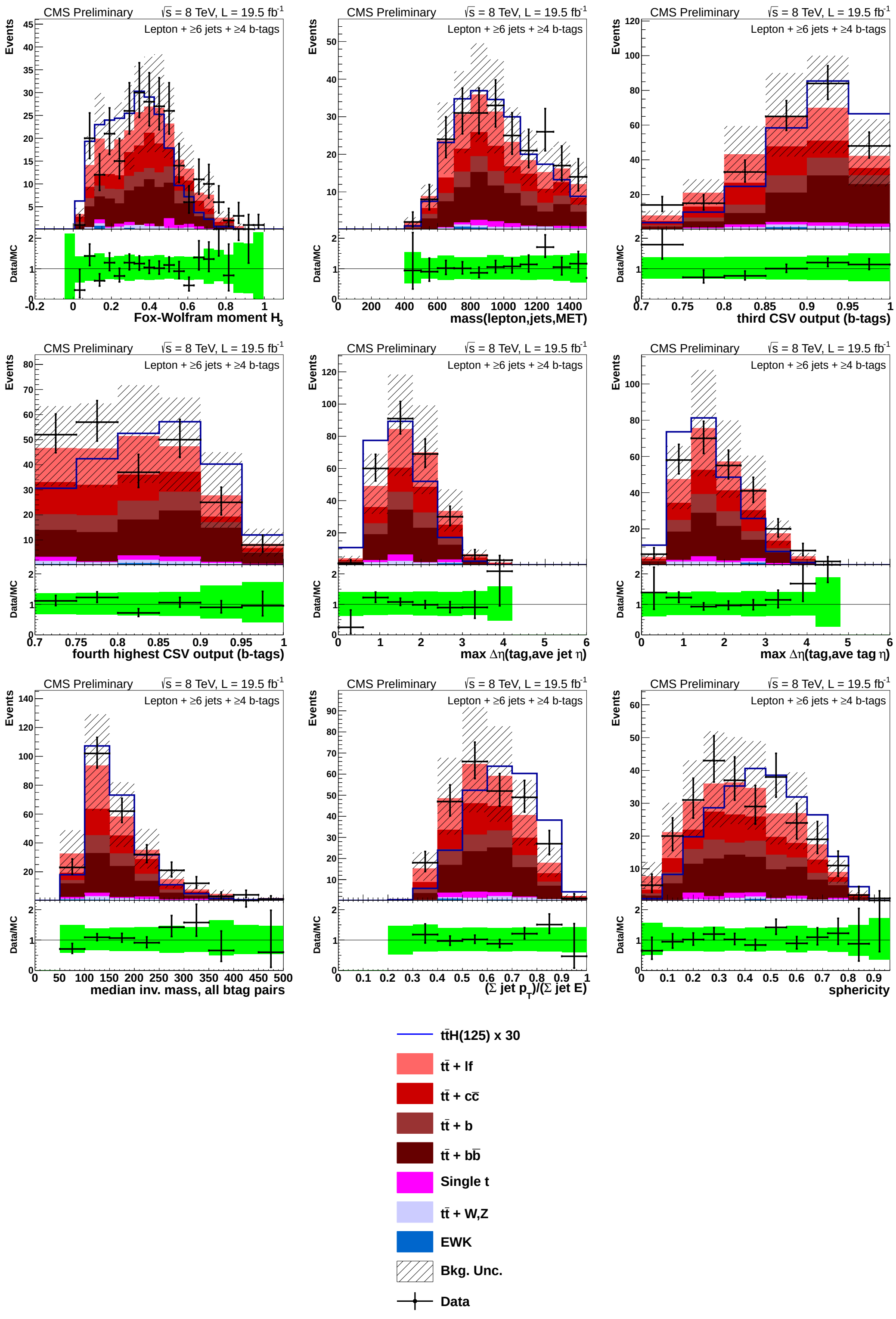

Figure 7.16: Data/MC comparisons for events with one lepton and $\geq$6 jets + $\geq$4 b-tags. The uncertainty band includes statistical and systematic uncertainties that affect both the rate and shape of the background distributions.

7.3.3 MVA Output, Data to Monte Carlo Comparisons

The distributions of the BDT output discriminators in each category are shown in Fig. 7.17. For these figures, the uncertainty band includes statistical and systematic uncertainties, e.g. JES and b-tag SF uncertainties, that are described in section 7.4.

7.4 Systematic Uncertainties

The evaluation of several of the systematic uncertainties follows the same procedure as described in the previous chapter. For these cases, the reader is directed to previous description of the uncertainty. Systematic uncertainties that are new to this analysis include those associated with the new b-tag calibration method and the top-p_T reweighting. Where appropriate, comparisons between the shapes of the nominal and $\pm 1\sigma$ variations are made.

Jet Energy Scale (JES): See section 6.4 for a description of the evaluation of this systematic. Shape comparisons between the nominal and the $\pm 1\sigma$ variations are shown in figure 7.18. Table 7.8 shows the effect on the rate for the ≥ 6 jets + ≥ 4 tags category.

JES systematic yield change			
		lepton+jets	
sys	shift	$t\bar{t}H(125)$	$t\bar{t}$ + $b\bar{b}$
JES	up	+9.1%	+8.3%
	down	-7.7%	-10.6%

Table 7.8: Relative yield change due to JES shift up/down for the $\geq$3 tag category in the dilepton channel and the ≥ 6 jets + ≥ 4 tags category in the lepton+jets channel.

Jet Energy Resolution (JER): See section 6.4 for a description of the evaluation of this systematic.

b-tag Scale Factors: New scale factors to account for the differences in in efficiency between data and simulation for the CSV b-tagging algorithm is described in section 7.2.1. There are three sources of systematic uncertainty on both the heavy flavor and light flavor scale factors: JES, purity, and statistics, and each source of variation is considered separately. The b-tag uncertainty associated with the JES is evaluated at the same time the overall JES uncertainty is considered. When the JES is shifted for the jet kinematics up or down by 1σ, the b-tag scale factor values, which depend on the p_T of the jet in question, shift as well. This correlates the b-tag uncertainty from JES with the overall JES uncertainty. The other two sources of b-tag uncertainty are each evaluated independently for light-flavor and heavy-flavor. The purity uncertainty is controlled by a separate nuisance parameter for light and heavy flavor. Variation of this parameter is associated with changing the pre-

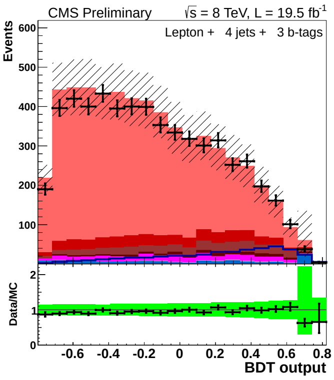

(a) 4 jets, 3 b-tags

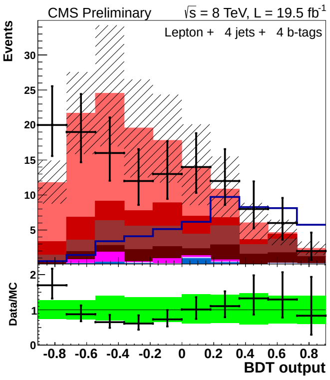

(b) 4 jets, 4 b-tags

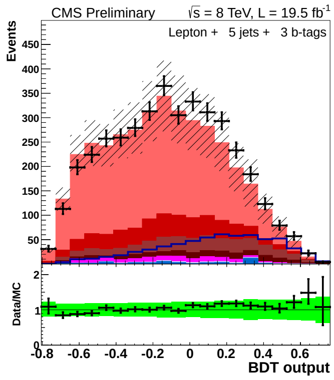

(c) 5 jets, 3 b-tags

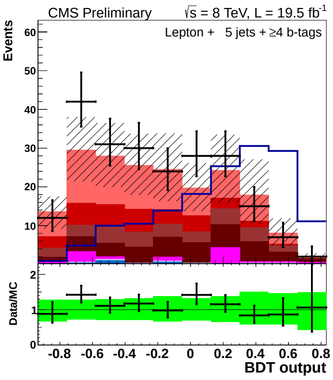

(d) 5 jets, ≥4 b-tags

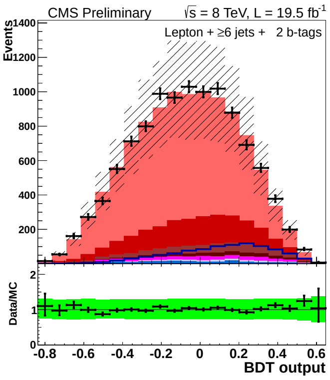

(e) ≥6 jets, 3 b-tags

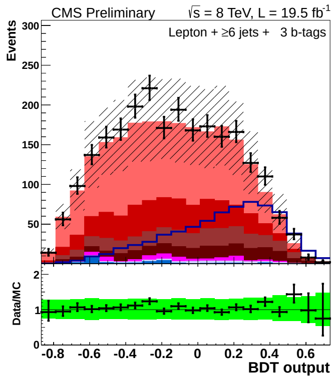

(f) ≥6 jets, 3 b-tags

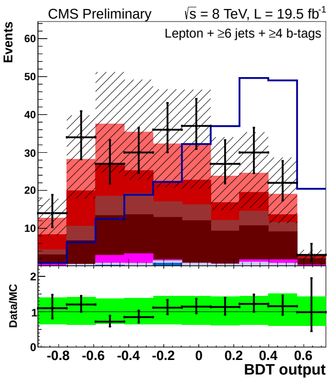

(g) ≥6 jets, ≥4 b-tags

(h) Legend

Figure 7.17: Final BDT output for lepton + jet events. Background-like events have a low BDT output value. Signal-like events have a high BDT output value. The uncertainty band includes statistical and systematic uncertainties that affect both the rate and shape of the background distributions. The top, middle and, bottom rows are events with 4, 5, and ≥6 jets, respectively, while the left, middle, and right-hand columns are events with 2, 3, and ≥4 b-tags, respectively. The $t\bar{t}H$ signal ($m_H = 125\,\mathrm{GeV}$) is normalized to 30 × SM expectation.

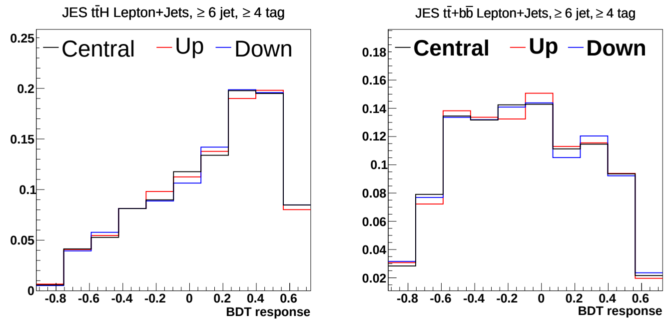

Figure 7.18: Comparison of the MVA discriminator for JES shift upwards (red) and downwards (blue) relative to the nominal (black) shape for the $t\bar{t}H(125)$ signal (left) and the main background sample $t\bar{t}+b\bar{b}$ (right). The plots are from the ≥ 6 jet ≥ 4 tag category in the lepton+jets channel. All plots are normalized to unit area.

diction of simulated heavy-flavor events in the light-flavor control region, and visa versa. Figures 7.19 and 7.20 and Table 7.9 show the effect of this uncertainty on the final BDT shapes. The impact of statistical uncertainties associated with the scale factor determination are controlled by means of four total nuisance parameters, two for heavy-flavor and two for light-flavor. For each jet flavor, the first nuisance parameter controls distortions in the CSV distribution corresponding to an overall tilt. This is consistent with a migration of events from one end of the CSV range to the other. The second nuisance parameter controls distortions of a more complicated nature, where the upper and lower ends of the distribution change relative to the center. Figures. 7.21 and 7.22, and Table 7.9 show the size of the shape and rate impact on the final BDT shape. For charm jets scale factors, the overall relative uncertainty is retained from the heavy flavor scale factors, doubled in size and used to construct two separate nuisance parameters to control the uncertainties. These two uncertainties associated with charm jets scale factors are not correlated with respect to all the uncertainties for the heavy flavor and light flavor scale factors. Figure 7.23 and Table 7.9 show the size of the shape and rate impact on the final BDT shape.

Electron and Muon ID and Trigger Scale Factors: A rate uncertainty of 1.4% is assigned for single-lepton events. A single nuisance parameter is used for all lepton-related and is correlated between muons and electrons. Uncertainties for electrons and muons are treated identically, and in the case where there is a difference, the larger uncertainty is used. Uncertainties from ID and isolation as fully uncorrelated and are combined in quadrature for the value of the nuisance parameter.

The total lepton efficiency uncertainty is composed of two parts. Both parts were measured using the method described in [172], which is a "tag and probe" method based on lepton events near the Z boson mass resonance. The first part is a 1% uncertainty on the lepton

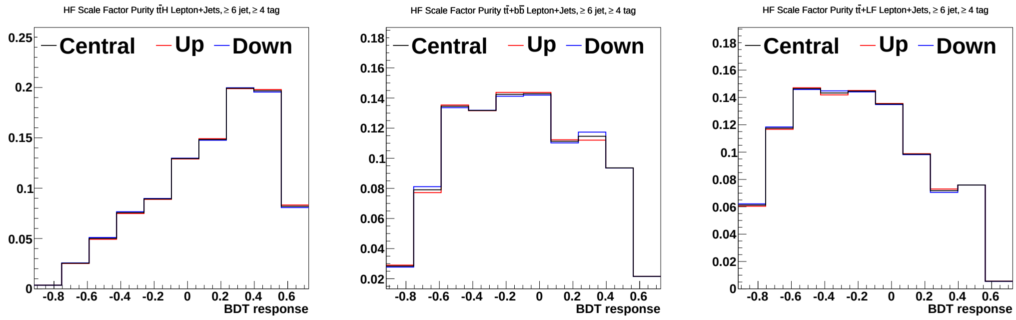

Figure 7.19: Comparison of the MVA discriminator when shifting the light flavor contamination in the heavy flavor scale factor determination shift upwards (red) and downwards (blue) relative to the nominal (black) shape for the $t\bar{t}H(125)$ signal (top row) and $t\bar{t}+b\bar{b}$ and $t\bar{t}$+LF background samples (middle row and bottom row respectively). The plots are from the LJ $\geq$ 6 jet $\geq$ 4 category. All plots are normalized to unit area.

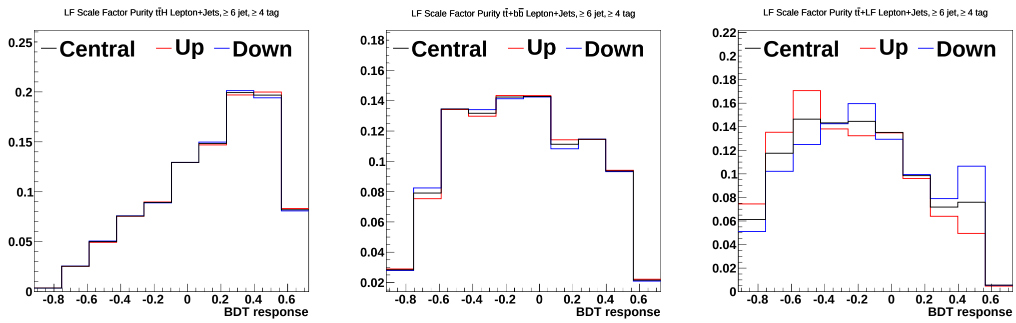

Figure 7.20: Comparison of the MVA discriminator when shifting the heavy flavor contamination in the light flavor scale factor determination shift upwards (red) and downwards (blue) relative to the nominal (black) shape for the $t\bar{t}H(125)$ signal (top row) and $t\bar{t}+b\bar{b}$ and $t\bar{t}$+LF background samples (middle row and bottom row respectively). The plots are from the LJ $\geq$ 6 jet $\geq$ 4 category. All plots are normalized to unit area.

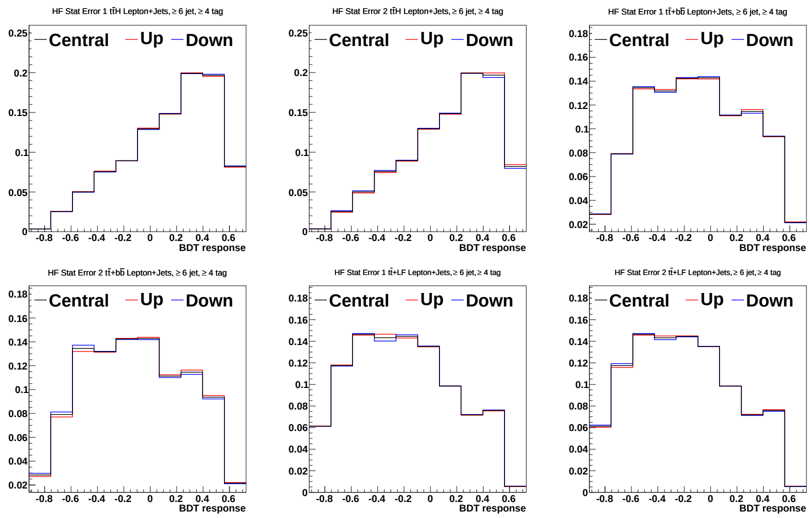

Figure 7.21: Comparison of the MVA discriminator when shifting to account for the statistical uncertainty on the heavy flavor scale factor extraction. Two classes of distortion in the scale factor are considered: linear distortions (labeled “Stat. Error 1”) and nonlinear distortions (labeled “Stat. Error 2”). Both shift upwards (red) and downwards (blue) relative to the nominal (black) shape for the $t\bar{t}H(125)$ signal (top row) and $t\bar{t}\ +b\bar{b}$ and $t\bar{t}$ +LF background samples (middle row and bottom row respectively) are shown. The plots are from the ≥ 6 jet ≥ 4 category. All plots are normalized to unit area.

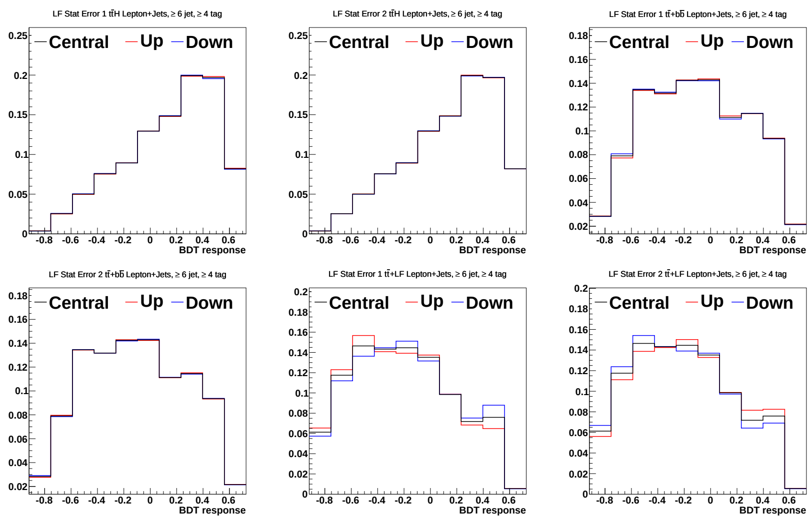

Figure 7.22: Comparison of the MVA discriminator when shifting to account for the statistical uncertainty on the light flavor scale factor extraction. Two classes of distortion in the scale factor are considered: linear distortions (labeled “Stat. Error 1”) and nonlinear distortions (labeled “Stat. Error 2”). Both shift upwards (red) and downwards (blue) relative to the nominal (black) shape for the $t\bar{t}H(125)$ signal (top row) and $t\bar{t}\ +b\bar{b}$ and $t\bar{t}$ +LF background samples (middle row and bottom row respectively) are shown. The plots are from the ≥ 6 jet ≥ 4 category. All plots are normalized to unit area.

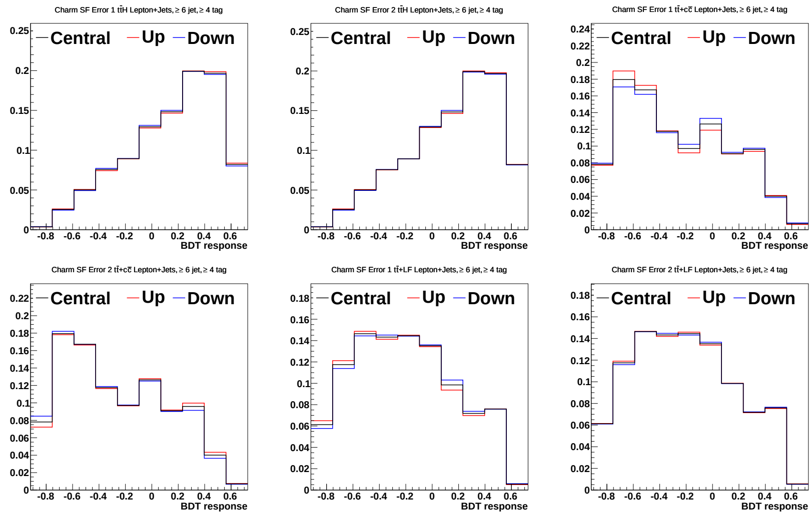

Figure 7.23: Comparison of the MVA discriminator when shifting to account for the uncertainty on the charm jets scale factor extraction. Two classes of distortion in the scale factor are considered: linear distortions (labeled "Error 1") and nonlinear distortions (labeled "Error 2"). Both shift upwards (red) and downwards (blue) relative to the nominal (black) shape for the $t\bar{t}H(125)$ signal (top row) and $t\bar{t}+c\bar{c}$ and $t\bar{t}$ +LF background samples (middle row and bottom row respectively) are shown. The plots are from the ≥ 6 jet ≥ 4 category. All plots are normalized to unit area.

b-tag systematic yield change				
		lepton+jets		
sys	shift	$t\bar{t}\ H(125)$	$t\bar{t}$ +LF	$t\bar{t}\ +b\bar{b}$
Heavy Flavor SF Purity	up down	+13.2% -12.1%	+7.4% -7.2%	+13.3% -12.1%
Light Flavor SF Purity	up down	-3.4% +3.4%	-32.2% +43.9%	-4.4% +4.4%
Heavy Flavor SF Stat. Err. 1	up down	-12.1% +13.3%	-6.6% +6.8%	-11.8% +12.9%
Heavy Flavor SF Stat. Err. 2	up down	+8.9% -8.3%	+5.0% -4.9%	+9.1% -8.5%
Light Flavor SF Stat. Err. 1	up down	+0.5% -0.5%	-15.6% +17.7%	+0.1% -0.1%
Light Flavor SF Stat. Err. 2	up down	+1.8% -1.7%	+10.1% -8.9%	+2.1% -2.0%
sys	shift	$t\bar{t}\ H(125)$	$t\bar{t}$ +LF	$t\bar{t}+c\bar{c}$
Charm jets SF Err. 1	up down	+5.1% -5.1%	-3.4% +3.3%	-5.6% +5.0%
Charm jets SF Err. 2	up down	+6.0% -5.9%	+4.2% -4.2%	+12.7% -11.7%

Table 7.9: This table summarizes the rate effect of the six independent nuisance parameters that characterize the *b*-tag uncertainties. (Note: The *b*-tag rate uncertainties associated with JES variations are already included with the JES rate uncertainties in Table 6.14. The impact of statistical uncertainties is in the heavy-flavor and light-flavor scale factor extraction is incorporated using two separate nuisance parameters, as described above. The uncertainty labeled "Stat. Err. 1" represents statistical uncertainties resulting a linear distortion of the CSV scale factor, while the one labeled "Stat. Err. 2" corresponds to nonlinear distortions.

identification and isolation scale factor. The second part of the total lepton efficiency uncertainty is a 1% trigger scale factor uncertainty.

Pileup Reweighting: See section 6.4 for a description of the evaluation of this systematic.

Top Quark p_{T} Reweighting: The systematic uncertainty on the top p_{T} reweighting is assessed as follows: the uncorrected Monte Carlo shapes are used as -1σ systematic uncertainty, and doubling the correction factor gives the $+1\sigma$ variation. This creates a deviation that is the same size as the original observed difference between data and Monte Carlo. This uncertainty is shown in Fig. 7.2. Fig. 7.24 shows the effects of the uncertainty on the top quark p_{T} on the BDT shape and Table 7.10 shows the effect on the rates.

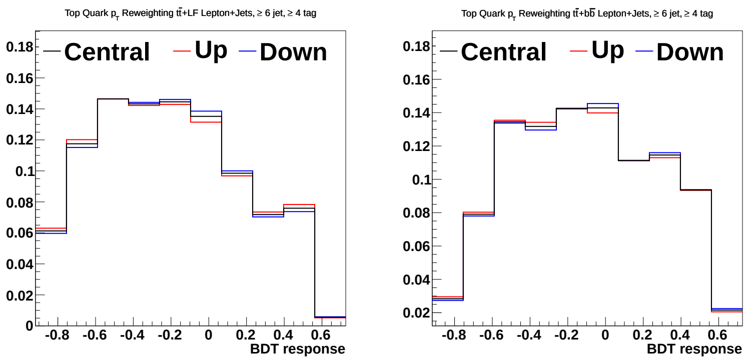

Figure 7.24: Comparison of the MVA discriminator for shifts in top quark p_{T} reweighting upwards (red) and downwards (blue) relative to the nominal (black) shape for the $t\bar{t}$ +LF background (left) and the $t\bar{t}\ + b\bar{b}$ (right). The plots are from the ≥ 6 jets + ≥ 4 tags category in the lepton+jets channel. All plots are normalized to unit area.

Top quark p_{T} reweighing systematic yield change			
		lepton+jets	
sys	shift	$t\bar{t}$	$t\bar{t}\ + b\bar{b}$
Top quark p_{T} Reweighting	up	-5.2%	-7.0%
	down	+5.2%	+7.0%

Table 7.10: Relative yield change due to varying the top quark p_{T} reweighting. The “up” variation corresponds to apply twice as much correction to the top quark p_{T} distribution as the nominal, while the “down” correction corresponds to applying no correction to the default MC top quark p_{T} distribution.

Cross Sections: See section 6.4 for a description of the evaluation of this systematic. Uncertainties affecting these normalizations are summarized in Table 7.11.

Luminosity: The uncertainty on the luminosity estimate is 2.2%. This affects all rates.

Madgraph Q^2 Uncertainty: See section 6.4 for a description of the evaluation of this systematic.

Process	pdf			QCD Scale			
	gg	qb	qg	$t\bar{t}$	V	VV	$t\bar{t}H$
$t\bar{t}H$	9%						12.5%
$t\bar{t}$+jets	2.6%			3%			
$t\bar{t}+W$		7%		15%			
$t\bar{t}+Z$	9%			15%			
Single top			4.6%	2%			
W+jets		4.8%			1.3%		
Z+jets		4.2%			1.2%		
Dibosons						3.5%	

Table 7.11: Cross section uncertainties used for the limit settings. Each column in the table is an independent source of uncertainty, except for the last column which represents uncertainties uncorrelated with any others. Uncertainties in the same column for two different processes (different rows) are completely correlated.

Figure 7.25 shows the shape and Table 7.12 shows the rate variations for selected event categories.

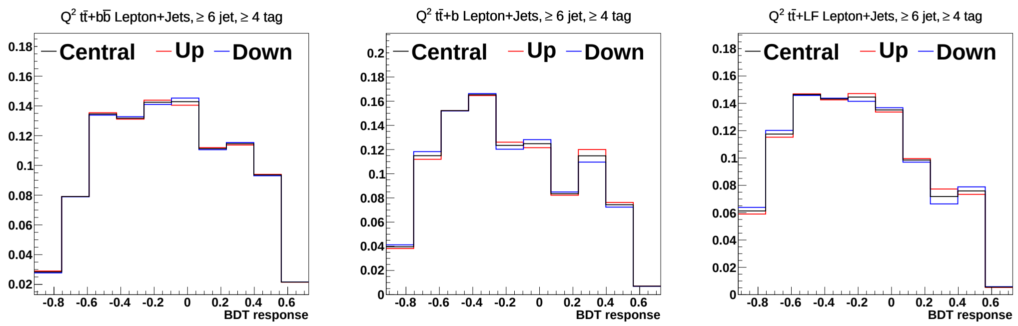

Figure 7.25: Comparison of the MVA discriminator when shifting the Q^2 scale up and down by its uncertainties. Shown are the shift upwards (red) and downwards (blue) relative to the nominal (black) shape for the $t\bar{t}$ $+b\bar{b}$ (top row) $t\bar{t}$ $+b$ (middle row) and $t\bar{t}$ +LF (bottom) background samples. The plots are from the LJ ≥ 6 jet ≥ 4 category. All plots are normalized to unit area.

Q^2 systematic yield change				
		lepton+jets		
sys	shift	$t\bar{t}$ +LF	$t\bar{t}$ $+b$	$t\bar{t}$ $+b\bar{b}$
Q^2 Uncertainty	up	-13.8%	-16.1%	-17.6%
	down	+17.6%	+20.8%	+23.3%

Table 7.12: This table summarizes the rate effect of shifting Q^2 scale uncertainty for Madgraph. Note that the shifts are made independently for the following topologies: $t\bar{t}$ $+0p$, $t\bar{t}$ $+1p$, $t\bar{t}$ $+2p$, $t\bar{t}+c\bar{c}$, $t\bar{t}$ $+b$, and $t\bar{t}$ $+b\bar{b}$.

MC Statistics Uncertainty: See section 6.4 for a description of the evaluation of this systematic.

Extra $t\bar{t}$+HF Rate Uncertainty: See section 6.4 for a description of the evaluation of this systematic.

Table 7.13 summarizes the systematic uncertainties assessed on the signal and backgrounds for this analysis. It describes how each systematic is treated in the fit used for signal extraction.

Source	Shape?	Notes
Luminosity	No	Signal and all backgrounds
Lepton ID/Trig	No	Signal and all backgrounds
Pileup	No	Signal and all backgrounds
Jet Energy Resolution	No	Signal and all backgrounds
Jet Energy Scale	Yes	Signal and all backgrounds
b-Tag HF fraction	Yes	Signal and all backgrounds
b-Tag HF stats (linear)	Yes	Signal and all backgrounds
b-Tag HF stats (quadratic)	Yes	Signal and all backgrounds
b-Tag LF fraction	Yes	Signal and all backgrounds
b-Tag LF stats (linear)	Yes	Signal and all backgrounds
b-Tag LF stats (quadratic)	Yes	Signal and all backgrounds
b-Tag Charm (linear)	Yes	Signal and all backgrounds
b-Tag Charm (quadratic)	Yes	Signal and all backgrounds
QCD Scale ($t\bar{t}H$)	No	Scale uncertainty for NLO $t\bar{t}H$ prediction
QCD Scale ($t\bar{t}$)	No	Scale uncertainty for NLO $t\bar{t}$ and single top predictions
QCD Scale (V)	No	Scale uncertainty for NNLO W and Z prediction
QCD Scale (VV)	No	Scale uncertainty for NLO diboson prediction
pdf (gg)	No	Pdf uncertainty for gg initiated processes ($t\bar{t}$, $t\bar{t}Z$, $t\bar{t}H$)
pdf ($q\bar{q}$)	No	Pdf uncertainty for $q\bar{q}$ initiated processes ($t\bar{t}W$, W, Z).
pdf (qg)	No	Pdf uncertainty for qg initiated processes (single top)
Madgraph Q^2 Scale ($t\bar{t}+0p, 1p, 2p$)	Yes	Madgraph Q^2 scale uncertainty for $t\bar{t}+jets$ split by parton number. There is one nuisance parameter per parton multiplicity and they are uncorrelated.
Madgraph Q^2 Scale ($t\bar{t}+b\bar{b}/c\bar{c}$)	Yes	Madgraph Q^2 scale uncertainty for $t\bar{t}$+jets/$b\bar{b}/c\bar{c}$.
Madgraph Q^2 Scale (V)	No	Varies by jet bin.
τ Energy Scale	Yes	Tau signal and background
τ ID efficiency	Yes	Tau signal and background
τ Jet Fake Rate	Yes	Tau signal and background
τ Electron Fake Rate	Yes	Tau signal and background

Table 7.13: Summary for the of the systematic uncertainties considered on the inputs to the limit calculation. Except where noted, each row in this table will be treated as a single, independent nuisance parameter.

Table 7.14 shows the results of the comparing the variation in rate for the sum of $t\bar{t}+lf$+$b\bar{b}$+$c\bar{c}$ backgrounds. The systematic that produces the largest variation of the backgrounds is the QCD scale uncertainty on the $t\bar{t}+b\bar{b}$ background. The next largest variation comes from: the amount of $t\bar{t}$+$b\bar{b}$, the b-tagging efficiency and fake rate, and the jet energy scale. The next most important effect is the top quark p_T correction, and it is more than three times smaller than the QCD scale uncertainty on $t\bar{t}+b\bar{b}$.

7.5 Statistical Methods

The same procedure that was used in the previous analysis, and descried in section 6.5.

Uncertainties on the sum of $t\bar{t}$ +lf, $t\bar{t}$ $+ b$, $t\bar{t}$ $+ b\bar{b}$, and $t\bar{t} + c\bar{c}$ events with $\geq$ 6 jets and $\geq$ 4 b-tags		
Source	Rate	Shape?
QCD Scale ($t\bar{t}$ $+ b\bar{b}$)	17%	No
b-Tag HF contamination	17%	Yes
QCD Scale ($t\bar{t} + c\bar{c}$)	11%	No
Jet Energy Scale	11%	Yes
b-Tag LF contamination	9.6%	Yes
b-Tag HF stats (linear)	9.1%	Yes
QCD Scale ($t\bar{t}$ $+ b$)	7.1%	No
Madgraph Q^2 Scale ($t\bar{t}$ $+ b\bar{b}$)	6.8%	Yes
b-Tag Charm Uncertainty (quadratic)	6.7%	Yes
Top Pt Correction	6.7%	Yes
b-Tag HF stats (quadratic)	6.4%	Yes
b-Tag LF stats (linear)	6.4%	Yes
Madgraph Q^2 Scale($t\bar{t}$ $+ 2$ partons)	4.8%	Yes
b-Tag LF stats (quadratic)	4.8%	Yes
Luminosity	4.4%	No
Madgraph Q^2 Scale ($t\bar{t} + c\bar{c}$)	4.3%	Yes
Madgraph Q^2 Scale ($t\bar{t}$ $+ b$)	2.6%	Yes
Lepton ID/Trig	1.4 (2.8)%	No
QCD Scale ($t\bar{t}$)	3%	No
pdf (gg)	2.6%	No
Jet Energy Resolution	1.5%	No
Pileup	1%	No
b-Tag Charm Uncertainty (linear)	0.6%	Yes

Table 7.14: Specific effect of systematics on predicted background yields for events with $\geq$ 6 jets and $\geq$ 4 b-tags. Here we only consider the sum of the largest backgrounds, $t\bar{t}$ +lf, $t\bar{t}$ $+b$, $t\bar{t}$ $+b\bar{b}$, and $t\bar{t} + c\bar{c}$. These three backgrounds account for 94% of all background events. The signal is 3.5% of the yield of the three main backgrounds. The signal fraction is directly comparable to the variations of the background in the table. The table shows that the signal is much smaller than many of the background variations.

7.6 Results and Conclusions

In the lack of a significant excess of events in data, upper limits are once again set on the $t\bar{t}H$ production rate. The shape of the BDT discriminator distribution is used to fit the simulated signal and backgrounds samples to the data. Besides the BDT discriminator shapes for data, background and signal, inputs to the limit setting include the number of events passing the selection for each process. Systematics that are used are nuisance parameters are described in the previous section. The Higgs mass points we set limits for are: 110, 115, 120, 125, 130, 135 and 140 GeV/c^2. For the lepton+jets channel, the limits are shown in Tab. 7.15 and Fig. 7.26.

		Expected		
Higgs Mass	Observed	Median	68% C.L. Range	95% C.L. Range
110 GeV/c^2	3.6	3.3	[2.4,4.7]	[1.8,6.6]
115 GeV/c^2	4.1	3.5	[2.4,4.9]	[1.8,6.9]
120 GeV/c^2	4.3	4.0	[2.9,5.8]	[2.1,8.1]
125 GeV/c^2	4.9	4.7	[3.3,6.7]	[2.5,9.4]
130 GeV/c^2	6.8	6.0	[4.3,8.6]	[3.2,12.0]
135 GeV/c^2	7.4	7.1	[5.0,10.2]	[3.7,14.2]
140 GeV/c^2	9.0	9.6	[6.9,13.7]	[5.2,18.9]

Table 7.15: Expected and observed upper limits for SM Higgs for lepton + jets channel using the 2012 dataset. These limits were extracted using the asymptotic method.

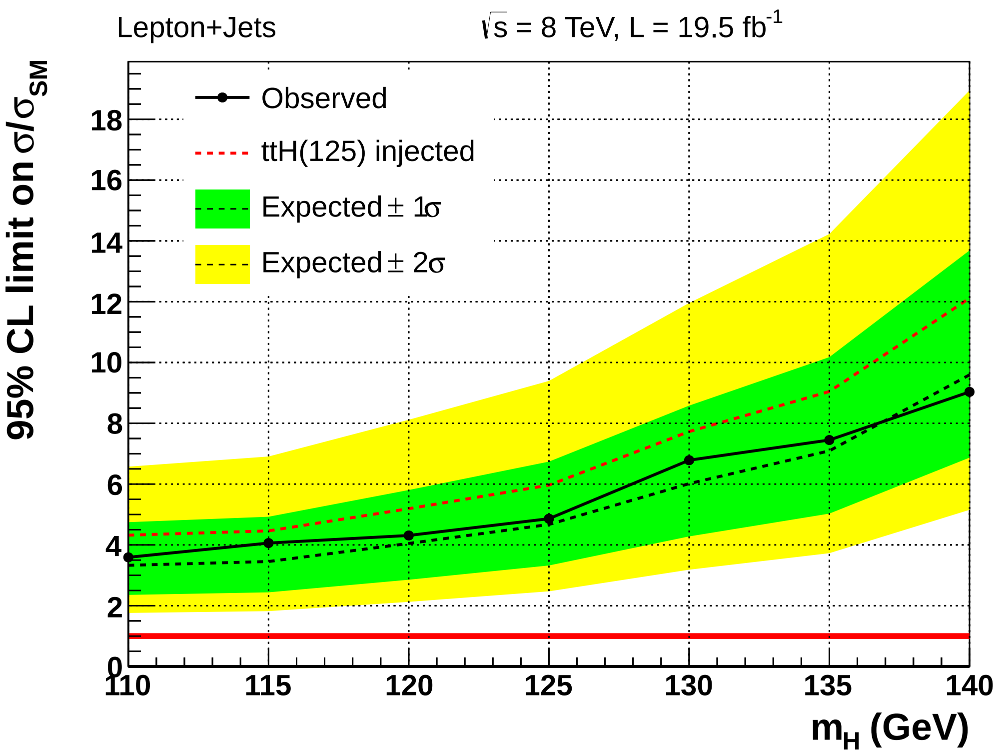

Figure 7.26: The expected and observed 95% CL upper limits on the signal strength parameter $\mu = \sigma/\sigma_{SM}$ for the lepton+jets channel using the 2012 dataset. These limits were extracted using the asymptotic method.

For the full 19.4 fb^{-1} of 8 TeV data collected by the CMS detector, an updated search for the Standard Model Higgs boson produced in association with top-quark pairs has been performed. The increase in expected sensitivity did not increase by a factor of ~ 2 that one would naively expect from increasing the statistics by a factor of ~ 4. This is because, largely due to the different set of systematic uncertainties used, the analysis entered a regime where statistical uncertainty was no longer the dominant factor that degraded sensitivity. If this data set was repeatedly collected, allowing for statistical fluctuations, it should be expected that, for a Standard Model Higgs boson, with mass, $m_H = 125\,\text{GeV}$, that 95% of the results would fail to observe the $t\bar{t}H$ signal unless its cross-section was modified by a factor of 4.9. From simulations alone, this expected factor is 4.7, an difference of less than 1 σ from the observed data.

The results of this analysis were combined with previous results in this channel from 7 TeV data and with di-lepton, same-sign di-lepton, hadronic tau, di-photon, and multi-lepton final state channels and published in the Journal of High Energy Physics (JHEP) in September of 2014 [173]. The combined analytical power of all of the channels allowed for an upper limit of 4.5 times the predicted Standard Model cross section. This is slightly more than 2σ away from the expected factor of 1.8 from simulations alone.

Relative the previous analysis, which was primarilly driven by my efforts, the addition of new members to our research group and the conclusion of the 7 TeV analysis allowed me to focus on specific tasks in greater detail. The validation of the b-tagging calibration factors involved extensive investigations, selecting both light and heavy-flavour enriched events, using a χ^2 minimization technique to identify $t\bar{t} + jets$ events and Z+jets events, in order to compare the simulations to data. I also was responsible for comparisons of this analysis to the results provided by ATLAS. This involved reproducing the ATLAS event selection and signal extraction techniques, then producing an exact account of the effect that each of the different choices made on the upper limits of this analysis. The results of the comparisons will be used to guide the design of the analysis in Run 2.

Chapter 8

Analysis Improvements

The analyses described in the previous two chapters use sophisticated multivariate analysis (MVA) techniques to perform signal extraction and limit setting. However, there are several improvements that can still be made to optimize signal extraction and increase sensitivity. The following section will describe the implementation of the latest simulation techniques in order to improve the modeling the signal and background processes. The final section will discuss variables from these new simulations that can be used to enhance the identification of final state jets with their roles in the $t\bar{t}$ system.

8.1 aMC@NLO, MadSpin, and Pythia8 Monte Carlo

One of the largest sources of uncertainty in each analysis comes from the theoretical uncertainty of the Leading Order (LO) monte carlo sample used to estimate background rates and shapes. In order to accurately model the high jet-multiplicity environment of the $t\bar{t}H$ final state, higher-order calculations in perturbation theory are necessary. Recently, the aMC@NLO framework has been released, and is an automated tool for event generation that utilizes Next-to-Leading Order (NLO) QCD predictions [174]. This framework takes advantage of recent theoretical developments in the automation of calculating spin-entangled decays from heavy resonances, which is packaged in the program MadSpin [175]. The event generator, aMC@NLO, using MadSpin to calculate the decays of the top quark, W and Z bosons, is then interfaced to Pythia 8 to framework perform the parton shower and hadronization [176]. Each stage of this event generation process uses the latest technological developments in monte carlo simulation, which were unavailable at the time of the previous analyses.

For process where additional jets are simulated in the final state, there will be an additional complication since the parton shower and hadronization are performed separately and the contributions for NLO processes will be double counted in several cases. This occurs when a process with an additional jet in the final state is created in the matrix element level by aMC@NLO and later, another event is created with no additional jets in the final state at the matrix element level, but when the parton shower occurs in Pythia 8, an additional jet can be generated, creating two event from a single underlying theoretical contribution. The removal of these overlapping events is carried out by a method known as FXFX merging [177]. This algorithm tracks the heritage of final state jets, in order to determine whether it was created as part of the matrix element or later during the parton shower. Due to the higher accuracy of modeling the kinematics of partons calculated in the matrix element stage, the algorithm removes events where additional jets are created in the parton shower, ensuring that the underlying process with an additional final state jets are created at the matrix element level, utilizing the NLO QCD calculations in aMC@NLO.

The utilization of these event generation techniques to simulate $t\bar{t}H$ and $t\bar{t}+jets$ backgrounds will improve the kinematic modeling of these high-jet multiplicity processes. A dedicated $t\bar{t}+b\bar{b}$ sample with a large number of events generated with this framework would improve the modeling of the irreducible background. Unfortunately, these event generation tools were only recently released and the computational time required to generate samples with the equivalent statistical power of those used in the previous analyses is prohibitive on the time scale of this dissertation. However, each of the following samples were created using the process described above with 500,000 events each:

- $t\bar{t}$ + 0, 1, and 2 additional jets
- $t\bar{t}+b\bar{b}$
- $t\bar{t}H$ + 0, and 1 additional jets

The number of events generated is not sufficient to create a control region to asses calibrations of jet energy, b-tag efficiency, or lepton identification and reconstruction efficiency. However, since all of these processes are generated in an identical framework, it is reasonable to assume that calibrations applied will be similar for each, and as such comparisons amongst the samples can still provide insight into how they can be used to improve the analysis. Figure 8.1 shows a comparison between the number of reconstructed jets and b-tagged jets that pass the selection used in the previous analysis, with a lowered p_{T} threshold of 25 GeV. As before, the jet multiplicity of $t\bar{t}H$ has a much longer distribution than the $t\bar{t}+jets$ backgrounds, making it very important that these high-multiplicity events are modeled with the highest precision available.

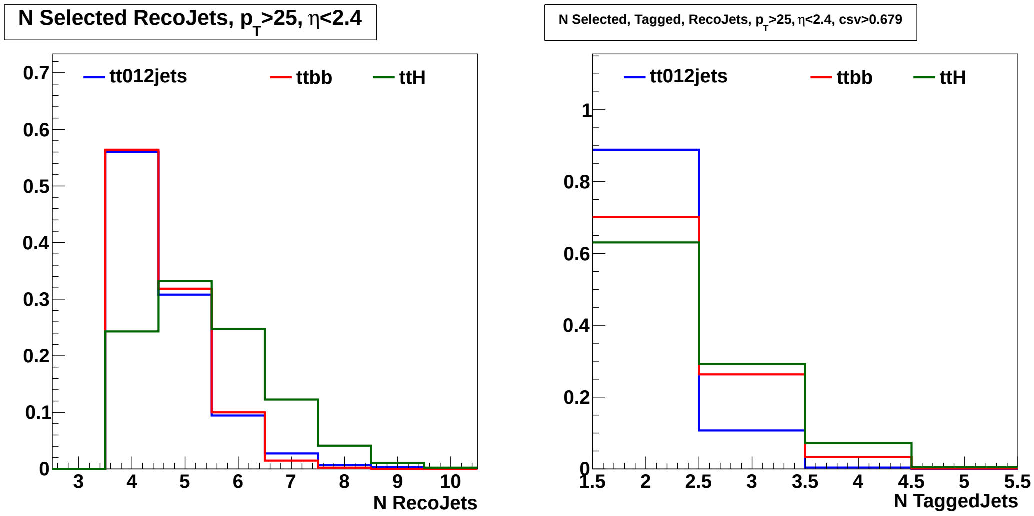

Figure 8.1: The number of reconstructed jets passing selection (left) and that have additionally been b-tagged (right) for $t\bar{t}H$, $t\bar{t} + jets$, and $t\bar{t} + b\bar{b}$ samples generated with the aMC@NLO and Pythia 8 framework

8.2 Analysis Techniques Under Development

One of the most difficult challenges of the $t\bar{t}H$ final state is the combinatorics of possible b-jet candidates coming from the Higgs decay. The correct associate of jets to their roles in the decay of the top quarks would greatly reduce the number of jets as candidates for Higgs daughters. This is done, in some degree, in the analyses described in previous chapters via the "best Higgs mass" variable. This is a χ^2 minimization that relies only on the masses of the top quark, W and Higgs bosons in the event, to decide which jets are associated to the decays of which particles. These mass variable will be useful in identifying jets from the $t\bar{t}$ system. Figure 8.2 shows the case for the W boson mass evaluated for jets which have been correctly associated to the MC truth generated partons in blue, and for the incorrect associations in green.

The implementation of Madspin in the aMC@NLO framework allows for the highest precision on the spin correlations of the decay products from the $t\bar{t}H$ and $t\bar{t}$ systems. The angular relationships among the decay products provide additional discrimination power for the correct association of jets to their roles in the $t\bar{t}H$ and $t\bar{t}$ systems. The spin correlations of the decay products are enhanced by boosting to a reference frame that is more sensitive to differences in the angles between the correctly and incorrectly associated objects in the event. The reference frame of choice is formed by first identifying all of the potential candidates of the semi-leptonic $t\bar{t}$ decay:

- $\bar{b}$-quark coming from the t-quark
- b-quark coming from $\bar{t}$-quark
- up-type quark from hadronic W boson decay

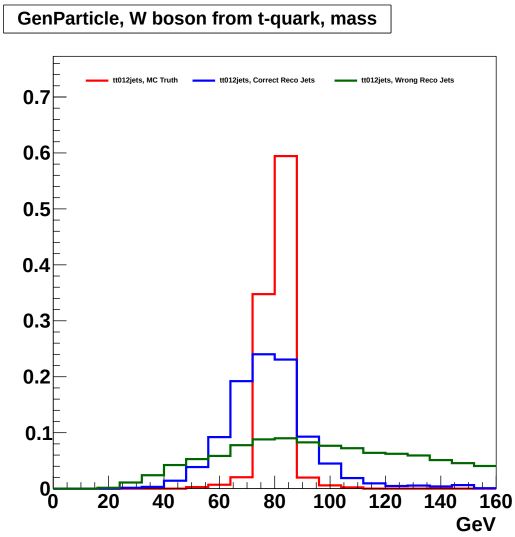

Figure 8.2: The invariant mass of the W boson in the $t\bar{t}$ decay for the case of the MC truth (red), correctly associated reconstructed jets (blue), and incorrectly associated reconstructed jets (green)

- down-type quark from the hadronic W boson decay

The four-vector of the entire $t\bar{t}$ system can be formed, and the hadronic candidates are boosted to a frame where the $t\bar{t}$ system itself is at rest. Then, the t-quark, and its daughters are boosted to a frame such that the t-quark is at rest. Finally, the $\bar{t}$-quark, and its daughters are boosted to a frame such that the $\bar{t}$-quark is at rest. Then the angles between their decay products is evaluated. Typically, these studies are performed in the di-lepton channel since the angular resolution is much better in leptons than in jets. Figure 8.3 shows the cosine of the momentum 3-vector between the b-quarks from t and $\bar{t}$, the lepton and the up-type W-boson daughter, and the lepton and the down-type W-boson daughter.

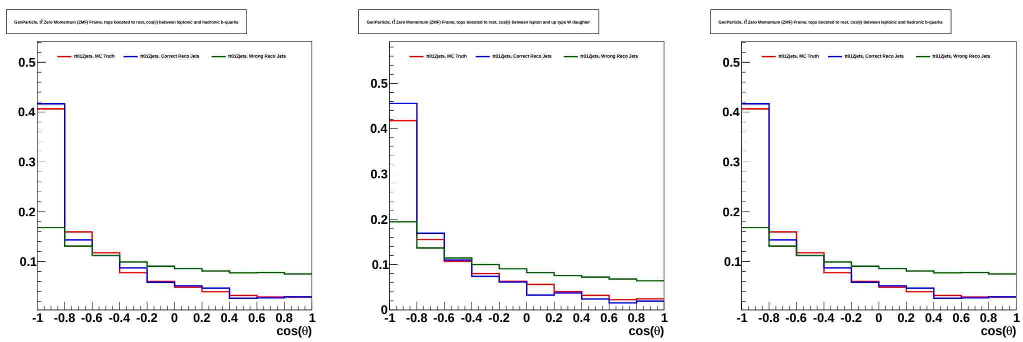

Figure 8.3: The cosine of the angle between the momentum three-vectors for the b-quarks from the top decays (left), the lepton and the up-type W boson daughter (center), and the lepton and the down-type W boson daughter (right)

All three distributions have peaking values that provide discrimination between the jets correctly associated to the MC truth generator-level partons of the $t\bar{t}$ decay, and the jets which are incorrectly associated. In each plot, the green represents the incorrect associations, while the blue represents the correct associations, and the red represents the MC truth from the generated parton. An additional angle of interest is the difference in the ϕ coordinate between daughters of the $t\bar{t}$ decay. Figure 8.4 shows the distributions for the $\Delta\phi$ between the b-quarks from the top decays, the lepton and up-type W-boson daughter, and the lepton and the down-type W-boson daughter. The case of the correctly associated jets has two sharp peaks near $\phi = \pm 2$, where the distribution is more uniform for incorrectly associated jets.

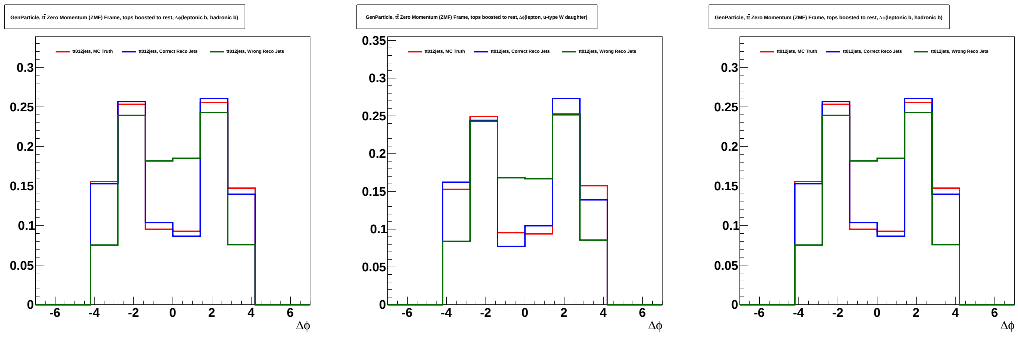

Figure 8.4: The difference in the ϕ coordinate between the momentum three-vectors for the b-quarks from the top decays (left), the lepton and the up-type W boson daughter (center), and the lepton and the down-type W boson daughter (right)

A final variable of interest for jet association would be the charge of lepton multiplied against the charge of the b-quark that is associated with the same top-quark. These two values, due to charge conservation, will always be negative when multiplied. The charge of the jet is calculated from a p_{T} weighted sum of the tracks contained in the cluster, where the curvature of each track tells the charge of the hadron creating the signature. Since there are many hadrons clustered together to form a jet, there is a large degradation on resolution of the charge of the jet, however for the peak of this distribution is negative for correctly associated jets, and positive for incorrect jets, as shown in figure 8.5.

A jet association algorithm can be formed by using an MVA technique to provide a discriminant for how likely a certain combination of jets from an event are correctly associated to their roles in the decay of the $t\bar{t}$ system. A training sample of correctly and incorrectly associated jets can be trained using the following variables:

- Invariant Mass of the Hadronic W boson
- Invariant Mass of the Leptonic W boson
- Invariant Mass of the Hadronic top-quark
- Invariant Mass of the Leptonic top-quark
- $\cos\theta_{b,\bar{b}}$ in the frame where $t\bar{t}$ system and t-quarks are at rest respectively

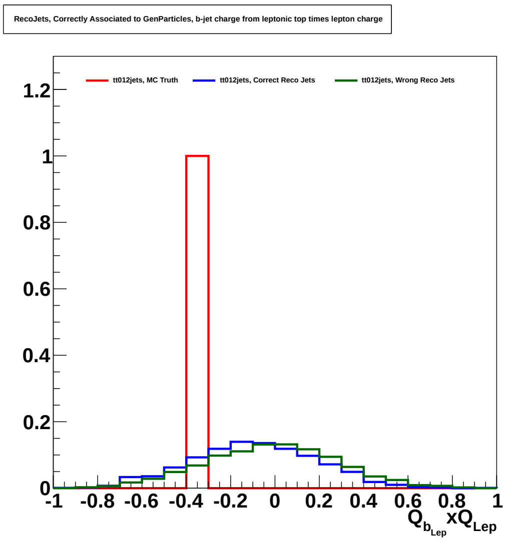

Figure 8.5: Jet times lepton charge, for the b-jet associated with the same top as the lepton. Green shows incorrectly associated reconstructed jets, blue shows correctly associated jets, and red is the MC truth

- $\cos\theta_{lep,up-typeW\,daughter}$ in the frame where $t\bar{t}$ system and t-quarks are at rest respectively
- $\cos\theta_{lep,down-typeW\,daughter}$ in the frame where $t\bar{t}$ system and t-quarks are at rest respectively
- $\Delta\phi(\theta_{b,\bar{b}})$ in the frame where $t\bar{t}$ system and t-quarks are at rest respectively
- $\Delta\phi(\theta_{lep,up-typeW\,daughter})$ in the frame where $t\bar{t}$ system and t-quarks are at rest respectively
- $\Delta\phi(\theta_{lep,down-typeW\,daughter})$ in the frame where $t\bar{t}$ system and t-quarks are at rest respectively
- The product of the lepton and b-quark associated with the same t-quark

An additional improvement to the analysis will rely on a dedicated MVA for each of the $t\bar{t}$ +X backgrounds, where X is light flavor, single c, $c\bar{c}$, single b, and $b\bar{b}$. A dedicated $t\bar{t}+b\bar{b}$ and even a $t\bar{t}+c\bar{c}$ sample with sufficiently large enough events to train an MVA would be ideal. The discriminants from each of the backgrounds would be combined as input variables to a second MVA, in order to produce a discriminant for how likely the event is from a $t\bar{t}H$ decay.

Chapter 9

Conclusions and Summary

In 2012, the Large Hadron Collider (LHC) produced the highest energy proton-proton collisions, with center of mass energies of 8 TeV. Protons, with humble beginnings in a bottle of Hydrogen, travel through a multi-stage accelerator complex, before being injected into the 27.6 km LHC ring as two counter-rotating beams. Superconducting radio-frequency cavities accelerate the beams during each revolution, constrained to the circular path by more than a thousand 8 T superconducting dipole magnets, as each beam is brought to an energy of 4 TeV.

At one of the four points on the LHC ring where the proton beams are squeezed together to produce collisions, sits the Compact Muon Solenoid (CMS) experiment, a general purpose particle detector designed to elucidate the mechanism of electroweak symmetry breaking, and explore physics interactions at the TeV energy scale. This 14,000 ton, 15 m tall device, provides hermetic, 4π, coverage of the interaction region, and is composed of a system of sub-detectors, with a cylindrical symmetry about the beam-line and interaction region, which work in parallel to identify and measure the kinematic properties of particles produced during pp collisions. The inner tracking system is composed of more than 70 million silicon pixel and strip detectors that provide μm spatial resolution on the trajectory of charged particles. An electromagnetic calorimeter (ECAL) surrounds the inner tracker, and is composed of more than 75,000 lead-tungstate crystals, which absorb energy from electromagnetically interacting particles, with electrons and photons depositing almost all of their energy in this sub-detector. The hadronic calorimeter (HCAL) surrounds the ECAL, absorbing the energy of charged and neutral hadrons with stacks of brass absorber material with layers of plastic scintillator to sample the energy in between. The outermost system are the muon chambers, which utilize three different types of detector technologies to provide fast timing to trigger measurements and excellent spatial resolution on muons, an important signature for many TeV energy scale processes. Hardware and firmware installed on the detector provide an instant, but basic reconstruction of a collision, allowing for the amount of collisions recorded to be reduced from a rate of 40 MHz down to 10 kHz. Events are additionally filtered through the use of software to a manageable rate of 100 Hz.

Once the first 5.1 fb^{-1} of 8 TeV data was collected by the CMS detector, a search for the Standard Model Higgs boson, produced in association with top-quark pairs ($t\bar{t}H$) was performed in the final state with a single lepton, at least 4 jets and at least 2 b-tags. The search region was divided into categories based on the jet and b-tag multiplicity of the final state, and a Clermond-Ferrand Multi-Layer Perceptron Artificial Neural Network (CFMlpANN) was trained to provide a one-dimensional discriminant for how likely the event is to be from the $t\bar{t}H$ signal, or one of the $t\bar{t}+jets$ backgrounds. No significant excess of events in the data was observed, and an observed (expected) upper limit on the production rate of $t\bar{t}H$ at 9.5 (5.4) times the rate predicted by the Standard Model. This final state was combined with a di-lepton final state, and the previous results from the 7 TeV dataset collected in 2011, produce an observed (expected) upper limit on the $t\bar{t}H$ process as 5.8 (5.2) times the Standard Model rate and published in the Journal of High Energy Physics (JHEP) in May of 2013.

A second analysis was performed on the full 19.5 fb^{-1} dataset of 8 TeV data collected by CMS. This also used a final state with a single lepton, at least 4 jets, and at least 2 b-tags, and a search region divided into categories based on the jet and b-tag multiplicity of the final state. A different multivariate analysis (MVA) technique was employed: a Boosted Decision Tree (BDT) was trained to separate the $t\bar{t}H$ signal from the $t\bar{t}+jets$ background for each of the jet/tag categorizations. Once again, no significant excess of events is observed, and an observed (expected) upper limit on the $t\bar{t}H$ production rate is set at 4.9 (4.7) times the Standard Model prediction. This analysis was combined with same and opposite sign di-lepton, mutli-lepton, and hadronic tau final states to produce an observed (expected) upper limit of 4.5 (2.5) time the predicted rate of $t\bar{t}H$ production.

In preparation to perform this search in the next dataset collected by CMS, several investigations have been performed on ways to improve the sensitivity of the analysis to the $t\bar{t}H$ signal. One of the most important improvements will be the incorporation of next-to-leading order (NLO) QCD effects into the simulation of $t\bar{t}H$ signal and $t\bar{t}+jets$ background. This will improve the modeling of high jet-multiplicity events, which characterize both the signal and background in this analysis. These improved simulations will also incorporate the latest techniques to calculate the spin-correlations of the decay products from heavy resonances in top-quark and W boson decays, via the MadSpin framework. This will allow the angular correlations of the daughters of the $t\bar{t}$ system to be used to correctly associate jets in an event to their roles in the $t\bar{t}$ decay, thereby reducing the combinatorics of jets that can possibly be associated with jets from the

Higgs decay.

With the experience gained in previous analyses, and improvements already underway, the observation of a $t\bar{t}H$ signal will be increasingly likely in the larger statistics, higher-energy datasets collected in the future by $t\bar{t}H$. In the lack of an observation, now or in the future, these upper limits can be used to constrain future models involving physics beyond the Standard Model (BSM) that would predict enhancements to final states explored in these first two $t\bar{t}H$ analyses.

Bibliography

[1] S. Bethke, "The 2009 World Average of alpha(s)", *Eur.Phys.J.* **C64** (2009) 689–703, doi:10.1140/epjc/s10052-009-1173-1, arXiv:0908.1135.

[2] "Image, Higgs Potential". URL http://inspirehep.net/record/1086544/files/higgspotential.png.

[3] "Image, CMS Standard Model Processes". URL https://twiki.cern.ch/twiki/bin/view/CMSPublic/PhysicsResultsSMP.

[4] "Image, Hierarchy Problem". URL http://upload.wikimedia.org/wikipedia/commons/thumb/6/68/Hqmc-vector.svg/300px-Hqmc-vector.svg.png.

[5] "LHC Aerial View". URL http://www.coepp.org.au/files/coepp/images/cern-aerial2.jpg.

[6] "LHC, Delivered Luminosity". URL http://cms-service-lumi.web.cern.ch/cms-service-lumi/publicplots/int_lumi_cumulative_pp_2.png.

[7] J.-L. Caron, "The LHC injection complex.. L'ensemble d'injection du LHC.", (May, 1993). AC Collection. Legacy of AC. Pictures from 1992 to 2002.

[8] L. Evans and P. Bryant, "LHC Machine", *JINST* **3** (2008) S08001, doi:10.1088/1748-0221/3/08/S08001.

[9] M. Barnes et al., "Injection and extraction magnets: Kicker magnets", arXiv:1103.1583.

[10] "Image, Klystron operations". URL http://upload.wikimedia.org/wikipedia/commons/a/aa/Klystron.enp.gif.

[11] "Image, Klystron operations". URL http://cds.cern.ch/record/43017?ln=en.

[12] "Image, CERN LHC, Layout of the 5 cryogenic islands". URL http://d29qn7q9z0j1p6.cloudfront.net/content/roypta/370/1973/3887/F12.medium.gif.

[13] P. Lebrun, "Large Cryogenic Helium Refrigeration System for the LHC", Technical Report LHC-Project-Report-629. CERN-LHC-Project-Report-629, CERN, Geneva, Feb, 2003. revised version number 1 submitted on 2003-02-19 11:44:11.

[14] "Image, CERN LHC, Beam Screen". URL `http://home.web.cern.ch/sites/home.web.cern.ch/files/image/engineering_page/2013/01/beam-screen_0.jpg`.

[15] CMS Collaboration, "The CMS experiment at the CERN LHC", *JINST* **3** (2008) S08004, `doi:10.1088/1748-0221/3/08/S08004`.

[16] "Image, CMS, Static Slice with tracks". URL `https://cms-docdb.cern.ch/cgi-bin/PublicDocDB/RetrieveFile?docid=4172&version=2&filename=CMS_Slice.gif`.

[17] "Image, CMS, Tracker cross-section". URL `http://cms.web.cern.ch/sites/cms.web.cern.ch/files/styles/small/public/field/image/Barrel.gif?itok=dc1cYUp-`.

[18] "Image, CMS, Tracker Pixel Resolution". URL `https://twiki.cern.ch/twiki/pub/CMSPublic/PixelOfflinePlots2013/207487_h420.png`.

[19] "Image, CMS, ECAL crystal shower evolution simulation". URL `http://www.lepp.cornell.edu/rsrc/Home/Research/CMS/EventReconstruction/fe24elwhite_small.gif`.

[20] "Image, CMS, HCAL built from Russian naval shells". URL `http://cms.web.cern.ch/sites/cms.web.cern.ch/files/styles/small/public/field/image/navy-shells-image_0095.jpg?itok=OtSvdvLx`.

[21] "Image, CMS, Muon chamber RPCs, exploded view". URL `http://cms.web.cern.ch/sites/cms.web.cern.ch/files/styles/small/public/field/image/RPClayers.jpg?itok=qtLqtQ89`.

[22] CMS Collaboration Collaboration, "Energy calibration and resolution of the CMS electromagnetic calorimeter in pp collisions at $\sqrt{s} = 7$ TeV", *J. Instrum.* **8** (Jun, 2013) P09009. 51 p. Comments: Submitted to JINST.

[23] "Image, CMS, ECAL LED pulsing calibration results". URL `https://twiki.cern.ch/twiki/pub//CMSPublic/EcalDPGResultsCMSDP2013007/histories_2011-2012.png`.

[24] CMS Collaboration Collaboration, "Particle-Flow Event Reconstruction in CMS and Performance for Jets, Taus, and MET", Technical Report CMS-PAS-PFT-09-001, CERN, 2009. Geneva, Apr, 2009.

[25] M. Cacciari, G. P. Salam, and G. Soyez, “The Anti-k(t) jet clustering algorithm”, *JHEP* **0804** (2008) 063, doi:10.1088/1126-6708/2008/04/063, arXiv:0802.1189.

[26] CMS Collaboration Collaboration, “Commissioning of the Particle-Flow reconstruction in Minimum-Bias and Jet Events from pp Collisions at 7 TeV”, Technical Report CMS-PAS-PFT-10-002, CERN, Geneva, 2010.

[27] “Image, b-Tagging”. URL http://www-d0.fnal.gov/Run2Physics/top/singletop_observation/b_tagging_graphic.png.

[28] “Image, basic ANN”. http://upload.wikimedia.org/wikipedia/commons/thumb/4/46/Colored_neural_network.svg/300px-Colored_neural_network.svg.png.

[29] “Image, CMS Higgs Physics Results, H-¿ZZ-¿4l Inv. Mass”. URL https://twiki.cern.ch/twiki/pub/CMSPublic/Hig13002PubTWiki/ZZMass_7Plus8TeV_70-1000_3GeV.pdf.

[30] “Image, CMS Higgs Physics Results, H-¿GammaGamma Inv. Mass”. URL https://twiki.cern.ch/twiki/pub/CMSPublic/Hig13001PubTWiki/Fig_19.pdf.

[31] CMS Collaboration, “Observation of a new boson at a mass of 125 GeV with the CMS experiment at the LHC”, *Phys.Lett.B* (2012) arXiv:1207.7235.

[32] ATLAS Collaboration, “Observation of a new particle in the search for the Standard Model Higgs boson with the ATLAS detector at the LHC”, *Phys.Lett.B* (2012) arXiv:1207.7214.

[33] M. E. Peskin and D. V. Schroeder, “An Introduction to Quantum Field Theory”. Westview Press, URL http://www.westviewpress.com, 1995.

[34] K. G. Wilson, “Renormalization Group and Critical Phenomena. I. Renormalization Group and the Kadanoff Scaling Picture”, *Phys. Rev. B* **4** (Nov, 1971) 3174–3183, doi:10.1103/PhysRevB.4.3174.

[35] K. G. Wilson, “Renormalization Group and Critical Phenomena. II. Phase-Space Cell Analysis of Critical Behavior”, *Phys. Rev. B* **4** (Nov, 1971) 3184–3205, doi:10.1103/PhysRevB.4.3184.

[36] H. Weyl, “The theory of groups and quantum mechanics”. Dover Press, URL https://ia700807.us.archive.org/20/items/ost-chemistry-quantumtheoryofa029235mbp/quantumtheoryofa029235mbp.pdf, 1930.

[37] C. N. Yang and R. L. Mills, "Conservation of Isotopic Spin and Isotopic Gauge Invariance", *Phys. Rev.* **96** (Oct, 1954) 191–195, `doi:10.1103/PhysRev.96.191`.

[38] M. Gell-Mann, "A Schematic Model of Baryons and Mesons", *Phys.Lett.* **8** (1964) 214–215, `doi:10.1016/S0031-9163(64)92001-3`.

[39] G. Zweig, "An SU_3 model for strong interaction symmetry and its breaking; Version 1", Technical Report CERN-TH-401, CERN, Geneva, Jan, 1964.

[40] G. Zweig, "An SU_3 model for strong interaction symmetry and its breaking; Version 2",.

[41] O. W. Greenberg, "Spin and Unitary-Spin Independence in a Paraquark Model of Baryons and Mesons", *Phys. Rev. Lett.* **13** (Nov, 1964) 598–602, `doi:10.1103/PhysRevLett.13.598`.

[42] P. Higgs, "Broken symmetries, massless particles and gauge fields", *Physics Letters* **12** (1964), no. 2, 132 – 133, `doi:http://dx.doi.org/10.1016/0031-9163(64)91136-9`.

[43] S. Weinberg, "A Model of Leptons", *Phys. Rev. Lett.* **19** (Nov, 1967) 1264–1266, `doi:10.1103/PhysRevLett.19.1264`.

[44] S. L. Glashow, "Partial-symmetries of weak interactions", *Nuclear Physics* **22** (1961), no. 4, 579 – 588, `doi:http://dx.doi.org/10.1016/0029-5582(61)90469-2`.

[45] A. Salam and J. Ward, "Electromagnetic and weak interactions", *Physics Letters* **13** (1964), no. 2, 168 – 171, `doi:http://dx.doi.org/10.1016/0031-9163(64)90711-5`.

[46] Nobelprize.org, "The Nobel Prize in Physics 1957". URL `http://www.nobelprize.org/nobel_prizes/physics/laureates/1957/`.

[47] N. Cabibbo, "Unitary Symmetry and Leptonic Decays", *Phys. Rev. Lett.* **10** (Jun, 1963) 531–533, `doi:10.1103/PhysRevLett.10.531`.

[48] M. Kobayashi and T. Maskawa, "CP Violation in the Renormalizable Theory of Weak Interaction", *Prog.Theor.Phys.* **49** (1973) 652–657, `doi:10.1143/PTP.49.652`.

[49] S. L. Glashow, J. Iliopoulos, and L. Maiani, "Weak Interactions with Lepton-Hadron Symmetry", *Phys. Rev. D* **2** (Oct, 1970) 1285–1292, `doi:10.1103/PhysRevD.2.1285`.

[50] G. Arnison et al., "Experimental observation of isolated large transverse energy electrons with associated missing energy at s=540 GeV", *Physics Letters B* **122** (1983), no. 1, 103 – 116, `doi:http://dx.doi.org/10.1016/0370-2693(83)91177-2`.

[51] G. Arnison et al., “Experimental observation of lepton pairs of invariant mass around 95 GeV/c2 at the {CERN} {SPS} collider”, *Physics Letters B* **126** (1983), no. 5, 398 – 410, doi:http://dx.doi.org/10.1016/0370-2693(83)90188-0.

[52] M. Banner et al., “Observation of single isolated electrons of high transverse momentum in events with missing transverse energy at the {CERN} pp collider”, *Physics Letters B* **122** (1983), no. 56, 476 – 485, doi:http://dx.doi.org/10.1016/0370-2693(83)91605-2.

[53] P. Bagnaia et al., “Evidence for Z0e+e at the {CERN} pp collider”, *Physics Letters B* **129** (1983), no. 12, 130 – 140, doi:http://dx.doi.org/10.1016/0370-2693(83)90744-X.

[54] The ALEPH, DELPHI, L3, OPAL, SLD Collaborations, the LEP Electroweak Working Group, the SLD Electroweak and Heavy Flavour Groups, “Precision Electroweak Measurements on the Z Resonance”, *Phys. Rept.* **427** (2006) 257, arXiv:hep-ex/0509008.

[55] The ALEPH, DELPHI, L3, OPAL Collaborations, the LEP Electroweak Working Group, “Electroweak Measurements in Electron-Positron Collisions at W-Boson-Pair Energies at LEP”, *Phys. Rept.* **532** (2013) 119, arXiv:1302.3415.

[56] “Image, LEP ZPole”. URL http://lepewwg.web.cern.ch/LEPEWWG/1/Nnu.eps.

[57] “Image, CDF Top Quark Mass”. URL http://www-cdf.fnal.gov/physics/new/top/public_mass.html.

[58] TEVNPH (Tevatron New Phenomina and Higgs Working Group), CDF, D0 Collaboration, “Combined CDF and D0 Upper Limits on Standard Model Higgs Boson Production with up to 8.6 fb^{-1} of Data”, arXiv:1107.5518.

[59] “Image, CMS Higgs Mass”. URL http://cms-higgs-results.web.cern.ch/cms-higgs-results/Comb/HIG-14-009-Paper/sqr_mass_all.pdf.

[60] F. Abe et al., “Observation of Top Quark Production in $\overline{p}p$ Collisions with the Collider Detector at Fermilab”, *Phys. Rev. Lett.* **74** (Apr, 1995) 2626–2631, doi:10.1103/PhysRevLett.74.2626.

[61] S. Abachi et al., “Search for High Mass Top Quark Production in $p\overline{p}$ Collisions at $\sqrt{s} =$ 1.8 TeV”, *Phys. Rev. Lett.* **74** (Mar, 1995) 2422–2426, doi:10.1103/PhysRevLett.74.2422.

[62] LHC Higgs Cross Section Working Group Collaboration, "Handbook of LHC Higgs Cross Sections: 3. Higgs Properties", doi:10.5170/CERN-2013-004, arXiv:1307.1347.

[63] W. Beenakker et al., "Higgs radiation off top quarks at the Tevatron and the LHC", *Phys.Rev.Lett.* **87** (2001) 201805, doi:10.1103/PhysRevLett.87.201805, arXiv:hep-ph/0107081.

[64] W. Beenakker et al., "NLO QCD corrections to t anti-t H production in hadron collisions", *Nucl.Phys.* **B653** (2003) 151–203, doi:10.1016/S0550-3213(03)00044-0, arXiv:hep-ph/0211352.

[65] R. Frederix et al., "Scalar and pseudoscalar Higgs production in association with a top-antitop pair", *Phys.Lett.* **B701** (2011) 427–433, doi:10.1016/j.physletb.2011.06.012, arXiv:1104.5613.

[66] M. Garzelli, A. Kardos, C. Papadopoulos, and Z. Trocsanyi, "Standard Model Higgs boson production in association with a top anti-top pair at NLO with parton showering", *Europhys.Lett.* **96** (2011) 11001, doi:10.1209/0295-5075/96/11001, arXiv:1108.0387.

[67] S. Dawson, L. Orr, L. Reina, and D. Wackeroth, "Associated top quark Higgs boson production at the LHC", *Phys.Rev.* **D67** (2003) 071503, doi:10.1103/PhysRevD.67.071503, arXiv:hep-ph/0211438.

[68] T. Gleisberg et al., "Event generation with SHERPA 1.1", *JHEP* **0902** (2009) 007, doi:10.1088/1126-6708/2009/02/007, arXiv:0811.4622.

[69] P. Artoisenet, R. Frederix, O. Mattelaer, and R. Rietkerk, "Automatic spin-entangled decays of heavy resonances in Monte Carlo simulations", *JHEP* **1303** (2013) 015, doi:10.1007/JHEP03(2013)015, arXiv:1212.3460.

[70] F. Cascioli, P. Maierhofer, and S. Pozzorini, "Scattering Amplitudes with Open Loops", *Phys.Rev.Lett.* **108** (2012) 111601, doi:10.1103/PhysRevLett.108.111601, arXiv:1111.5206.

[71] F. Krauss, R. Kuhn, and G. Soff, "AMEGIC++ 1.0: A Matrix element generator in C++", *JHEP* **0202** (2002) 044, doi:10.1088/1126-6708/2002/02/044, arXiv:hep-ph/0109036.

[72] T. Gleisberg and F. Krauss, "Automating dipole subtraction for QCD NLO calculations", *Eur.Phys.J.* **C53** (2008) 501–523, doi:10.1140/epjc/s10052-007-0495-0, arXiv:0709.2881.

[73] Planck Collaboration, “Planck 2013 results. I. Overview of products and scientific results”, *Astron.Astrophys.* **571** (2014) A1, `doi:10.1051/0004-6361/201321529`, `arXiv:1303.5062`.

[74] V. Rubin, N. Thonnard, and J. Ford, W.K., “Rotational properties of 21 SC galaxies with a large range of luminosities and radii, from NGC 4605 /R = 4kpc/ to UGC 2885 /R = 122 kpc/”, *Astrophys.J.* **238** (1980) 471, `doi:10.1086/158003`.

[75] Super-Kamiokande Collaboration Collaboration, “Measurements of the solar neutrino flux from Super-Kamiokande’s first 300 days”, *Phys.Rev.Lett.* **81** (1998) 1158–1162, `doi:10.1103/PhysRevLett.81.1158`, `arXiv:hep-ex/9805021`.

[76] KamLAND Collaboration Collaboration, “Measurement of neutrino oscillation with KamLAND: Evidence of spectral distortion”, *Phys.Rev.Lett.* **94** (2005) 081801, `doi:10.1103/PhysRevLett.94.081801`, `arXiv:hep-ex/0406035`.

[77] MINOS Collaboration Collaboration, “Observation of muon neutrino disappearance with the MINOS detectors and the NuMI neutrino beam”, *Phys.Rev.Lett.* **97** (2006) 191801, `doi:10.1103/PhysRevLett.97.191801`, `arXiv:hep-ex/0607088`.

[78] S. P. Martin, “A Supersymmetry primer”, *Adv.Ser.Direct.High Energy Phys.* **21** (2010) 1–153, `doi:10.1142/9789814307505_0001`, `arXiv:hep-ph/9709356`.

[79] J. Aguilar-Saavedra, R. Benbrik, S. Heinemeyer, and M. Prez-Victoria, “Handbook of vectorlike quarks: Mixing and single production”, *Phys.Rev.* **D88** (2013), no. 9, 094010, `doi:10.1103/PhysRevD.88.094010`, `arXiv:1306.0572`.

[80] G. Burdman, M. Perelstein, and A. Pierce, “Large Hadron Collider tests of a little Higgs model”, *Phys.Rev.Lett.* **90** (2003) 241802, `doi:10.1103/PhysRevLett.90.241802`, `arXiv:hep-ph/0212228`.

[81] M. Perelstein, M. E. Peskin, and A. Pierce, “Top quarks and electroweak symmetry breaking in little Higgs models”, *Phys.Rev.* **D69** (2004) 075002, `doi:10.1103/PhysRevD.69.075002`, `arXiv:hep-ph/0310039`.

[82] H.-C. Cheng, I. Low, and L.-T. Wang, “Top partners in little Higgs theories with T parity”, *Phys. Rev. D* **74** (Sep, 2006) 055001, `doi:10.1103/PhysRevD.74.055001`.

[83] H.-C. Cheng, B. A. Dobrescu, and C. T. Hill, “Electroweak symmetry breaking and extra dimensions”, *Nucl.Phys.* **B589** (2000) 249–268, `doi:10.1016/S0550-3213(00)00401-6`, `arXiv:hep-ph/9912343`.

[84] M. S. Carena, E. Ponton, J. Santiago, and C. E. Wagner, "Light Kaluza Klein States in Randall-Sundrum Models with Custodial SU(2)", *Nucl.Phys.* **B759** (2006) 202–227, doi:10.1016/j.nuclphysb.2006.10.012, arXiv:hep-ph/0607106.

[85] C. T. Hill, "Topcolor: Top quark condensation in a gauge extension of the standard model", *Phys.Lett.* **B266** (1991) 419–424, doi:10.1016/0370-2693(91)91061-Y.

[86] R. Contino, L. Da Rold, and A. Pomarol, "Light custodians in natural composite Higgs models", *Phys.Rev.* **D75** (2007) 055014, doi:10.1103/PhysRevD.75.055014, arXiv:hep-ph/0612048.

[87] "CERN Linac2 Duoplasmatron Schematic". URL http://linac2.home.cern.ch/linac2/sources/source.htm.

[88] "CERN Linac2 Duoplasmatron Image". URL http://linac2.web.cern.ch/linac2/CF002521-ProtonSourceDuoplasmatronRichardChristianss.jpg.

[89] "RFQ Schematic". URL http://www.lnl.infn.it/images/acc_fig14.jpg.

[90] "Example RFQ Image". URL http://www.toyama-en.com/accelerator/images/rfq_downstream_webLarge.jpg.

[91] "Inside an Alvarez Tube". URL https://cds.cern.ch/record/1281668/files/DTL_proto_assembled_image.jpg?subformat=icon.

[92] "CERN Linac2 Alvarez Tubes". URL http://www.toyama-en.com/accelerator/images/rfq_downstream_webLarge.jpg.

[93] M. Benedikt et al., "LHC Design Report Vol3 - The Injection Chain". CERN, Geneva, 2004.

[94] C. Hill et al., "Tests of the CERN proton linac performance for LHC - type beams", *eConf* **C000821** (2000) TUD17, arXiv:physics/0008102.

[95] "Image, CERN PSbooster injection from Linac2". URL http://www.lhc-facts.ch/img/psb/psb_injektion.jpg.

[96] "Image, CERN PSbooster is 4 verticaly stacked synchotrons". URL http://www.lhc-facts.ch/img/psb/psb.jpg.

[97] "Image, CERN PSbooster Layout". URL http://psb-machine.web.cern.ch/psb-machine/layout.gif.

[98] "Image, CERN PSbooster Section 10 Layout". URL http://psb-machine.web.cern.ch/psb-machine/sectors/sect10.gif.

[99] "Image, CERN PSbooster CO2 RF Cavity". URL http://cern-accelerators-optics.web.cern.ch/cern-accelerators-optics/PS_BOOSTER/Pictures/P10L1.JPG.

[100] "Image, CERN PSbooster 2 batch filling scheme of the PS". URL http://ps-div.web.cern.ch/ps-div/LHC-PS/schindlrf.gif.

[101] K. S. Klaus Hanke, and Michel Chanel.

[102] "Image, CERN PSbooster Layout". URL http://psb-machine.web.cern.ch/psb-machine/.

[103] S. Baird, "Accelerators for pedestrians; rev. version", Technical Report AB-Note-2007-014. CERN-AB-Note-2007-014. PS-OP-Note-95-17-Rev-2. CERN-PS-OP-Note-95-17-Rev-2, CERN, Geneva, Feb, 2007.

[104] "Image, CERN PS Layout". URL http://psring.web.cern.ch/psring/psring/pscomplex.gif.

[105] "Image, CERN PS Dipoles". URL http://home.web.cern.ch/sites/home.web.cern.ch/files/styles/medium/public/image/accelerator/2013/01/accelerators-ps.jpg?itok=5E3Tp4Q0.

[106] "Image, CERN SPS, Layout". URL https://espace.cern.ch/be-dep/OP/sps/pictures/sps2.PNG.

[107] "Image, CERN SPS Beamline". URL http://home.web.cern.ch/sites/home.web.cern.ch/files/styles/medium/public/image/accelerator/2013/01/sps.jpg?itok=iLnNGjdI.

[108] "Image, CERN SPS, Inside 200 MHz RF Cavity". URL http://rsta.royalsocietypublishing.org/content/roypta/370/1973/3887/F24.large.jpg?width=800&height=600&carousel=1.

[109] "Image, CERN SPS 200 MHz RF Cavity". URL https://cds.cern.ch/record/969086/files/7505156X.jpg?subformat=icon-1440.

[110] "CERN Website, Super Proton Synchrotron". URL http://home.web.cern.ch/about/accelerators/super-proton-synchrotron.

[111] G. Dme, "The SPS acceleration system travelling wave drift-tube structure for the CERN SPS",.

[112] O. S. Brning et al., "LHC Design Report Vol1 - The Main Ring". CERN, Geneva, 2004.

[113] "CERN, List of All LHC Magnets". URL `http://lhc-machine-outreach.web.cern.ch/lhc-machine-outreach/components/magnets/types_of_magnets.htm`.

[114] M. Barnes, J. Borburgh, B. Goddard, and M. Hourican, "Injection and extraction magnets: septa", `arXiv:1103.1062`.

[115] "Image, CERN LHC, Dipole Magnet, Dual Bore". URL `http://lhc-machine-outreach.web.cern.ch/lhc-machine-outreach/components/magnets_files/image002.jpg`.

[116] "Image, CERN LHC, Dipole Magnet, field". URL `http://lhc-machine-outreach.web.cern.ch/lhc-machine-outreach/images/dipole-field.gif`.

[117] J. Beauquis, "LHC Dipole Geometry Parameters, Comparisons between Producers", *eConf* **C04100411** (2004) 046.

[118] "Image, CERN LHC, Dipole Magnet, Staging Area". URL `https://cds.cern.ch/record/994212/files/transp-2001-001_05.jpg?subformat=icon-1440`.

[119] "Image, CERN LHC, Quadrupole Magnet, Cross Section Schematic". URL `https://cds.cern.ch/record/841485`.

[120] "Image, CERN LHC, Quadrupole Magnet, Staging Area". URL `http://www.triumf.ca/sites/default/files/images/twinquadrupolemagnets.preview.jpg`.

[121] "Image, CERN LHC, Quadrupole Magnet, Focusing Schematic". URL `http://www.lhc-closer.es/img/subidas/4_6_3_3.png`.

[122] "Image, CERN LHC, Multipole Magnet, Focusing Schematic". URL `http://www.lhc-closer.es/img/subidas/Multipoles.jpg`.

[123] "Image, CERN LHC, Magnetic Cell Layout". URL `http://www.lhc-closer.es/img/subidas/4_6_3_4.png`.

[124] "Image, CERN LHC, Interaction Region Schematic". URL `http://www.lhc-closer.es/img/subidas/4_6_3_6.jpg`.

[125] J.-L. Caron, "Superconducting cavity with its cryostat. Cavit supraconductrice dans son cryostat.", May, 1994. AC Collection. Legacy of AC. Pictures from 1992 to 2002.

[126] "Image, CERN LHC, Superconducting RF Cavities, Staged". URL `http://www.lhc-closer.es/img/subidas/4_7_2_2.jpg`.

[127] "Image, CERN LHC, Superconducting RF Cavities, Installed". URL http://home.web.cern.ch/sites/home.web.cern.ch/files/image/engineering_page/2013/01/rf-cavity.jpg.

[128] "Outreach, CERN LHC, Cryogenic System". URL http://home.web.cern.ch/about/engineering/cryogenics-low-temperatures-high-performance.

[129] "The challenge of keeping cool",.

[130] "Outreach, CERN LHC, Vacuum System". URL http://home.web.cern.ch/about/engineering/vacuum-empty-interplanetary-space.

[131] "Image, CMS, Tracker Strip Efficiency". URL https://twiki.cern.ch/twiki/pub//CMSPublic/DPGResultsTRK/efficiency_end2010.png.

[132] "Image, CMS, Tracker Strip Resolution". URL https://twiki.cern.ch/twiki/pub//CMSPublic/DPGResultsTRK/StripHitRes2.gif.

[133] "Image, CMS, ECAL VPT with pen for scale". URL http://hepwww.rl.ac.uk/CMSecal/Meetings/2005/VPT_RIE_front.jpg.

[134] R. M. Brown et al., "The vacuum phototriodes for the CMS electromagnetic calorimeter", *PoS* **HEP2001** (2001) 255.

[135] CMS Collaboration, "Description and performance of track and primary-vertex reconstruction with the CMS tracker", *JINST* **9** (2014), no. 10, P10009, doi:10.1088/1748-0221/9/10/P10009, arXiv:1405.6569.

[136] R. Fruhwirth, "Application of Kalman filtering to track and vertex fitting", *Nucl.Instrum.Meth.* **A262** (1987) 444–450, doi:10.1016/0168-9002(87)90887-4.

[137] CMS Electromagnetic Calorimeter Group Collaboration, "Intercalibration of the barrel electromagnetic calorimeter of the CMS experiment at start-up", *JINST* **3** (2008) P10007, doi:10.1088/1748-0221/3/10/P10007.

[138] K. Cankocak, Y. Onel, P. de Barbaro, and D. Vishnevskiy, "CMS HCAL Installation and Commissioning", Technical Report CMS-CR-2008-047, CERN, Geneva, Jul, 2008.

[139] CMS Collaboration Collaboration, "Commissioning of the CMS ECAL calibration with muons from cosmic rays and beam dumps", Technical Report CMS-CR-2009-339, CERN, Geneva, Nov, 2009.

[140] CMS Collaboration Collaboration, "Performance of the CMS Hadron Calorimeter with Cosmic Ray Muons and LHC Beam Data", *J. Instrum.* **5** (Nov, 2009) T03012 . 35 p.

[141] CMS Collaboration Collaboration, "HCAL performance from first collisions data",.

[142] "Image, CMS, Muon Partlicle-Flow Commissioning". URL `https://twiki.cern.ch/twiki/bin/view/CMSPublic/PhysicsResultsMUO`.

[143] CMS Collaboration Collaboration, "Particle-flow commissioning with muons and electrons from J/Psi and W events at 7 TeV", Technical Report CMS-PAS-PFT-10-003, CERN, 2010. Geneva, 2010.

[144] W. Adam, R. Frhwirth, A. Strandlie, and T. Todor, "Reconstruction of Electrons with the Gaussian-Sum Filter in the CMS Tracker at the LHC",.

[145] "Image, CMS, Electron Partlicle-Flow Commissioning". URL `https://twiki.cern.ch/twiki/bin/view/CMSPublic/EGMElectronsMoriond2010`.

[146] CMS Collaboration, "Electromagnetic calorimeter calibration with 7 TeV data",.

[147] Particle Data Group Collaboration, "Review of Particle Physics", *Chin.Phys.* **C38** (2014) 090001, `doi:10.1088/1674-1137/38/9/090001`.

[148] A. Schalicke et al., "Geant4 electromagnetic physics for the LHC and other HEP applications", *J.Phys.Conf.Ser.* **331** (2011) 032029, `doi:10.1088/1742-6596/331/3/032029`.

[149] "MET Optional Filters". `https://twiki.cern.ch/twiki/bin/view/CMS/MissingETOptionalFilters`.

[150] CMS Collaboration, "Jet Energy Resolution in CMS at sqrt(s)=7 TeV",.

[151] C. Weiser, "A Combined Secondary Vertex Based B-Tagging Algorithm in CMS", Technical Report CMS-NOTE-2006-014, CERN, Geneva, Jan, 2006.

[152] "Operating Points for b-Tag Algorithms". `https://twiki.cern.ch/twiki/bin/viewauth/CMS/BTagPerformanceOP`.

[153] "b-Jet Identification in the CMS Experiment",.

[154] VHbb Team, "Search for the SM Higgs Boson Produced in Association with W or Z and Decaying to Bottom Quarks (ICHEP 2012)", CMS Note 2012/181, 2012.

[155] A. Hocker et al., "TMVA - Toolkit for Multivariate Data Analysis", *PoS* **ACAT** (2007) 040, `arXiv:physics/0703039`.

[156] J. D. Bjorken and S. J. Brodsky, "Statistical Model for Electron-Positron Annihilation into Hadrons", *Phys. Rev. D* **1** (1970) 1416, `doi:10.1103/PhysRevD.1.1416`.

[157] G. C. Fox and S. Wolfram, “Event Shapes in $e^{+}e^{-}$ Annihilation”, *Nucl. Phys. B* **149** (1979) 413, doi:10.1016/0550-3213(79)90003-8.

[158] “Jet Energy Scale Uncertainties”. https://twiki.cern.ch/twiki/bin/view/CMSPublic/WorkBookJetEnergyCorrections.

[159] “Jet Energy Resolution Uncertainties”. https://twiki.cern.ch/twiki/bin/view/CMS/JetResolution.

[160] “b-Tag Scale Factor Uncertainties”. https://twiki.cern.ch/twiki/bin/viewauth/CMS/BtagPOG.

[161] T. Peiffer., “Q^2 Systematic MC Samples re-weighting”. https://indico.cern.ch/getFile.py/access?contribId=5&resId=0&materialId=slides&confId=177717, 2012.

[162] R. Barlow and C. Beeston, “Fitting using finite Monte Carlo samples”, *Computer Physics Communications* **77** (1993) 219–228.

[163] J. S. Conway, “Incorporating Nuisance Parameters in Likelihoods for Multisource Spectra”, (2011). arXiv:1103.0354.

[164] A. Bredenstein, A. Denner, S. Dittmaier, and S. Pozzorini, “NLO QCD corrections to top anti-top bottom anti-bottom production at the LHC: 2. full hadronic results”, (2010). arXiv:1001.4006.

[165] The ATLAS Collaboration, The CMS Collaboration, The LHC Higgs Combination Group Collaboration, “Procedure for the LHC Higgs boson search combination in Summer 2011”, Technical Report CMS-NOTE-2011-005. ATL-PHYS-PUB-2011-11, CERN, Geneva, Aug, 2011.

[166] J. Conway, “Incorporating Nuisance Parameters in Likelihoods for Multisource Spectra”, arXiv:1103.0354.

[167] G. Cowan, K. Cranmer, E. Gross, and O. Vitells, “Asymptotic formulae for likelihood-based tests of new physics”, *Eur.Phys.J.* **C71** (2011) 1554, doi:10.1140/epjc/s10052-011-1554-0,10.1140/epjc/s10052-013-2501-z, arXiv:1007.1727.

[168] CMS Collaboration, “Search for the standard model Higgs boson produced in association with a top-quark pair in pp collisions at the LHC”, *JHEP* **1305** (2013) 145, doi:10.1007/JHEP05(2013)145, arXiv:1303.0763.

[169] CMS Collaboration, "Measurement of the differential top-quark pair production cross section in the dilepton channel in pp collisions at $\sqrt{7} = 8$ TeV.", CMS PAS TOP-12-028, 2012.

[170] CMS Collaboration, "Measurement of the differential top-quark pair production cross section in the lepton+jets channel in pp collisions at $\sqrt{7} = 8$ TeV.", CMS PAS TOP-12-027, 2012.

[171] CMS Collaboration, "Calibration of the Combined Secondary Vertex b-Tagging discriminant using dileptonic ttbar and Drell-Yan events", CMS Note 2013/130, 2013.

[172] CMS Collaboration, "Dilepton trigger and lepton identification efficiencies for the top quark pair production cross section measurement at 8 TeV in the dilepton decay channel.", CMS AN AN-12-389, 2012.

[173] CMS Collaboration, "Search for the associated production of the Higgs boson with a top-quark pair", *JHEP* **1409** (2014) 087, doi:10.1007/JHEP09(2014)087,10.1007/JHEP10(2014)106, arXiv:1408.1682.

[174] J. Alwall et al., "The automated computation of tree-level and next-to-leading order differential cross sections, and their matching to parton shower simulations", *JHEP* **1407** (2014) 079, doi:10.1007/JHEP07(2014)079, arXiv:1405.0301.

[175] P. Artoisenet, R. Frederix, O. Mattelaer, and R. Rietkerk, "Automatic spin-entangled decays of heavy resonances in Monte Carlo simulations", *JHEP* **1303** (2013) 015, doi:10.1007/JHEP03(2013)015, arXiv:1212.3460.

[176] T. Sjostrand, S. Mrenna, and P. Z. Skands, "A Brief Introduction to PYTHIA 8.1", *Comput.Phys.Commun.* **178** (2008) 852–867, doi:10.1016/j.cpc.2008.01.036, arXiv:0710.3820.

[177] R. Frederix and S. Frixione, "Merging meets matching in MC@NLO", *JHEP* **1212** (2012) 061, doi:10.1007/JHEP12(2012)061, arXiv:1209.6215.

List of Acronyms

ATLAS A Toroidal LHC Apparatus

BSM Beyond the Standard Model

CERN European Center for Nuclear Research

CMS Compact Muon Solenoid

ECAL Electromagnetic Calorimeter

FSR Final State Radiation

HCAL Hadronic Calorimeter

ISR Initial State Radiation

JHEP Journal of High Energy Physics

LHC Large Hadron Collider

LO Leading Order

MVA Multi-Variate Analysis

NLO Next to Leading Order

QCD Quantum Chromodynamics

QED Quantum Electrodynamics

QFT Quantum Field Theory

SM Standard Model